To the Graduate Council:

I am submitting herewith a thesis written by Kalia Kothandapany entitled "Effect Of Nb Concentration on the $\gamma^{\circ} \rightarrow \alpha$" Martensitic Reaction in U-Nb Alloys." I have examined the final copy of this thesis for form and content and recommend that it be accepted in partial fulfillment of the requirements for the degree of Master of Science, with a major in Metallurgical Engineering.

Charlie R. Brooks

C.R.Brooks, Major Professor

We have read this thesis
and recommend its acceptance:

Medvazza

J E Spruell

Accepted for the Council:

Lewis Winkel

Vice Provost
and Dean of The Graduate School

STATEMENT OF PERMISSION TO USE

In presenting this thesis in partial fulfillment of the requirements for a Master's degree at The University of Tennessee, Knoxville, I agree that the Library shall make it available to borrowers under rules of the library. Brief quotations from this thesis are allowable without special permission, provided that accurate acknowledgment of the source is made. Permission for extensive quotation from or reproduction of this thesis may be granted by my major professor, or in his absence, by the Head of Interlibrary Services when, in the opinion of either, the proposed use of the material is for scholarly purposes. Any copying or use of the material in this thesis for financial gain shall not be allowed without my written permission.

Signature Kalia Trumbull

Date 3/6/87

EFFECT OF NB CONCENTRATION ON THE γ°---> α'' MARTENSITIC TRANSFORMATION IN U+NB ALLOYS

A Thesis

Presented For The

Master Of Science

Degree

The University Of Tennessee, Knoxville

Kalia Kothandapany

March 1987

ACKNOWLEDGMENTS

The author wishes to thank Dr.R.A.Vandermeer and Dr.C.R.Brooks for their support and guidance in this research. Appreciation is extended to Dr.J.E.Spruiell for his help and assistance in completing this thesis. Appreciation is also extended to Professor A.J.Pedraza for serving in the thesis committee.

ABSTRACT

The martensitic reaction in five Uranium-Nb alloys (14.5,15.0, 15.5, 15.5, and 16.0 at% Nb) was studied by means of x-ray diffraction experiments in order to establish the temperature range of this reaction. The experiments were carried out in a cryostat on a diffractometer in which minimum temperatures close to liquid N_2 temperature were obtained. All the samples were solution heat treated at 800°C and water quenched. They were then electropolished prior to diffraction experiments. The diffraction patterns were taken from about 25°C down to about -190°C. The intensity-Bragg angle data were digitized and the relative amounts of the parent phase $\gamma°$ and the martensite phase α'' were determined by means of a peak separation and analysis program.

The 14.5 at% Nb alloy was completely martensitic at 25°C, and the 16.0 at% Nb alloy remained completely $\gamma°$ phase down to -192°C. For the other alloys, as the temperature decreased, the amount of the martensitic α'' phase increased, and that of $\gamma°$ decreased. For all three alloys, the M_f temperature was below the lowest temperature of measurement (-192°C), and the M_S was above 25°C. At a given temperature, the amount of α'' decreased with increasing Nb content.

TABLE OF CONTENTS

SECTION PAGE

1. INTRODUCTION....1
2. LITERATURE SURVEY....3
3. EXPERIMENTAL PROCEDURE....39
4. THEORY OF PHASE FRACTION DETERMINATION....46
5. CALCULATION OF PHASE FRACTION....50
6. RESULTS AND DISCUSSION....74
7. CONCLUSION AND RECOMMENDATIONS....82

REFERENCES....84

APPENDIX....88

VITA....169

LIST OF TABLES

TABLE		PAGE
1.	X-ray identification of phases produced in U-Nb alloys after fast and slow cooling rates from the gamma phase and the values of crystalline parameters in water-quenched alloys	6
2.	Quench rate dependency of transformation temperatures for a U + Nb alloy	29
3.	Comparison of the E values for two diffraction patterns at +22° C and -40° C	58
4.	Optimization for $\delta 2\theta$	67
A.1.	Compositions of the five U-Nb alloys	89
A.2.	Chemical analysis of alloys 183, 196, and 198	90
A.3.	The calculated and observed d values for the observed hkl's	93
A.4.	The input parameters 2θ, H, S, and I shown with their initial experimental values and the computer calculated final values along with the E's of each peak(h k l's) determined by the computer	94
A.5.	The h k l's, E's and R's that were used for phase fraction determination from first analysis (Table A.4)	101
A.6.	The input parameters 2θ, H, S, and I shown with their initial experimental values and the computer calculated final values along with the E's of each peak(h k l's) determined by the computer after optimization of incremental input parameter values	105
A.7.	The α" and γ° phase fractions calculated at various temperatures	112

LIST OF FIGURES

FIGURE		PAGE
1.	Corrugated layer of α-uranium atoms	8
2.	The 12 nearest neighbours of U atom	8
3.	Primitive cell γ° generated from γ	11
4.	Projection of atoms in bcc structure on to a {110} bcc plane showing the sequence of {112} bcc planes	15
5.	Variation of structure parameter and monoclinic angle with composition	17
6.	Structural relationship between bcc γ and α"	18
7.	A [110] projection of the bcc lattice points with the various unit cells and lattice parameters defined	20
8.	A plot of the $\hat{\gamma}$ angle versus at% Nb	20
9.	A plot of the c lattice parameter versus at% Nb	21
10.	The U-Nb phase diagram	23
11.	Modelistic explanation for the consecutiveness and the thermal reversibilty of the γ <--> γ° <--> α" <--> α' transformation	26
12.	Constrictive curve, i.e., plot of change in length versus temperature, for the U+14 at% Nb helium-gas-quenched from the γ phase at a fast rate	27
13.	Plot of CTE versus temperature for the U + 14 at% Nb, helium-gas-quenched from the γ phase at a moderate rate	27
14.	Effect of accumulated aging time at 600 K on the nature of the anomalous constriction during subsequent helium-gas-quench	31
15.	Isothermal and athermal nature of γ --> γ° --> α" reaction	32
16.	Metastable transition phase diagram for U-Nb alloys near the monotectoid compositions	34
17.	A group x-ray diffractometer scans depicting the effect of deformation on the transformation of γ° to α"	36
18.	The effect of strain on the $\hat{\gamma}$ angle during the stress-assisted γ° to α" transformation	37

FIGURE PAGE

19. The shape change involved in the γ° to α'' phase change based on the new lattice parameter measurements, is shown in terms of the unit cell change....38

20. A plot of volume fraction of α'' versus strain....38

21. Hot rolled plate of 15.24 cm x 1.59 cm crossection....41

22. Cold rolled plate for x-ray diffraction samples....41

23. Plot of f,the scattering factor versus $\sin\theta / \lambda$ for U and Nb atoms....51

24. Illustration of the curve fit by the computer for a diffraction pattern 54

25. Illustration of the curve fit by the computer for the same diffraction pattern as in Fig.24 after varying the input incremental values....55

26. The computer generated curve fit at +22°C....56

27. The computer generated curve fit at -40°C.... 57

28. The variation of % α'' with temperature as determined by the three methods for alloys 142, 183 and 196....60

29. The computer generated curve fit for the diffraction pattern when $\delta\theta = 0.1$....64

30. The computer generated curve fit for the diffraction pattern when $\delta\theta = 0.01$.... 65

31. The computer generated curve fit for the diffraction pattern when $\delta\theta = 0.001$....66

32. Comparison of % α'' Vs temperature variation for alloys 142, 183 and 196 before and after optimization of the incremental values of the input parameters....69

33. Variation of % α'' with temperature at different Nb content....78

34. Variation of % α'' with Nb content at two different temperature range....80

35. An approximate transition metastable phase diagram....81

A.1. Computer generated diffraction pattern curve fit for alloy 142 at +22°C....113

A.2. Computer generated diffraction pattern curve fit for alloy 142 at -40°C....114

FIGURE PAGE

A.3 Computer generated diffraction pattern curve fit for alloy 142 at -80°C....115

A.4. Computer generated diffraction pattern curve fit for alloy 142 at -120°C....116

A.5. Computer generated diffraction pattern curve fit for alloy 142 at -154°C....117

A.6. Computer generated diffraction pattern curve fit for alloy 142 at -187°C....118

A.7. Computer generated diffraction pattern curve fit for alloy 183 at +22°C....119

A.8. Computer generated diffraction pattern curve fit for alloy 183 at -40°C....120

A.9. Computer generated diffraction pattern curve fit for alloy 183 at -81°C....121

A.10. Computer generated diffraction pattern curve fit for alloy 183 at -121°C....122

A.11. Computer generated diffraction pattern curve fit for alloy 183 at -161°C....123

A.12. Computer generated diffraction pattern curve fit for alloy 183 at -190°C....124

A.13. Computer generated diffraction pattern curve fit for alloy 196 at +25°C....125

A.14. Computer generated diffraction pattern curve fit for alloy 196 at -40°C....126

A.15. Computer generated diffraction pattern curve fit for alloy 196 at -80°C....127

A.16. Computer generated diffraction pattern curve fit for alloy 196 at -123°C....128

A.17. Computer generated diffraction pattern curve fit for alloy 196 at -189°C....129

A.18. Computer generated diffraction pattern curve fit for alloy 142, after optimization, at +22°C....130

FIGURE PAGE

A.19. Computer generated diffraction pattern curve fit for alloy 142, after optimization, at -40°C....131

A.20. Computer generated diffraction pattern curve fit for alloy 142, after optimization, at -80°C....132

A.21. Computer generated diffraction pattern curve fit for alloy 142, after optimization, at -120°C....133

A.22. Computer generated diffraction pattern curve fit for alloy 142, after optimization, at -154°C....134

A.23. Computer generated diffraction pattern curve fit for alloy 142, after optimization, at -187°C....135

A.24. Computer generated diffraction pattern curve fit for alloy 183, after optimization, at +22°C....136

A.25. Computer generated diffraction pattern curve fit for alloy 183, after optimization, at -40°C....137

A.26. Computer generated diffraction pattern curve fit for alloy 183, after optimization, at -81°C....138

A.27. Computer generated diffraction pattern curve fit for alloy 183, after optimization, at -121°C....139

A.28. Computer generated diffraction pattern curve fit for alloy 183, after optimization, at -161°C....140

A.29. Computer generated diffraction pattern curve fit for alloy 183, after optimization, at -190°C....141

A.30. Computer generated diffraction pattern curve fit for alloy 196, after optimization, at +25°C....142

A.31. Computer generated diffraction pattern curve fit for alloy 196, after optimization, at -40°C....143

A.32. Computer generated diffraction pattern curve fit for alloy 196, after optimization, at -80°C....144

A.33. Computer generated diffraction pattern curve fit for alloy 196, after optimization, at -123°C....145

A.34. Computer generated diffraction pattern curve fit for alloy 196, after optimization, at -189°C....146

FIGURE PAGE

A.35. Diffraction pattern of alloy 142 (15.0 at% Nb) at +22°C.....147

A.36. Diffraction pattern of alloy 142 (15.0 at% Nb) at -40°C.....148

A.37. Diffraction pattern of alloy 142 (15.0 at% Nb) at -80° C.....149

A.38. Diffraction pattern of alloy 142 (15.0 at% Nb) at -120° C.....150

A.39. Diffraction pattern of alloy 142 (15.0 at% Nb) at -154° C.....151

A.40. Diffraction pattern of alloy 142 (15.0 at% Nb) at -187° C.....152

A.41. Diffraction pattern of alloy 183 (15.5* at% Nb) at +22° C.....153

A.42. Diffraction pattern of alloy 183 (15.5* at% Nb) at -40° C.....154

A.43. Diffraction pattern of alloy 183 (15.5* at% Nb) at -81° C.....155

A.44. Diffraction pattern of alloy 183 (15.5* at% Nb) at -121° C.....156

A.45. Diffraction pattern of alloy 183 (15.5* at% Nb) at -161° C.....157

A.46. Diffraction pattern of alloy 183 (15.5* at% Nb) at -190° C.....158

A.47. Diffraction pattern of alloy 196 (15.5** at% Nb) at +25° C.....159

A.48. Diffraction pattern of alloy 196 (15.5** at% Nb) at -40° C.....160

A.49. Diffraction pattern of alloy 196 (15.5** at% Nb) at -80° C.....161

A.50. Diffraction pattern of alloy 196 (15.5** at% Nb) at -123° C.....162

A.51. Diffraction pattern of alloy 196 (15.5** at% Nb) at -189° C.....163

A.52. Diffraction pattern of alloy 198 (16.0 at% Nb) at +22° C.....164

A.53. Diffraction pattern of alloy 198 (16.0 at% Nb) at -40° C.....165

A.54. Diffraction pattern of alloy 198 (16.0 at% Nb) at -80° C.....166

A.55. Diffraction pattern of alloy 198 (16.0 at% Nb) at -120° C.....167

A.56. Diffraction pattern of alloy 198 (16.0 at% Nb) at -192° C.....168

1. INTRODUCTION

The U-Nb alloys considered in this research display shape memory effects (SME). Previous study of this effect for these alloys has been limited to the composition range where the martensitic reactions occur above room temperature. The potential value of a heat-shrinking U-alloy coupling-clamp that, at some later time may be released merely by cooling, has recently been recognized [1] and the martensitic transformation temperature range for such an alloy should be below -30°C or so. It is the intent of this research to obtain x-ray diffraction data below room temperature to -150°C or so, so that the low temperature martensitic reaction of these alloys can be studied. Also from these data, the M_s and M_f temperatures as a function of alloy composition can be determined in the sub-zero temperature range. Thus, by gathering such data, one of the metallurgical parameters required to utilize SME in these alloys below room temperature, namely the temperature range of martensitic reaction, can be established and the feasibility in the above mentioned application proven.

The approach to such data gathering and evaluation is described below. The U-Nb alloys considered were subjected to x-ray diffraction experiments in which the diffraction pattern was obtained by a continuous scan. This was done for each alloy at various sub-zero temperatures. From these diffraction patterns, 2θ values of each peak were determined and the peaks indexed; that is, h k l values found. From this, the phases present and their unit cell parameters can be determined. However in order to find the M_s and M_f temperatures the amount of each phase present must be known. This is done by evaluating the integrated intensities of selected peaks belonging to each phase, since the integrated intensity is directly proportional to the relative amount of phase present [2].

Once the relative amount of phases is determined, for each of the alloys, we can find the M_s and M_f temperatures, by knowing that the first detectable presence of

product phase gives the M_s temperature and the complete absence of parent phase gives the M_f temperature. The range of M_s and M_f temperatures as a function of alloy composition can be plotted, which gives the temperature range of sub-zero martensitic reaction as a function of solute content. From this, a transition metastable phase diagram can be formulated, which can be used in the feasibility of developing a sub-zero uranium SME alloy.

2. LITERATURE SURVEY

2.1 Uranium And its alloys And Their Allotropes

Pure elemental uranium has three allotropic modifications depending on the temperature. These are 1) a high temperature b.c.c phase, called gamma (γ), stable up to the melting point of 1131°C; 2) beta (β), which is a complex tetragonal structure and forms at 772°C, and is stable down to 664°C; 3) alpha (α), which is an orthorhombic structure and forms at 664°C and is stable at lower temperatures. In pure elemental U, none of the allotropic modifications can be suppressed even with cooling rates as high as 10^4 K/s [3]. However, by alloying some metastable phases can be made to exist at room temperature and these are actually modifications of the low temperature allotropes β and α of the pure elemental uranium. Initially there were many theories [4] trying to prove that either one or the other of the transformation modes, viz diffusional or shear, alone took place in U-alloys. However, there were always evidences indicating that both transformations indeed took place, depending upon the temperature. The presence of both diffusional and shear reactions during the β --> α transition has been indicated. For pure U this transition occurs by diffusional growth at slow cooling rates, while above a critical cooling rate of some 65°C/s the phase change occurs martensitically [5]. Thus the β --> α transition can occur either by shear or diffusion mechanisms. With small alloy additions, the reaction becomes more sluggish and the martensitic transformation is markedly displaced to lower temperatures. For unalloyed U and its dilute alloys, the decomposition of γ proceeds directly to β by a diffusion-nucleation-and-growth process. With sufficient alloying in excess of 2 to 5 at%, depending on the type of solute, and by moderate quenching, the decomposition of γ readily by-passes the β phase; that is, γ transforms directly to α or to one or more metastable phases that can be described as modifications of α or γ.

The suppression or elimination of the γ --> β transition is attributed to the difficulty of nucleating the β structure [7,8]. It has been observed that an increase in solute content results in a greater distortion in the martensitic product phase. This distortion causes the product phase to be a modification of the α structure. However increased cooling rate has a reverse effect; that is, it increases the shear process [4]. The degree of departure from the α structure and hence the distortion in the product phase is considered to be a function of the stiffening of the lattice, caused by alloying, which works against shear. The transformation processes of the high temperature γ phase in alloys which form the metastable phases are quite complex. Beyond minimal solute content, the β phase formation was found to be suppressed completely. This minimal solute content to suppress the β phase is between 2 to 5 at% [3,4] depending on the type of solute (eg., Mo, Nb).

Also increasing the cooling rate favours the shear process [4,9]. This presumably arises from increased hydrostatic pressure caused by faster cooling rates and increased transformation stresses due to faster rate of transformation once shear has started. Thus a stress/stiffness ratio was proposed, which should be optimal to generate any martensitic phase by shear.

Tangri and Chaudhuri [10] investigated U-Nb alloys to determine the effect of solute concentration on the type of end product formed on quenching at 1000°C/s. From their studies, it was found that up to a composition of 10.00 at% Nb, the phase formed on quenching was α', which is an orthorhombic structure like α, with the difference that the 'b' parameter has undergone a contraction. At 11 to 20 at% Nb the existence of a monoclinic structure, designated α'', was reported by these authors. The variation of $\hat{\gamma}$, the monoclinic angle, with composition showed a sharp rise begining at 10 at% Nb to a value of $\hat{\gamma} = 91.07^\circ$ at 11.93 at% Nb. However, the extrapolation of a curve through their data to a $\hat{\gamma} = 90^\circ$, corresponds to a composition of 7.6 at% Nb instead of

a compositional value between 10 at% and 11.2 at% Nb. Thus there was the question whether α" was present below 10 at% Nb concentration.

The results of Tangri and Chaudhuri are shown in Table 1. From Table 1 and from the possibility of existence of α" below 10 at% Nb, the α'/ α" composition boundary could be between 10 at% and 11.2 at% Nb. The α'/ α" composition boundary, according to Anagnostidis et al [11], is 8.8 at% Nb. The lattice parameter changes depend on the compositional range. In the α' and α" composition range, the 'a' parameter is not sensibly affected; also a steady decrease in 'b' parameter with a maximum rate of decrease between 10 at% and 11.2 at% Nb was reported. The 'c' parameter increased at a continuously decreasing rate up to 10 at% Nb and then increased linearly at an increased rate up to 15.8 at% Nb. With increased solute content the unit cell volume decreases linearly; a similar behaviour was also found in the U-Mo system [12].

In the compositional range of the γ° tetragonal phase (Table 1), the 'a' parameter decreases, the 'c' parameter and the c/a value increase linearly with increased Nb content. The U-Nb and U-Mo systems both show identical behaviour in the formation of these metastable phases [10]. Tangri and Williams [13] have concluded that α' and α" are two individual phases in the U-Mo system and from x-ray observations of Tangri [10] it was established that α' and α" phases were two separate phases indeed, having orthorhombic and monoclinic crystal structures, respectively.

Also form Table 1, a minimum value of 5.802 Å for the 'b' parameter is reached in the alloy showing the last presence of α' at the α' / α" composition boundary. The minimum value of 'b' for the α' phase, according to Tangri, was in good agreement with the extrapolated value of 5.80 Å given by Anagnostidis et al [11]. This pattern of variation of 'b' and 'c' parameters was also found in U-Mo system [13], with a minimum value of 5.800 Å for the 'b' parameter in the last α' phase. These

TABLE 1

X-ray identification of phases produced in U-Nb alloys after fast and slow cooling rates from the gamma phase and the values of crystalline parameters in water-quenched alloys.

At % Nb	Phases produced by		Crystalline parameters of water quenched alloys				
	Water-quench cooling rate ~ 1000° C/sec	Air cooling cooling rate ~ 10° C/sec	aÅ	bÅ	cÅ	$\hat{\gamma}$ (degrees)	c/a
0	α		2.8503	5.8610	4.9474	90	
1.00	α'		2.8503	5.8526	4.9557	90	
1.50	α'		2.8503	5.8508	4.9595	90	
2.92	α'		2.8503	5.8446	4.9671	90	
6.20	α'		2.8503	5.8309	4.9803	90	
8.30	α'		2.8503	5.8177	4.9855	90	
9.20	α'	α''	2.8503	5.8076	4.9877	90	
10.00	α'	α''	2.8503	5.8020	4.9880	90	
11.20	α''		2.8503	5.7887	4.9900	90.883	
11.93	α''		2.8503	5.7793	4.9929	91.070	
13.00	α''		2.8503	5.7718	4.9948	91.200	
13.80	α''		2.8503	5.7646	4.9971	91.300	
15.08	α''	γ°	2.8503	5.7556	5.0000	91.470	
15.80	α''	γ°	2.8503	5.7508	5.0023	91.550	
16.80	γ°		6.9683	—	3.3832	90	0.4855
17.10	γ°		6.9620	—	3.3838	90	0.4860
17.73	γ°		6.9507	—	3.3854	90	0.4871
18.15	γ°		6.9425	—	3.3865	90	0.4878

observations indicate that possibly the 'b' parameter in the uranium lattice can be made to contract only up to 5.800 Å without affecting the ^γ angle. Thus, the inference was that as long as 'b' contraction does not go beyond 5.800 Å, the α" is not formed since the ^γ still remains at 90°. Thus the α' to α" structural change took place at a 'b' value of 5.800 Å.

2.2 Crystal Structure Of Uranium And Its Transition Phases

The three allotropic forms of pure elemental U were already seen to be γ, β, and α with decreasing temperature. Each of these are discussed briefly below.

2.2.1 The Alpha Uranium

This low temperature phase is an orthorhombic structure with lattice parameters a = 2.8536 Å, b = 5.8688 Å, and c = 4.9555 Å [14]. This is a complex structure in that the atoms or so positioned that they form corrugated layers, and each uranium atom has 12 nearest neighbours. Due to the complex orientation of these 12 neighbouring atoms, the following explanation will facilitate the visualization of these atoms. Each corrugated layer of atoms has the puckering angle of 128.2°, as shown in Fig.1. For any atom considered there are 4 neighbours lying on the same layer as that of the reference atom; two atoms at 2.852 Å each in a polar direction and two at 2.762 Å each with 128.2° angle between them (atoms numbered 3 and 4 in Fig.1). There are 6 atoms lying on one adjacent layer and 2 on the other adjacent layer, which form the remaining 8 neighbours. From Fig.2 it is seen that out of the 8 atoms, 4 atoms lying on layer-1 are at 3.342 Å and

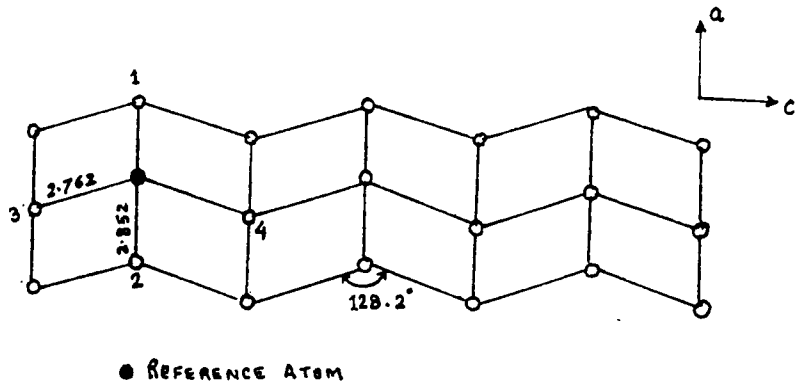

Figure 1. Corrugated layer of α-uranium atoms.

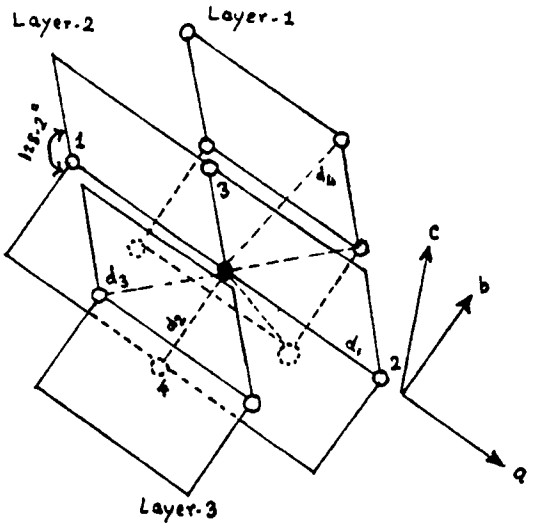

Figure 2. The 12 nearest neighbours of U atom.

the remaining 4 atoms are positioned 2 on each of layer-1 and layer-3 at 3.263 Å from the reference atom. Thus there are four interatomic distances d_1 ,d_2 , d_3 , and d_4 , as shown in Fig.2. The corrugated layers of atoms are parallel to the a and c axes and are normal to the b-axis. The interatomic distance d_3 is called the short contact, and there are 4 short contacts; the remaining contacts are termed long contacts, viz d_1 , d_2 and d_4 . Above 0°C the 'a' and 'c' parameters increase with temperature whereas 'b' decreases. However, between 43 K (-230°C) and 283 K (10°C), all 'a', 'b' and 'c' of α-uranium have been reported to increase with temperature [15,16]. Since the axis normal to the corrugated layers is the b-axis, the decrease in 'b' parameter can be thought of as if the layers were coming close together.

But observations [17,15,18] on 'b' parameter values with temperature showed that only the short contacts increase 2% with temperature and the long contacts remain unchanged when compared to the room temperature values. From this observation then, the layers would not come close together and the above mentioned mechanism does not seem plausible.

2.2.2 The Beta and Gamma Uranium

The β uranium is a complex tetragonal structure with a unit cell of 30 atoms per cell and whose lattice parameters are, a =10.52 Å and c = 5.57 Å. The γ uranium is a b.c.c structure, with a = 3.53 Å and is the high temperature phase.

2.3 Transition Phases In Uranium Alloys

2.3.1 Alpha-like phases

The transition alpha phase in U-based alloys is an orthorhombic phase, similar to the α-uranium, for solute concentrations in excess of room temperature solid solubility.

This is designated α' and the only structural difference is a relative contraction in 'b' parameter [19]. However observations have shown [20,11] that besides 'b' parameter, 'a' and 'c' parameters were know to vary for α'. Also, changes of α' lattice constants with quenching rate were expected, since a greater rate should favour a lattice shearing process [13] for higher solute contents or slightly more concentrated alloys, and with rapid quenching the α-like phase obtained is a monoclinic structure (designated α''). This is formed only at solute contents high enough to suppress γ --> β transformation, for all solutes that produce α' (Zr and Ru are exceptions). The α'' is a c-centered monoclinic lattice whose unique axis is c-axis. This, like α-uranium, contains 4 atoms per unit cell and has a space group $C2_1/m$.

2.3.2 Gamma-Like Phases

Whenever alloys containing solute content much in excess of the α phase solubility limit are quenched from regions of γ phase stability, the end product is related to γ-uranium. The higher the solute content or slower the quenching rate, the greater the tendency to form these γ derivatives. The structures of these phases were so much like the b.c.c γ phase that they went undetected for a long time. The transition phase, designated γ°, is one such γ derivative and is a c-centered tetragonal phase with $a_{\gamma^\circ} = 2a_\gamma$ and c_{γ° slightly less than a_γ. When $c/a \approx 0.5$, the phase was called γ° and when $c/a < 0.5$, the phase was designated γ_d° due to deformation markings.

Thus, the primitive cell representation would be a cell with $a_{\gamma^\circ} = \sqrt{2}a_\gamma$ and $c/a \leq 0.707$, and is shown in Fig.3 and has a space group p_4/nmm. The γ° phase is obtained by displacements of half of the atoms from their body-centered sites [21,22]. These displacements are in $<100>_\gamma$ directions, the particular direction chosen becoming the tetragonal c axis. According to Hatt and Stewart [21] and Yakel [22], when $c/a = 0.5$, x-ray diffraction maxima from γ° crystals are classified as sharp (corresponding to the

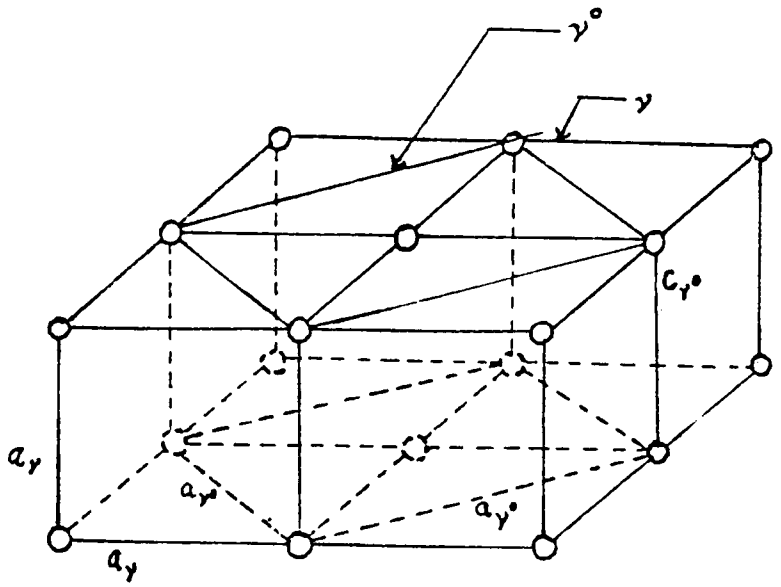

Figure 3. Primitive cell γ° generated from γ.

basic b.c.c structure) and diffuse caused by superlattice reflections due to atom shifts. The sharp reflections were strictly due to cubic lattice but the diffuse reflections were displaced as they may be produced by $\gamma_d°$ lattice (c/a<0.5) where the c-axis could lie on any one of the <100> directions. The U-based alloys, while transforming to $\gamma°$, go through a phase γ^S, which was also true for U-Nb alloys. The phase γ^S which preceeds $\gamma°$ formation, was found to have reflections in positions other than expected from a b.c.c structure; these additional reflections were weak and broad.

Tangri's proposed structure based on chemical ordering for γ^S was suggested to be incorrect based on inspection [22] of the variations of intensities of the weak reflections with scattering angle: The weak reflections do not decrease in intensity with increasing $\sin\theta/\lambda$, as would be the case if their intensities were due to structure factor terms depending on differences in atom scattering powers. This would be true if chemical ordering were present; that is, atoms of different scattering powers on the atom sites of the original γ phase. Rather, it was found that the intensity of the diffuse reflection increased with increasing $\sin\theta/\lambda$; this would be expected if the diffuse reflection intensity was due to structure factor terms containing a factor for small displacements of an average atom from its symmetry position.

Thus, the unit cell of γ^S is made of 8 unit cells of b.c.c cells, with the 8 body-centered atoms displaced in correlated $<100>_\gamma$ directions. The γ^S is also a cubic structure with 8 body-centered atoms, which can occupy 24 positions due to the correlated displacements that can occur in any of the 3 $<100>_\gamma$ directions. Thus, each of the atoms must occupy one of the three positions such as (1/4, 1/4, 0.22), (1/4, 0.22, 1/4) or (0.22, 1/4, 1/4) instead of the symmetric site (1/4, 1/4, 1/4). None of the 8 atoms in the γ^S phase are in the original body-centered position of the parent γ phase. Also, x-ray studies [22] showed that the displacements of body-centered atoms in any

particular region along the z-direction was the same; that is, atoms do not move in opposite directions.

Thus the transition from the γ phase to the metastable γ^S and γ° phases was characterized by small average atom displacements and it was clear that the $\gamma \rightarrow \gamma^S \rightarrow \gamma^\circ$ represents successive steps by which the alloy lowers its free energy and approaches a structural arrangement more like that of the equilibirium α phase. The tendency to retain more γ-like structure as the solute content is increased was demonstrated by Tangri [23], and was interpreted as due to the decrease in the atom displacement parameter due to alloying.

2.4 Effect Of Cooling Rate And The Shear Mechanism Of Transformation

That the transformation of $\gamma \rightarrow \beta \rightarrow \alpha$ could be either martensitic or diffusion controlled was already seen. The shear induced martensitic transformation takes place once an optimal stress/stiffness ratio is realized [9]. Harding and Waldron [24] have reported that in U+10 at% Mo alloy the α' phase is formed by a shear mechanism. Lehmann [25] and Tangri [26] observed an α'' monoclinic phase to be formed by a shear mechanism also. For lower composition limits the $\gamma \rightarrow \alpha'$ transformation was through an intermediate stage β and above this composition range it was a direct $\gamma \rightarrow \alpha'$ without a β stage [27].

For certain alloys lying in the compositional boundary range of the transition phases, increasing the quench rate makes the reaction proceed forward. From this it was inferred that γ° and α'' were progressive stages in the generation of α' from b.c.c γ phase; that is, $\gamma \rightarrow \gamma^\circ \rightarrow \alpha'' \rightarrow \alpha'$ sequence of transformation was established [27]. It has been shown [28] that the structure can be generated by a shear on $\{112\}_\gamma$ planes in a $<111>_\gamma$ direction. While shear on only one set of $\{112\}_\gamma$ planes is required to generate α' and

α" phases, shear on two sets of $\{112\}_\gamma$ planes is involved in the generation of γ° structure. Fig.4 shows the projection of atoms in a b.c.c γ structure onto a $\{110\}_\gamma$ plane, showing an edge view sequence of $\{112\}_\gamma$ planes. From Fig.4 it is seen that a shear AC is required to change $\hat{\gamma}$ to 90° and produce the orthorhombic α' sructure.

In the lower solute range, this shear was realized and hence α' results. However, as the solute content increases, it is believed [28] that the lattice stiffens more and more and restricts the shear, producing only a limited shear AB. This makes the $\hat{\gamma} \neq 90°$, consequently a monoclinic α" structure ($\hat{\gamma} > 90°$) results. For very high solute content, that is beyond the α" range, the lattice is highly stiffened, which produces a very limited amount of shear on two $\{112\}_\gamma$ planes resulting in the γ° structure. For a given composition, the lattice stiffness is fixed and faster cooling produces larger stresses causing a larger reduction in $\hat{\gamma}$ (that is, the reaction tends towards the α' phase), and slower cooling produces smaller stresses restricting the reduction of $\hat{\gamma}$ angle (that is, forward reaction to α' is restricted). This explains the formation of two different phases for different quench rates for a given composition. Hence, for compositions lying in the boundary range of transition phases one or the other phase is formed depending on cooling rate. Thus the effect of rapid quenching is to produce a structure further removed from the parent b.c.c phase than that obtained with slower cooling rates in the γ --> γ° --> α" --> α' sequence, indicating severe quenching makes the transformation go towards completion.

The α" monoclinic structure discussed above is common among several U-based alloys. While its atomic structure is similar to that of α-uranium, the sides of the cell and the $\hat{\gamma}$ angle are different from α-uranium. The effect of the monoclinic angle is that certain of the original α-uranium diffraction peaks split into two components of unequal intensities. Ordering was not a possible cause for this effect since ordering would produce only very weak superlattice diffraction and cause negligible changes in the main

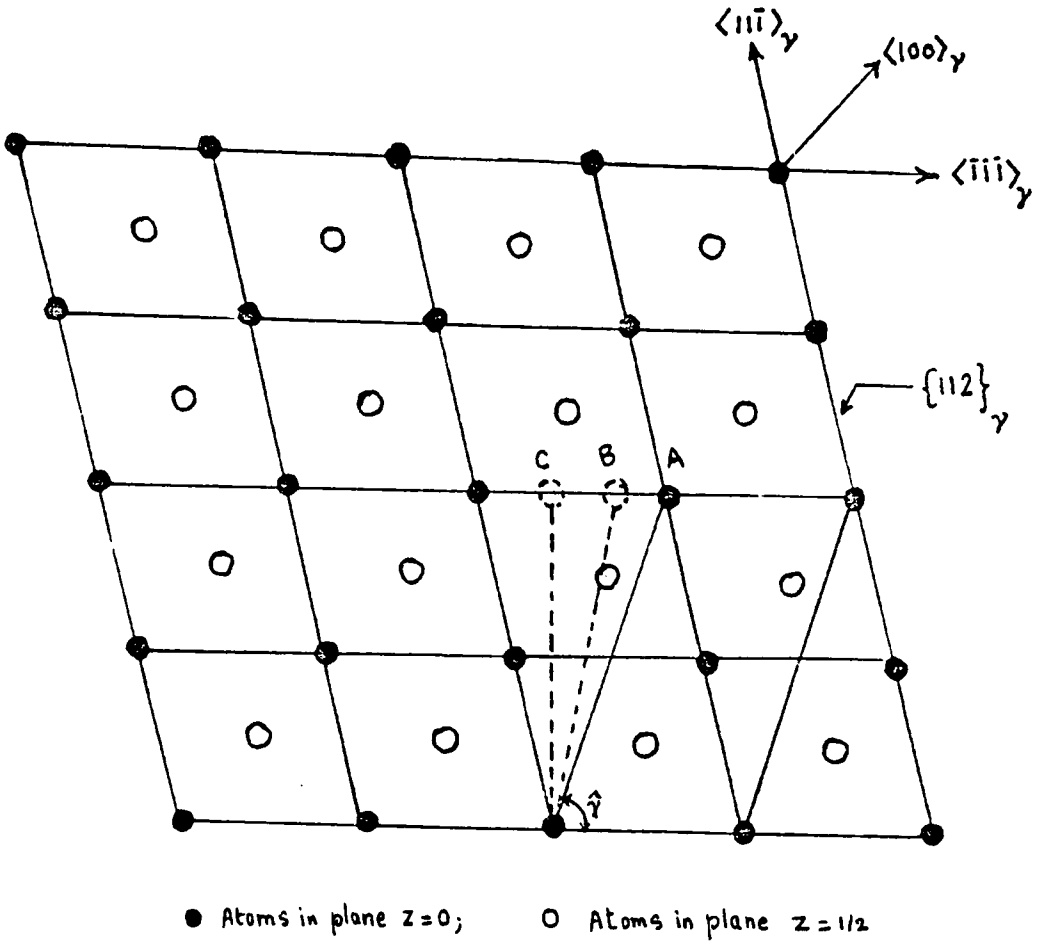

Figure 4. Projection of atoms in bcc structure onto a {110} bcc plane showing the sequence of {112} bcc planes [27].

atoms along the a-axis from their positions in the α-uranium [29]. This movement is the one which the x-parameter defines and is the chief difference between the monoclinic structure and the α-uranium stucture. The variation of 'x' with alloy composition is shown in Fig.5 for a U-Mo alloy; it is seen that 'x' increases rapidly as the composition approaches the upper limit of the α" range (11 at% Mo). The magnitude of the $\hat{\gamma}$ angle in the U-Mo alloys decreases with more rapid quenching and a similar behaviour is true for the U-Nb alloys [11].

Because of the diffusionless transformation of γ° --> α", structural relationships between the phases should exist and the following explanation indeed proves it to be the case. The relationship between b.c.c γ and α" can be understood from Fig.6(a), which shows the projection of atoms from a group of b.c.c cells onto their $(1\bar{1}0)_\gamma$ plane. The projection from a single b.c.c cell is shown at the top right corner of the figure. The lattice parameter of this cell is 3.45 Å (for a 10 at% Mo). This gives the atomic spacing as 2.98 Å and the separation of atomic layers in a direction perpendicular to the figure as 2.45 Å. The equivalent monoclinic unit cell which may be derived is also shown in the figure with lattice parameters a = 2.98 Å, b = 5.73 Å, and c = 2 x 2.45 Å, with $\hat{\gamma}$ = 100°. The isometric view of this derived monoclinic cell is shown in Fig.6(b). This monoclinic cell is very similar to the actual monoclinic cell formed by a 10 at% U-Mo alloy where the respective values were 2.87, 5.75 and 2 x 2.47 Å and $\hat{\gamma} = 92.3°$ [29]. The structure parameter 'x' and hence the angle which the linked atoms (or the 'dumb-bells') from each layer make with the axis of the monoclinic cell can decrease smoothly over a range of values to zero, when the structure becomes similar to the α-uranium structure, that is $\hat{\gamma} = 90°$.

As shown in Fig.6(a) the $\{112\}_\gamma$ planes are sheared progressively with respect to the one containing atoms A and A'; the atoms at z = 0.25 are brought into positions so that these can assume their positions in the cell with but little extra movements. This

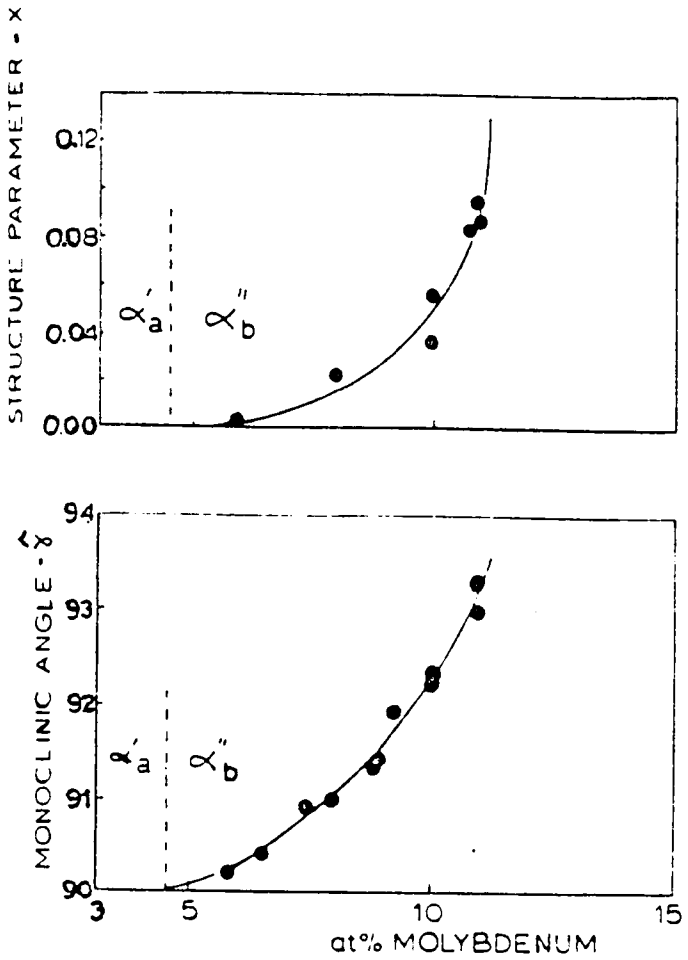

Figure 5. Variation of structure parameter and monoclinic angle with composition [29].

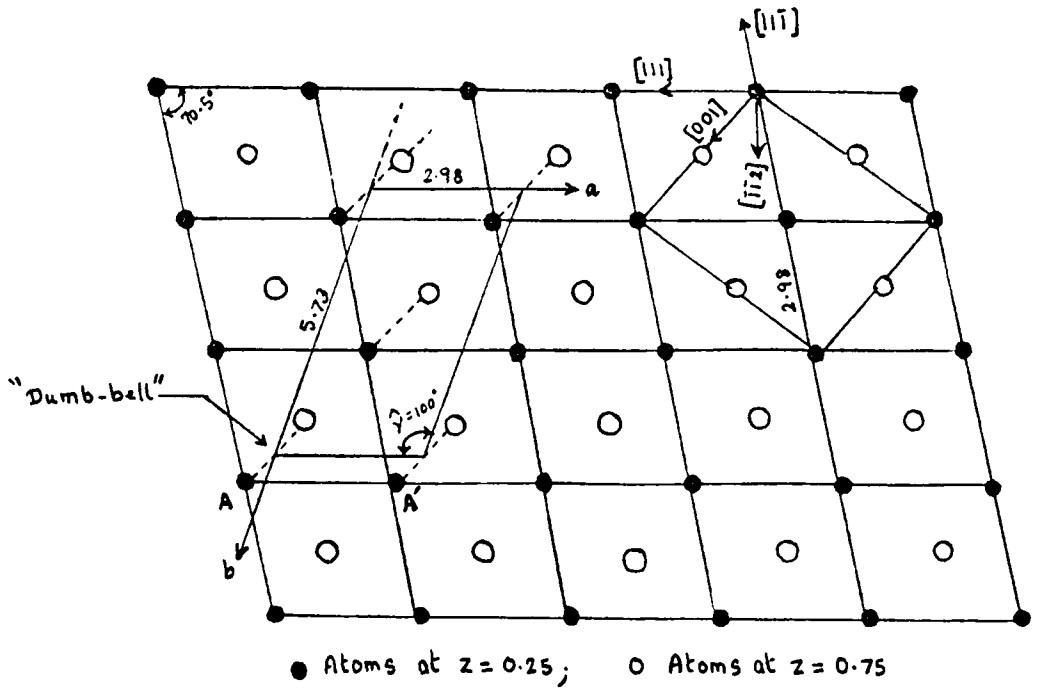

a) Projection of atoms in the bcc structure onto a 110 plane showing the monoclinic cell which may be derived with its ac plane parallel to {112} planes of the original bcc structure. Z, normal distance along z-axis [29]

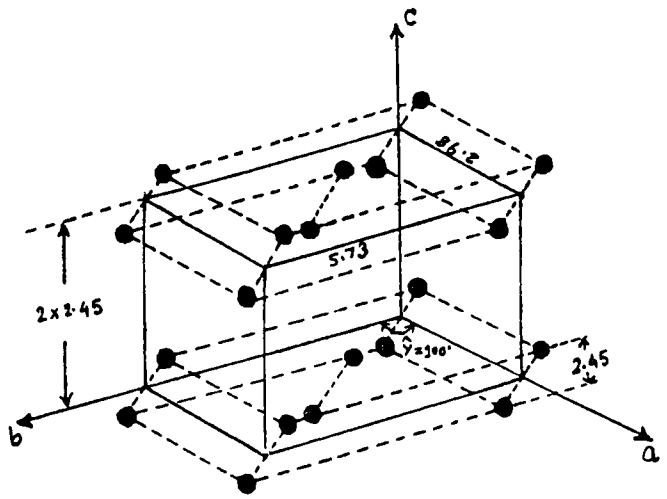

b) Isometric view of the monoclinic cell

Figure 6. Structural relationship between b.c.c γ and α".

causes the atoms forming the 'dumb-bells' to come closer together (the atoms in the adjacent parallel $\{110\}_\gamma$ layers). Resistance to this movement can cause an expansion in the 'c' parameter. The martensitic γ to α' transformation in U-alloys can thus be explained by a Burger shear mechanism [30]. By progressively restricting the shear, a continuous series of displacively produced transition states could be developed as follows, viz γ --> γ° --> α'' --> α'. The shear mechanism is a shear on {112} cubic planes in a <111> cubic direction which is the primary distortion with secondary shuffling of some of the atoms needed to complete the crystal structure change.

In Fig.7, a monoclinic cell projected on (001) monoclinic plane identified with a, b and $\hat{\gamma}$ and the c-axis lying normal to the plane of Fig.7, is shown. The b.c.c lattice projection shown gives a $\hat{\gamma} = 100.02^\circ$, and the Burger mechanism as proposed would alter this cell by shearing it in the 'a' direction on a plane parallel to 'a' and 'c' directions (that is a plane normal to Fig.7), so as to decrease the angle to 90° (that is, to form α'). The orientation relationships between γ and α' are $[100]_{\alpha'} \parallel [111]_\gamma$, $[010]_{\alpha'} \parallel [\bar{2}1\bar{1}]_\gamma$, $[001]_{\alpha'} \parallel [011]_\gamma$.

It has been proposed [26,31,11] that by progressive restriction of the magnitude of shear (that is restricting the amount of the decrease in the $\hat{\gamma}$ angle), a continuous sequence of displacively formed phases could be developed as follows, γ --> γ° --> α'' --> α'. That is, a progression of lattice parameter changes from one structure to the other with no co-existence of phases occurs sequentially. There is evidence [31,22] that γ --> γ° and α'' --> α' are indeed continuous in the sense there is no co-existence of phases. However for the γ° --> α'', from the lattice parameter versus composition plots shown in Fig.8 and Fig.9, this is not known for sure [32]. It will be seen later that γ° --> α'' is not continuous in the above mentioned sense.

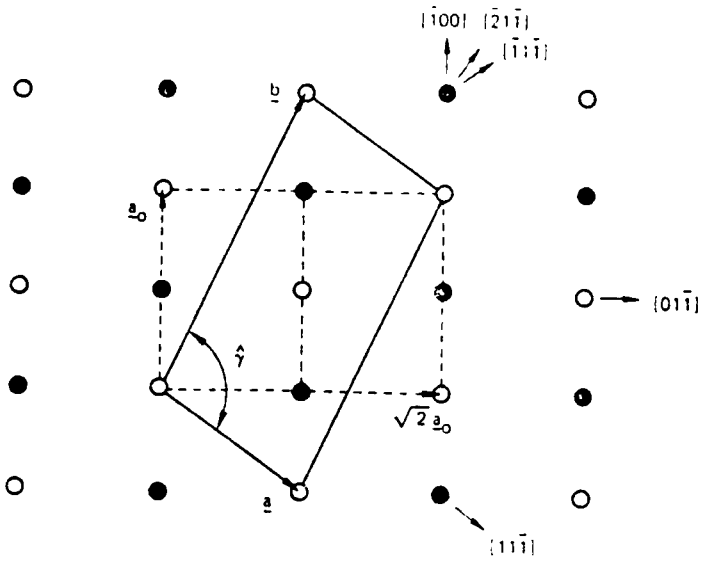

Figure 7. A [110] projection of the bcc lattice points with the various unit cells and lattice parameters defined [32].

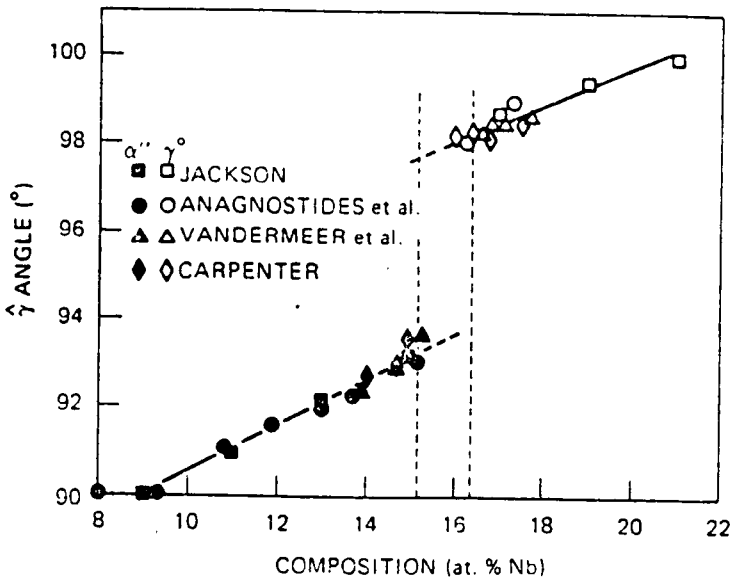

Figure 8. A plot of the $\hat{\gamma}$ angle versus At% Nb [32].

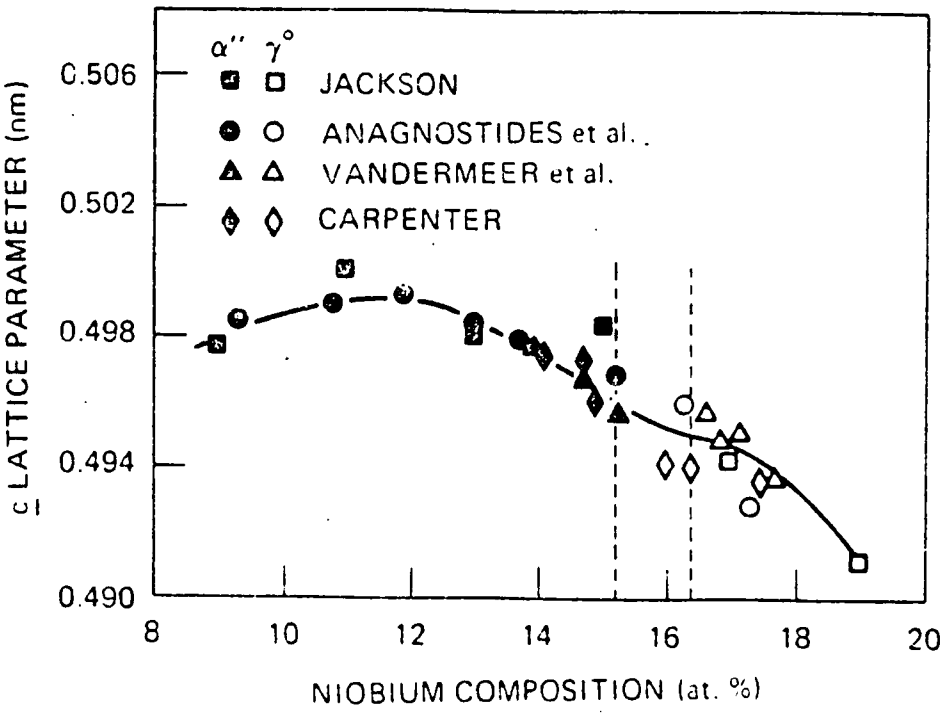

Figure 9. A plot of the 'c' lattice parameter versus at% Nb [32].

2.5 The Uranium-Niobium Alloys

The following review is in addition to that given in section 2.1.

The phase diagram for a U-Nb system is shown in Fig.10. In this system the following transition phases and their composition range stability were observed after quenching from b.c.c γ solid solution [34].

a) Between 1 to 5 at% Nb content an orthorhombic structure α'_a is formed but it is formed by a martensitic β --> α'_a intermediate step. Thus, this is still a dilute alloy, in the sense β formation is not suppressed.

b) Between 5 to 9 at% Nb again an orthorhombic structure designated α'_t is formed; however here β formation does not take place, and hence, the reaction is direct from γ .

c) From 9 to 16 at% Nb a monoclinic structure α'', forms directly from γ . For alloys containing 16 to 20 at% Nb a tetragonal structure γ° is formed, which is similar to γ except two axes have expanded and one shortened in a 2:2:1 ratio.

The behaviour of transition phases according to Jackson's observations [34] was 1) a significant continuous, diffusionless, athermal, reversible and highly anisotropic change in unit cell parameters on heating and cooling, and 2) at certain combination of temperature and composition the martensitic like changes in the unit cell parmeters manifest themselves as symmetry changes, which are likewise athermal.

Again from Jackson [34], for the α' and α'' phases the 'a' and 'c' parmeters increase with Nb content, and 'b' decreases significantly in a proportionate manner. The cell angle $\hat{\gamma}$ in α'' gradually increases with Nb content from 90° to 92.8° for alloy contents of 9 to 15 at% Nb. For the γ° phase, the value of 'a' increases and 'c' decreases with increasing Nb content and for 20.5 at%, the c/a axial ratio of the subcell of γ equals one. The reason for the decrease in 'b' parameter by adding Nb is thought to be due to the ellipsoidal shape of U atom. Thus when spherical Nb atoms are substituted for U atoms, the b-lattice parameter reduces. This is indeed true in the α-uranium lattice

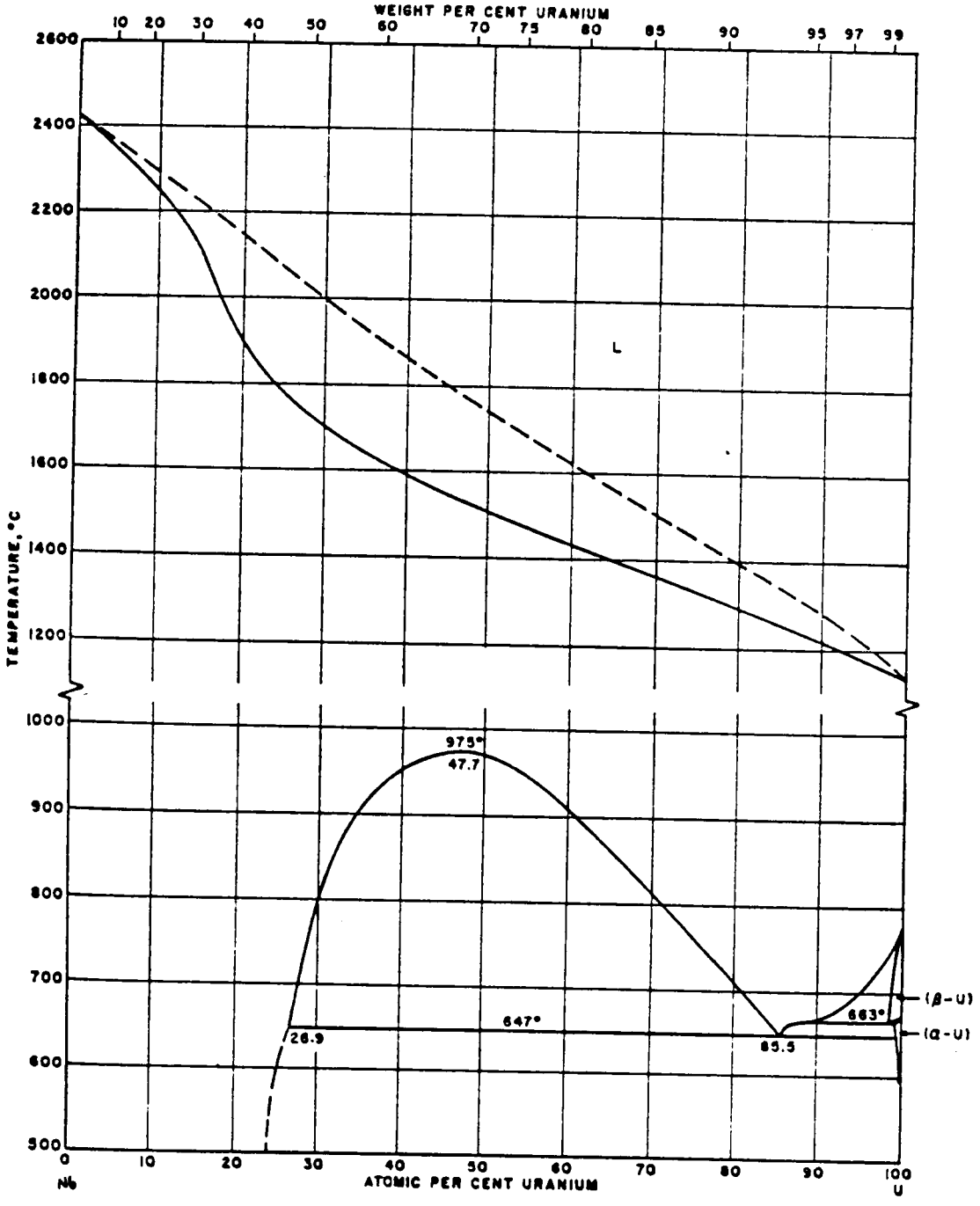

Figure 10. The U-Nb phase diagram [33].

In the U+15 at% Nb alloy, a single phase monoclinic structure α" results at 23°C on quenching from 850°C, with $\hat{\gamma} = 92.6°$. On heating to higher temperatures, the monoclinic cell angle increases reaching a limiting value of 92.8° at 60°C. Between 60°C and 90°C, there is a change in symmetry to a tetragonal γ° structure having a 0.477 c/a axial ratio. Thus, between A_s (60°C) and A_f (90°C), α" and γ° coexist [34]. The α" --> γ° transformation is reversible and the reverse transformation took place approximately at the same temperature as the forward transformation did. The transformation temperatures are strongly dependent on the solute content, and increasing Nb lowers the transformation temperatures.

In the U+19 at% Nb alloy, the single phase tetragonal structure γ° is formed at 23°C on quenching from 850°C. The c/a ratio is 0.487, which reduces to 0.482 when the alloy is cooled to -130°C and increases to 0.495 when heated to 200°C. The variation of c/a with temperature is completely reversible. If these c/a data are extrapolated after plotting, the symmetry change from γ° --> γ would approximately occur at 300°C and likewise a symmetry change from γ° --> α" would occur at approximately -210°C, provided a c/a ratio of 0.477 is the limiting value. The effect of Nb content and temperature on the cell parameters can be rationalized by assuming that the uranium atoms become more spherical as the Nb content is increased and as the temperature is increased.

This tendency to become more sphere-like with increase in temperature is attributed to the delocalization of bonding electrons; that is, a more metallic type of bonding is formed from a covalent type in each individual layer of atoms. In the α-uranium, the increase of temperature or Nb content causes a contraction in 'b' parameter but has little or no effect on 'a' and 'c' parameters. This shortening of 'b' with increased temperature or Nb content cannot continue since, after a limiting value of 5.38 Å is reached, the Nb

atoms are accomodated by an increase in cell angle (which is indicated by the appearance of α" phase).

The ^γ now increases to a maximum of 92.8°, at which there is a change to γ° tetragonal structure (c/a= 0.477) due to shear acting on additional planes of atoms. Continued increase of Nb content or temperature increases the c/a ratio until a cubic symmetry is achieved. The temperature and composition dependency of the cell parameters and consecutiveness of α', α", γ° and γ can be explained by a shear mechanism [34] assuming that the close-packed planes in the parent γ phase become the close-packed planes in the γ°, α", α' product phases. Under this assumption then, the following orientation relationships are apparent, as can be seen from Fig.11. $[001]_{\gamma} \parallel [001]_{\gamma^\circ}$, $[100]_{\gamma} \parallel [100]_{\gamma^\circ}$, $[100]_{\alpha', \alpha''} \parallel [111]_{\gamma, \gamma^\circ}$, $[001]_{\alpha', \alpha''} \parallel [101]_{\gamma, \gamma^\circ}$.

The γ° structure can be generated from the γ phase by a shear on two sets of $(110)_{\gamma}$ planes in $<111>_{\gamma}$ direction. This double shear maintains an orthogonal relationship in the $(110)_{\gamma^\circ}$ plane. It is this shear which is also responsible for reducing the ^γ angle continuously (from 96° to 93°). When the c/a axial ratio of γ° decreases to a value of 0.477, there is a symmetry change due to preference of shear on one set of $(112)_{\gamma}$ planes in one $<111>_{\gamma}$ direction. This has the effect of destroying the orthogonal relationship in the $(110)_{\gamma^\circ}$ planes and monoclinic symmetry becomes apparent. In a U+14 at% Nb alloy, x-ray studies showed that phase changes had indeed taken place and that these were martensitic in nature was confirmed by microstructure studies [3]. On quenching this alloy a single phase α" was observed. However, on very slow cooling a two phase product of α (Nb poor) and γ (Nb rich) was observed. This is illustrated by Fig.12 and Fig.13. Fig.12 shows, from dialatometric studies, the phase transformation that occurred for a fast cooling rate, and the anamolous constriction indicates that γ --> α" is a two stage process as manifested by an expansion during continuous cooling, instead of a contraction (stage II). The stage I is indicated by a change in slope at 570 K (297° C)

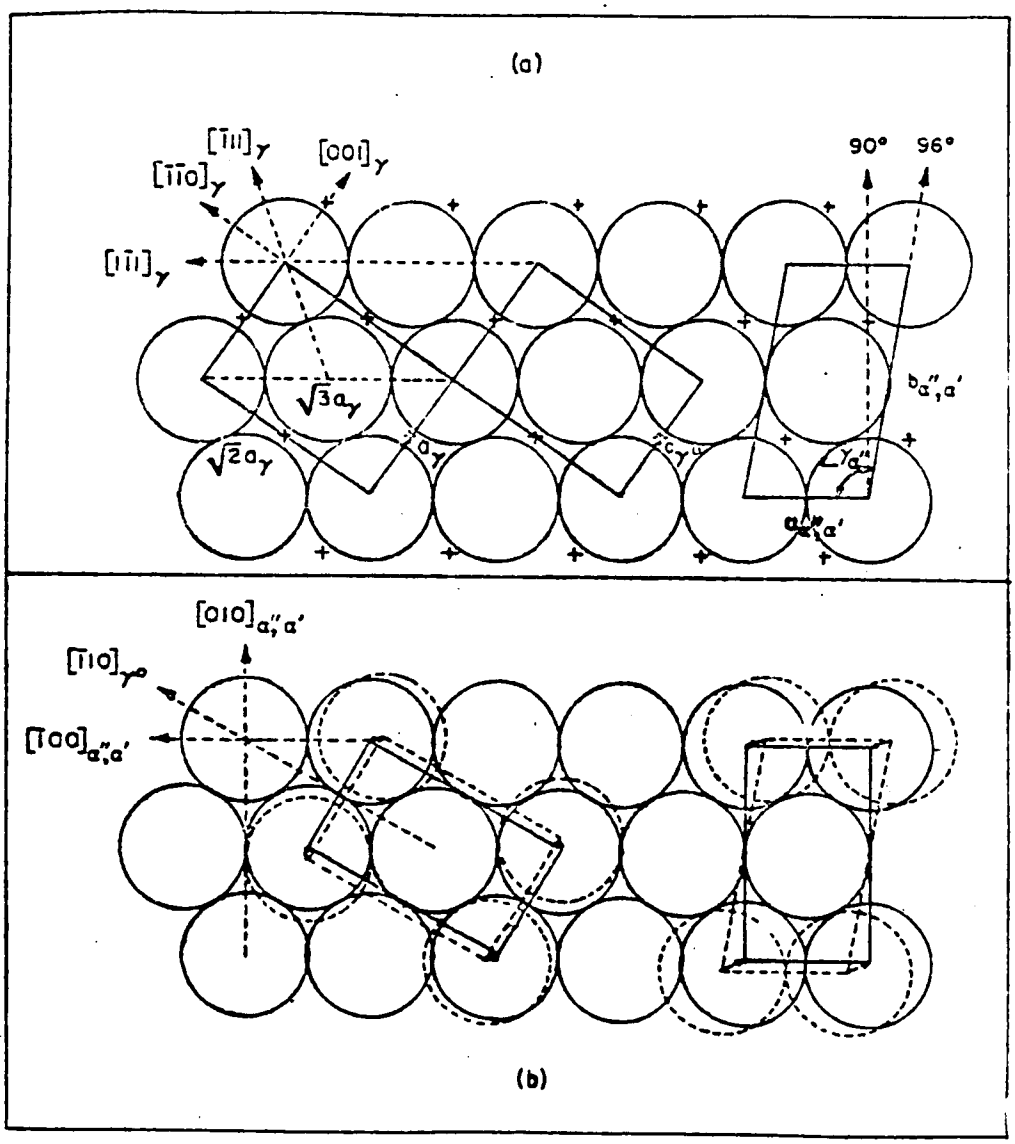

Figure 11. Modelistic explanation for the consecutiveness and the thermal reversibility of the γ <--> γ ° <--> α" <--> α' transformation [34].
a) The close-pack plane of the bcc structure;
b) The close-pack plane of the hcp structure.

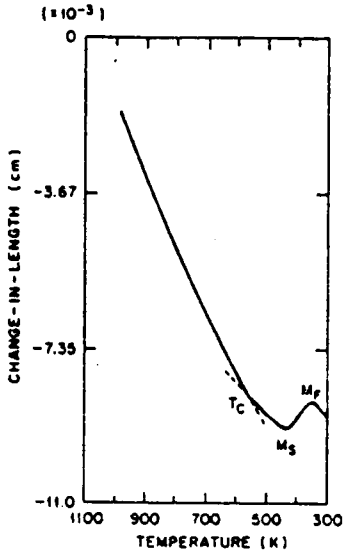

Figure 12. Constrictive curve, ie, plot of change-in-length versus temperature, for the U + 14 at% Nb Helium-gas-quenched from the γ phase at a fast rate [3].

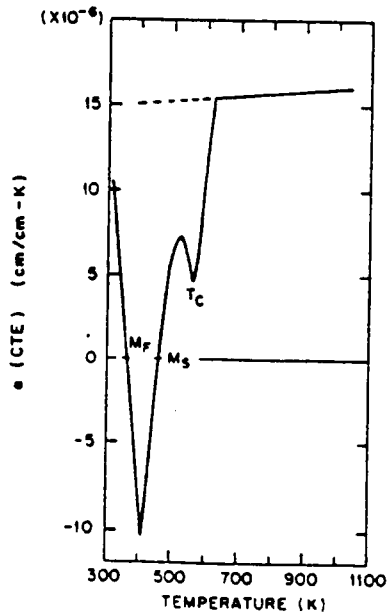

Figure 13. Plot of CTE versus temperature for the U + 14at% Nb, Helium-gas-quenched from the γ phase at a moderate rate [3].

and is called the constrictive arrest. Fig.13, coefficient of thermal expansion (CTE), versus temperature clearly indicates this two stage process of $\gamma \rightarrow \alpha''$. Thus constrictive arrest represents stage I (that is, γ (b.c.c) $\rightarrow \gamma^{\circ}$ (tetragonal)) and anomolous expansion represents stage II (that is, $\gamma^{\circ} \rightarrow \alpha''$). However, by increasing the solute content, the anamolous expansion could be completely suppressed [29,35]; that is, the end product phase is γ° alone and this behaviour was also found in a 16.35 wt% Nb alloy [3]. The following circumstantial evidences indicate that $\gamma^{\circ} \rightarrow \alpha''$ could be a thermoelastic martensitic reaction.

i) The α'' microstructure itself due to its plate like morphology

ii) Relatively small volume expansion accompanying the transformation which appears to be first order [36].

iii) Narrow thermal transformation hysteresis associated with reverse transformation [36].

iv) The substantial heat activated SME displayed by the alloy [36].

The γ° is thought to be the result of a displacement ordering reaction of the γ phase [37,38] in alloys with high solute content. For the 14 at% Nb alloy the transformation temperature depend strongly on cooling and heating reate, and varies inversely with heating and cooling rate as indicated in Table 2. This implies that the γ to α'' transformation sequence was not entirely athermal in nature, but could be complicated by time-dependent thermally activated factors. The reverse transformation temperatures for the $\alpha'' \rightarrow \gamma^{\circ}$ showed hysteresis only on slow heating, and the A_s and A_f temperatures increased significantly, which could be interpreted as evidence of aging reactions taking place.

It is common among actinide metals and their alloys to find martensitic characteristics in phases that have been formed either athermally or isothermally [4]. That this was the case in the 14 at% Nb alloy for the $\gamma \rightarrow \alpha''$ transformation was

TABLE 2

Quench rate dependency of transformation temperatures for a U + 14at% Nb alloy

Transformation Temperature	Helium gas quench			Vacuum quench‖
	Fast†	Moderate‡	Slow§	
T_c(K)	565	590	605	655
M_S(K)	435	460	475	555
M_F(K)	340	340	350	

The instantaneous cooling rates at 625 K were.
† 243 K/s, ‡ 107 K/s, § 34 K/s and ‖ 2.1 K/s.

demonstrated by dialotometry for two different modes of cooling, which showed the influence of cooling rate on the nature of the transformation. In the first mode, a specimen was continuously cooled to room temperature and the displayed constrictive arrest was at 575 K (302° C). Another specimen was interrrupted at 575 K (302° C) and held at this temperature for 2400 secs before cooling to room temperature, and no constrictive arrest occured (that is, no γ° phase formed in between the $\gamma \rightarrow \alpha''$ phase change). In both cases, x-ray studies showed that the end product was α'', the difference being in the microstructure alone. Aging at a temperature above M_S causes the transformation to proceed forward. The longer the time spent, the more the transformation proceeds, and around 700 secs it is complete (that is, all α''), as no anamolous constriction was displayed as shown in Fig.14. The $\gamma \rightarrow \gamma^{\circ}$ is a displacement ordering reaction and the $\gamma^{\circ} \rightarrow \alpha''$ is a martensitic reaction. Both reactions could take place isothermally as well as athermally as demonstrated by the experiment represented in Fig.15(a). On aging the γ phase obtained on reheating after quenching, there is a continuous transition of $\gamma \rightarrow \gamma^{\circ}$ and $\gamma^{\circ} \rightarrow \alpha''$ as the aging time is increased at 600 K (327° C); the M_S temperature is also found to increase with aging temperature. Thus the time dependent nature of $\gamma \rightarrow \gamma^{\circ} \rightarrow \alpha''$ is demonstrated clearly.

The reason for such a time dependent adjustment in this γ-like phases was due to spinoidal decomposition reaction, considering that a near monotectoid composition of U+Nb alloy (14 at%) was studied. The M_S temperature was raised as the solute content was lowered and aging above the M_S temperature increased the M_S temperature of further transformation. The α'' formed after aging contained less solute content than the directly quenched α'', clearly indicating solute rearrangement during aging. Further, it was observed [3] that on reheating to the γ phase, there were emerging γ-like phases in aged samples. This is indicated by the 'shoulder' in the curves in Fig.15 (b), and was presumed to be the result of an endothermic heat effect. With longer aging times, as for

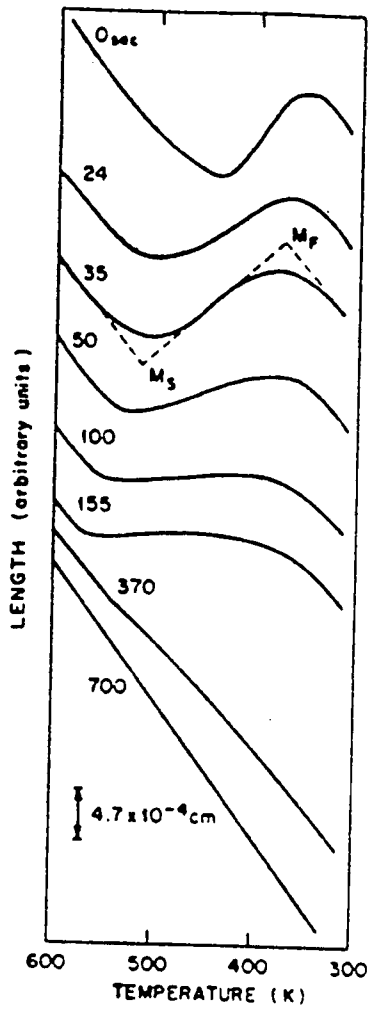

Figure 14. Effect of accumulated aging time at 600 K on the nature of the anomalous constriction during subsequent Helium-gas-quench [3].

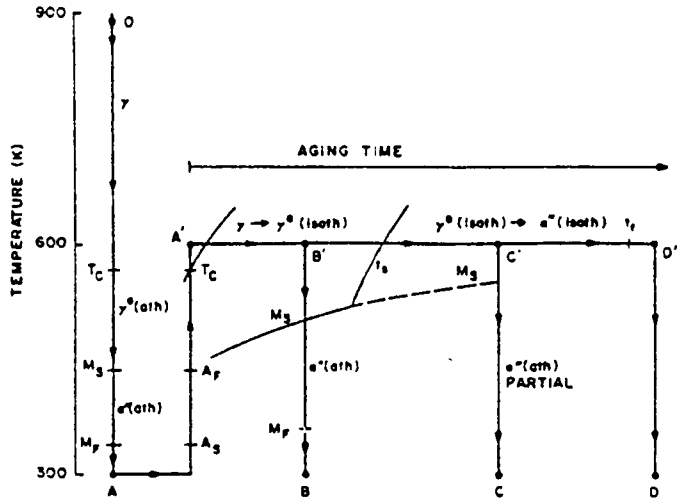

a)Schematic diagram depicting the proposed time-temperature-transformation behaviour of the U + 14at% Nb alloy during quenching from γ and aging at 600 K.

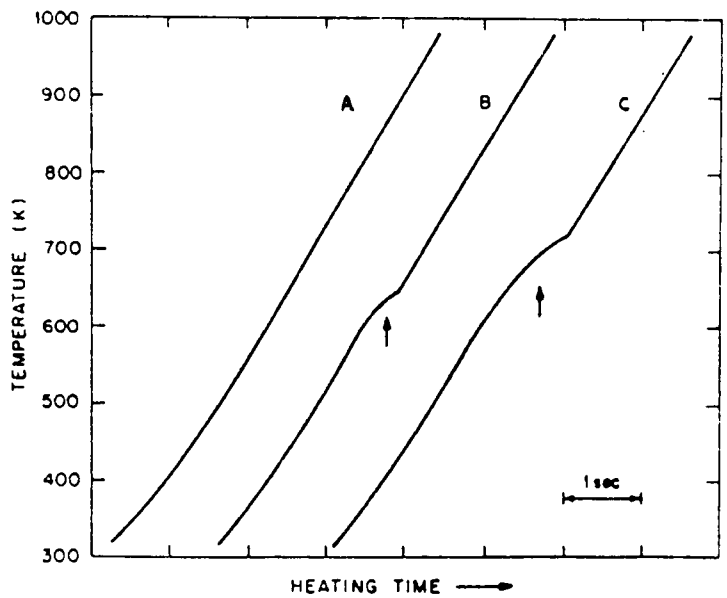

b) Effect of transformation state on the development of an endothermic heat effect during reversion to the γ phase.

Figure 15. Isothermal and athermal nature of the γ --> γ° --> α" reaction [3].

the sample c in Fig.15(b), this heat effect was more pronounced. Assuming this endothermic heat effect was due to solute segregation (no such effect was observed in directly quenched samples) leads to the conclusion that solute segregation and isothermal transformation occur simultaneously if not as cause and effect. Thus in 14 at% Nb alloy, rapid quenching leads to α'', in two stages: 1) $\gamma \rightarrow \gamma^{\circ}$, 2) $\gamma^{\circ} \rightarrow \alpha''$. The $\gamma \rightarrow \alpha''$ can be accomplished isothermally as well, and in this case an endothermic heat effect was observed during the reverse transformation. That the $\gamma \rightarrow \gamma^{\circ} \rightarrow \alpha''$ transition could be affected by solute segregation in the unstable parent phase is a possibility. From recent studies [39] the 15.2 at% Nb alloy gave on quenching two transition phases, α'' and γ°. The γ° phase was found to be present in trace amounts. Alloys containing less than 15.2 at% Nb exhibited a constrictive arrest and a constrictive anamoly. Alloys containing greater than 15.2 at% Nb showed constricitve arrest only. On quenching to 25° C, the former alloys transformed to α'' and the latter ones to γ° as indicated in Fig.16.

Thus the constrictive anomaly was assumed to be associated with the transition to α''. At higher Nb content where only $\gamma \rightarrow \gamma^{\circ}$ takes place, the first deviation from γ and the constrictive arrest did not happen at the same temperature, as was the case for compositions that eventually transformed to α''. This behaviour is explained by ascribing the first deviation from γ to the onset of short-range displacement ordering, and the constrictive arrest to the beginning of long-range order (that is, at Tc (Fig.16)). The transformation patterns were reversed upon reheating to γ, provided the heating was rapid.

In another study [32], a 6.4 wt% Nb alloy was made to transform by stressing the alloy. From x-ray diffraction patterns, it was found that aging produced the γ° phase at room temperature, along with α'' varying from traces to 50%. This shows that M_S temperature was slightly above room temperature. The x-ray pattern showed that for 0%

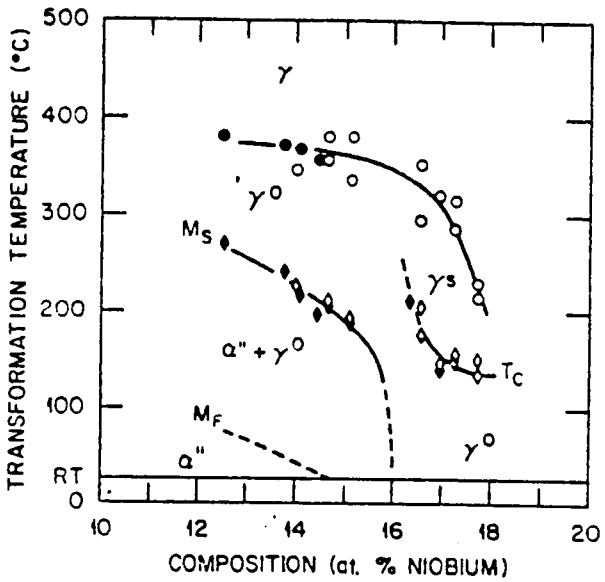

Figure 16. Metastable transition phase diagram for U-Nb alloys near the monotectoid compositions [39].

strain only a trace of α" was present and γ° was the predominant phase (Fig.17). In the stressed condition, i.e., after 3% strain, the α" was the predominant phase and γ° was present in traces. At 1% strain, the γ° and α" phases coexisted in amounts that were nearly equal. This showed that one phase grows at the expense of other when stress is applied. Thus a discrete crystal structure change as opposed to the postulated continuous change is evident. This becomes more apparent upon examining the lattice parameter $\hat{\gamma}$ in Fig.18. $\hat{\gamma}$ angles betweeen 94° and 97° were not observed in U-Nb alloys, confirming the data in Fig.8. In the α" phase formed by stressing, certain expected x-ray peaks were not observed (Fig.17), specifically (110) and (111). The absence of these peak was due to preferred orientation in the samples. A net volume expansion of 1.85% was calculated for the γ° --> α" transformation indicating that this is a first order phase change. Fig.19 and Fig.20 show the nature of the lattice distortions involved in γ° --> α" and the reversible nature of stress-induced α" formation, respectively. The reversibiltiy of transformation is reduced as the amount of deformation increases, and the α" phase tends to become increasingly stabilized.

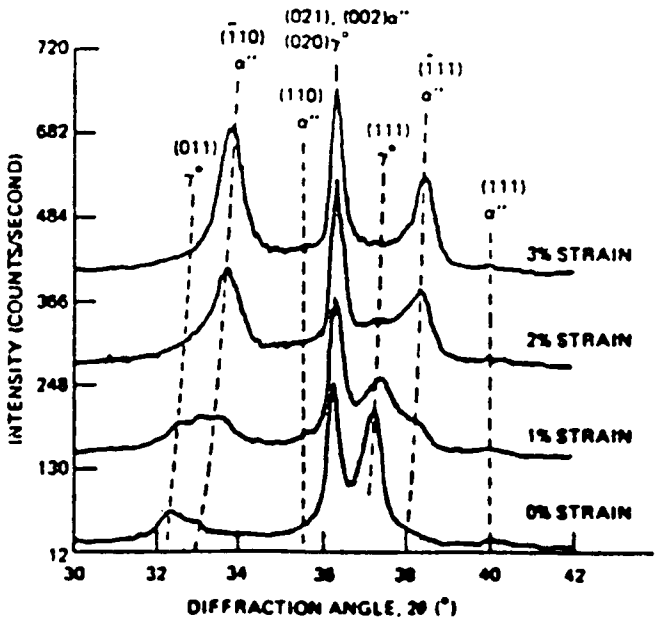

Figure 17. A group of x-ray diffractometer scans depicting the effect of deformation on the transformation of γ° to α'' [32].

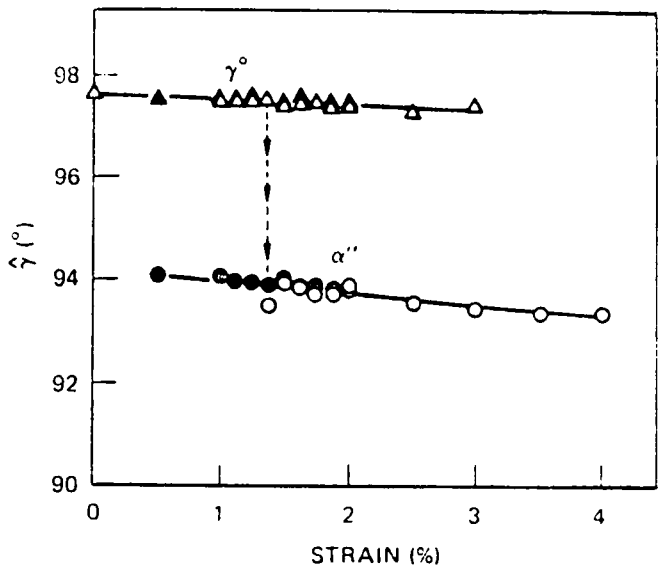

Figure 18. The effect of strain on the $\hat{\gamma}$ angle during the stress-assisted $\gamma°$ to α'' transformation [32].

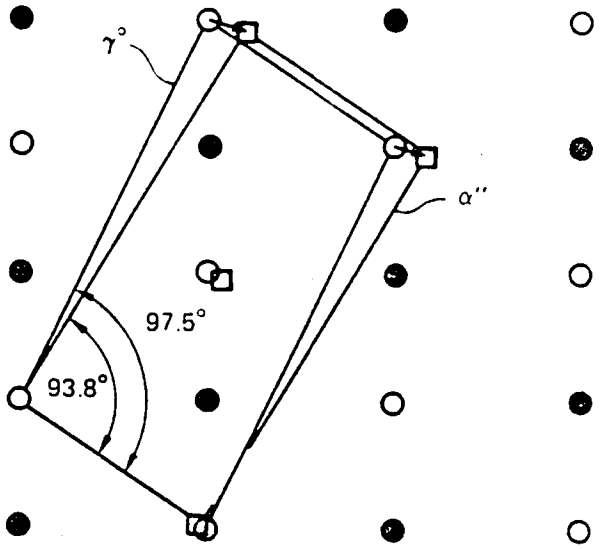

Figure 19. The shape change involved in the γ° to α" phase change based on the new lattice parameter measurements, is shown in terms of the unit cell change. The circle points represent a projection of the γ° lattice along a [010] direction which is parallel to 'c'. The square points correspond to the α" lattice [32].

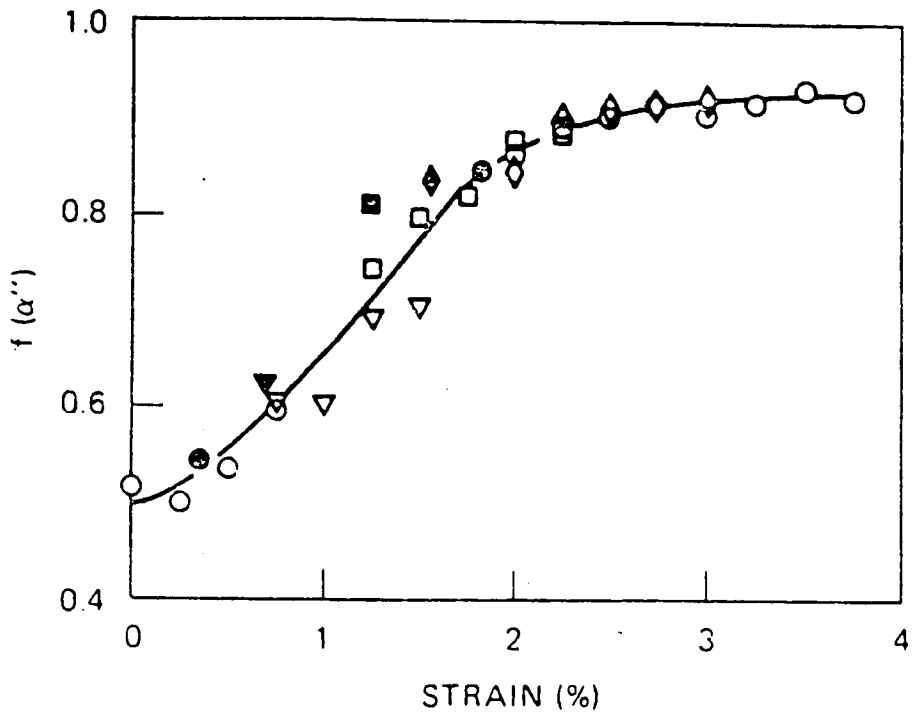

Figure 20. A plot of volume fraction of α" versus strain. Open points refer to the stressed condition while the filled points indicate the unloaded states [32].

3. EXPERIMENTAL PROCEDURE

3.1 Materials

The alloys for x-ray studies were prepared at the Oak Ridge Y-12 production plant. The charge material consisted of commercial scrap of composition U + 5.8 wt% Nb, and a previously made alloy of U + 10 wt% Nb. This charge was melted in a graphite crucible coated with a double layer of yittria. The melt was cast into 13 cm x 18 cm x 4 cm slabs weighing 18 kgs. These were then homogenized in vacuum ($<10^{-5}$ torr) according to the following schedule. The temperature was first raised to 1100° C and held there for 1/2 hour, after which the temperature was further raised to 1150° C and again held there for 1/2 hour, followed by another temperature increase to 1200° C where the slab was held for 2 hours. Then the furnace was turned off and the slab was furnace cooled to room temperature.

The chemical composition of the alloys considered is shown in Table A.1 and the analysis for three of the alloys is shown in Table A.2 (see appendix). The chemical analysis was done for the slabs, before homogenization, on drill chips taken from the top and bottom of the slabs and not from the diffractometer sample. From Table A.1, it is clear that there is a marked difference between the top and bottom drill chip compositions, which in effect gives alloy compositions to an accuracy of $\pm 0.5\%$ only. Hence, the actual average alloy compositions were rounded off to this accuracy, and are shown in Table A.1 as the average composition. Because of this discrepancy, alloys having nominal compositions of 16.17 and 16.37 are listed as having the same composition of 15.5 at% Nb.

3.2 Sample Preparation

The hot rolling was done at 820° C after holding at this temperature for 10 min in a salt bath. The rolled plates were 15 cm wide and 2 cm thick. After the last pass, the plates were held in the salt bath for 20 min and then removed and air cooled. This plate was now sectioned into 6 blocks a, b, c, d, e and f as shown in Fig.21, each of size 8 cm x 10 cm x 2 cm. Each block was then solution heat treated at 800° C for one hour in vacuum and water quenched. This quenched block was cold rolled at ambient temperature to a size of 15 cm x 10 cm x 0.8 cm plate (Fig.22(a)). The cold rolled plate was again solution heat treated for 1/2 hour at 800° C in vacuum and then water quenched. X-ray diffraction samples were machined from this quenched plate. The size of the sample was in accordance with the Rigaku low temperature sample holder. The x-ray diffraction sample was further shaped (Fig.22(b)) by hand grinding on a water cooled and lubricated SiC grinding wheel. The grinding was done to give the specific shape in order to fit the sample holder. In this condition, the samples were given the desired heat treatment prior to x-ray diffraction experiments. The same procedure delineated above was followed for each x-ray sample of any particular composition.

3.3 Diffraction Experiments

3.3.1 Preparation Of Diffraction Sample

Each sample was given a solutionizing heat treatment in flowing argon at 800° C for 1 hour followed by water quenching. After the heat treatment, electropolishing was done at a power of 45V and 2.4A, using a D.C power source. The electrolyte was made of 45% $H_3 PO_4$ + 40% $H_2 SO_4$ + 15% $H_2 O$. The polishing was done intermittently in steps of 60 secs at a time. A stainless steel beaker was used as the cathode. Polishing was continued with constant inspection till the sample was completely scale free and

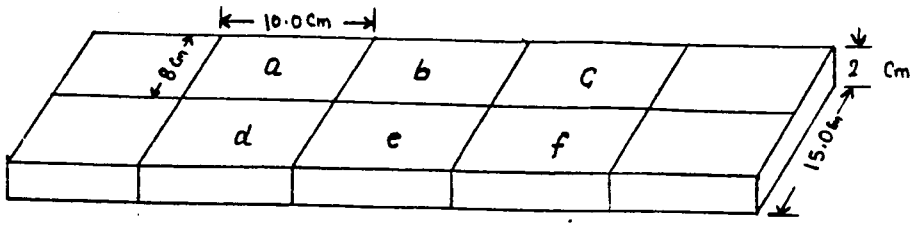

Figure 21. Hot rolled plate of 15.24 cm x 1.59 cm crossection.

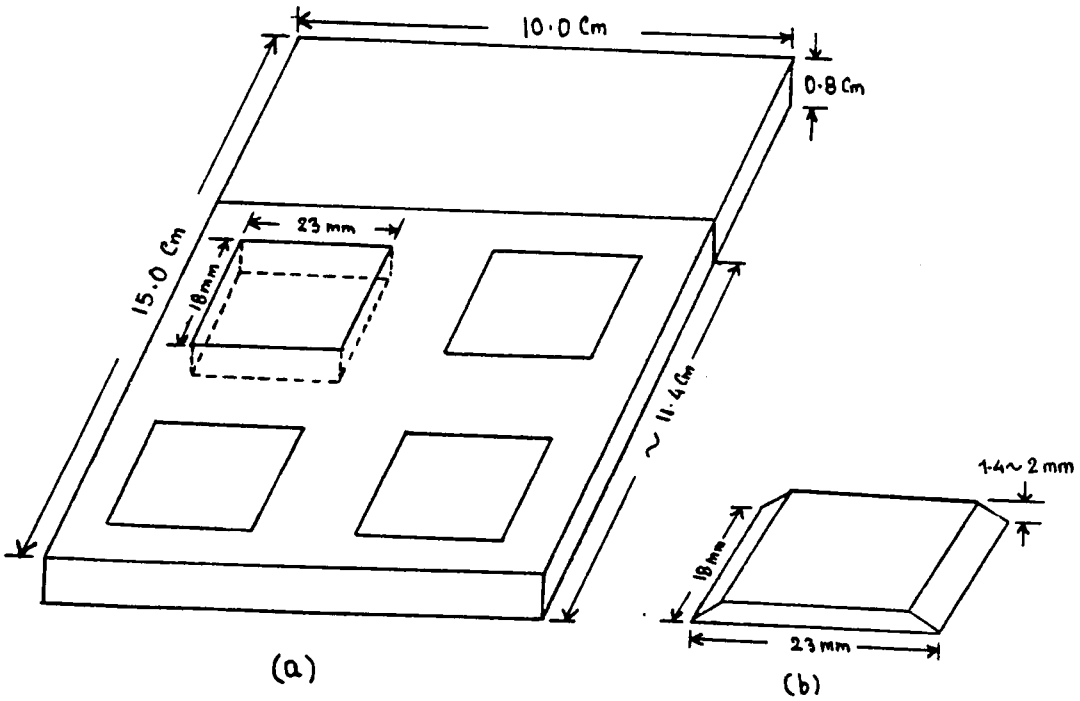

Figure 22. Cold rolled plate for x-ray diffraction samples.
a) The 15.24 cm x 10.16 cm x 0.79 cm plate from which x-ray diffraction samples were machined,
b) Cryostat sample.

shiny, or till a 50% current drop was observed. However, the use of current drop to mark the end of polishing was applicable only for freshly made electrolyte. Generally, the weaker the electrolyte the higher the power needed for electropolishing.

3.3.2 Experiment

A room temperature diffraction pattern of the polished specimen using the standard flat specimen holder was taken. The low temperature cryostat of the Rigaku diffractometer was then mounted on the goniometer table after the specimen was placed in it. Then, this specimen was aligned using the room temperature diffraction pattern as the reference and by observing that the peaks should occur at the same 2θ values as they did for the flat specimen holder.

Once the alignment was done, the low temperature unit was evacuated to a pressure of 10^{-3} torr, after which the refrigerant (liquid N_2) was poured in slowly till the vessel was full. After the vessel was filled, the current for the heating element of the cryostat was adjusted to maintain the desired low temperature, and care was also taken to ensure that the cryostat was filled with liquid N_2 to 8/9th of the capacity throughout the course of the experiment.

The diffraction patterns were taken, beginning with room temperature and progressing down to liquid N_2 temperature, at desired temperatures obtained by adjusting the current as neccessary. The experiment was repeated in a reverse manner also; ie., diffraction patterns were taken from liquid N_2 tempeature all the way to room temperature. The x-ray data were collected using a scan speed of 1° per minute. The background radiation was kept to a minimum by varying the tube power between 32 and 35 KV and 20 mA, as necessary. The scanning was done from 30° to 70° 2θ values, without scanning between 2θ values of 41° to 47° as no peaks were present between these values for all alloys considered. For the analysis, however, only the peaks

observed between 30° and 41° were considered as these were better resolved than the rest. All the alloys considered in this study showed complete reversibility of the phase transformation without any high degree of thermal hysteresis.

3.4 Indexing And Phase Identification

For each alloy considered, the following procedure was adopted for identifying and indexing the observed reflections. From the diffraction patterns, the 2θ values of each peak and hence the corresponding 'd' values, knowing the λ of the Cu-K_α incident radiation, were determined.

Knowing that the alloys considered contain both monoclinic α" and tetragonal γ° when quenched to room temperatures, the following approach was taken for indexing the individual reflections. First, the α" monoclinic phase was considered. The lattice parameters were calculated from Tangri and Chaudhuri's results [10] by direct interpolation for the specific alloy composition considered. From these lattice parameters, the 'd' values were calculated for α" by using the following equation for d, knowing that $\hat{\gamma}$ is a unique angle.

$$\frac{1}{d^2} = \frac{1}{\sin^2 \hat{\gamma}} \left\{ \frac{h^2}{a^2} + \frac{l^2 \sin \hat{\gamma}}{c^2} + \frac{k^2}{b^2} - \frac{2\,h\,k \cos \hat{\gamma}}{ab} \right\}$$

This was done for all the monoclinic reflections and the theoretically calculated 'd' values were compared with the observed experimental 'd' values. The results thus obtained are shown in Table A.3. The remaining unmatched experimental 'd' values were then tested for their identity with the γ° phase. Knowing that γ° is a tetragonal structure the following equation [40] must hold.

$$\sin^2\theta = A(h^2 + k^2) + Cl^2$$

where A and C are constants, and h, k, l are the Miller indices. The A and C are related to the lattice parameters and the wave length of radiation as follows.

$A = \lambda^2/4a^2$, and $C = \lambda^2/4c^2$

The A and C values need to be determined, and, once found, they will disclose the cell parameters 'a' and 'c' and enable the line indices to be calculated. The A value is determined from h k 0 lines, when the above equation becomes

$\sin^2\theta = A(h^2 + k^2)$

The allowed values of $(h^2 + k^2)$ are 1,2,4,5,8 etc. Therefore, the h k 0 lines must have $\sin^2\theta$ values in the ratio of these integers, and A will be some number which is 1, 1/2, 1/4, 1/5, 1/8, etc., times the $\sin^2\theta$ values of these lines. The constant C can then be found from other lines on the pattern and the use of the initial equation in the form

$\sin^2\theta - A(h^2 + k^2) = Cl^2$.

Thus differences from the left-hand side of the above equation, for various assumed values of h and k in an attempt to find a consistent set of Cl^2 values, must be in the ratio of 1, 4, 9, 16 etc. Once these values are found, C can be determined. When the above approach was applied to the peaks from the 15.0 at% Nb alloy, the observed peak positions along with the $\sin^2\theta$ values given below were obtained. The h k l values shown are the assumed ones.

2θ	$\sin^2\theta$	h k l
32.20	0.0769	0 1 1
36.15	0.0963	0 2 0
36.85	0.1000	1 1 1

Using (020) the equation reduces to give the value of A as 0.0241 and using (011), along with the value of A just obtained, the value of C was determinied as 0.0528. From these values, the 'a' and 'c' values were found and the d values were then determined by using the following equation

$$\frac{1}{d^2} = \frac{h^2 + k^2}{a^2} + \frac{l^2}{c^2}$$

These values were matched with the observed d values and the peaks indexed, as shown in Table A.3. Thus, the peaks were indexed for the 15.0 at% Nb alloy. The rest of the alloys had the same peaks in varying intensities depending upon the alloy composition and temperature of diffraction experiment.

4. THEORY OF PHASE FRACTION DETERMINATION

The basis of the x-ray technique and its reliability and precision lies in the fact that the intensity of a diffraction line of a particular phase is a function of the volume fraction of that phase present in the aggregate. The ratio of the intensity of a diffraction line of a phase in the aggregate to the intensity of a second phase diffraction line yields the ratio of the volume fractions of each phase present [2]. This is the principle used in determining volume fractions for each phase, and is commonly called the direct comparison method. This technique enables one to use all available, experimentally observed diffraction peaks and thus is well suited for the use of computer analysis. The integrated intensity of the ith diffraction peak of a resolved spectra from the α phase in the aggregate is given by:

$$E_i^{\alpha} = K R_i^{\alpha} V^{\alpha} \text{ -------(1)}$$

where,

$$K = I_o A_o A_s \left[\frac{e^4}{m^2 c^4}\right] \left[\frac{\lambda^3}{32 \pi r^2 \bar{\mu} \omega}\right]$$

and for each ith peak

$$R_i = m N^2 F^2 e^{-2D} \frac{1}{\text{Cos}\theta \, \text{Sin}^2\theta} P$$

For a second phase β in the aggregate we have

$$E_j^{\beta} = K R_j^{\beta} V^{\beta} \text{ -------(2)}$$

Here, V^{α} and V^{β} are the volume fractions of the α and β phases, respectively. K is a independent constant (depends on experimental conditions alone), whereas R is a factor

depending on θ and h k l values of each reflection. The various terms used in the K and R factors are given in Appendix. From (1) and (2) we can write the following sets of equations.

$$KV_i^{\alpha} = \left(\frac{E_i}{R_i}\right)_{\alpha}$$

$$KV_j^{\beta} = \left(\frac{E_j}{R_j}\right)_{\beta}$$

The ratio E/R is referred to as the normalized energy and can be determined experimentally. For theoretically perfect data, the average value of the normalized energies for the various h k l spectra would equal to the individual values of the normalized energy. For real data, the individual values of the normalized energy would fluctuate about the theoretical value of K, i.e., E/R, due to the presence of preferred orientation, grain size and statistical effects [2]. Under such conditions, the best estimate of E/R is simply the average value of all the peaks present in the real data.

4.1 Factors Affecting Measured Intensity

4.1.1 Extinction

This arises from two independent experimental conditions, and are termed primary and secondary extinctions. The primary extinction is due to the individual grains in the aggregate becoming more perfect. In any real crystal, there is a certain imperfection due to the fact that the higher dislocation densities group together to form sub-grain boundaries, isolating lower dislocation density areas as sub-grains; that is, a mosaic structure in a single grain is formed. This mosaic structure causes greater reflection whenever such sub-grains are very fine and nonparallel. However, with increased

sub-grain size, when some or all are parallel, there is a decrease in integrated intensity and this is called primary extinction. The secondary extinction, on the other hand, is due to the nonrandomness of the grains or single crystals in a polycrystal aggregate, which again reduces integrated intensity, specifically of the stronger spectra relative to the weaker ones.

4.1.2 Microabsorption

This leads to a loss in intensity due to one phase having linear absorption coefficient different from the other in the mixture, or the grain size being much larger than the other. This effect is negligible if the linear absorption coefficients of the two phases are nearly the same or the particle size of both phases very small.

4.1.3 Preferred Orientation

This effect negates the assumption of perfect random orientation of the crystals in a polycrystalline material. This causes certain spectra to exhibit increased intensity while at the same time, others show reduced intensity. In a polycrystalline material which has preferred orientation its effect cannot be eliminated other than by rotating the sample in particular ways during the intensity measurement [2]. Secondary extinction effects may reduce the anomalously strong spectra to a certain degree.

4.1.4 Statistical Fluctuations

The x-ray diffraction energy, which is quantitatively measured by the diffractometer, is the total diffracted energy of an h k l spectrum; that is, the integrated intensity measured after being affected by the above mentioned factors. This, in turn, is subjected to statistical fluctuations which are due to:

i) the statistical nature of the x-ray emission and reflection processes

ii) fluctuation in electron flux at the source tube, due to imperfect control over tube voltage and current

iii) instability of the counting system

iv) experimental error of a random nature.

4.1.5 Superposition

If the number of phases present in the aggregate is large or if one or more phases have large lattice parmeters or a low symmetry structure, the probability of peak overlap is increased, preventing separation of peaks into individual energy components. Even when there is only partial overlap any separation technique becomes tedious. Also, as the background increases, the minimum diffracted energy which can accurately be measured decreases.

5. CALCULATION OF PHASE FRACTIONS

5.1 Determination of R

In calculating the factor R, the unit cell volume and the structure factor F were the two quantities which were calculated. The LP factor and 'm', the multiplicity factor for each h k l value, were easily available from published literature [41,42]. The temperature factor e^{-2D}, used to compensate intensity loss due to thermal vibrations of the atoms was ignored since the thermal vibrations at room temperature and below are too low [40] to significantly affect the measured intensities in this experiment. The unit cell volume 1/N was calculated using the equations below knowing the lattice parameters at room temperature of each phase. The lattice parameter changes with temperature were not taken into consideration.

$$1/N_{\alpha''} = a\ b\ c\ \mathrm{Sin}\ \hat{\gamma}$$

$$1/N_{\gamma^{o}} = a^2\ c$$

The structure factor was determined by knowing the atom positions of each phase [29,22] and the atomic scattering factor f. The latter was determined by graphical interpolation from values [43] of f of U and Nb atoms plotted for the 2θ range considered (Fig.23). As the phases studied were random solid solutions, the f values were weighted averaged values for U and Nb, knowing the atomic percent of U and Nb in the alloys. The atom positions in α" and γ °, along with the equation to determine $|F|^2$, are shown below.

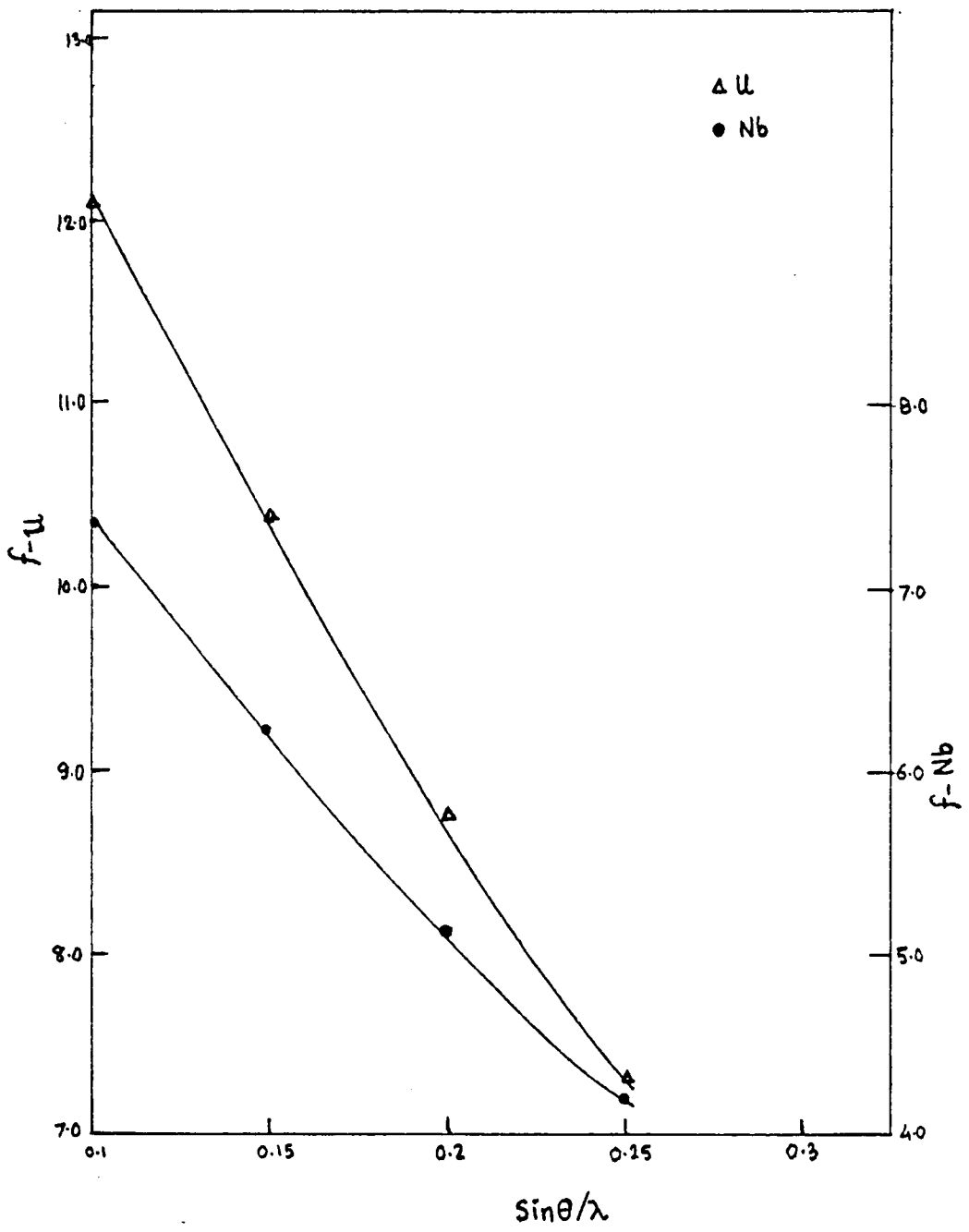

Figure 23. Plot of f, the scattering factor versus Sinθ / λ for U and Nb atoms [44].

α"			γ°		
u	v	w	u	v	w
0.036	0.102	0.25	0.0	0.5	0.453
0.036	0.102	0.75	0.5	0.0	-0.453
0.464	0.602	0.25			
0.536	0.398	0.75			

$$|F|^2 = [f_1 \cos2\theta\,(hu_1 + kv_1 + lw_1) + f_2 \cos2\theta\,(hu_2 + kv_2 + lw_2) + f_3 \cos2\theta\,(hu_3 + kv_3 + lw_3) + \ldots]^2 + [f_1 \sin2\theta\,(hu_1\, kv_1\, lw_1) + f_2 \sin2\theta\,(hu_2 + kv_2 + lw_2) + f_3 \sin2\theta\,(hu_3 + kv_3 + lw_3) + \ldots]^2$$

5.2 Determination of E

The integrated intensity E was determined by using the Pearson VII peak separation computer program developed by Zieminski [44]. The pen-chart plot of the diffraction pattern is first digitized using a digitizing program, where each digitized point has 2θ and intensity as its coordinates. These digitized points of the pattern are now input data for the peak separation program. Apart from this, for each peak the 2θ value, maximum intensity I, half-height width H and shape factor S, along with a step-size or increment in each of these parameters, were also given as the initial input. By means of the shape factor, the program is instructed about the type of peaks, namely sharp or broad, it can expect to analyse. A value of 1 to 10 for S is generally given for crystalline materials. In this analysis, S was given a value of 5 for all the data analysed. The program, with these initial parameters, simulates a diffraction peak curve as a first approximation. Then the digitized data are compared to the simulated curve and an attempt is made to fit these data points to this curve. Once a "best fit" is obtained the program computes the individual area under each peak, which is the integrated intensity.

5.3 Problems In Evaluating E using the Peak Separation Program

The area calculated under each peak (i.e., the integrated intensity E of each peak) was found to be sensitive to the initial input parameters 2θ, H, S and I and their increments δ2θ, δH , δS, and δI. However, inspection of the curve fit shows that the experimental data points and the computer generated points fit fairly well even when the E values were unusually high for certain peaks in a particular data set. Also, in such cases the computer evaluated input parameters were in correspondence with the initial input parameters reflecting the good curve fit. Manipulation of the increments in the input parameters seem to affect E to a larger extent than the curve fit itself, thereby indicating that the manner in which the computer program evaluates areas under each peak is rather ambiguous. Because of the above difficulties inherent in the computer program itself, the following approach was taken to determine E values and hence the phase fractions.

First, each data set was analysed so as to get a best curve fit by varying the increments for the input parameters. This is illustrated in Fig.24 and Fig.25, where Fig.25 clearly shows a better fit than Fig.24, in the weak peaks around 33.5 and 40° 2θ. However, this in itself is no guarantee that the E values calculated after such a fit were in correspondence with the experimental intensities. This is illustrated by Fig.26 and Fig.27, which show two diffraction patterns having fairly good curve fits from the same alloy at +22°C and -40°C, and Table 3 shows the results of these patterns. Inspection of Table 3 shows that while E values pertaining to the Fig.27 are in correspondence with experimental intensity, the E value of peak 1 for Fig.26 has a value much higher than peak 5, which is the strongest peak in Fig.26. Thus this E value for peak 1 of Fig.26 is an abnormal value. This shows that the curve fit in itself is

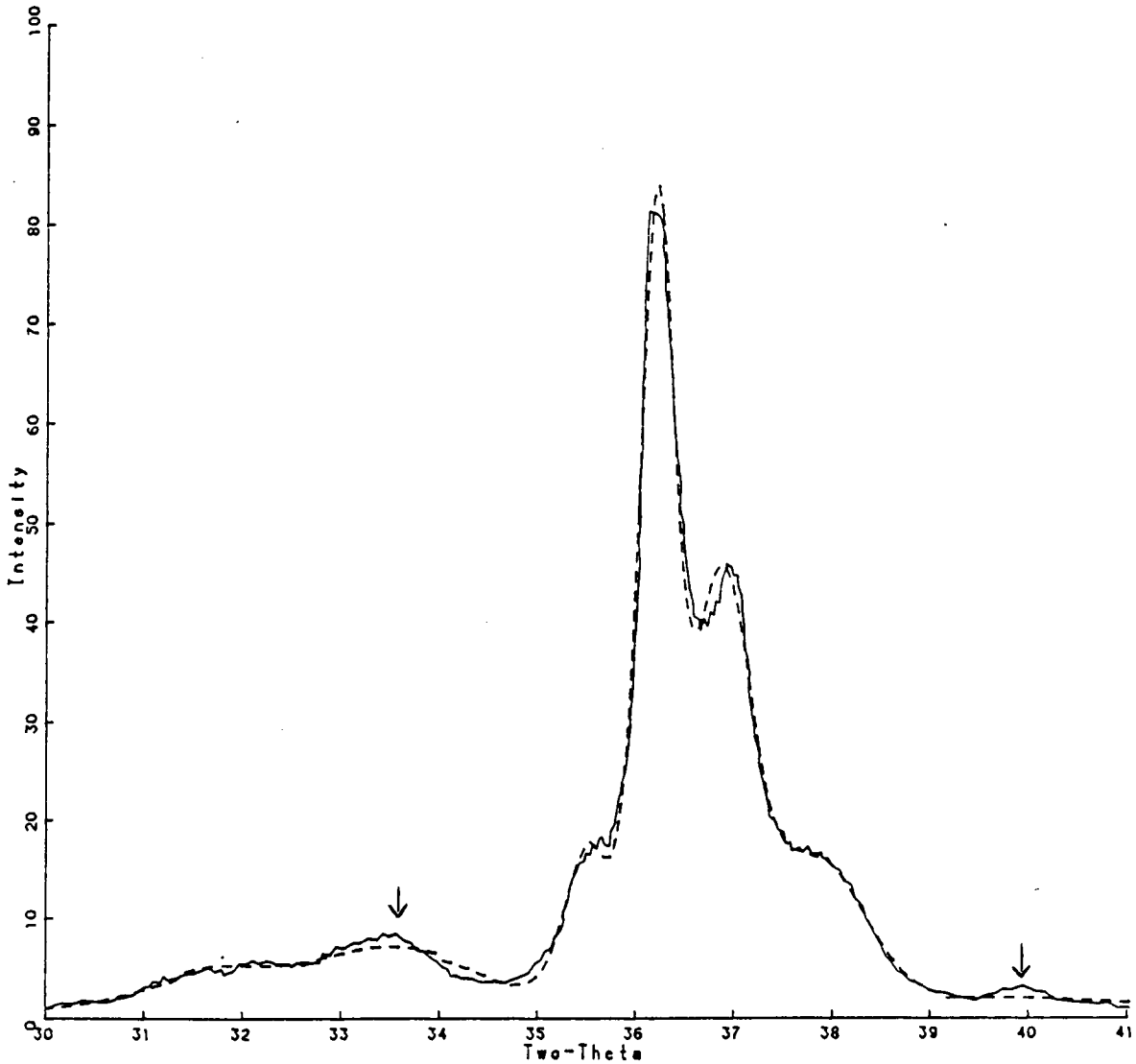

Figure 24. Illustration of the curve fit by the computer for a diffraction pattern.

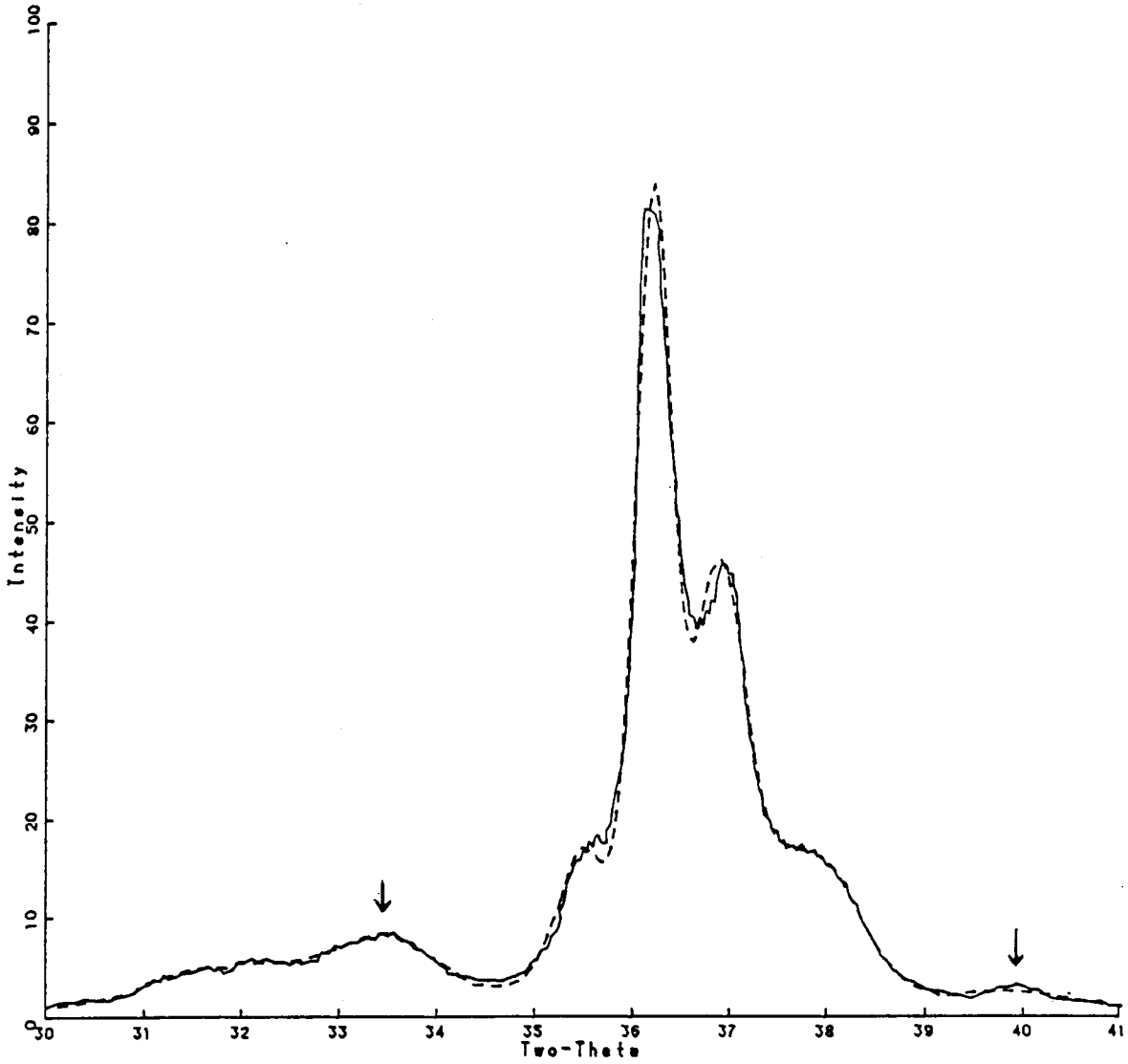

Figure 25. Illustration of the curve fit by the computer for the same diffraction pattern as in Fig. 24, after varying the input incremental values.

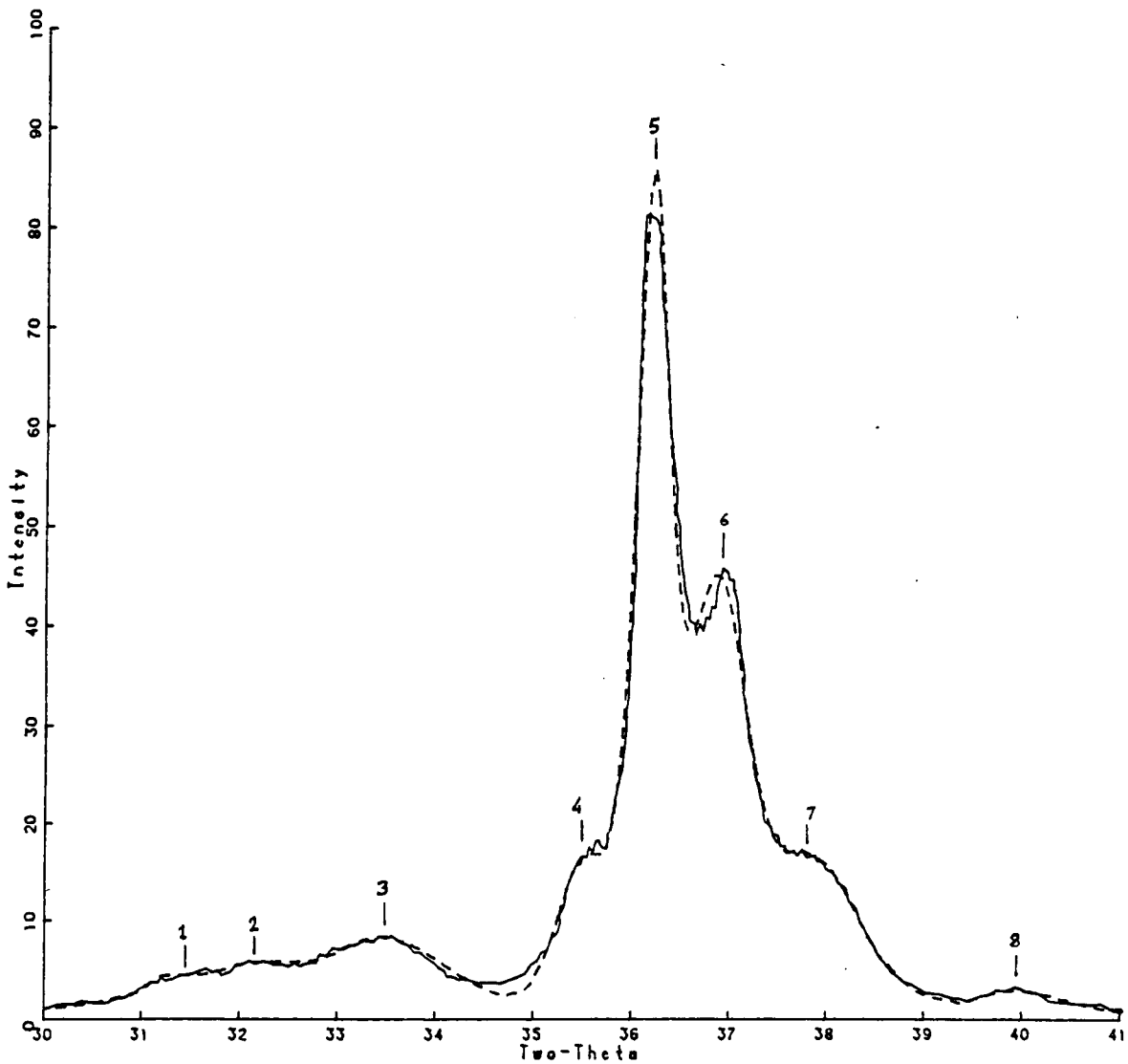

Figure 26. The computer generated curve fit at +22 °C

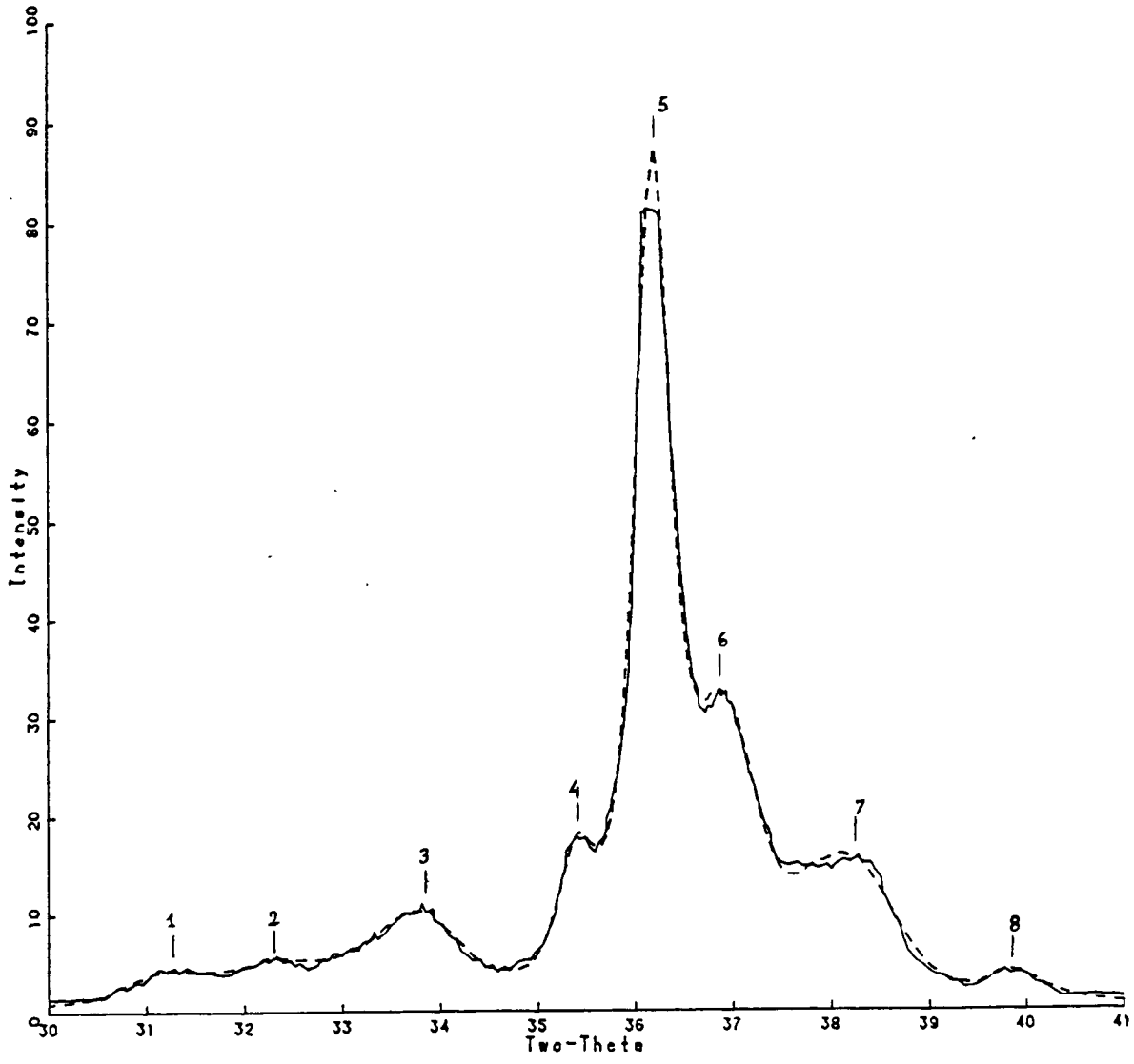

Figure 27. The computer generated curve fit at -40 °C

TABLE 3

Comparison of the E values for two diffraction patterns at +22 °C and -40 °C.

Peak	h k l	E's at +22 °C (fig.26)	E's at -40 °C (fig.27)
1	$(020)_{\alpha''}$	75.51*	14.12
2	$(011)_{\gamma\circ}$	4.20	7.60
3	$(\bar{1}10)_{\alpha''}$	17.11	14.38
4	$(110)_{\alpha''}$	7.91	8.20
5	$(002)_{\alpha''}$	43.43	51.38
6	$(111)_{\gamma\circ}$	28.98	21.63
7	$(\bar{1}11)_{\alpha''}$	21.45	20.35
8	$(111)_{\alpha''}$	5.77	9.22

no indication that corresponding E values would be evaluated properly by the computer program.

The abnormally high values of E calculated by the program almost always happened for the weak and broad peaks for all the data analysed. Thus, apart from looking for best curve fit, the E values were also observed so that no abnormally high values are assigned for peaks when compared to their experimental data. With the above conditions in mind, all the data were analysed by varying the increments for the input parameters till "best curve fits" were obtained for each data set. In all the data the strong superposed peak $(002)_{\alpha''}$, $(021)_{\alpha''}$, and $(020)_{\gamma}$ occuring at about 36.2° was ignored, since this peak cannot be separated into individual peaks corresponding to the respective phases α'' and γ °. Although it was impossible to completely avoid abnormal E value for some peaks in the overall data as mentioned above, such peaks were deleted from phase fraction evaluation, i.e., after arriving at a good fit if some peaks had abnormally high E values such peaks were not considered for phase fraction determination. Thus, all the data were analysed and the final curve fits at each temperature are shown in Fig A.1 through Fig A.17. The corresponding input parameters and the E's computed by the program are shown in Table A.4. It is from the E values in Table A.4 which did not have abnormally high values that the phase fraction of α'' and γ ° were determined. These E values are also shown separately in Table A.5.

The percent α'' thus calculated is plotted versus temperature in Fig.28(a), (b) and (c). There is another plot shown by dashed line as determined by Vandermeer [45] (see below), and it is evident that the variation of % α'' with temperature follows a similar behaviour, as the one found in this research. Vandermeer's calculation gave about 30% less α'' than the present results. A non-linear regression analysis was used by Vandermeer which computed two parameters for selected resolved peaks. Assuming triangular symmetry for each peak, these two parameters were the base and height of the

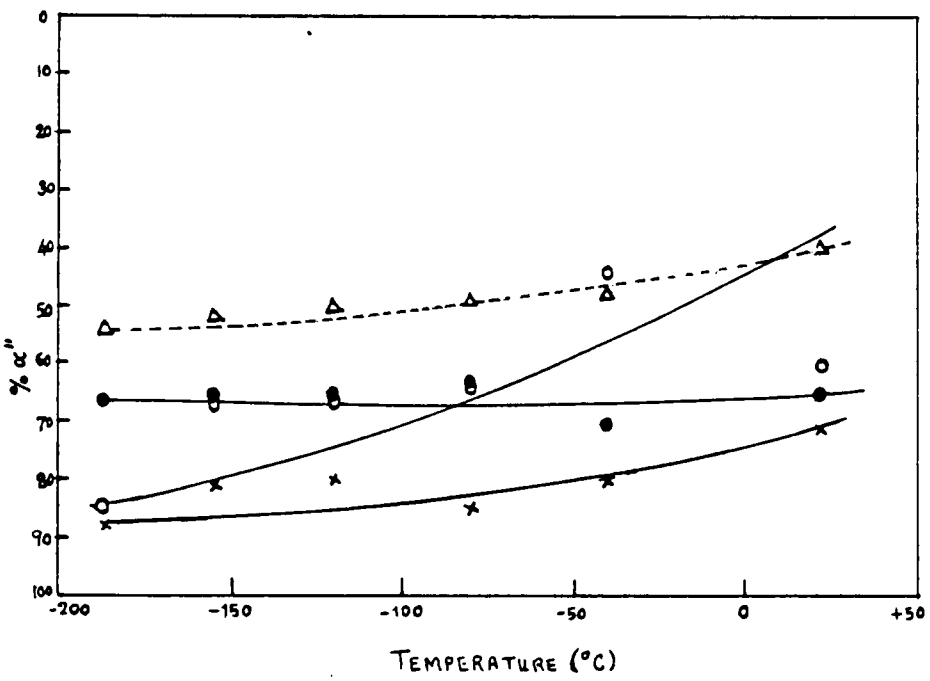

(a) Alloy 142

× - This analysis
o - Phase fraction using E_p
● - Phase fraction using E_c
Δ - Vandermeer's results

Figure 28. The variation of % α" with temperature as determined by the three methods for alloys 142, 183 and 196.

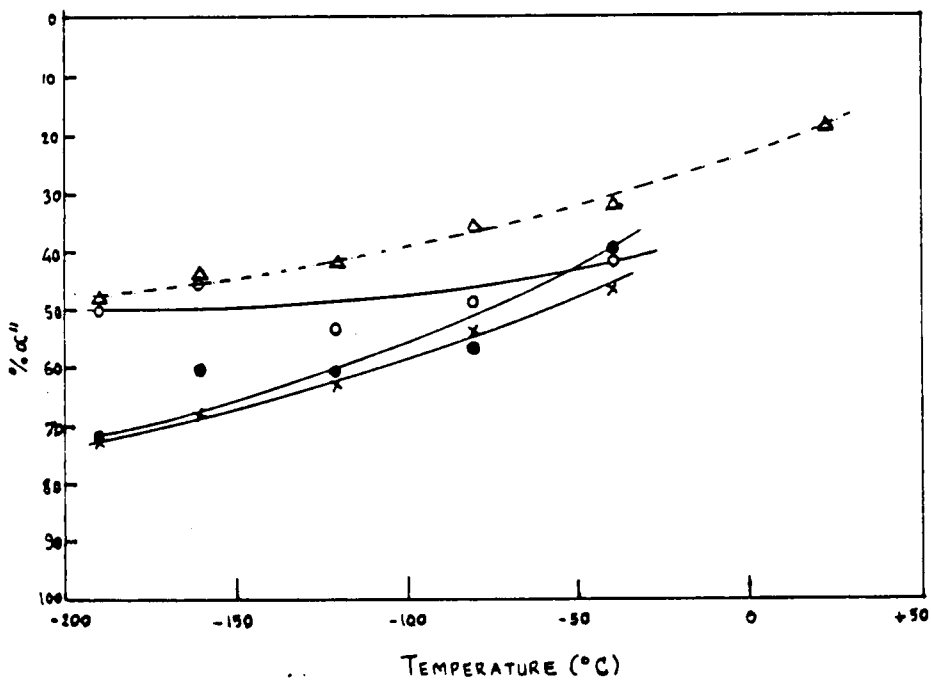

(b) Alloy 183

× - This analysis
○ - Phase fraction using E_P
● - Phase fraction using E_c
△ - Vandermeer's results

Figure 28 (continued).

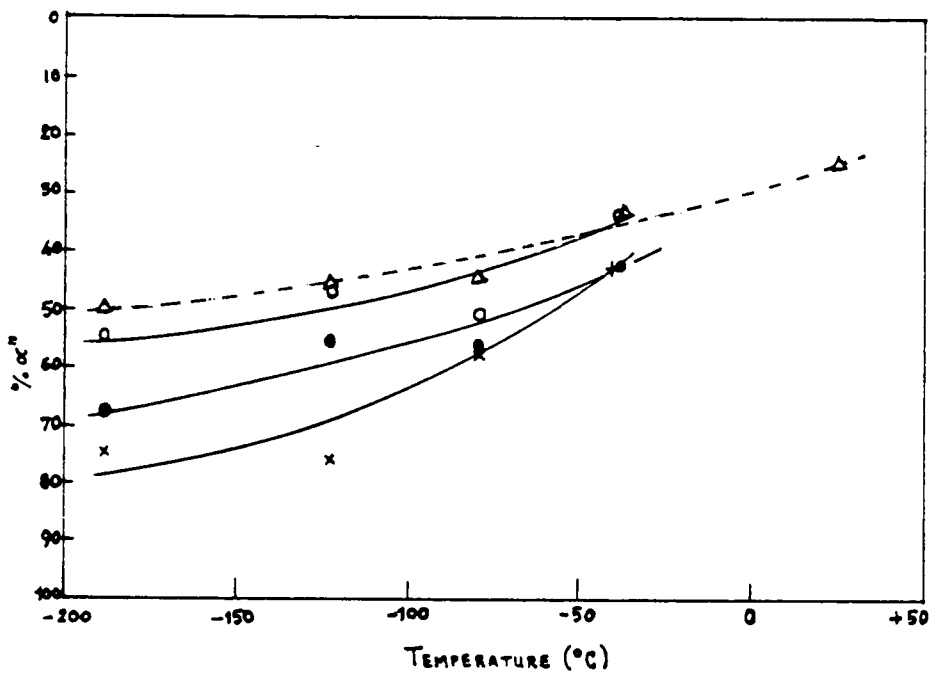

(c) Alloy 196

× - This analysis
○ - Phase fraction using E_p
● - Phase fraction using E_c
△ - Vandermeer's results

Figure 28 (continued).

triangle, from which the area under each peak was determined using E = 1/2 base x height. It is not known whether any peak separation was performed by this method to include the peak extermities which overlapped.

To make a comparison with Vandermeer's results, the initial input parameter I and H, values read from the pen-chart diffraction patterns, and the I and H values calculated by the computer, were considerd selectively only for those peaks which did not yield an abnormal E value as mentioned earlier, i.e., the peaks in Table A.5. For these peaks, two sets of E values were determined using $E_p = 1/2\ I_p\ H_p$ and $E_C = 1/2\ I_c\ H_c$ where E_p denotes that I_p and H_p values used were taken from pen-chart diffraction patterns and E_C denotes that I_c and H_c values used were computer evaluated. Thus two sets of phase fractions were determined, one using E_p's and one using E_C's. The variation of these phase fractions with temperature is also shown in Fig.28. From Fig.28 the phase fraction variation with temperature obtained using two the E values described above did not show similarity with the previously obtained results except for alloy 196. Also for each alloy this variation was different. The net phase fraction in this case also was lower than that obtained by the first analysis.

Because of the sensitivity of E to the incremental values of the input parameters, an attempt was made to optimize these values so that a uniform incremental value could be found and used consistently for all the data without having to individually manipulate a particular data set, as was done in the first analysis described above. The data for the alloy 183 at -121° C was considered for this purpose. First the $\delta 2\theta$ was varied, keeping the other incremental parameters constant, (see Table 4) as 0.001, 0.01, and 0.1. The curve fit when $\delta 2\theta$ = 0.001, 0.01 and 0.1 is shown in Fig.29, Fig.30 and Fig.31 respectively. Inspection of these show that the curve fit with $\delta 2\theta$ = 0.01 is the best fit (Fig.30). Thus $\delta 2\theta$ was selected to be 0.01. Also inspection of E values shown in Table 4 calculated by the computer for the above curve fits show that E values with $\delta 2\theta$

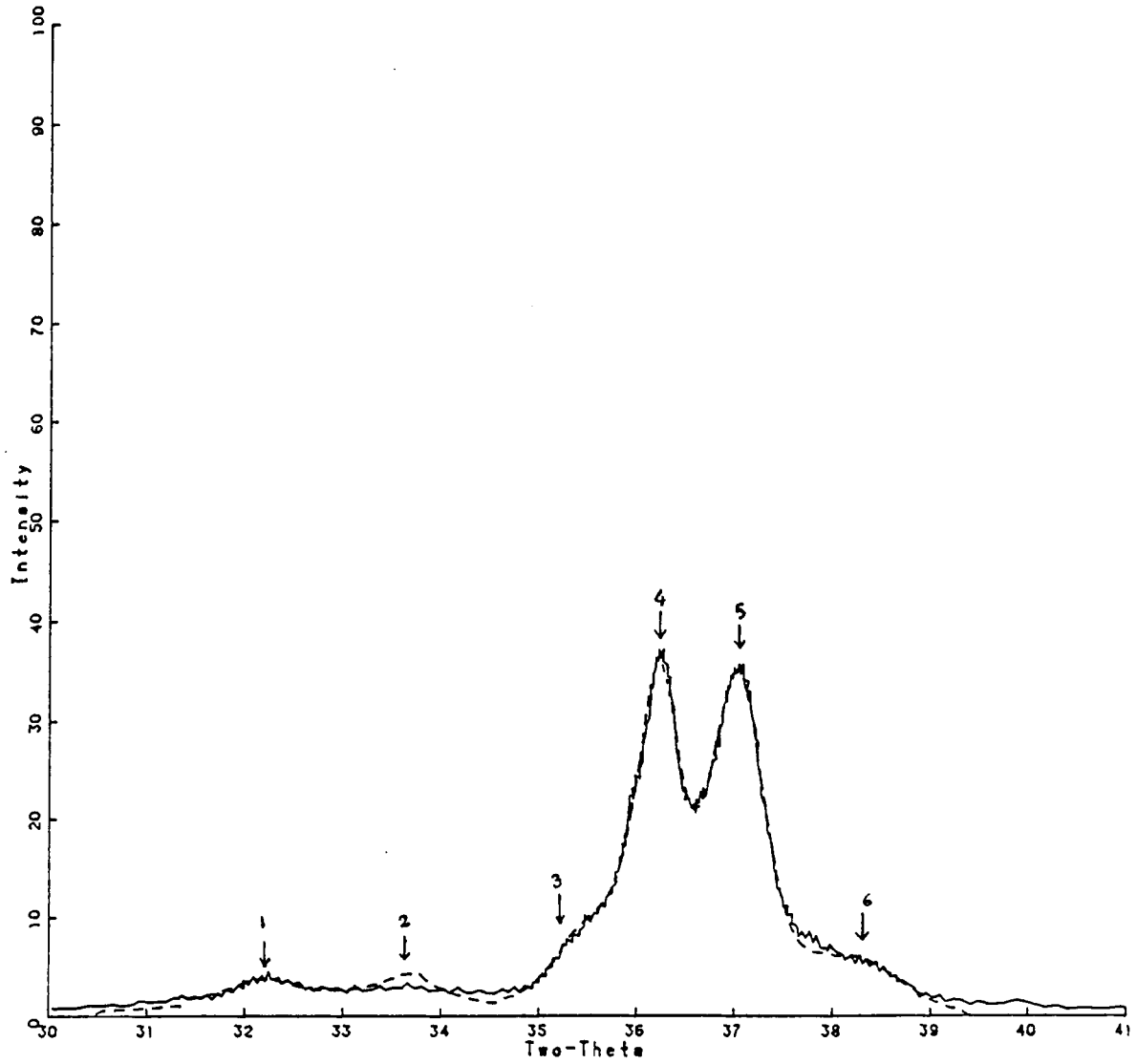

Figure 29. The computer generated curve fit for the diffraction pattern when $\delta\theta = 0.1$.

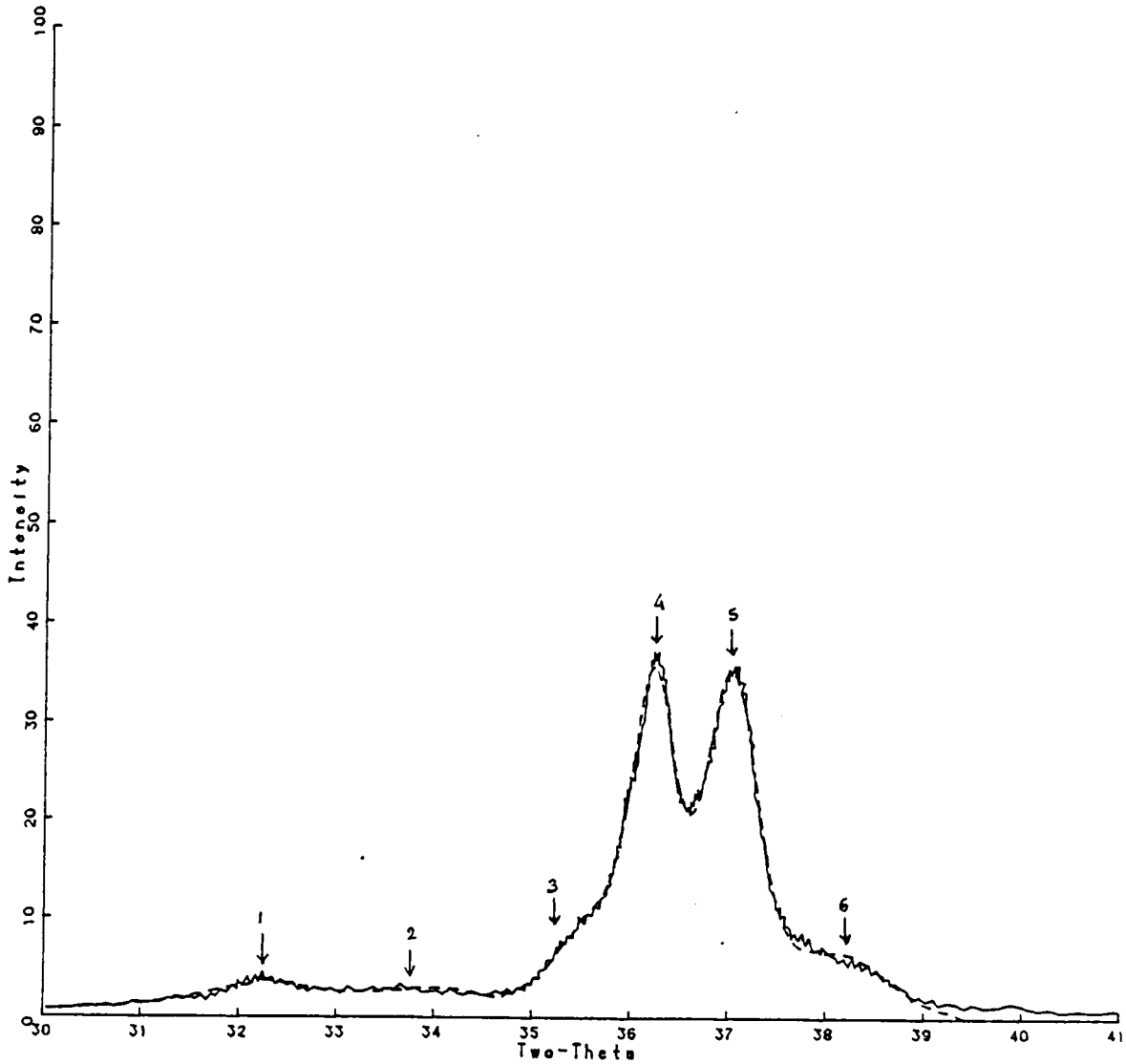

Figure 30. The computer generated curve fit for the diffraction pattern when $\delta\theta = 0.01$.

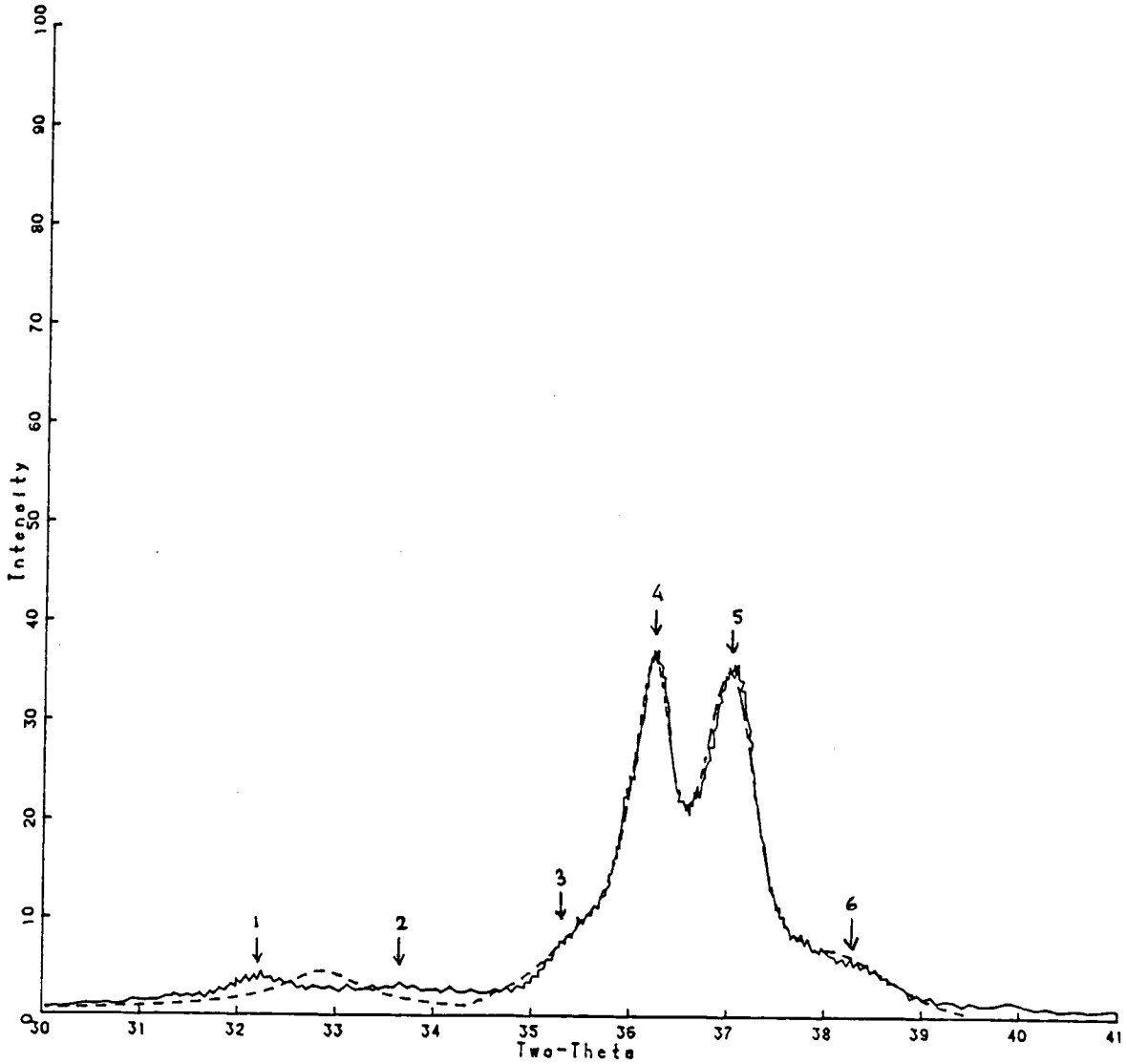

Figure 31. The computer generated curve fit for the diffraction pattern when $\delta\theta$ = 0.001.

TABLE 4

Optimization for δ2θ. The abnormal E values are indicated by '*'.

δ2θ = 0.1

Peak	2θ	δ2θ	δH	δS	δI	E
1	32.25	0.001	0.01	1.0	0.1	13.25
2	33.60	0.001	0.01	1.0	0.1	64.59*
3	35.45	0.001	0.01	1.0	0.1	10.22
4	36.20	0.001	0.01	1.0	0.1	21.19
5	37.00	0.001	0.01	1.0	0.1	24.09
6	38.25	0.001	0.01	1.0	0.1	8.43

δ2θ = 0.01

Peak	2θ	δ2θ	δH	δS	δI	E
1	32.25	0.01	0.01	1.0	0.1	23.03
2	33.60	0.01	0.01	1.0	0.1	14.67
3	35.45	0.01	0.01	1.0	0.1	10.34
4	36.20	0.01	0.01	1.0	0.1	19.48
5	37.00	0.01	0.01	1.0	0.1	24.62
6	38.25	0.01	0.01	1.0	0.1	8.68

δ2θ = 0.001

Peak	2θ	δ2θ	δH	δS	δI	E
1	32.25	0.1	0.01	1.0	0.1	0.00*
2	33.60	0.1	0.01	1.0	0.1	184.69*
3	35.45	0.1	0.01	1.0	0.1	6.99
4	36.20	0.1	0.01	1.0	0.1	24.86
5	37.00	0.1	0.01	1.0	0.1	20.27
6	38.25	0.1	0.01	1.0	0.1	12.94

= 0.01 are more in correspondence with the experimental data, apart from having a better fit.

Now, keeping $\delta 2\theta$ to be 0.01, δS was varied as 0.01, 0.05, and 0.1 and by a similar method described above the best δS was found to be 0.1. In a similar fashion the δH and δI were optimized as 0.005 and 0.1, respectively. Using these new uniform values, all the data of the three alloys were once again analysed to determine E values. The curve fit and the respective E values and input parameters computed from this second analysis are shown in Fig. A.18 through Fig. A.34 and Table A.6, respectively. From Table A.6 it is seen that here also there are abnormally high values for certain peaks, and compared to the first analysis, i.e., Table A.4, the abnormally high values in the present case (Table A.6) are much more prevalent. Inspection of Fig. A.18 through Fig. A.34 shows that the curve fits were good, again indicating that the program has an inherent defect in calculating the area under the separated peaks, even though it was able to make a curve fit.

Thus it was found that there seems to be no logical process by which the incremental values of the input paramerters affect the area calculated under each peak after the curve fit. The phase fractions were calculated from this second analysis by considering only the peaks which do not have abnormally high E values, and the net phase fractions were found to be very close to those of the first analysis (Fig.32), especially for alloys 183 and 196 (Fig.32(b) and (c)). Thus even though the net phase fractions calculated in both these analysis were close, the % α" calculated from the first analysis (Table A.5) was used to determine the metastable phase diagram, as this had less abnormal E values present, and this permitted more peaks to be included in phase fraction determination. In both the analyses the abnormal E values were not used to determine phase fractions, as already discussed. In spite of the inherent problem of the computer program to determine

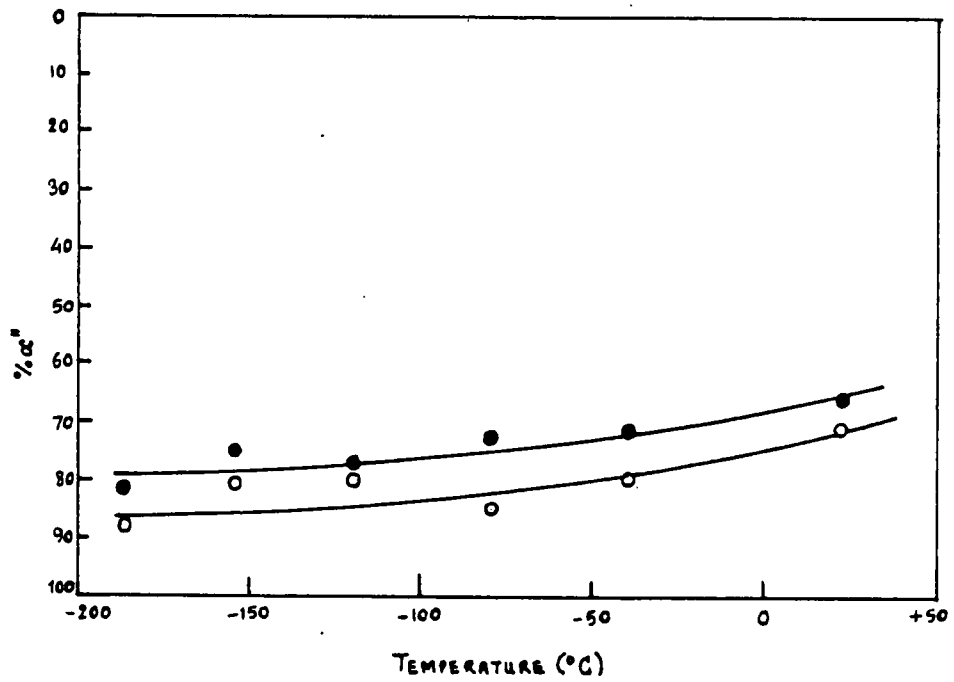

(a) Alloy 142

o - Before optimization

● - After optimization

Figure 32. Comparison of % α" Vs temperature variation for alloys 142, 183 and 196 before and after optimization of the incremental values of the input parameters.

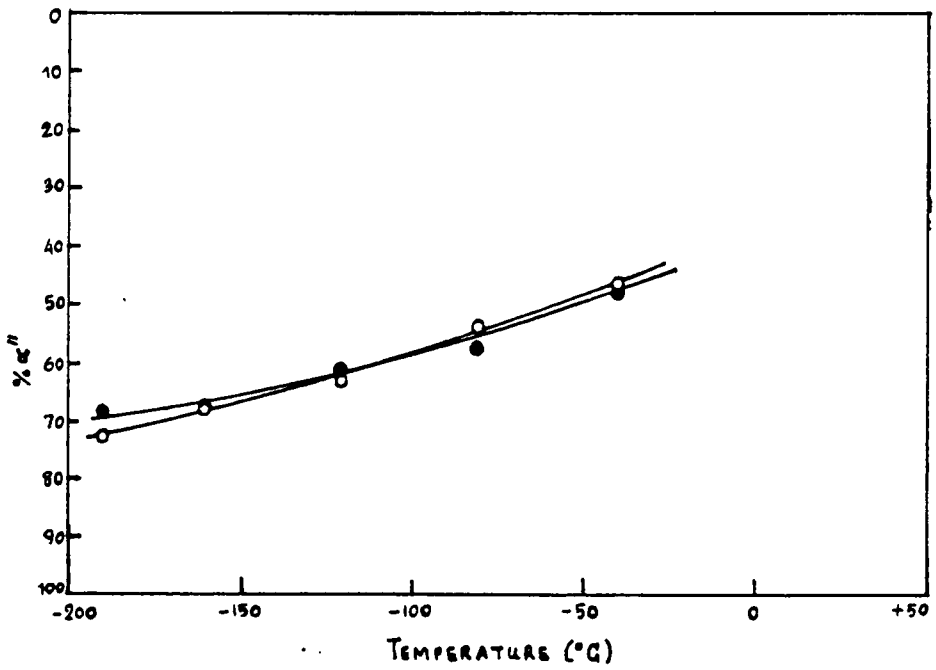

(b) Alloy 183

o - Before optimization

● - After optimization

Figure 32 (continued).

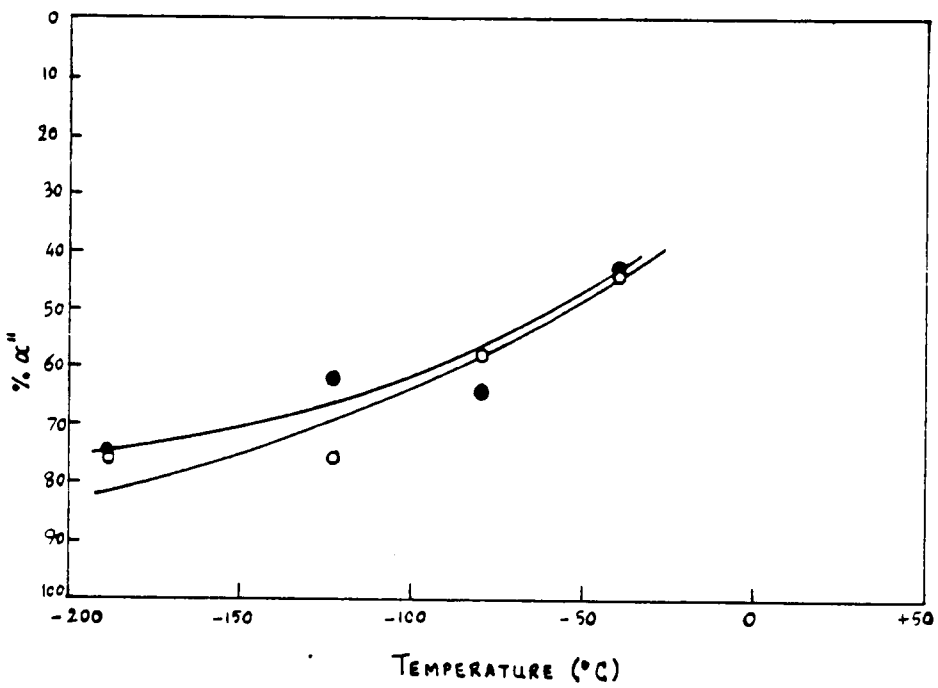

(c) Alloy 196

o - Before optimization

● - After optimization

Figure 32 (continued).

E values directly, the E values obtained by the above method gave a variation of % α'' with temperature similar to that given by Vandermeer.

5.4 Phase Fraction Determination

Considering the two phase mixture of α'' and $\gamma°$, we have the following equations, again from Eqs.(1) and (2).

$$KV_i^{\alpha''} = \left(\frac{E_i}{R_i}\right)_{\alpha''}, \qquad \text{and} \quad KV_j^{\gamma°''} = \left(\frac{E_i}{R_j}\right)_{\gamma°}$$

Thus the mean normalized energy values for the resolved spectra are given by:

$$K(V)^{\alpha''} = \frac{1}{I} \sum_{i=1}^{I} \left(\frac{E_i}{R_i}\right)_{\alpha''} \quad \text{and} \quad K(V)^{\gamma°} = \frac{1}{J} \sum_{j=1}^{J} \left(\frac{E_j}{R_j}\right)_{\gamma°}$$

where i = 1,2,3 ...,and j = 1,2,3 ... are the number of peaks considered in each phase. From this, we have volume fraction equations for each phase as:

$$(V)^{\alpha''} = \frac{1}{K} \left\{ \frac{1}{I} \sum_{i=1}^{I} \left(\frac{E_i}{R_i}\right)_{\alpha''} \right\} \text{ ---------(3)}$$

$$(V)^{\gamma°} = \frac{1}{K} \left\{ \frac{1}{J} \sum_{j=1}^{J} \left(\frac{E_i}{R_j}\right)_{\gamma°} \right\} \text{ ----------(4)}$$

and knowing that

$$V^{\alpha''} + V^{\gamma°} = 1 \text{ -----(5)},$$

for a two phase mixture, the individual phase fractions can be determined from Eqs.(3),(4) and (5). For example, consider the 15.0 at% Nb alloy. The two $\gamma°$ peaks

and five α'' peaks at +22° C and their respective R and E values are listed in Table A.5. From Eqs.(3) and (4) we can write the α'' and $\gamma°$ volume fractions as:

$$(V)^{\alpha''} = \frac{1}{K}\{\frac{1}{5}[\frac{10.03}{2.8414} + \frac{12.02}{9.7615} + \frac{13.50}{9.1233} + \frac{21.25}{1.4340} + \frac{6.61}{0.3256}]\}$$

$$(V)^{\alpha''} = \frac{1}{K}(8.2725) \text{ --------(6)}$$

and for the $\gamma°$ phase:

$$(V)^{\gamma°} = \frac{1}{K}\{\frac{1}{2}[\frac{4.06}{0.7040} + \frac{10.20}{9.4804}]\}$$

$$(V)^{\gamma°} = \frac{1}{K}(3.4215) \text{ --------(7)}$$

From Eqs. (6) and (7) we have:

$$\frac{(V)^{\alpha''}}{(V)^{\gamma°}} = 2.4178$$

and using eq.(5) we obtain the α'' and $\gamma°$ phase fractions as 70.74 and 29.26 respectively. In a similar way the phase fractions at each temperature were determined for all the alloys. In using x-ray analysis an error of about 5% of the amount of phase measured is normally present, in the absence of preferred orientation [40]. Considering that no compensation was made for preferred orientation the error in this analysis could be higher than 5%. Thus the phase fractions for α'' and $\gamma°$ should be rounded off to 70 and 30% respectively.

6. RESULTS AND DISCUSSION

The results are discussed with respect to the evaluation of d values, the factors affecting the integrated intensity and the calculation of the volume fractions. The errors that are present or have been introduced experimentally, or otherwise, in evaluating the above entities are also considered.

6.1 Indexing Peaks

In indexing peaks and thus identifying the respective phases present, the 'd' value is the calculated quantity from which the rest of the calculations were done. The main source of erorr which could be introduced in determining 'd' values is the error in the experimentally determined Bragg angle 2θ. The 2θ values were read to $\pm$ 0.05°. Indeed, peak shifts were observed at different temperatures. However, since 'd' values were used merely to identify h k l values, any error introduced here will not affect the volume fraction of the phases being determined.

6.2 Factors Affecting The Integrated Intensities

6.2.1 Extinction

Both primary and secondary extinctions are independet of experimental conditions and depend upon the degree of perfection and orientation of the crystals. The phases, having been formed by a martensitic transformation by quenching, have severe non-uniform strains in them. Thus both γ ° and α" crystals can be assumed to be highly imperfect due to these strains.

The sample being fine grained (ASTM # 8) reduces parallelism among sub-grains (mosiac blocks) [40]. Thus this crystal imperfection along with the fine grain structure reduces primary extinction effects to a certain degree. The secondary extinction is

caused by the parallel alignment or non-randomness of diffracting grains and cannot be truly avoided in any metallurgically prepared sample, since perfect randomness is difficult to obtain even in powdered samples.

6.2.2 Absorption

The microabsorption considered here can alter the intensity data obtained from multiphased aggregates, whenever the linear absorption coefficient of these phases are very different. In the present case we only have two phases which are solid solutions having the same chemical composition, hence, making absorption effects negligible.

6.2.3 Grain Size And Preferred Orientations

The presence of large grains along with preferred orientation causes certain spectra to be more intense and others to be weak. This is a major factor which affects the measured intensities. In this experiment all the alloys showed similar grain size, with an average grain size of ASTM # 8; that is, 22 μm grain diameter, which is fairly fine grained. Even though preferred orientation cannot be avoided in a real polycrystalline sample, its presence can be detected by comparing the R values with E, the measured intensity. The calculated R values for one phase are simply the theoretical line intensities, in arbitratry units, for that phase in the absence of preferred orientation.

Thus if the measured intensities of the various lines of a particular phase are not in the same ratio as their R values, then preferred orientation exists. In this analysis, some preferred orientation must exist as the samples were polycrystalline, but secondary extinction may reduce anomalously strong spectra arising due to preferred orientation.

6.2.4 Statistical Fluctuation

In this analysis the electron flux fluctuation was assumed to be minimal since a stable voltage and current was maintained by the diffractometer. There could be counting losses due to the random arrival of the x-ray quanta at the counter. Therefore, pulse production at the counter is random in time. As the counting rate increases, the time interval between pulses decreases and may become so small that the adjacent pulses merge with one another and are no longer resolved, or counted as separate pulses. This is the point where counting loss has begun. When this occurs, the number of quanta absorbed is no longer proportional to the quanta detected.

Since quanta absorbed is the x-ray intensity, an error in counting or measured intensity has been introduced. in this case counts of 1000, 2000, and 4000 per second were measured and are neither too high or too low. Thus, a decrease in resolving time due to an increase in counting rate is not a factor [40]. Also the x-ray quanta absorbed and the quanta detected follow a linear no-loss behaviour in most modern counters [40]. However, there will be some counting efficiency loss due to the absorption of x-ray quanta by the counter window, and the extent of this depends on the wavelength of the radiaiton. For the Cu-K_α used in this experiment the loss was not significant.

6.3 Phase Fractions

The two main factors in determining the relative volume fractions of each phase involved are R and E. The R strictly depends upon the individual h k l spectrum, such as the multiplicity factor m, LP factor and the structure factor F . Among these quantities the structure factor depends on the atomic positions and the atomic scattering factor f, which in turn depends on the Bragg angle and the incident radiation wavelength. In this analysis, due to the nature of the low temperature experiments, there were 2θ shifts due to the lattice parameter changes with decreasing temperatures. Since these lattice

parameter changes were not taken into account at each temperature when the diffraction pattern data were analysed, the unit cell volume changes were not accommodated in the calculation of R factors. Thus any error introduced in the R factor was mainly due to these lattice parameter changes, and due to the f values considered in calculating F, since the f values were graphically interpolated values. The factor E, i.e., the integrated intensity, could have been affected statistically since for some samples a large number of peaks were considered. The main source of experimental error may have been due to the nature of the method in determining E, as already seen above in section 5.4.

The phase fractions calculated for alloys of composition 15.0, 15.5* and 15.5** at% Nb are shown in Table A.7, and the diffraction patterns are shown in Fig. A.35 through Fig. A.56. The alloys of composition 14.5 and 16.0 at% Nb were completely α" and γ° phases, respectively, at room temperature. The 16.0 at% Nb alloy remained all γ° down to -192° C. However the intensity of the $(111)_{\gamma^\circ}$ peak of this alloy reduced with decreasing temperatures as is seen in Fig.A.52 through Fig.A.56, thereby possibly indicating that there may be trace amounts of α" appearing. But the superposed peak containing both α" and γ° peaks (at 36.2°, 2θ) showed no increase at all to indicate any increase in the α" phase.

6.4 Metastable Phase Diagram

The variation of % α" phase with temperature for the three alloys is shown in Fig.33. From this it is obvious that the amount of the α" phase increases with decreasing temperature, showing that the γ° --> α" reaction proceeds in the forward direction by supercooling. From Fig.33 it is seen that at roughly -65° C and above, the % α" reduces with increasing Nb content as expected in these alloys, but below -65°C it is seen from Fig.33 that the nominally higher Nb content (15.5** at%) alloy retains more α" than the lower Nb content alloy (15.5* at%). This behaviour is the reverse of what

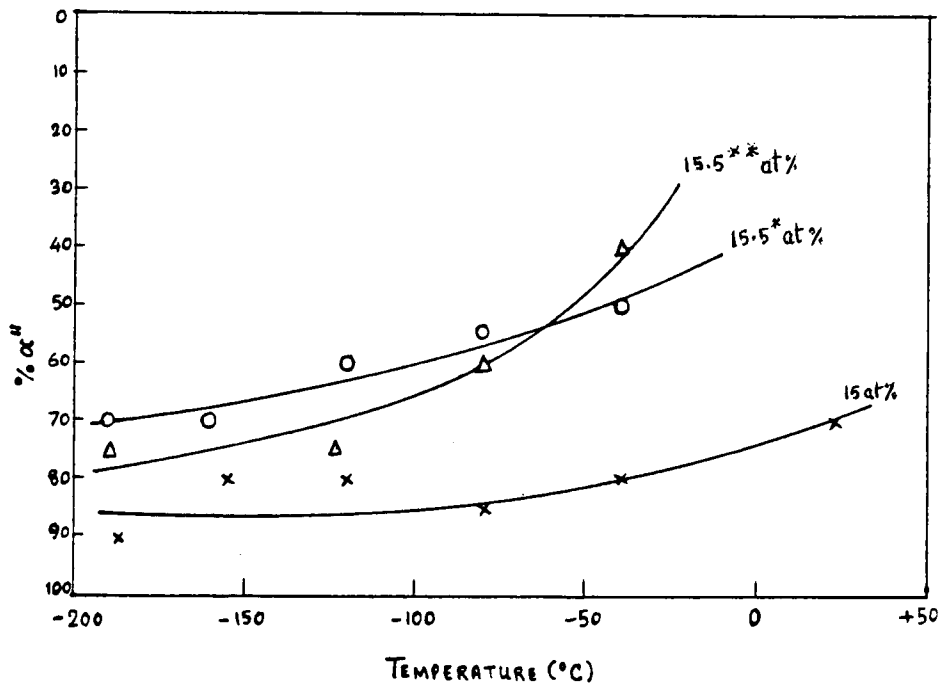

× - 15.0 at % Nb (Alloy 142)

○ - 15.5* at % Nb (Alloy 183)

△ - 15.5** at % Nb (Alloy 196)

Figure 33. Variation of % α" with temperature at different Nb content.

happened in the higher temperature range and opposite to what is expected in these alloys, since the higher the solute content the lower the amount of α" retained in these alloys. Thus, the α" variation behaves in opposite ways at the two extremes of the considered temperature range, with the behaviour changing direction at a temperature roughly below -65° C. The unusual behaviour seen in the lower temperature range in Fig.33 may be attributed to the uncertainty in the alloy compositions (± 0.5%). That is, the alloy with the apparently lower Nb content (15.5* at%) may have a composition higher than this (i.e., 15.73 instead of 15.51 at%, Table A.1). Below -65° C, the curves, although shown separated in Fig.33, may be indistinguishable as the estimated accuracy in the determination of the % α" is ± 5%.

The variation at room temperature of % α" with at% Nb is shown in Fig.34(a). This indicates that with increased Nb content the supercooling necessary to start the γ° --> α" reaction increases, i.e., the M_s temperature decreases. Thus it can be inferred that the M_s temperature would decrease with Nb content. The variation of % α" with % Nb at about -190° C is shown in Fig.34(b). From this it is seen that the M_f temperature also is lowered with increased Nb content, and higher supercooling is needed to force the reaction forward in order to form more of α". The M_s temperature variation between 13 and 15 at% Nb alloys is known [39]. In the present analysis, the 14.5 at% alloy gave complete α" phase at room temperature, and the 16.0 at% alloy remained completely γ° down to -192° C. The M_s temperature for the 14.5 at% alloy is clearly above room temperature. From the results of the 16.0 at% alloy the M_s and M_f curves cannot extend beyond 16 at% and should slope down. The M_f temperatures for the 13 and 14 at% alloys are approximately above room temperature [39]. From the present research, the M_f temperature is below -192° C for the three alloys. All of the above information was used to construct the transition metastable phase diagram shown in Fig.35.

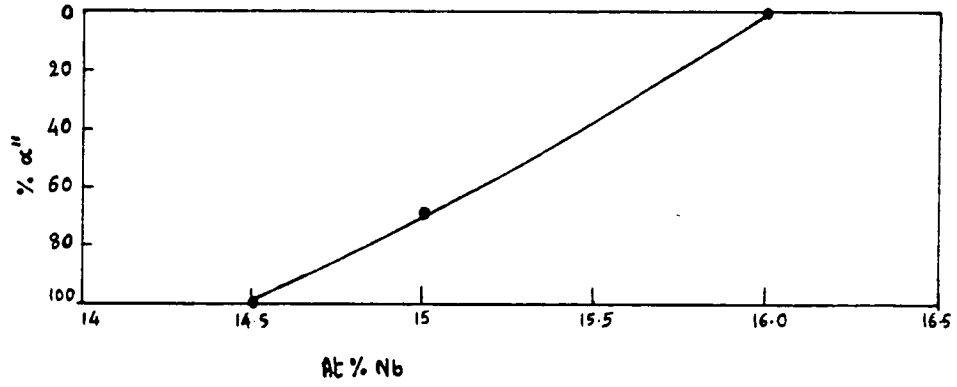

a) Plot of % α'' versus at% Nb at room temperature.

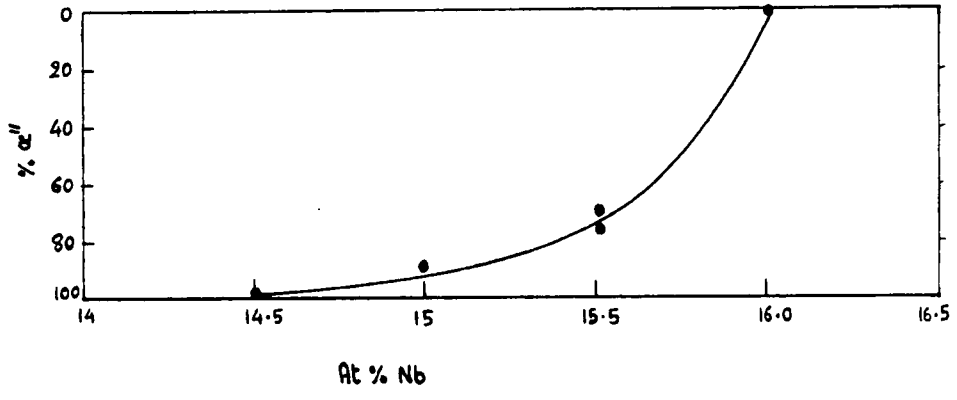

b) Plot of % α'' versus at% Nb at -188 ± 2 °C.

Figure 34. Variation of % α''with Nb content at two different temperature range.

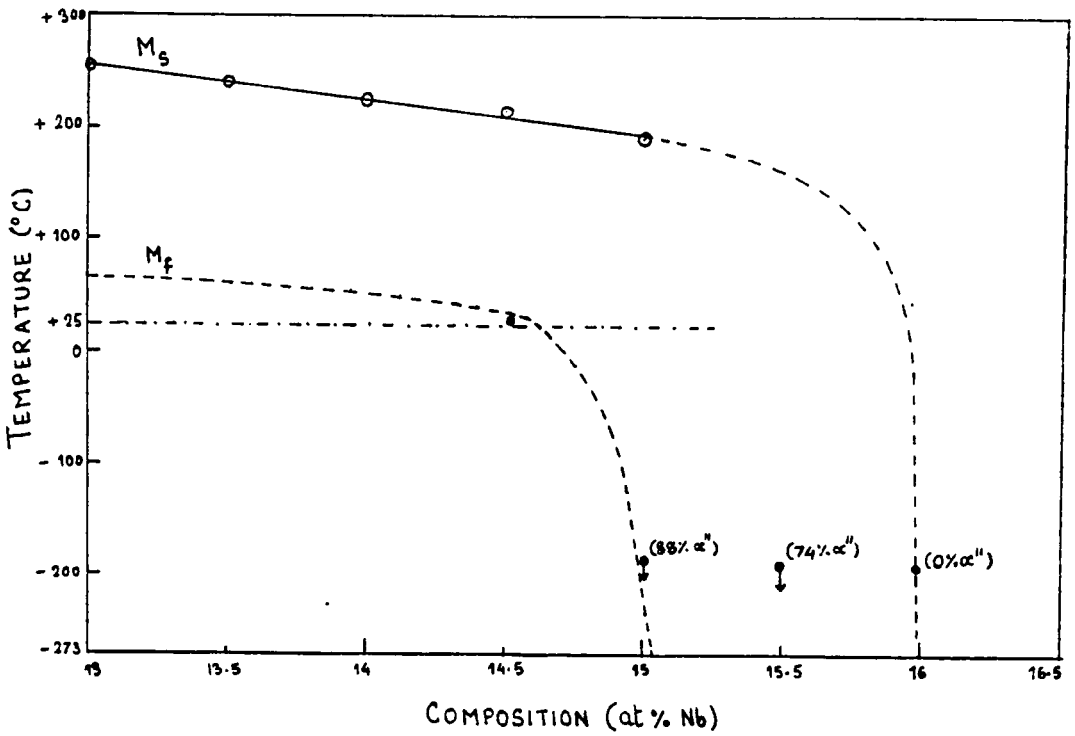

Figure 35. An approximate transition metastable phase diagram.

7. CONCLUSIONS AND RECOMMENDATIONS

The addition of increased amount of Nb to U stabilized the γ° phase, thus needing higher supercooling for the reaction to proceed forward as expected in these alloys. The martensitic reaction at sub-zero temperatures of the alloys studied shows that the M_f temperature range lies close to liquid N_2 temperature or even lower.

There are many areas that need extensive study to accumulate comprehensive low temperature data for the martensitic reaction in these alloys. Accurate chemical analysis should be done on the diffraction samples to ensure correct alloy compositions. High temperature studies could be conducted to determine M_s temperatures of these alloys, and additional low temperature experiments should be done to check out the possibility of driving the reactions to completion. This would shed more light on the M_f temperatures of these alloys. More alloys between 15 and 17 at% Nb compositions should be studied, since only five alloys were considered in this study. This will give more continuous data and hence a better picture of the reaction path and better data from which to construct a transition metastable phase diagram.

Because of considerable background radiation and superpositioning of the peaks, a step-scan technique, where the counts are digitized, should be used since this would give more accurate intensity values. As the intensity values are exact counts, they are readily amenable for statistical corrections by means of computer techniques, and this would enable the evaluation of more accurate integrated intensity values [46]. Also in future study, the lattice parameter changes with temperature should be considered and appropriate values used in calculations. Thus, a more accurate value of the M_s and M_f temperatures at sub-zero temperatures for these alloys can be obtained.

REFERENCES

REFERENCES

[1] R.A.Vandermeer. Private communication.

[2] A.F.Giamei and E.J.Freise. Optimization of x-ray diffraction quantitative analysis. Transaction of the Met Society of AIME, V.239, pp.1676, 1967.

[3] R.A.Vandermeer. Phase transformations in a U+14at% Nb alloy. Acta Metallurgica, V.28, pp.383, 1980.

[4] A.Goldberg, T.B.Masalaski. Phase transformations in the actinides. Nuclear Metallurgy, V.17, part-II, ed, W.N.Miner, TMS-AIME, New York, pp.875, 1970.

[5] R.D.Townsend and J.Burke. Direct evidence for three transformation mechanisms for the β ---> α phase change in uranium-chromium alloys. Nature, V.205, pp.794, 1965.

[6] M.Colombie and M.Foure. Contribution a l'etude du alliages d'uranium peu charges. Mem.Sci.Rev.Met, V.63, pp.253, 1966.

[7] J.Besson, P.L.Blum, and J.Laugier. Sur l'existence d'une transformation directe α ---> γ dans l'uranium disperse dans un milieu inerte. J.Nucl.Matr., V.16, pp.74, 1965.

[8] J.Besson, P.L.Blum, P.Guinet, and J.Laugier. Sur la anomalies du polymorphisme de l'uranium pulverulent disperse dans un milieu inerte. Comptes Rend, Acad Sci. V.259, pp.3012, 1964.

[9] K.Tangri. Memoire no:90, Journees Metallurgiques d'Automme, Paris, Oct 1960.

[10] K.Tangri and D.K.Chaudhuri. Metastable phases in U-alloys with high solute solubility in the b.c.c γ phase U-Nb system. J.Nucl.Matr., V.15,4, pp.278, 1965.

[11] M.Anagnostidis, M.Colombie and H.Monti. Phase metastables dans les alliages Uranium-Niobium. J.Nucl.Matr., V.11, pp.67, 1964.

[12] J.Lehmann. Phases monocliniques dans les alliages Uranium-Moybdene. J.Nucl.Matr., V.4, pp.218, 1961.

[13] K.Tangri and G.I.Williams. Metastable phases in the U-Mo system and their origin. J.Nucl.Matr., V.4, pp.226, 1961.

[14] H.L.Yakel. A review of x-ray diffraction studies in U-alloys. Ed. by J.J.Burke, et.al., Brookhill Publishing Company, Chestnut Hill, MA, 1976.

[15] P.Chiotti, H.H.Klepfer, and R.W.White. Lattice parameters of uranium from 25° to 1132° C. Trans.ASM, V.51, pp.772, 1959.

[16] C.S.Barrett, M.H.Mueller, and R.L.Hitterman. Crystal structure variations in α -U at low temperatures. Phys.Rev, V.129, pp.625, 1963.

[17] M.H.Mueller, R.L.Hitterman, and H.W.Knott. The atomic position parameter in α -U, R.T and above. Acta Cryst., V.15, pp.421, 1962.

[18] A.L.Sutton, W.T.Eeles, and A.M.Price. Interatomic distances in α -U at 20° C and 630° C, in the measurement and interpretation of diffraction line profiles. United Kingdom Atomic Energy Research Establishment, Harwell, England, Report no:AERE-R.3818, pp.45 Apr 1962.

[19] J.Lehmann, and R.F.Hills. Proposed nomenclature for phases in U-alloys. J.Nucl.Matr., V.2, pp.261-268, 1960.

[20] A.F.Berndt. Room temperature lattice constants of α-U, plutonium alloys. Argonne National Laboratory, Ill, U.S.Atomic Energy Commission Report no:ANL-6460, Oct 1962.

[21] B.A.Hatt, and D.Stewart. The metastable γ° phase in U-alloys. Fulmer Research Institute Ltd, For The Atomic Energy Establishment, Harwell England, Report no:R189/10/Aug 1967.

[22] H.L.Yakel. Crystal structures of transition phases formed in U/16.6 at%Nb/5.64 at%Zr alloys. J.Nucl.Matr., V.33, pp.286, 1969.

[23] K.Tangri. Les phases gamma metastables dans les alliages d'uranium contenant du Molybdene. Mem.Sci.Rev Met V.58, pp.169, 1961.

[24] A.G.Harding and M.B.Waldron. UKAEA, Harwell report no:AERE M/R-2673. part-I, 1958.

[25] J.Lehmann. Carateristiques d'une phase martensitique obtenue dans des alliages uranium-molybdene. Comptes Rend, Acad Sci. Paris, V.248, pp.2098, 1959.

[26] J.Heywood., K.Tangri., G.I.Williams. Fulmer Research Institute Report R-137/1, 1959.

[27] K.Tangri and G.I.Williams. Metastable phases in U-Mo system and their origins. J.Nucl.Matr, V.4,2, pp.226, 1961.

[28] B.Hatt. Fulmer Research Institute, Report no.R-114/9, 1960.

[29] D.Stewart and G.I.Williams. The structure and occurence of the metastable monoclinic phase, α''_b , in U-Mo alloys. J.Nucl.Matr, V.20. pp.262, 1968.

[30] W.G.Burgers. Physica, V.1, pp.561, 1934.

[31] R.J.Jackson. Dow Chemical Co, Rocky Flats Div, Golden Colo. Report no:REP-996, 1970.

[32] D.A.Carpenter and R.A.Vandermeer. An x-ray diffraction study on a martensitic transformation in U-alloys. Journal de Physique,C4, V.43. pp.395, 1982.

[33] R.P.Elliott. Constituiton of Binary Alloys, first supplement. McGraw-hill Book Company, 1965.

[34] R.J.Jackson. Reversible martensitic transformation between transition phases of U-Nb alloys. The Dow Chemical Company Co., Rocky Flats Div, Golden Colo. Rept no:RFP1535, 1970.

[35] B.W.Howlett. A study of the shear transformation from the gamma phase in U-Mo alloys containing 6.0-12.5 at% Mo. J.Nucl.Matr., V.35, pp.278, 1970.

[36] R.A.Vandermeer., J.C.Ogle and W.B.Snyder,Jr. Shape memory effects in a uranium+14 at% niobium alloy. Scripta Met., V.12, pp.243, 1978.

[37] R.H.Richman and R.G.Davis. Ordering reactions in unfamiliar systems. Met.Trans, V.4, pp.2731, 1973.

[38] H.L.Yakel. The Physical metallurgy of uranium alloys. Ed. by J.J.Burke, et.al., Brookhill Publishing Company, Chestnut hill MA, pp.259, 1976.

[39] R.A.Vandermeer, J.C.Ogle and W.G.Northcutt,Jr. A phenomenological study of the shape memory effect in polycrystalline U-Nb alloys. Met.Trans.A, V.12A, pp.733, 1981.

[40] B.D.Cullity. Elements of X-ray Diffraction, 2nd edition, Addison Wesley Publishing Company, Reading, MA, 1978.

[41] International Tables for X-ray Crystallography, V-II, Table 5.2.5B, pp270, 1965.

[42] International Tables for X-ray Crystallography, V-I, pp.31, 1965.

[43] International Tables for X-ray Crystallography, V-III, Table 3.3.3A(2), pp.220, 1965.

[44] K. Zieminski. Peak separation program using pearson VII curves to mathematically model each diffraction peak. University Of Tennessee, Knoxville, Summer 1984.

[45] R.A.Vandermeer. Shape memory effect in U-Nb alloys below room temperature. Final report, subcontract 1262605, Lawrence Livermore National Laboratory. Livermore, CA, 1985.

[46] L.E.Alexander and H.P.Klug, X-ray diffraction procedures for polycrystalline and amorphous materials, 2nd edition, John Wiley and Sons, New York 1974.

APPENDIX

APPENDIX

E_i^{α} total diffracted energy for ith spectrum of α phase, counts

K angular independent constant for given $\bar{\mu}$ and I_o, counts-cm^{-6}

$R_i^{\alpha}(\theta)$ angular dependent term depending on ith spectrum of α phase, cm^{-6}

I_o incident beam intensity per unit area, counts-cm^{-2} -sec^{-1}

A_o cross-sectional area of incident beam, sq cm

A_s cross-sectional area of receiving slit, sq cm

e^4/m^2c^4 Thompson factor, sq cm

λ wave length of radiation, cm

r radius of diffractometer, cm

$\bar{\mu}$ mean linear absorption coefficient for sample, cm^{-1}

ω angular speed of counter, sec^{-1}

m multiplicity of ith spectrum for α phase

N number of unit cells per unit volume for α phase, cm^{-3}

F structure factor for ith spectrum from α phase

e^{-2D} temperature factor for ith spectrum from α phase

θ Bragg angle for ith spectrum of α phase

P polarization factor

TABLE A.1.

Compositions of the five U-Nb alloys

Alloy	Composition (at% Nb)			
	Nominal	Actual		Average
		Top	Bottom	
141	15.23	—	—	14.5
142	15.54	15.04	14.44	15.0 (14.74)
183	16.17	15.75	15.27	15.5* (15.51)
196	16.37	16.09	15.37	15.5** (15.73)
198	16.58	16.09	15.54	16.0 (15.82)

* Actual average composition is 15.51 at%

** Actual average composition is 15.73 at%

TABLE A.2.

Chemical analysis of alloys 183, 196, and 198

Casting # 183 TOP

A025-02 Y-12 PLANT LABORATORY REPORT

RECEIVED	REPORT DATE	TYPE REPORT	BATCH-NUMBER	LOC	MTC	REQUISITION
06-14-83	06-23-83	FINAL			0305-X	455080

CHEMICAL ANALYSIS

.930900 G/G U
.068000 G/G NB
69 PPM C

SPECTROGRAPHIC ANALYSIS

PLATE SHEET(S): 87775
SPECTROCHEMICAL METHOD (EMISSION)
REPORT UNIT: MICRO-G/G (PPM) REPORT BASIS: METAL

AG		AL	< 2	AS	< 10	AU	< 2	B	< .1	BA	< 4
BE	< .02	BI	< 6	BR		CA	< 10	CD	< .4	CO	< 1
CR	< 10	CS		CU	2	FE	100	GA	< 1	GE	< 1
HF		HG		IN		IR		K		LI	< 2
MG	< 2	MN	10	MO	< 10	NA	< 10	NB		NI	15
NP		OS		P	< 100	PB	2	PD	< 20	PT	
PU		RB		RE		RH		RU		S	
SB		SC		SE		SI	25	SN	< 2	SR	< 20
TA		TE		TH		TI	< 10	TL		U	
V	< 5	W	< 60	Y		ZN	< 40	ZR			

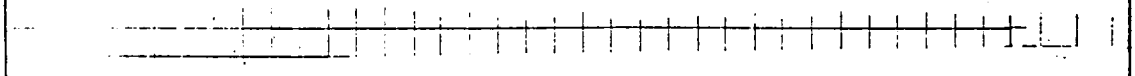

A025-02 Y-12 PLANT LABORATORY REPORT Bottom.

RECEIVED	REPORT DATE	TYPE REPORT	BATCH-NUMBER	LOC	MTC	REQUISITION
06-14-83	06-23-83	FINAL			0305-X	455081

CHEMICAL ANALYSIS

.936900 G/G U
.065700 G/G NB
79 PPM C

SPECTROGRAPHIC ANALYSIS

PLATE SHEET(S): 87775
SPECTROCHEMICAL METHOD (EMISSION)
REPORT UNIT: MICRO-G/G (PPM) REPORT BASIS: METAL

AG		AL	< 2	AS	< 10	AU	< 2	B	< .1	BA	< 4
BE	< .02	BI	< 6	BR		CA	< 10	CD	< .4	CO	< 1
CR	< 10	CS		CU	2	FE	95	GA	< 1	GE	< 1
HF		HG		IN		IR		K		LI	< 2
MG	< 2	MN	10	MO	< 10	NA	< 10	NB		NI	10
NP		OS		P	< 100	PB	2	PD	< 20	PT	
PU		RB		RE		RH		RU		S	
SB		SC		SE		SI	20	SN	< 2	SR	< 20
TA		TE		TH		TI	< 10	TL		U	
V	< 5	W	< 60	Y		ZN	< 40	ZR			

TABLE A.2 (continued)

Casting #196 Top

RA025-02 Y-12 PLANT LABORATORY REPORT

RECEIVED	REPORT DATE	TYPE REPORT	BATCH-NUMBER LOC	MTC	REQUISITION
07-22-83	07-28-83	FINAL		0305-X	455096

CHEMICAL ANALYSIS

.932400 G/G U
.069600 G/G NB
76 PPM C

SPECTROGRAPHIC ANALYSIS

PLATE SHEET(S): 7856
SPECTROCHEMICAL METHOD (EMISSION)
REPORT UNIT: MICRO-G/G (PPM) REPORT BASIS: METAL

AG		AL	< 2	AS	< 10	AU	< 2	B	.1	BA	< 4
BE	< .02	BI	< 6	BR		CA	< 10	CD	< .4	CO	< 1
CR	< 10	CS		CU	8	FE	80	GA	< 1	GE	< 1
HF		HG		IN		IR		K		LI	< 2
MG	< 2	MN	15	MO	10	NA	< 10	NB		NI	15
NP		OS		P	< 100	PB	2	PD	< 20	PT	
PU		RB		RE		RH		RU		S	
SB		SC		SE		SI	30	SN	< 2	SR	< 20
TA		TE		TH		TI	< 10	TL		U	
V	< 5	W	< 60	Y		ZN	< 40	ZR			

RA025-02 Y-12 PLANT LABORATORY REPORT

RECEIVED	REPORT DATE	TYPE REPORT	BATCH-NUMBER LOC	MTC	REQUISITION
07-22-83	07-28-83	FINAL		0305-X	455097

CHEMICAL ANALYSIS

.934700 G/G U
.066200 G/G NB
90 PPM C

Casting #196 bottom

SPECTROGRAPHIC ANALYSIS

PLATE SHEET(S): 7856
SPECTROCHEMICAL METHOD (EMISSION)
REPORT UNIT: MICRO-G/G (PPM) REPORT BASIS: METAL

AG		AL	< 2	AS	< 10	AU	< 2	B	.1	BA	< 4
BE	< .02	BI	< 6	BR		CA	< 10	CD	< .4	CO	< 1
CR	< 10	CS		CU	8	FE	80	GA	< 1	GE	< 1
HF		HG		IN		IR		K		LI	< 2
MG	< 2	MN	15	MO	10	NA	< 10	NB		NI	15
NP		OS		P	< 100	PB	2	PD	< 20	PT	
PU		RB		RE		RH		RU		S	
SB		SC		SE		SI	30	SN	< 2	SR	< 20
TA		TE		TH		TI	< 10	TL		U	
V	< 5	W	< 60	Y		ZN	< 40	ZR			

TABLE A.2 (continued)

Casting #198 Top

RA025-02 Y-12 PLANT LABORATORY REPORT

RECEIVED	REPORT DATE	TYPE REPORT	BATCH-NUMBER LOC	MTC	REQUISITION
07-26-83	08-03-83	FINAL		0305-X	836356

CHEMICAL ANALYSIS

.926300 G/G U
.069600 G/G NB
67 PPM C

SPECTROGRAPHIC ANALYSIS

PLATE SHEET(S): 7868
SPECTROCHEMICAL METHOD (EMISSION)
REPORT UNIT: MICRO-G/G (PPM) REPORT BASIS: METAL

AG		AL	< 2	AS	< 10	AU	< 2	B	< .1	BA	< 4
BE	< .02	BI	< 6	BR		CA	< 10	CD	< .4	CO	< 1
CR	< 10	CS		CU	5	FE	60	GA	< 1	GE	< 1
HF		HG		IN		IR		K		LI	< 2
MG	< 2	MN	12	MO	< 10	NA	< 10	NB		NI	15
NP		OS		P	< 100	PB	2	PD	< 20	PT	
PU		RB		RE		RH		RU		S	
SB		SC		SE		SI	30	SN	< 2	SR	< 20
TA		TE		TH		TI	30	TL		U	
V	< 5	W	< 60	Y		ZN	< 40	ZR			

Casting #198 Bottom

RA025-02 Y-12 PLANT LABORATORY REPORT

RECEIVED	REPORT DATE	TYPE REPORT	BATCH-NUMBER LOC	MTC	REQUISITION
07-26-83	08-03-83	FINAL		0305-X	836357

CHEMICAL ANALYSIS

.930500 G/G U
.067000 G/G NB
71 PPM C

SPECTROGRAPHIC ANALYSIS

PLATE SHEET(S): 7868
SPECTROCHEMICAL METHOD (EMISSION)
REPORT UNIT: MICRO-G/G (PPM) REPORT BASIS: METAL

AG		AL	< 2	AS	< 10	AU	< 2	B	< .1	BA	< 4
BE	< .02	BI	< 6	BR		CA	< 10	CD	< .4	CO	< 1
CR	< 10	CS		CU	6	FE	60	GA	< 1	GE	< 1
HF		HG		IN		IR		K		LI	< 2
MG	< 2	MN	15	MO	< 10	NA	< 10	NB		NI	15
NP		OS		P	< 100	PB	2	PD	< 20	PT	
PU		RB		RE		RH		RU		S	
SB		SC		SE		SI	30	SN	< 2	SR	< 20
TA		TE		TH		TI	20	TL		U	
V	< 5	W	< 60	Y		ZN	< 40	ZR			

TABLE A.3.

The calculated and observed d values for the observed hkl's

Alloy	2θ	h k l	d-calculated	d-observed
142	31.6	$(0\ 2\ 0)_{\alpha''}$	2.8717	2.8314
	32.2	$(0\ 1\ 1)_{\gamma\circ}$	2.7890	2.7800
	33.5	$(\bar{1}\ 1\ 0)_{\alpha''}$	2.5805	2.6750
	35.6	$(1\ 1\ 0)_{\alpha''}$	2.5275	2.5219
	36.15	$(0\ 0\ 2)_{\alpha''}$	2.5003	2.4847
	36.88	$(1\ 1\ 1)_{\gamma\circ}$	2.4317	2.4375
	37.68	$(\bar{1}\ 1\ 1)_{\alpha''}$	2.2932	2.3876
	39.9	$(1\ 1\ 1)_{\alpha''}$	2.2551	2.2594
183	32.05	$(0\ 1\ 1)_{\gamma\circ}$	2.7964	2.7926
	35.45	$(1\ 1\ 0)_{\alpha''}$	2.5814	2.5322
	36.2	$(0\ 0\ 2)_{\alpha''}$	2.5057	2.4814
	36.93	$(1\ 1\ 1)_{\gamma\circ}$	2.4379	2.4344
	38.3	$(\bar{1}\ 1\ 1)_{\alpha''}$	2.2948	2.3500
196	32.1	$(0\ 1\ 1)_{\gamma\circ}$	2.7964	2.7883
	35.65	$(1\ 1\ 0)_{\alpha''}$	2.5817	2.5322
	36.25	$(0\ 0\ 2)_{\alpha''}$	2.5070	2.4814
	36.95	$(1\ 1\ 1)_{\gamma\circ}$	2.4379	2.4344
	38.15	$(\bar{1}\ 1\ 1)_{\alpha''}$	2.2953	2.3590
198	32.08	$(0\ 1\ 1)_{\gamma\circ}$	2.7905	2.7905
	36.35	$(0\ 2\ 0)_{\gamma\circ}$	2.4717	2.4715
	37.0	$(1\ 1\ 1)_{\gamma\circ}$	2.4301	2.4296

TABLE A.4.

The input parameters 2θ, H, S, and I shown with their initial experimental value and the computer calculated final values along with the E's of each peak (h k l) determined by the computer. The abnormal E values are indicated by '*'.

Alloy 142:

+22° C

	2θ		H		S		I		E
h k l	Initial	final	Initial	final	Initial	final	Initial	final	
$(020)_{\alpha''}$	31.60	31.58	1.00	1.91	5.0	1.21	5.0	3.72	10.03
$(011)_{\gamma\circ}$	32.20	32.27	1.00	1.80	5.0	1.52	5.0	1.74	4.06
$(\bar{1}10)_{\alpha''}$	33.50	33.57	1.50	1.52	5.0	5.22	10.0	7.11	12.02
$(110)_{\alpha''}$	35.60	35.50	0.75	0.67	5.0	2.23	20.0	16.92	13.50
$(002)_{\alpha''}$	36.15	36.20	0.50	0.44	5.0	15.98	100.0	78.73	37.04
$(\bar{1}11)_{\alpha''}$	37.68	37.79	1.50	1.19	5.0	51.83	22.0	16.67	21.25
$(111)_{\alpha''}$	39.90	39.80	1.00	2.00	5.0	1.60	5.0	2.57	6.61
$(111)_{\gamma\circ}$	36.88	36.87	0.80	0.67	5.0	72.41	55.0	42.57	10.20

-40° C

	2θ		H		S		I		E
h k l	Initial	final	Initial	final	Initial	final	Initial	final	
$(020)_{\alpha''}$	31.40	31.38	1.25	1.47	5.0	2.15	5.0	4.40	7.80
$(011)_{\gamma\circ}$	32.30	32.25	1.20	0.52	5.0	2.52	7.0	2.35	1.43
$(\bar{1}10)_{\alpha''}$	33.80	33.70	1.25	1.71	5.0	11.00	14.0	9.17	17.01
$(110)_{\alpha''}$	35.45	35.54	0.70	0.74	5.0	3.72	22.0	14.76	14.76
$(002)_{\alpha''}$	36.15	36.17	0.50	0.41	5.0	22.96	100.0	70.52	30.75
$(\bar{1}11)_{\alpha''}$	38.25	38.16	1.00	0.99	5.0	75.12	20.0	16.17	10.39
$(111)_{\alpha''}$	39.83	39.75	0.75	1.40	5.0	1.80	5.0	3.50	6.09
$(111)_{\gamma\circ}$	36.85	36.81	0.95	1.05	5.0	97.76	40.0	33.07	11.86

TABLE A.4. (continued)

-80° C

	2θ		H		S		I		E
h k l	Initial / final		Initial / final		Initial / final		Initial / final		
$(020)_{\alpha''}$	31.20	31.28	1.00	1.24	5.0	5.60	6.0	3.17	4.35
$(011)_{\gamma\circ}$	32.30	32.51	1.20	1.31	5.0	0.54	5.0	4.04	39.58*
$(\bar{1}10)_{\alpha''}$	33.88	33.87	1.20	1.19	5.0	1.53	14.0	10.11	15.55
$(110)_{\alpha''}$	35.38	35.37	0.50	0.47	5.0	13.67	23.0	16.53	8.37
$(002)_{\alpha''}$	36.15	36.15	0.50	0.44	5.0	2.84	100.0	72.18	36.78
$(111)_{\gamma\circ}$	36.90	36.78	1.00	1.19	5.0	113.42	34.0	27.22	12.77
$(\bar{1}11)_{\alpha''}$	38.35	38.26	0.75	1.13	5.0	16.58	20.0	15.22	18.47
$(111)_{\alpha''}$	39.85	39.86	0.85	1.02	5.0	1.02	6.0	3.92	6.19

-120° C

	2θ		H		S		I		E
h k l	Initial / final		Initial / final		Initial / final		Initial / final		
$(020)_{\alpha''}$	31.18	31.13	1.0	1.13	5.0	0.6	6.0	4.16	18.05
$(011)_{\gamma\circ}$	32.30	32.37	1.2	1.30	5.0	61.0	5.0	3.94	9.35
$(\bar{1}10)_{\alpha''}$	33.90	33.92	1.0	1.10	5.0	3.0	15.0	12.06	15.33
$(110)_{\alpha''}$	35.40	35.43	0.7	0.63	5.0	3.4	23.0	18.66	13.34
$(002)_{\alpha''}$	36.18	36.19	0.5	0.48	5.0	8.4	100.0	75.60	39.30
$(\bar{1}11)_{\alpha''}$	38.43	38.34	1.2	1.03	5.0	8.7	20.0	15.46	17.38
$(111)_{\alpha''}$	39.85	39.87	0.5	0.67	5.0	0.6	7.0	4.76	12.17
$(111)_{\gamma\circ}$	36.90	36.90	1.1	1.06	5.0	8.4	30.0	24.86	28.78

-154° C

	2θ		H		S		I		E
h k l	Initial / final		Initial / final		Initial / final		Initial / final		
$(020)_{\alpha''}$	31.20	31.09	0.75	0.92	5.0	0.60	6.0	4.26	15.05
$(011)_{\gamma\circ}$	32.35	32.45	1.20	1.60	5.0	92.40	4.0	3.54	11.52
$(\bar{1}10)_{\alpha''}$	33.95	33.96	1.20	1.06	5.0	1.40	15.0	11.86	16.76
$(110)_{\alpha''}$	35.35	35.45	0.65	0.61	5.0	124.40	23.0	17.76	13.38
$(002)_{\alpha''}$	36.18	36.18	0.50	0.46	5.0	8.00	100.0	76.60	38.20

TABLE A.4. (continued)

-154° C

	2θ		H		S		I		E
h k l	Initial / final		Initial / final		Initial / final		Initial / final		
$(\bar{1}11)_{\alpha''}$	38.50	38.37	0.80	1.17	5.0	6.30	20.0	15.16	19.56
$(111)_{\alpha''}$	39.80	39.90	0.70	0.67	5.0	5.00	7.0	4.16	3.09
$(111)_{\gamma\circ}$	36.9	36.83	1.10	1.06	5.0	148.40	28.0	24.56	14.62

-187° C

	2θ		H		S		I		E
h k l	Initial / final		Initial / final		Initial / final		Initial / final		
$(020)_{\alpha''}$	31.20	31.23	0.70	1.0	5.0	0.60	6.0	4.78	18.41
$(011)_{\gamma\circ}$	32.35	32.57	1.20	1.18	5.0	58.17	5.0	4.12	9.13
$(\bar{1}10)_{\alpha''}$	34.00	33.98	1.25	1.01	5.0	6.26	15.0	12.60	14.03
$(110)_{\alpha''}$	35.35	35.35	0.65	0.60	5.0	59.17	23.0	17.49	9.21
$(002)_{\alpha''}$	36.18	36.18	0.50	0.49	5.0	3.10	100.0	79.94	45.48
$(\bar{1}11)_{\alpha''}$	38.50	38.45	1.10	1.10	5.0	4.80	21.0	15.19	18.65
$(111)_{\alpha''}$	39.80	39.90	0.60	0.61	5.0	1.31	7.0	4.83	4.02
$(111)_{\gamma\circ}$	36.90	36.93	0.50	1.21	5.0	60.20	26.0	20.66	9.29

Alloy 183

+22° C

	2θ		H		S		I		E
h k l	Initial / final		Initial / final		Initial / final		Initial / final		
$(011)_{\gamma\circ}$	32.05	32.03	0.70	1.2	5.0	0.60	6.0	3.50	15.99
$(002)_{\alpha''}$	36.20	36.19	0.50	0.60	5.0	0.60	43.0	34.76	79.13
$(111)_{\gamma\circ}$	36.93	36.92	0.40	0.40	5.0	3.60	80.0	59.60	25.96

TABLE A.4. (continued)

-40° C

	2θ		H		S		I		E
h k l	Initial / final		Initial / final		Initial / final		Initial / final		
$(011)_{\gamma}$	32.20	32.15	0.75	2.03	5.0	1.60	4.0	3.54	9.22
$(\bar{1}10)_{\alpha''}$	33.65	34.60	1.20	1.86	5.0	44.30	4.0	2.66	5.30
$(110)_{\alpha''}$	35.50	35.63	0.80	0.77	5.0	68.20	9.0	5.74	9.90
$(002)_{\alpha''}$	36.20	36.20	0.60	0.49	5.0	1.80	45.0	32.10	19.52
$(111)_{\gamma}$	36.98	36.97	0.60	0.53	5.0	1.50	55.0	43.90	30.24
$(\bar{1}11)_{\alpha''}$	38.27	38.13	0.80	1.24	5.0	8.40	7.0	4.74	6.42

-81° C

	2θ		H		S		I		E
h k l	Initial / final		Initial / final		Initial / final		Initial / final		
$(011)_{\gamma}$	32.20	32.09	1.0	2.70	5.0	0.60	5.0	2.46	2.50
$(\bar{1}10)_{\alpha''}$	33.50	33.69	1.0	1.64	5.0	0.60	4.0	2.86	18.00
$(110)_{\alpha''}$	35.52	35.60	0.60	0.79	5.0	29.40	12.0	7.55	6.45
$(002)_{\alpha''}$	36.20	36.22	0.60	0.52	5.0	2.40	44.0	32.66	19.98
$(111)_{\gamma}$	36.98	36.99	0.60	0.60	5.0	2.40	48.0	36.96	26.56
$(\bar{1}11)_{\alpha''}$	38.30	38.17	1.0	1.27	5.0	18.40	7.0	5.99	8.20

-121° C

	2θ		H		S		I		E
h k l	Initial / final		Initial / final		Initial / final		Initial / final		
$(011)_{\gamma}$	32.25	32.36	1.0	2.23	5.0	1.60	5.0	3.46	9.89
$(\bar{1}10)_{\alpha''}$	33.60	34.53	1.0	2.04	5.0	63.30	4.0	2.16	9.53
$(110)_{\alpha''}$	35.45	35.55	0.75	0.83	5.0	10.40	11.0	6.40	5.78
$(002)_{\alpha''}$	36.20	36.22	0.70	0.57	5.0	2.40	47.0	33.66	22.60
$(111)_{\gamma}$	37.00	37.02	0.50	0.64	5.0	7.40	45.0	32.66	22.77
$(\bar{1}11)_{\alpha''}$	38.25	38.10	0.80	1.29	5.0	74.60	8.0	6.74	10.35

TABLE A.4. (continued)

-161° C

	2θ		H		S		I		E
h k l	Initial / final		Initial / final		Initial / final		Initial / final		
$(011)_{\gamma}$ ∘	32.25	32.09	1.0	3.20	5.0	0.60	5.0	1.96	24.08
$(\bar{1}10)_{\alpha''}$	33.65	33.79	1.0	2.94	5.0	13.0	4.0	2.46	7.82
$(110)_{\alpha''}$	35.43	35.51	0.75	0.66	5.0	108.40	11.0	7.16	12.49
$(002)_{\alpha''}$	36.23	36.22	0.60	0.57	5.0	2.40	48.0	35.06	23.53
$(111)_{\gamma}$ ∘	37.00	37.04	0.80	0.67	5.0	7.40	42.0	30.46	22.24
$(\bar{1}11)_{\alpha''}$	38.30	38.16	1.0	1.33	5.0	99.70	7.0	6.36	11.97

-190° C

	2θ		H		S		I		E
h k l	Initial / final		Initial / final		Initial / final		Initial / final		
$(011)_{\gamma}$ ∘	32.25	32.31	1.0	1.84	5.0	0.60	5.0	3.5	24.79
$(\bar{1}10)_{\alpha''}$	33.85	34.23	0.75	1.40	5.0	40.60	5.0	2.56	3.86
$(110)_{\alpha''}$	35.43	35.50	0.75	0.69	5.0	1.73	11.0	7.22	6.30
$(002)_{\alpha''}$	36.25	36.26	0.60	0.62	5.0	1.90	50.0	36.70	27.97
$(111)_{\gamma}$ ∘	37.00	37.07	0.80	0.62	5.0	5.0	38.0	24.82	17.21
$(\bar{1}11)_{\alpha''}$	38.32	38.15	0.85	1.58	5.0	108.26	9.0	6.82	12.48

Alloy 196

+25° C

	2θ		H		S		I		E
h k l	Initial / final		Initial / final		Initial / final		Initial / final		
$(011)_{\gamma}$ ∘	32.10	32.08	1.0	0.87	5.0	0.60	7.0	4.46	14.90
$(002)_{\alpha''}$	36.20	36.19	0.60	0.70	5.0	0.70	52.0	40.29	67.77
$(111)_{\gamma}$ ∘	36.93	36.93	0.35	0.35	5.0	2.60	96.0	67.90	27.50

TABLE A.4. (continued)

-40° C

	2θ		H		S		I		E
h k l	Initial /	final	Initial /	final	Initial /	final	Initial /	final	
$(020)_{\alpha''}$	31.20	31.19	0.40	0.0	5.0	0.60	2.0	0.35	0.0
$(011)_{\gamma\circ}$	32.00	32.01	1.0	1.58	5.0	47.62	6.0	3.35	5.65
$(\bar{1}10)_{\alpha''}$	33.60	33.76	1.0	2.42	5.0	63.82	4.0	2.76	9.57
$(110)_{\alpha''}$	35.60	35.62	0.75	0.67	5.0	116.31	19.0	14.91	12.94
$(002)_{\alpha''}$	36.18	36.2	0.65	0.51	5.0	9.56	52.0	37.22	20.77
$(111)_{\gamma\circ}$	36.98	36.95	0.65	0.56	5.0	3.40	61.0	46.97	30.26
$(\bar{1}11)_{\alpha''}$	38.00	37.90	1.0	0.96	5.0	13.40	7.0	6.62	6.88
$(111)_{\alpha''}$	39.90	39.75	0.75	1.58	5.0	0.60	2.0	1.75	10.57

-80° C

	2θ		H		S		I		E
h k l	Initial /	final	Initial /	final	Initial /	final	Initial /	final	
$(020)_{\alpha''}$	31.20	31.23	0.40	0.39	5.0	8.33	2.0	0.00	0.00
$(011)_{\gamma\circ}$	32.00	32.16	1.0	3.09	5.0	1.60	6.0	2.65	10.46
$(\bar{1}10)_{\alpha''}$	33.60	33.76	1.0	2.28	5.0	0.94	4.0	1.95	7.29
$(110)_{\alpha''}$	35.65	35.54	0.75	0.72	5.0	107.66	21.0	13.38	12.44
$(002)_{\alpha''}$	36.23	36.22	0.60	0.54	5.0	3.34	53.0	41.27	25.39
$(111)_{\gamma\circ}$	36.95	36.96	0.65	0.65	5.0	20.28	44.0	32.57	22.76
$(\bar{1}11)_{\alpha''}$	38.00	37.85	1.0	1.32	5.0	87.70	10.0	7.92	11.23
$(111)_{\alpha''}$	39.90	39.83	0.75	1.28	5.0	0.60	2.0	1.81	8.88

-123° C

	2θ		H		S		I		E
h k l	Initial /	final	Initial /	final	Initial /	final	Initial /	final	
$(020)_{\alpha''}$	31.20	31.18	0.40	1.37	5.0	0.60	2.0	1.90	10.02
$(011)_{\gamma\circ}$	32.20	32.27	1.0	1.06	5.0	50.60	6.0	1.66	1.88
$(\bar{1}10)_{\alpha''}$	33.60	33.73	1.1	2.57	5.0	3.0	5.0	3.36	9.98
$(110)_{\alpha''}$	35.65	35.54	0.75	0.73	5.0	119.40	22.0	13.66	13.11
$(002)_{\alpha''}$	36.20	36.24	0.60	0.53	5.0	2.40	57.0	42.96	26.80

TABLE A.4. (continued)

-123° C

	2θ		H		S		I		E
h k l	Initial /	final	Initial /	final	Initial /	final	Initial /	final	
$(111)_{\gamma^\circ}$	37.00	37.00	0.80	0.70	5.0	87.40	40.0	28.96	11.21
$(\bar{1}11)_{\alpha''}$	38.15	38.06	0.90	1.08	5.0	101.40	10.0	7.96	12.07
$(111)_{\alpha''}$	39.90	39.69	0.75	1.83	5.0	10.60	2.0	1.70	3.39

-189° C

	2θ		H		S		I		E
h k l	Initial /	final	Initial /	final	Initial /	final	Initial /	final	
$(020)_{\alpha''}$	31.20	31.27	0.50	0.77	5.0	0.60	3.0	2.43	7.22
$(011)_{\gamma^\circ}$	32.25	32.35	0.75	1.18	5.0	40.60	6.0	2.36	2.97
$(\bar{1}10)_{\alpha''}$	33.75	33.86	1.10	2.10	5.0	1.30	6.0	3.15	9.08
$(110)_{\alpha''}$	35.52	35.50	0.75	0.71	5.0	150.01	22.0	12.30	14.69
$(002)_{\alpha''}$	36.25	36.26	0.60	0.57	5.0	1.67	58.0	43.85	31.53
$(\bar{1}11)_{\alpha''}$	38.15	38.04	1.10	1.49	5.0	123.79	10.0	7.78	13.34
$(111)_{\alpha''}$	39.80	38.86	0.75	1.05	5.0	0.53	3.0	2.04	21.27
$(111)_{\gamma^\circ}$	36.95	37.02	0.80	0.70	5.0	112.13	33.0	21.15	12.70

Table A.5.

The h k l's, E's and R's that were used for phase fraction determination from first analysis (Table A.4).

Alloy 142

+22° C

Peak	Phase	R (x 10^{48})	E
(020)	α"	2.8414	10.03
($\bar{1}$10)	α"	9.7615	12.02
(110)	α"	9.1233	13.50
($\bar{1}$11)	α"	1.4340	21.25
(111)	α"	0.3256	6.61
(011)	γ°	0.7040	4.06
(111)	γ°	9.4804	10.20

-40° C

Peak	Phase	R (x 10^{48})	E
(020)	α"	2.8880	7.80
($\bar{1}$10)	α"	9.6332	17.01
(110)	α"	9.2848	14.76
($\bar{1}$11)	α"	1.3552	10.39
(111)	α"	0.3256	6.09
(011)	γ°	0.6986	1.43
(111)	γ°	9.4804	11.86

-80° C

Peak	Phase	R (x 10^{48})	E
(020)	α"	2.9583	4.35
($\bar{1}$10)	α"	9.4639	15.55
(110)	α"	9.3347	8.37
($\bar{1}$11)	α"	1.3511	18.47
(111)	α"	0.3255	6.19
(111)	γ°	9.5088	12.77

Table A.5. (continued)

-120° C

Peak	Phase	R (x 10^{48})	E
(020)	α"	2.9675	18.05
($\bar{1}$10)	α"	9.3913	15.33
(110)	α"	9.3347	13.34
($\bar{1}$11)	α"	1.3503	17.38
(111)	α"	0.3255	12.17
(111)	γ°	9.5088	28.78

-154° C

Peak	Phase	R (x 10^{48})	E
(020)	α"	2.9583	15.05
($\bar{1}$10)	α"	9.4639	16.76
(110)	α"	9.3347	13.38
($\bar{1}$11)	α"	1.3246	19.56
(111)	α"	0.3269	3.09
(111)	γ°	9.5088	14.62

-187° C

Peak	Phase	R (x 10^{48})	E
(020)	α"	2.9583	18.41
($\bar{1}$10)	α"	9.4639	14.03
(110)	α"	9.3347	9.21
($\bar{1}$11)	α"	1.3246	18.65
(111)	α"	0.3269	4.02
(111)	γ°	9.5088	9.29

Alloy 183:

-40° C

Peak	Phase	R (x 10^{48})	E
(110)	α"	9.0586	9.90

Table A.5. (continued)

-40° C			
Peak	Phase	R (x 10^{48})	E
($\bar{1}$11)	α"	1.3474	6.42
(111)	γ°	9.2792	30.24
-81° C			
Peak	Phase	R (x 10^{48})	E
(110)	α"	9.0586	6.45
($\bar{1}$11)	α"	1.3474	8.20
(111)	γ°	9.2792	26.56
-121° C			
Peak	Phase	R (x 10^{48})	E
(110)	α"	9.2580	5.78
($\bar{1}$11)	α"	1.3516	10.35
(111)	γ°	9.3070	22.77
-161° C			
Peak	Phase	R (x 10^{48})	E
(110)	α"	9.3096	12.49
($\bar{1}$11)	α"	1.3474	11.97
(111)	γ°	9.3070	22.24
-190° C			
Peak	Phase	R (x 10^{48})	E
(110)	α"	9.3096	6.30
($\bar{1}$11)	α"	1.3474	12.48
(111)	γ°	9.3070	17.21

Table A.5. (continued)

Alloy 196.

-40° C

Peak	Phase	R (x 10^{48})	E
($\bar{1}10$)	α"	9.5475	9.57
(110)	α"	9.0018	12.94
($\bar{1}11$)	α"	1.3679	6.88
(111)	γ°	9.2792	30.26

-80° C

Peak	Phase	R (x 10^{48})	E
($\bar{1}10$)	α"	9.5475	7.29
(110)	α"	9.0196	12.44
($\bar{1}11$)	α"	1.3829	11.23
(111)	γ°	9.3070	22.76

-123° C

Peak	Phase	R (x 10^{48})	E
($\bar{1}10$)	α"	9.5475	9.98
(110)	α"	9.0196	13.11
($\bar{1}11$)	α"	1.3654	12.07
(111)	γ°	9.3070	11.21

-189° C

Peak	Phase	R (x 10^{48})	E
($\bar{1}10$)	α"	9.3868	9.08
(110)	α"	9.0586	14.69
($\bar{1}11$)	α"	1.3654	13.34
(111)	γ°	9.3070	12.70

Table A.6.

The input parameters 2θ, H, S, and I shown with their initial experimental value and the computer calculated final values along with the E's of each peak (h k l) determined by the computer, after optimization of incremental input parameter values.
The abnormal E values are indicated by '*'.

Alloy 142

+22° C

	2θ		H		S		I		E
h k l	Initial /	final	Initial /	final	Initial /	final	Initial /	final	
$(020)_{\alpha''}$	31.60	31.19	1.0	1.45	5.0	0.52	5.0	3.06	75.51*
$(011)_{\gamma\circ}$	32.20	32.19	1.0	1.13	5.0	1.46	5.0	2.81	4.20
$(\bar{1}10)_{\alpha''}$	33.50	33.57	1.5	1.51	5.0	1.19	10.0	7.93	17.11
$(110)_{\alpha''}$	35.60	35.48	0.75	0.57	5.0	5.97	20.0	12.63	7.91
$(002)_{\alpha''}$	36.15	36.20	0.50	0.42	5.0	1.83	100.0	82.82	43.43
$(111)_{\gamma\circ}$	36.88	36.88	0.80	0.69	5.0	17.13	55.0	38.72	28.98
$(\bar{1}11)_{\alpha''}$	37.68	37.84	1.50	1.18	5.0	6.90	22.0	16.51	21.45
$(111)_{\alpha''}$	39.90	39.96	1.0	1.32	5.0	1.12	5.0	2.98	5.77

-40° C

	2θ		H		S		I		E
h k l	Initial /	final	Initial /	final	Initial /	final	Initial /	final	
$(020)_{\alpha''}$	31.40	31.19	1.25	1.23	5.0	0.61	5.0	3.18	14.12
$(011)_{\gamma\circ}$	32.30	32.27	1.20	1.33	5.0	1.13	7.0	3.91	7.60
$(\bar{1}10)_{\alpha''}$	33.80	33.79	1.25	1.27	5.0	2.69	14.0	9.67	14.38
$(110)_{\alpha''}$	35.45	35.40	0.70	0.50	5.0	1.99	22.0	13.52	8.20
$(002)_{\alpha''}$	36.15	36.18	0.50	0.46	5.0	1.45	100.0	85.31	51.38
$(111)_{\gamma\circ}$	36.85	36.92	0.95	0.76	5.0	15.18	40.0	26.51	21.63
$(\bar{1}11)_{\alpha''}$	38.25	38.10	1.0	1.19	5.0	41.69	20.0	15.98	20.35
$(111)_{\alpha''}$	39.83	39.82	0.75	0.93	5.0	0.69	5.0	4.0	9.22

Table A.6. (continued)

-80° C

	2θ		H		S		I		E
h k l	Initial /	final	Initial /	final	Initial /	final	Initial /	final	
$(020)_{\alpha''}$	31.20	31.12	1.0	1.07	5.0	0.51	6.0	3.52	94.75*
$(011)_{\gamma\circ}$	32.30	32.14	1.20	1.54	5.0	45.35	5.0	2.81	4.62
$(\bar{1}10)_{\alpha''}$	33.88	33.82	1.20	1.29	5.0	1.77	14.0	10.90	17.52
$(110)_{\alpha''}$	35.38	35.36	0.50	0.47	5.0	8.44	23.0	12.84	6.55
$(002)_{\alpha''}$	36.15	36.18	0.50	0.47	5.0	1.39	100.0	85.80	53.47
$(111)_{\gamma\circ}$	36.90	36.95	1.0	0.86	5.0	18.80	34.0	21.70	20.02
$(\bar{1}11)_{\alpha''}$	38.85	38.22	0.75	1.18	5.0	31.22	20.0	14.74	18.70
$(111)_{\alpha''}$	39.85	39.86	0.85	1.16	5.0	0.51	6.0	3.89	112.40*

-120° C

	2θ		H		S		I		E
h k l	Initial /	final	Initial /	final	Initial /	final	Initial /	final	
$(020)_{\alpha''}$	31.18	31.26	1.0	1.32	5.0	0.83	6.0	4.50	11.07
$(011)_{\gamma\circ}$	32.30	32.54	1.20	1.14	5.0	13.98	5.0	3.78	4.65
$(\bar{1}10)_{\alpha''}$	33.90	33.92	1.0	1.05	5.0	2.74	15.0	12.23	14.95
$(110)_{\alpha''}$	35.40	35.37	0.70	0.47	5.0	7.11	23.0	13.92	7.17
$(002)_{\alpha''}$	36.18	36.19	0.50	0.50	5.0	1.39	100.0	86.29	57.65
$(111)_{\gamma\circ}$	36.90	37.01	1.10	0.79	5.0	14.21	30.0	18.53	15.91
$(\bar{1}11)_{\alpha''}$	38.43	38.28	1.20	1.24	5.0	16.68	20.0	14.93	19.89
$(111)_{\alpha''}$	39.85	39.89	0.50	0.57	5.0	0.51	7.0	4.97	70.29*

-154° C

	2θ		H		S		I		E
h k l	Initial /	final	Initial /	final	Initial /	final	Initial /	final	
$(020)_{\alpha''}$	31.20	31.22	0.75	1.07	5.0	0.51	6.0	4.95	164.33*
$(011)_{\gamma\circ}$	32.35	32.45	1.20	1.09	5.0	11.87	4.0	3.58	4.23
$(\bar{1}10)_{\alpha''}$	33.95	33.94	1.20	1.10	5.0	2.71	15.0	11.53	14.88
$(110)_{\alpha''}$	35.35	35.37	0.65	0.55	5.0	2.95	23.0	14.30	9.05
$(002)_{\alpha''}$	36.18	36.19	0.50	0.48	5.0	1.58	100.0	86.06	53.05

Table A.6. (continued)

-154° C

	2θ		H		S		I		E
h k l	Initial / final		Initial / final		Initial / final		Initial / final		
$(111)_{\gamma}$ ◦	36.90	37.02	1.10	0.89	5.0	15.92	28.0	18.39	17.59
$(\bar{1}11)_{\alpha''}$	38.50	38.34	0.80	1.19	5.0	19.08	20.0	14.56	18.69
$(111)_{\alpha''}$	39.80	39.88	0.70	0.62	5.0	0.51	7.0	4.41	78.30*

-187° C

	2θ		H		S		I		E
h k l	Initial / final		Initial / final		Initial / final		Initial / final		
$(020)_{\alpha''}$	31.20	31.07	0.70	1.06	5.0	1.48	6.0	3.64	5.04
$(011)_{\gamma}$ ◦	32.35	32.43	1.20	1.57	5.0	10.78	5.0	4.06	6.94
$(\bar{1}10)_{\alpha''}$	34.00	34.01	1.25	0.98	5.0	1.44	5.0	12.58	16.37
$(110)_{\alpha''}$	35.35	35.36	0.65	0.50	5.0	2.40	23.0	14.38	8.58
$(002)_{\alpha''}$	36.18	36.19	0.50	0.51	5.0	1.64	100.0	88.48	57.46
$(111)_{\gamma}$ ◦	36.90	37.02	0.50	0.78	5.0	27.52	26.0	16.88	14.03
$(\bar{1}11)_{\alpha''}$	38.50	38.31	1.10	1.37	5.0	7.86	21.0	14.74	22.05
$(111)_{\alpha''}$	39.80	39.92	0.60	0.68	5.0	0.54	7.0	4.24	23.53

Alloy 183

+22° C

	2θ		H		S		I		E
h k l	Initial / final		Initial / final		Initial / final		Initial / final		
$(011)_{\gamma}$ ◦	32.05	32.04	0.70	0.86	5.0	0.51	5.0	4.20	108.20*
$(002)_{\alpha''}$	36.20	36.19	0.50	0.60	5.0	0.63	43.0	34.03	64.50
$(111)_{\gamma}$ ◦	36.93	36.91	0.35	0.38	5.0	2.58	80.0	60.43	26.91

Table A.6. (continued)

-40° C

	2θ		H		S		I		E
h k l	Initial / final		Initial / final		Initial / final		Initial / final		
$(011)_{\gamma}$ ∘	32.20	31.98	0.75	1.33	5.0	0.81	4.0	3.62	9.24
$(\bar{1}10)_{\alpha''}$	33.65	34.10	1.20	1.77	5.0	1.10	4.0	3.13	8.18
$(110)_{\alpha''}$	35.50	35.57	0.80	0.73	5.0	9.33	9.0	6.63	5.29
$(002)_{\alpha''}$	36.20	36.19	0.60	0.51	5.0	2.20	45.0	32.71	19.94
$(111)_{\gamma}$ ∘	36.98	36.96	0.60	0.53	5.0	1.89	55.0	43.81	28.67
$(\bar{1}11)_{\alpha''}$	38.24	38.04	0.80	1.08	5.0	6.59	7.0	5.72	6.77

-81° C

	2θ		H		S		I		E
h k l	Initial / final		Initial / final		Initial / final		Initial / final		
$(011)_{\gamma}$ ∘	32.20	32.16	1.00	1.53	5.0	0.51	5.0	3.36	153.41*
$(\bar{1}10)_{\alpha''}$	33.50	33.86	1.00	1.36	5.0	0.51	4.0	2.77	112.39*
$(110)_{\alpha''}$	35.52	35.52	0.60	0.80	5.0	6.89	12.0	7.48	6.64
$(002)_{\alpha''}$	36.20	36.22	0.60	0.55	5.0	2.93	44.0	33.79	21.69
$(111)_{\gamma}$ ∘	36.98	37.00	0.60	0.59	5.0	4.36	48.0	36.79	24.23
$(\bar{1}11)_{\alpha''}$	38.30	38.03	1.00	1.09	5.0	11.41	7.0	7.12	8.62

-121° C

	2θ		H		S		I		E
h k l	Initial / final		Initial / final		Initial / final		Initial / final		
$(011)_{\gamma}$ ∘	32.25	32.17	1.00	1.28	5.0	0.51	5.0	3.84	147.06*
$(\bar{1}10)_{\alpha''}$	33.60	33.87	1.00	1.51	5.0	0.85	4.0	2.29	6.23
$(110)_{\alpha''}$	35.45	35.57	0.75	0.88	5.0	11.82	11.0	5.69	5.43
$(002)_{\alpha''}$	36.20	36.23	0.70	0.58	5.0	1.24	47.0	33.91	27.40
$(111)_{\gamma}$ ∘	37.00	37.03	0.50	0.61	5.0	5.42	45.0	31.11	21.13
$(\bar{1}11)_{\alpha''}$	38.25	38.11	0.80	1.22	5.0	6.99	8.0	6.61	8.86

Table A.6. (continued)

-161° C

	2θ		H		S		I		E
h k l	Initial /	final	Initial /	final	Initial /	final	Initial /	final	
$(011)_{\gamma\circ}$	32.25	31.94	1.00	1.68	5.0	1.01	5.0	3.03	7.96
$(\bar{1}10)_{\alpha''}$	33.65	33.84	1.00	1.66	5.0	0.84	4.0	3.30	10.07
$(110)_{\alpha''}$	35.43	35.42	0.75	0.70	5.0	16.23	11.0	4.81	3.65
$(002)_{\alpha''}$	36.23	36.22	0.60	0.60	5.0	1.30	48.0	35.72	29.49
$(111)_{\gamma\circ}$	37.00	37.04	0.80	0.59	5.0	4.32	42.0	28.22	18.66
$(\bar{1}11)_{\alpha''}$	38.30	38.03	1.00	1.44	5.0	4.20	7.0	6.54	10.58

-190° C

	2θ		H		S		I		E
h k l	Initial /	final	Initial /	final	Initial /	final	Initial /	final	
$(011)_{\gamma\circ}$	32.25	32.37	1.00	1.38	5.0	0.51	5.0	3.92	178.67*
$(\bar{1}10)_{\alpha''}$	33.85	34.03	0.75	1.13	5.0	0.73	5.0	2.95	7.36
$(110)_{\alpha''}$	35.23	35.61	0.75	0.80	5.0	12.33	11.0	6.64	5.73
$(002)_{\alpha''}$	36.25	36.27	0.60	0.58	5.0	1.29	50.0	37.34	29.49
$(111)_{\gamma\circ}$	37.00	37.06	0.80	0.63	5.0	7.262	38.0	25.04	17.32
$(\bar{1}11)_{\alpha''}$	38.32	38.11	0.85	1.14	5.0	8.32	9.0	7.71	9.56

Alloy 196

+25° C

	2θ		H		S		I		E
h k l	Initial /	final	Initial /	final	Initial /	final	Initial /	final	
$(011)_{\gamma\circ}$	32.10	32.16	1.00	1.45	5.0	0.51	7.0	4.69	224.29*
$(002)_{\alpha''}$	36.20	36.15	0.60	0.60	5.0	1.13	52.0	35.17	30.64
$(111)_{\gamma\circ}$	36.93	36.92	0.35	0.34	5.0	0.80	96.0	75.47	50.15

Table A.6. (continued)

-40° C

	2θ		H		S		I		E
h k l	Initial /	final	Initial /	final	Initial /	final	Initial /	final	
$(020)_{\alpha''}$	31.20	30.78	0.40	0.43	5.0	6.30	2.0	0.00	0.00
$(011)_{\gamma\circ}$	32.00	32.27	1.00	1.47	5.0	1.19	6.0	4.48	9.40
$(\bar{1}10)_{\alpha''}$	33.60	34.45	1.00	1.57	5.0	1.38	4.0	2.69	5.65
$(110)_{\alpha''}$	35.60	35.63	0.75	0.68	5.0	14.62	19.0	14.32	10.58
$(002)_{\alpha''}$	36.18	36.23	0.65	0.50	5.0	7.42	52.0	36.28	19.86
$(111)_{\gamma\circ}$	36.98	36.95	0.65	0.56	5.0	2.10	61.0	47.58	31.95
$(\bar{1}11)_{\alpha''}$	38.00	37.92	1.0	0.94	5.0	4.22	7.0	5.68	6.00
$(111)_{\alpha''}$	39.90	39.60	0.75	1.91	5.0	0.98	2.0	1.71	5.20

-80° C

	2θ		H		S		I		E
h k l	Initial /	final	Initial /	final	Initial /	final	Initial /	final	
$(020)_{\alpha''}$	31.20	31.20	0.40	0.49	5.0	0.51	2.0	0.24	3.63
$(011)_{\gamma\circ}$	32.20	32.18	1.00	1.10	5.0	0.51	6.0	4.17	116.28*
$(\bar{1}10)_{\alpha''}$	33.60	33.85	1.20	1.57	5.0	0.71	4.0	3.07	11.30
$(110)_{\alpha''}$	35.65	35.51	0.75	0.63	5.0	22.52	21.0	13.14	8.96
$(002)_{\alpha''}$	36.23	36.21	0.60	0.55	5.0	2.94	53.0	42.0	26.52
$(111)_{\gamma\circ}$	36.95	36.96	0.65	0.63	5.0	10.20	44.0	32.40	22.30
$(\bar{1}11)_{\alpha''}$	38.00	37.78	1.00	1.20	5.0	9.06	10.0	8.29	10.88
$(111)_{\alpha''}$	40.00	39.54	0.75	1.58	5.0	0.80	2.0	1.93	5.95

-123° C

	2θ		H		S		I		E
h k l	Initial /	final	Initial /	final	Initial /	final	Initial /	final	
$(020)_{\alpha''}$	31.20	31.35	0.70	1.35	5.0	0.75	2.0	2.21	6.33
$(011)_{\gamma\circ}$	32.20	32.42	1.00	1.18	5.0	16.51	4.0	2.24	2.84
$(\bar{1}10)_{\alpha''}$	33.60	33.85	1.20	1.79	5.0	2.13	5.0	3.70	7.99
$(110)_{\alpha''}$	35.65	35.53	0.75	0.69	5.0	18.49	22.0	12.25	9.11
$(002)_{\alpha''}$	36.20	36.24	0.60	0.55	5.0	1.48	57.0	43.18	31.54

Table A.6. (continued)

-123° C

	2θ		H		S		I		E
h k l	Initial / final		Initial / final		Initial / final		Initial / final		
$(111)_{\gamma^\circ}$	37.00	37.01	0.80	0.66	5.0	16.09	40.0	27.31	19.33
$(\bar{1}11)_{\alpha''}$	38.15	37.94	0.90	0.96	5.0	10.87	10.0	7.71	8.04
$(111)_{\alpha''}$	40.00	39.23	1.00	1.92	5.0	34.13	2.0	2.19	4.50

-189° C

	2θ		H		S		I		E
h k l	Initial / final		Initial / final		Initial / final		Initial / final		
$(020)_{\alpha''}$	31.20	31.35	0.50	1.39	5.0	0.51	3.0	2.24	62.73*
$(011)_{\gamma^\circ}$	32.25	32.38	0.75	0.99	5.0	9.92	6.0	2.55	2.73
$(\bar{1}10)_{\alpha''}$	33.75	33.79	1.10	1.43	5.0	103.25	6.0	4.21	12.18
$(110)_{\alpha''}$	35.52	35.48	0.75	0.71	5.0	30.87	22.0	12.23	9.36
$(002)_{\alpha''}$	36.25	36.26	0.60	0.57	5.0	1.25	58.0	44.35	34.90
$(111)_{\gamma^\circ}$	36.95	37.01	0.80	0.67	5.0	16.36	33.0	20.24	14.70
$(\bar{1}11)_{\alpha''}$	38.15	38.01	1.10	1.46	5.0	26.83	10.0	7.62	11.96
$(111)_{\alpha''}$	39.80	39.83	0.75	1.03	5.0	0.50	3.0	2.32	77.32*

TABLE A.7.

The α" and γ° phase fractions calculated at various temperatures.

Alloy 142 (15.0 at% Nb)

T(° C)	+22	-40	-80	-120	-154	-187
% α"	70 (70.74)	80 (79.73)	85 (84.53)	80 (79.70)	80 (80.88)	90 (87.78)
% γ°	30 (29.26)	20 (20.27)	15 (15.47)	20 (20.30)	20 (19.12)	10 (12.22)

Alloy 183 (15.5* at% Nb)

T(° C)	-40	-81	-121	-161	-190
% α"	50 (47.33)	55 (54.29)	60 (62.86)	70 (68.15)	70 (72.88)
% γ°	50 (52.67)	45 (45.71)	40 (37.14)	30 (31.85)	30 (27.12)

Alloy 196 (15.5** at% Nb)

T(° C)	-40	-80	-123	-189
% α"	40 (42.94)	60 (58.33)	75 (75.86)	75 (75.13)
% γ°	60 (57.06)	40 (41.67)	25 (24.14)	25 (24.87)

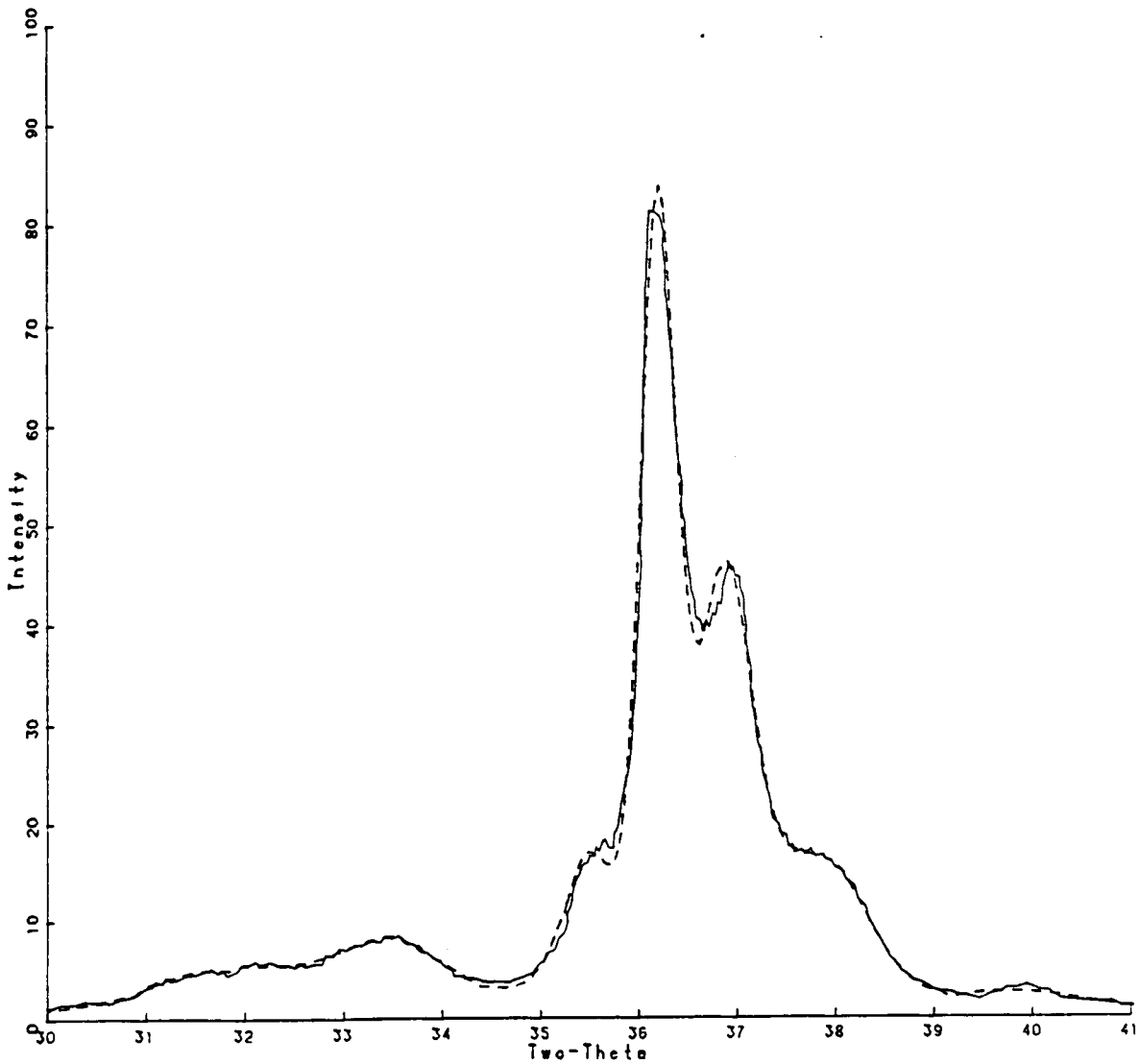

Figure A.1. Computer generated diffraction pattern curve fit for alloy 142 at +22 °C.

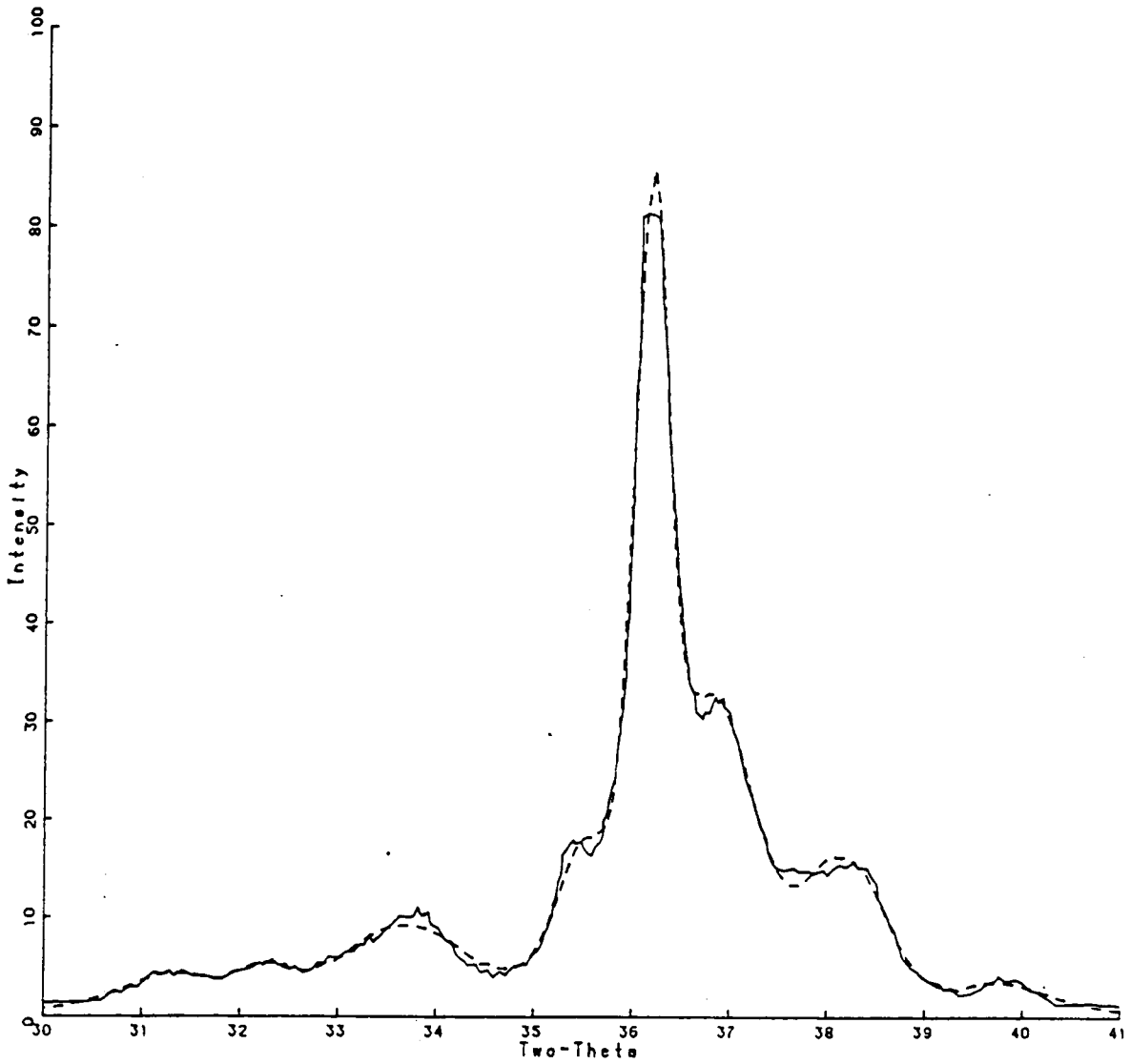

Figure A.2. Computer generated diffraction pattern curve fit for alloy 142 at -40 °C.

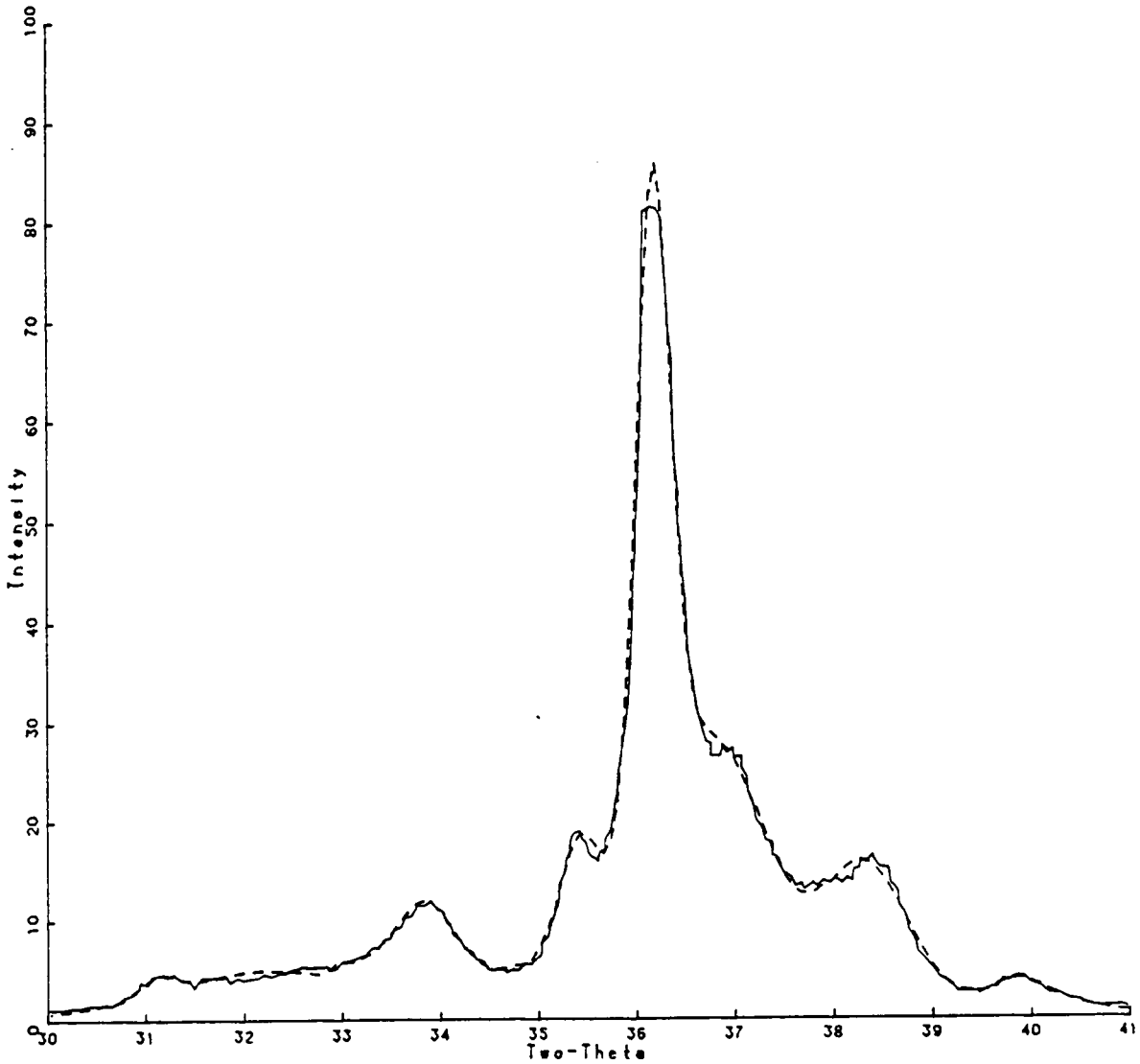

Figure A.3. Computer generated diffraction pattern curve fit for alloy 142 at -80 °C.

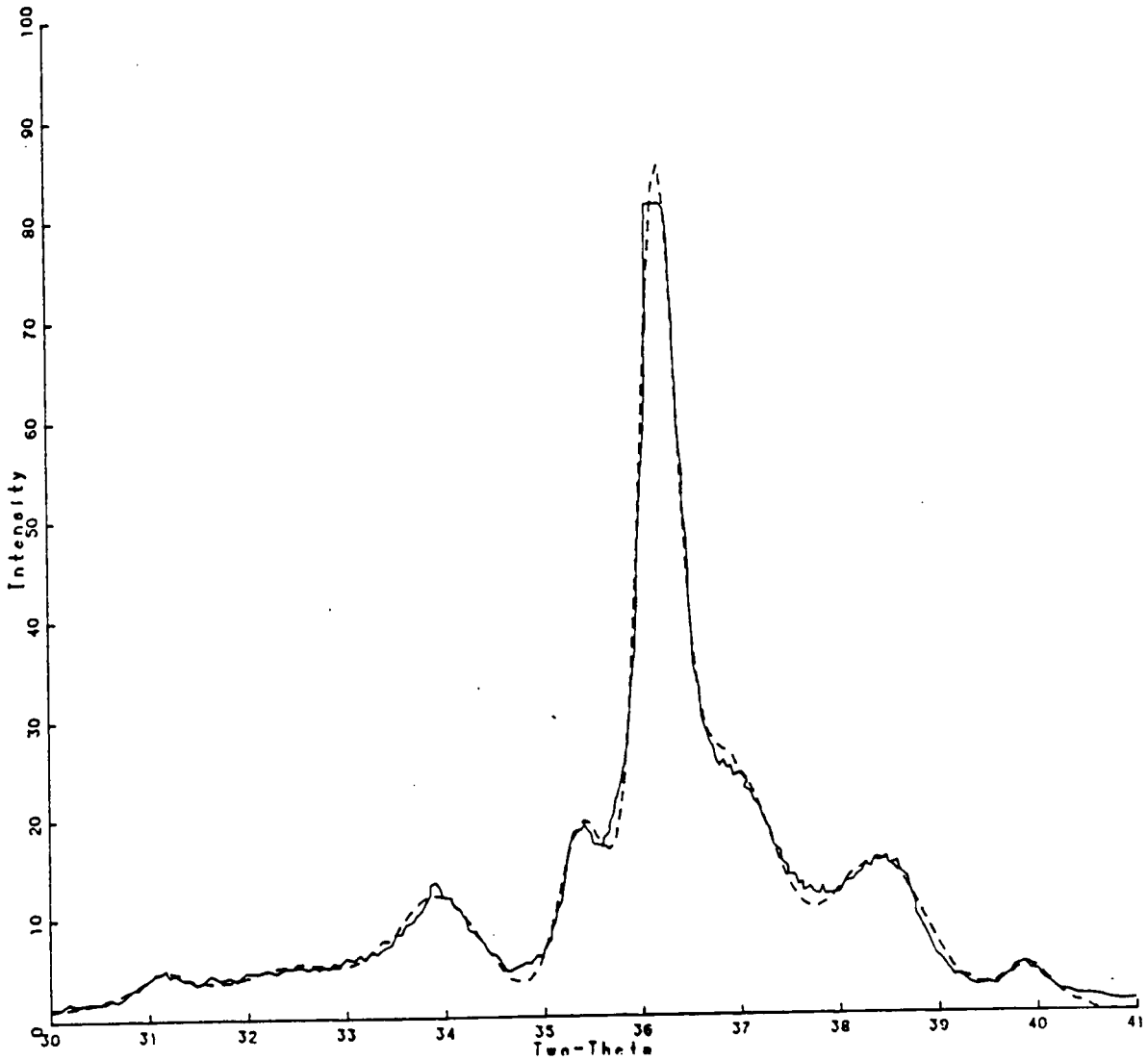

Figure A.4. Computer generated diffraction pattern curve fit for alloy 142 at -120 °C.

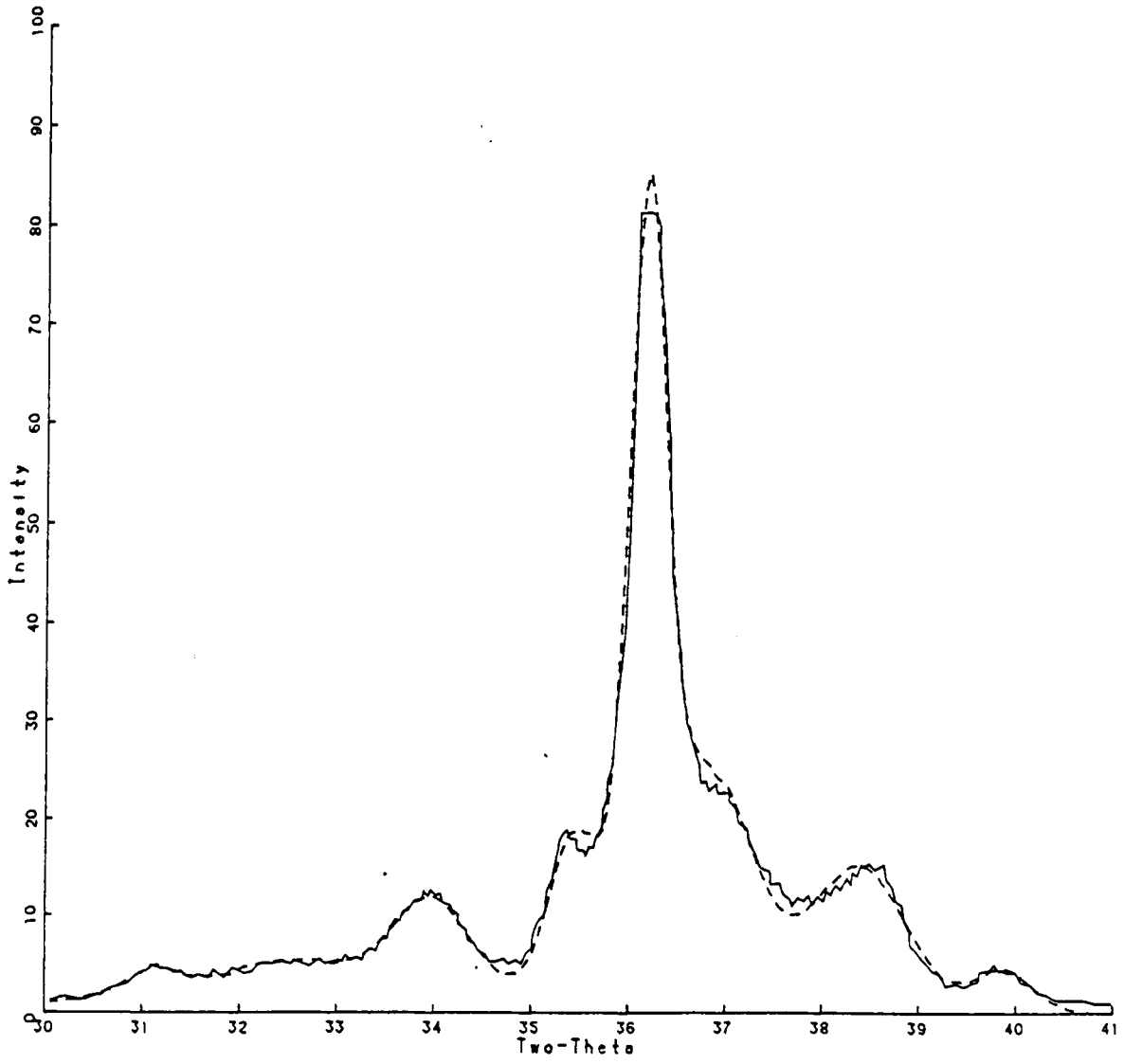

Figure A.5. Computer generated diffraction pattern curve fit for alloy 142 at -154 °C.

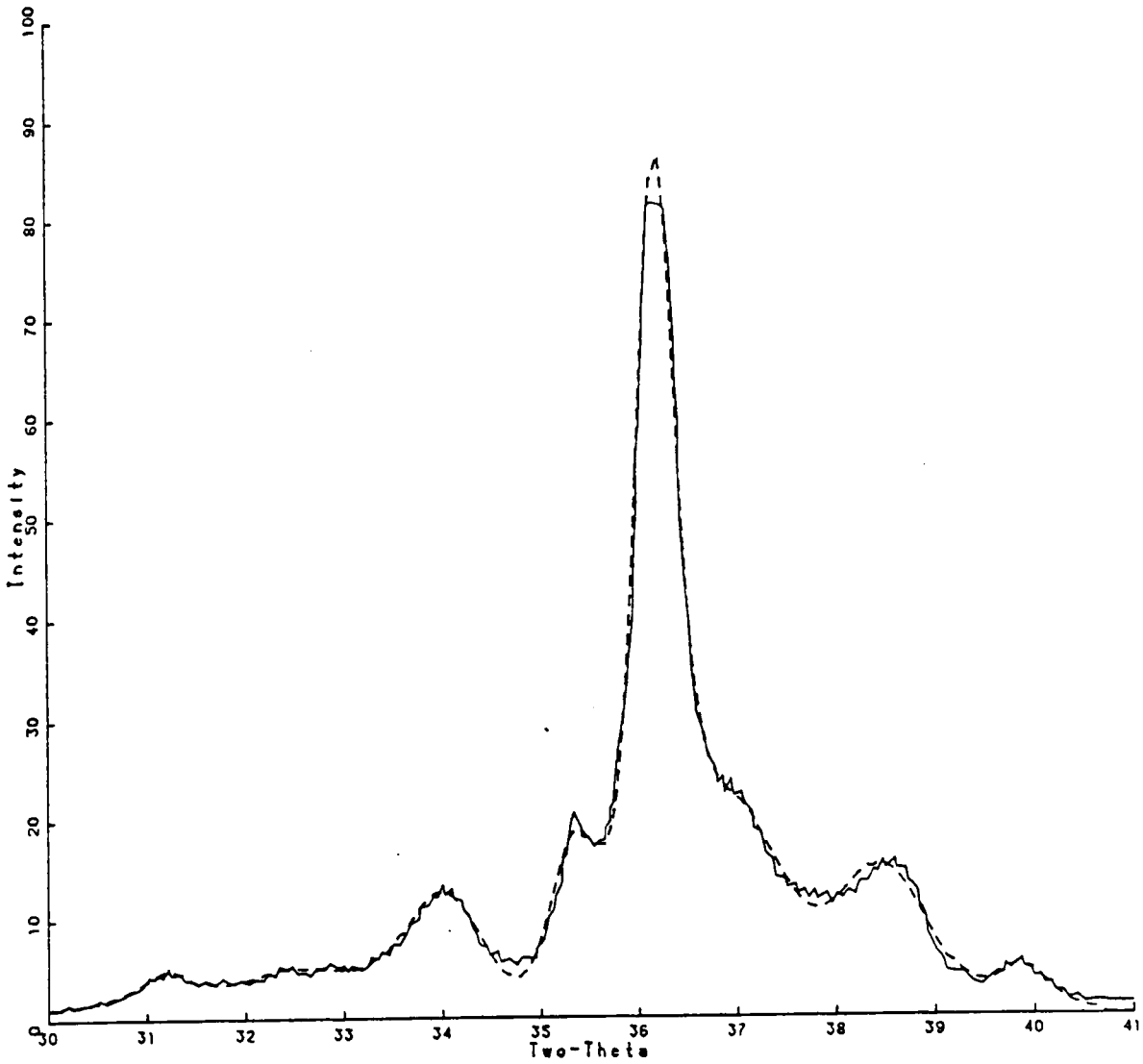

Figure A.6. Computer generated diffraction pattern curve fit for alloy 142 at -187 °C.

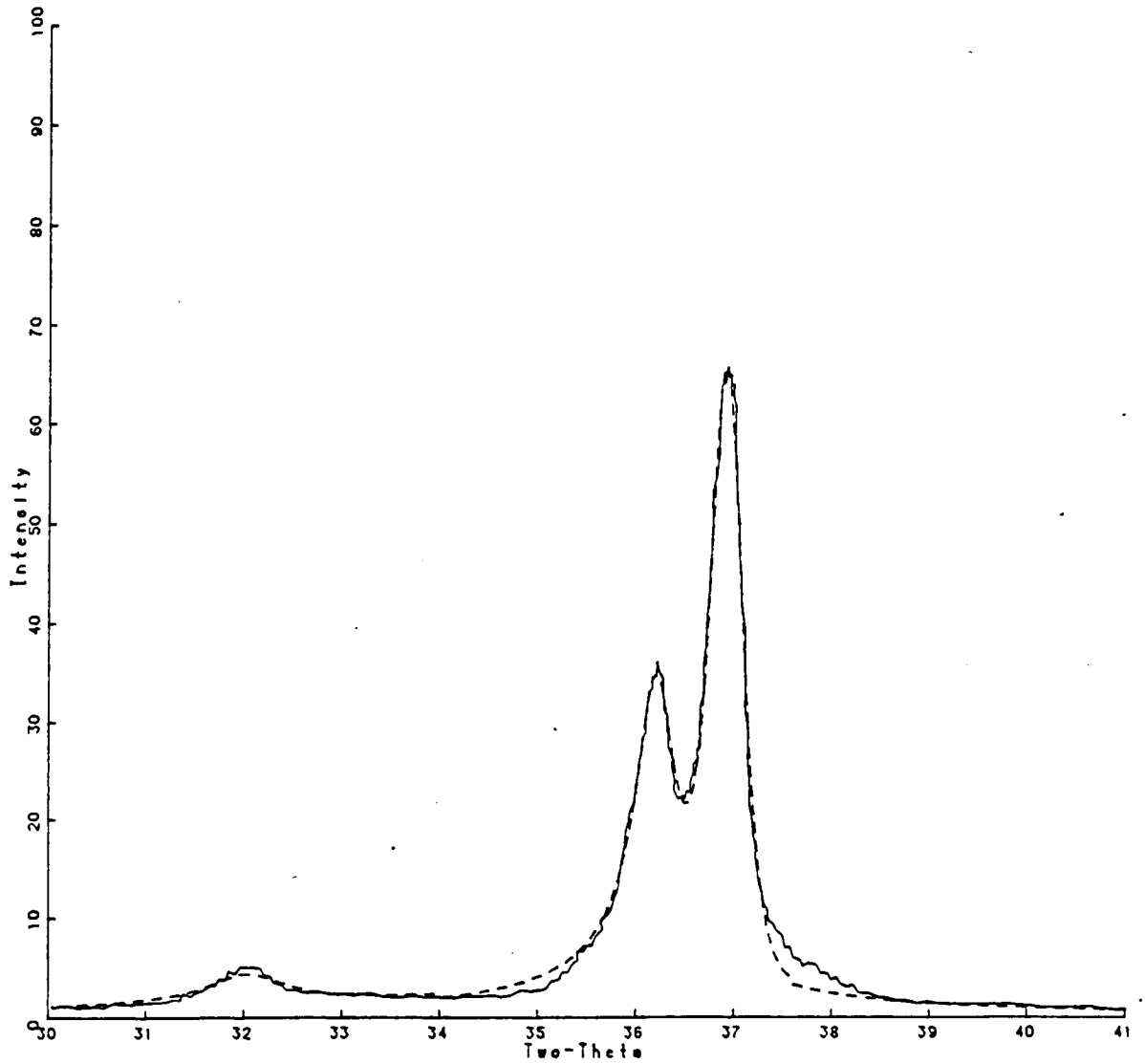

Figure A.7. Computer generated diffraction pattern curve fit for alloy 183 at +22 °C.

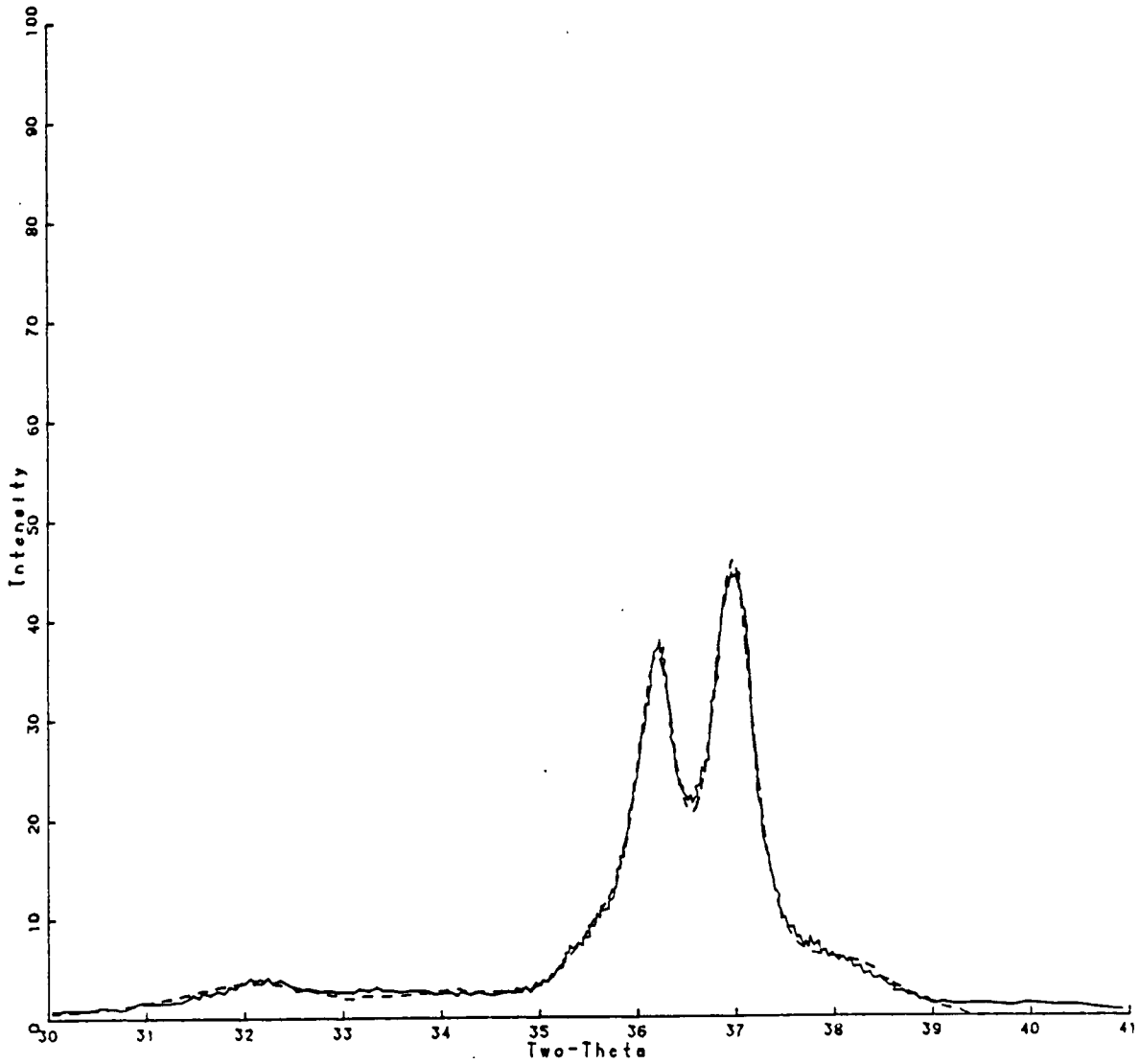

Figure A.8. Computer generated diffraction pattern curve fit for alloy 183 at -40 °C.

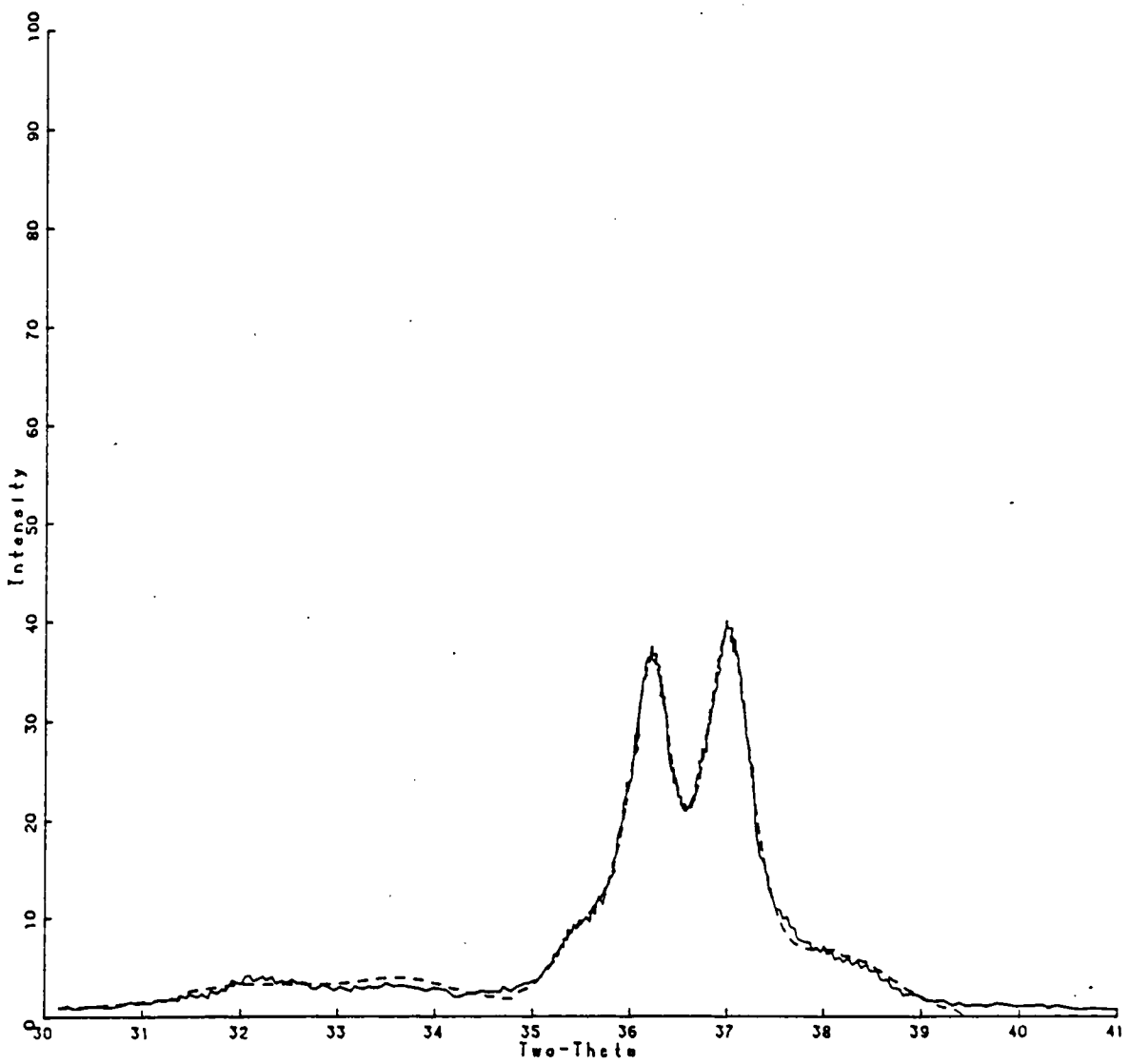

Figure A.9. Computer generated diffraction pattern curve fit for alloy 183 at -81 °C.

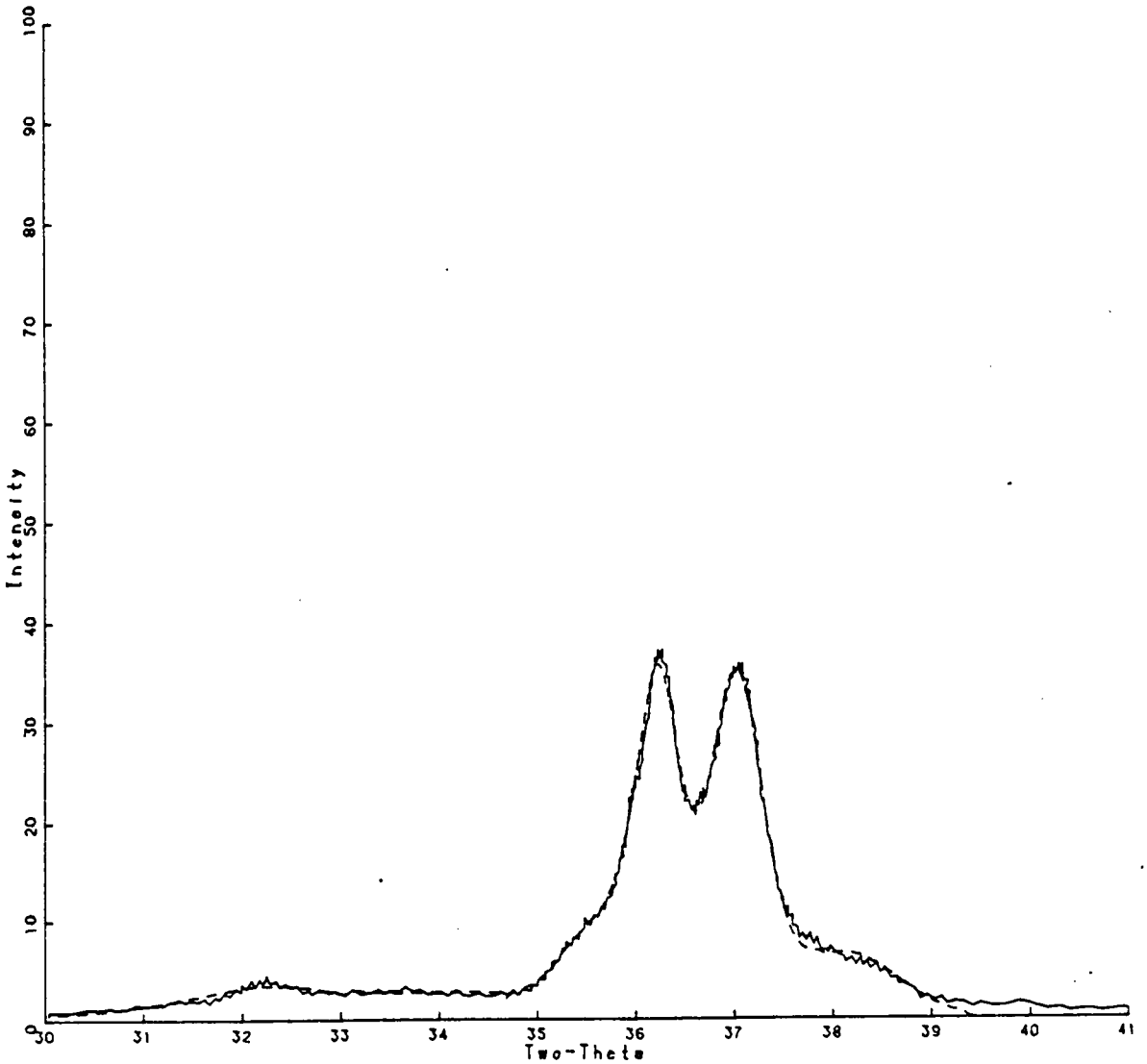

Figure A.10. Computer generated diffraction pattern curve fit for alloy 183 at -121 °C.

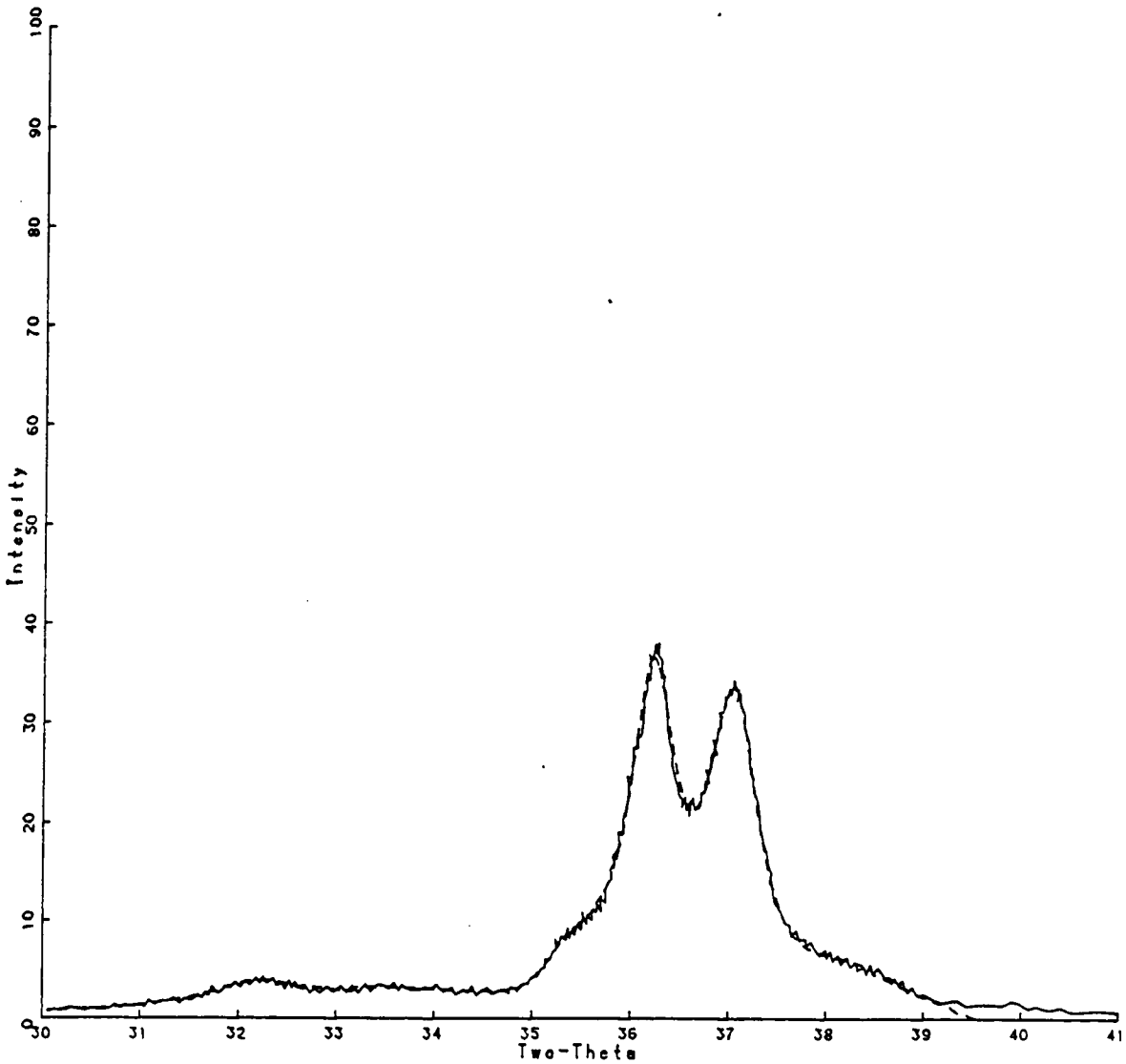

Figure A.11. Computer generated diffraction pattern curve fit for alloy 183 at -161 °C.

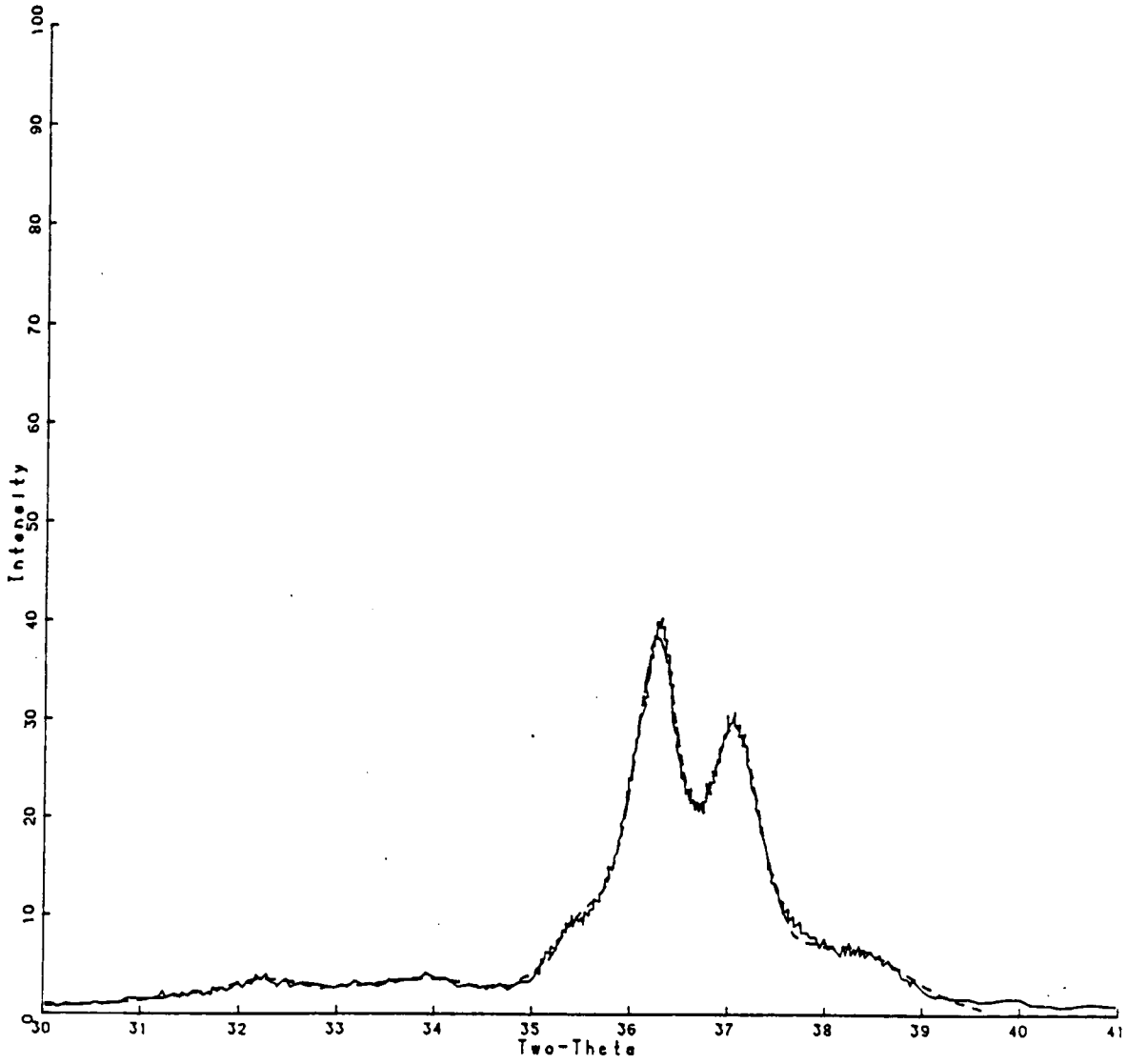

Figure A.12. Computer generated diffraction pattern curve fit for alloy 183 at -190 °C.

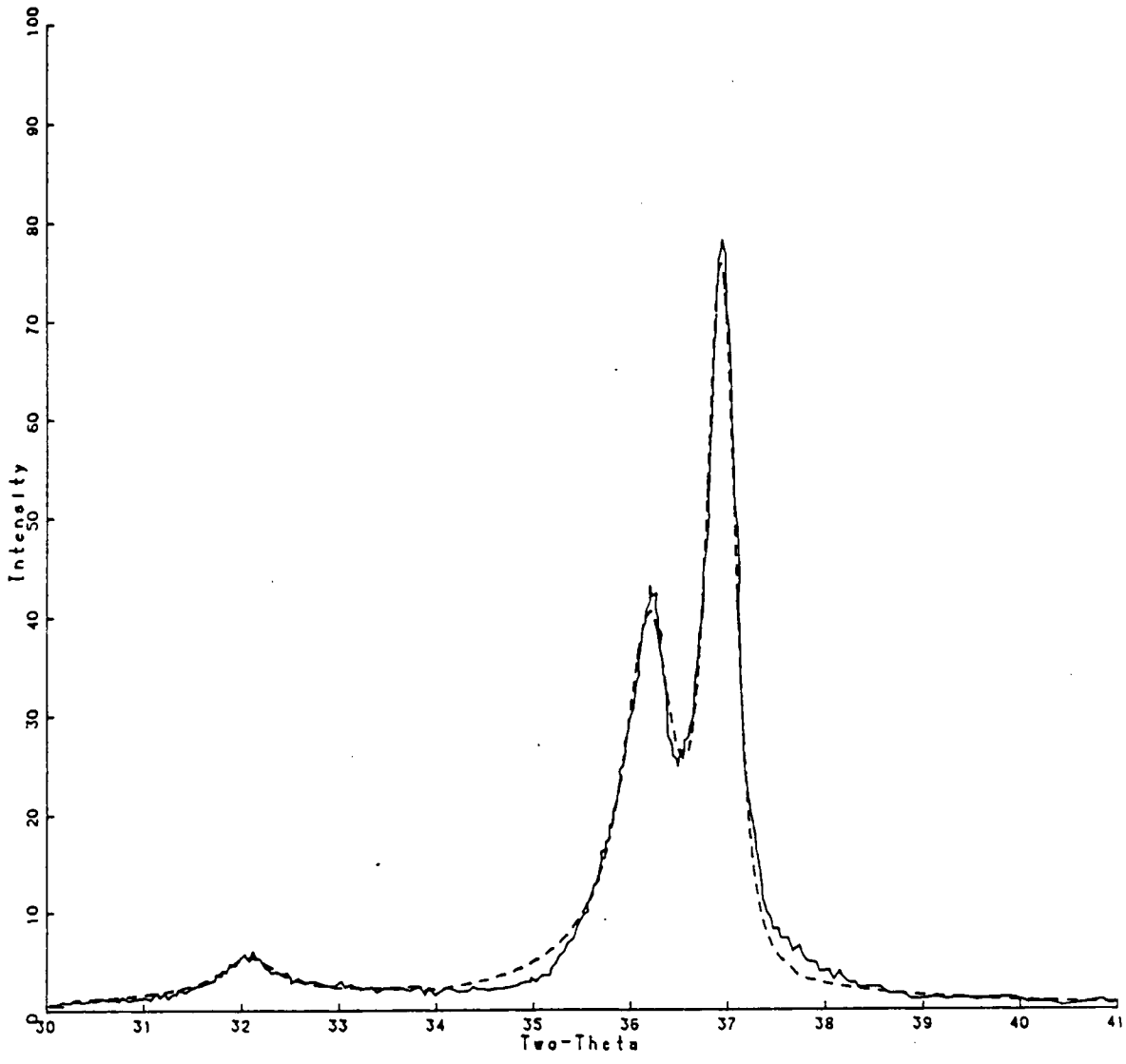

Figure A.13. Computer generated diffraction pattern curve fit for alloy 196 at +25 °C.

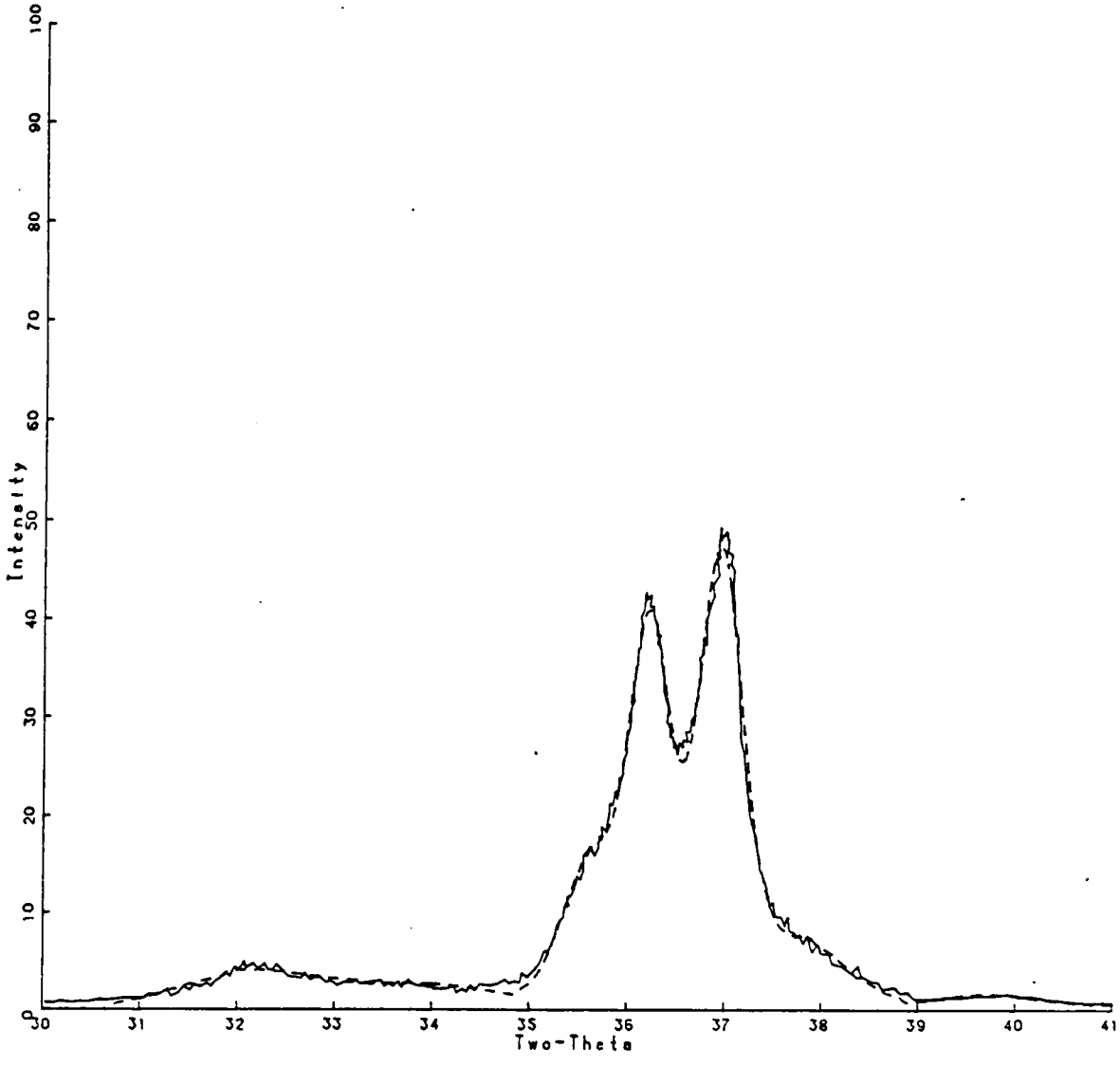

Figure A.14. Computer generated diffraction pattern curve fit for alloy 196 at -40 °C.

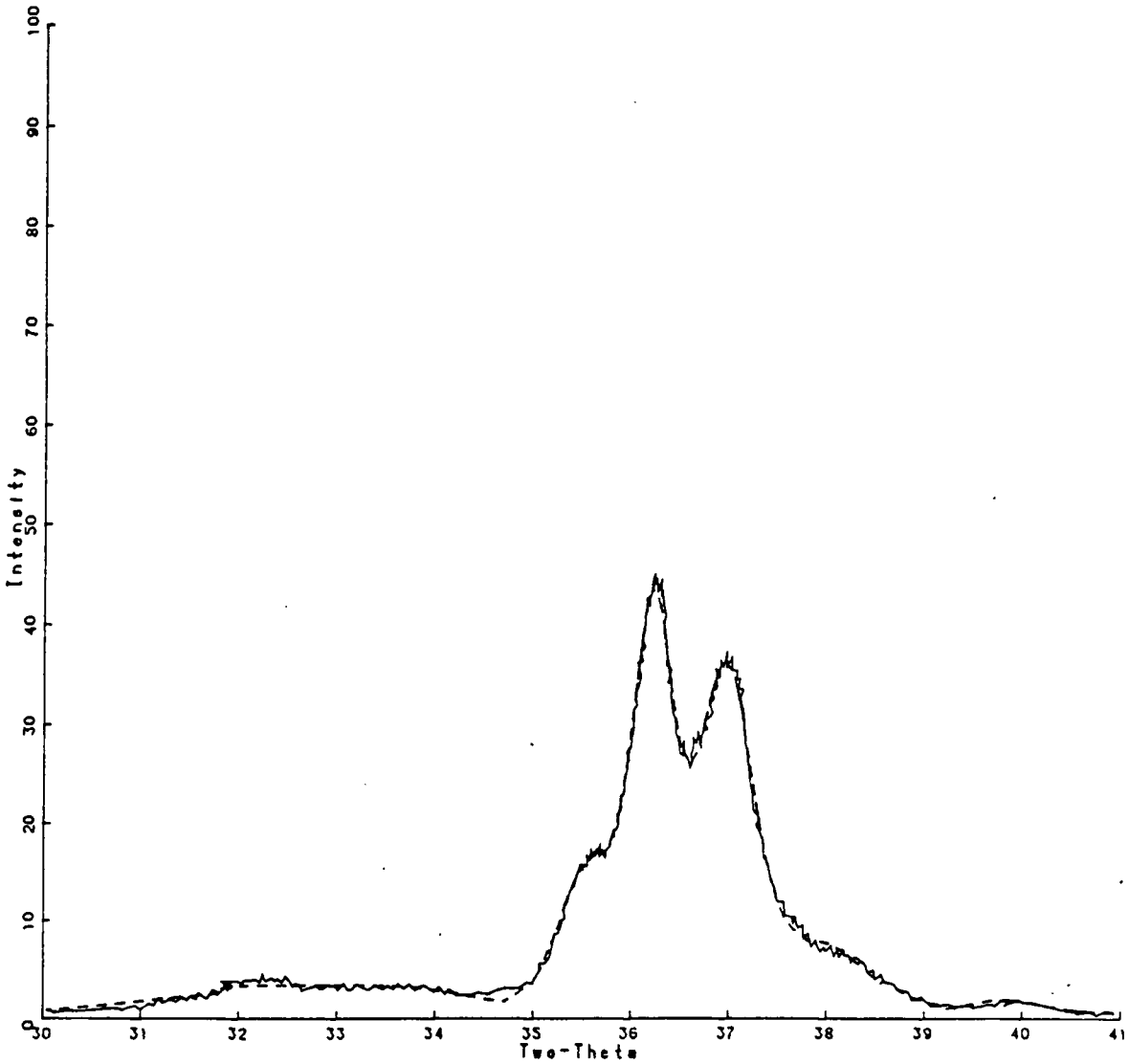

Figure A.15. Computer generated diffraction pattern curve fit for alloy 196 at -80 °C.

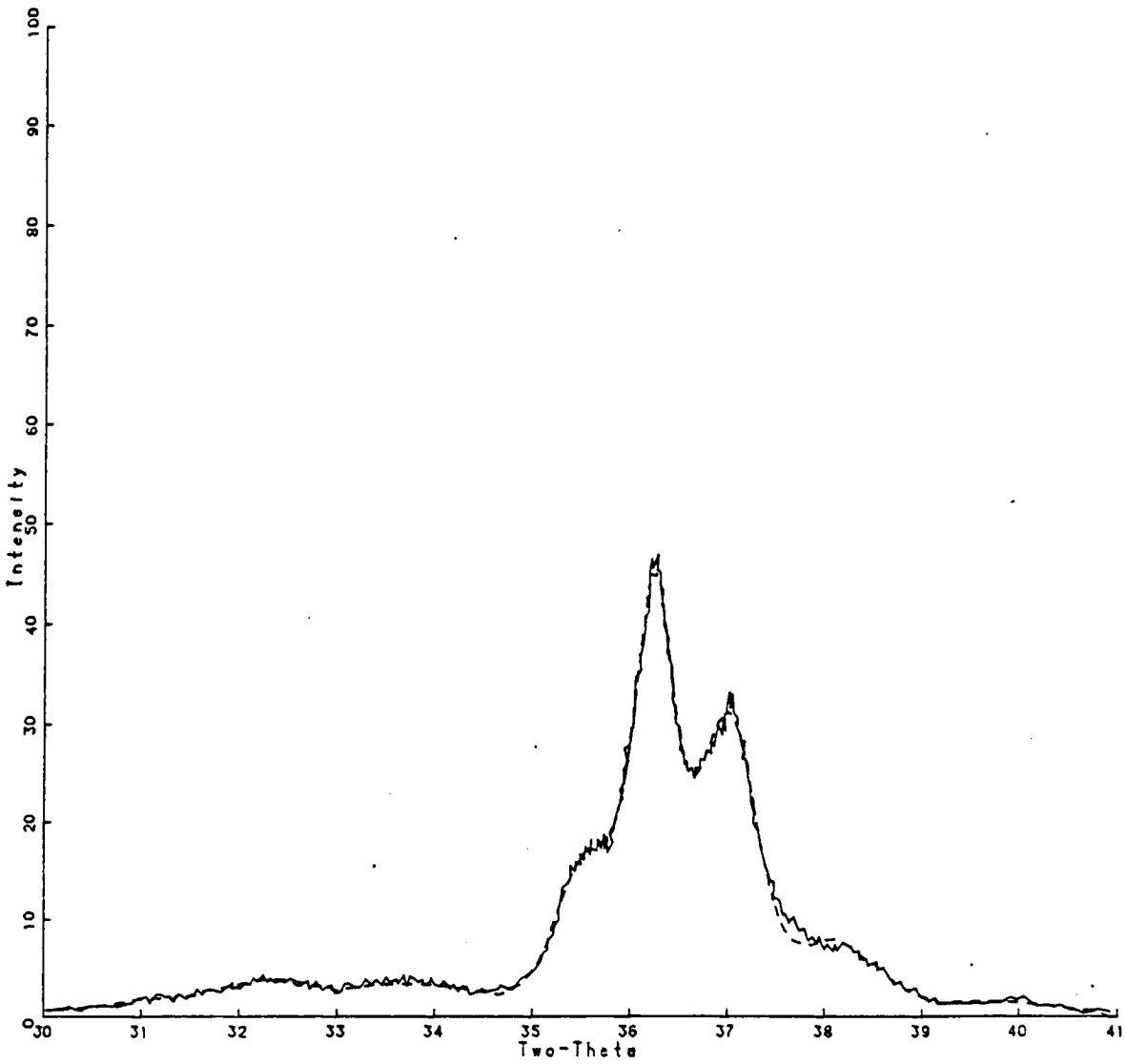

Figure A.16. Computer generated diffraction pattern curve fit for alloy 196 at -123 °C.

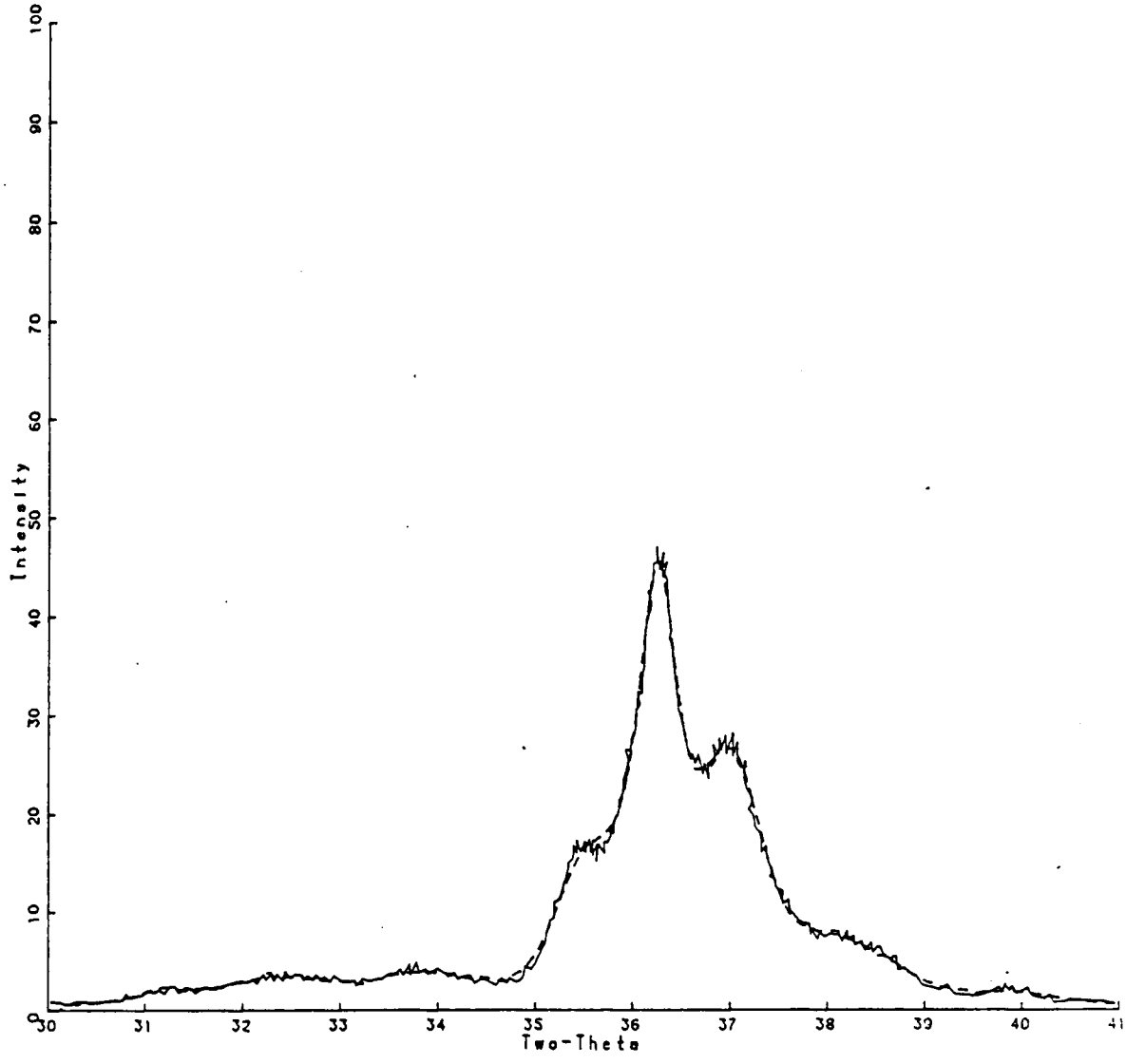

Figure A.17. Computer generated diffraction pattern curve fit for alloy 196 at -189 °C.

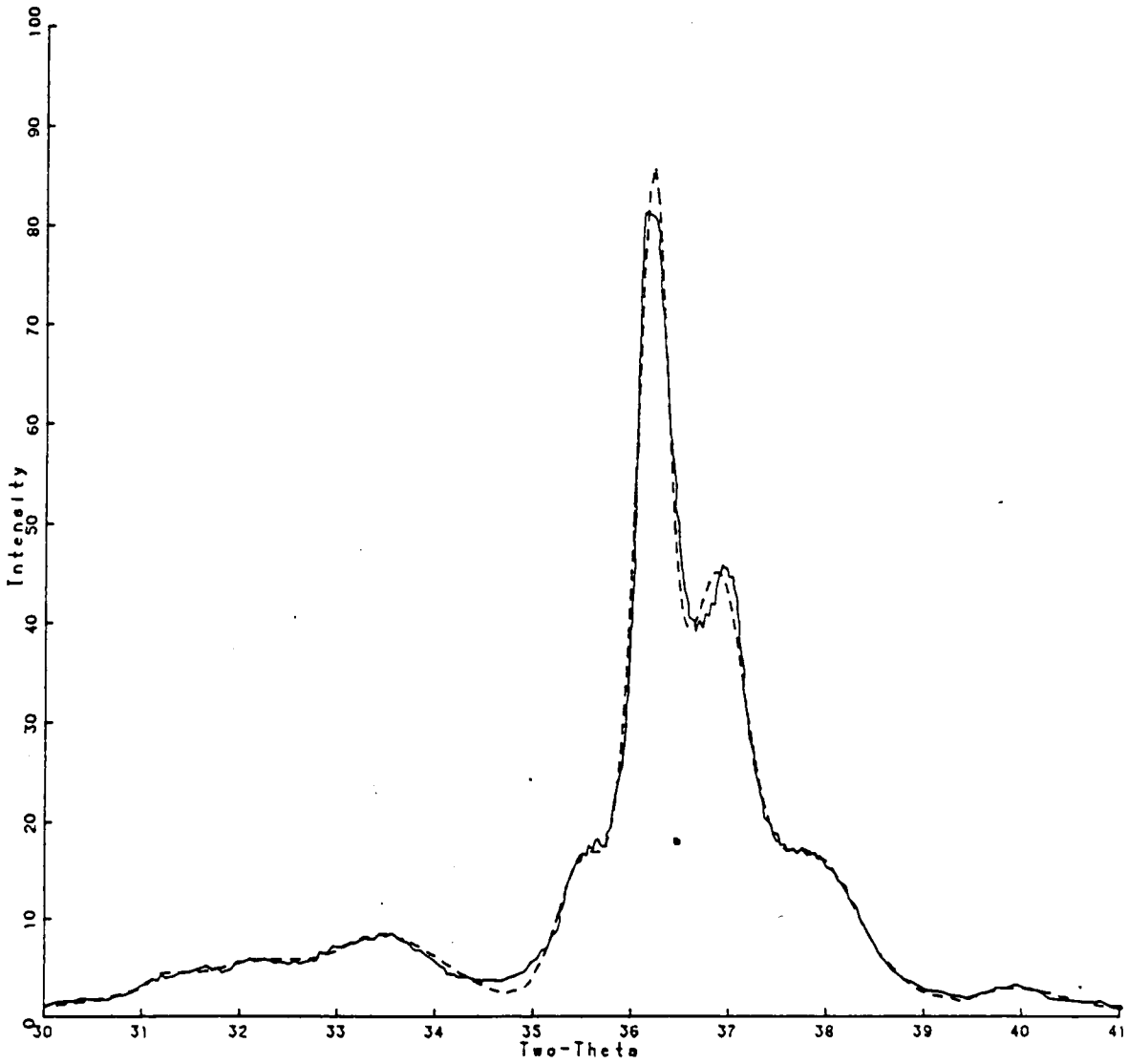

Figure A.18. Computer generated diffraction pattern curve fit for alloy 142, after optimization, at +22 °C.

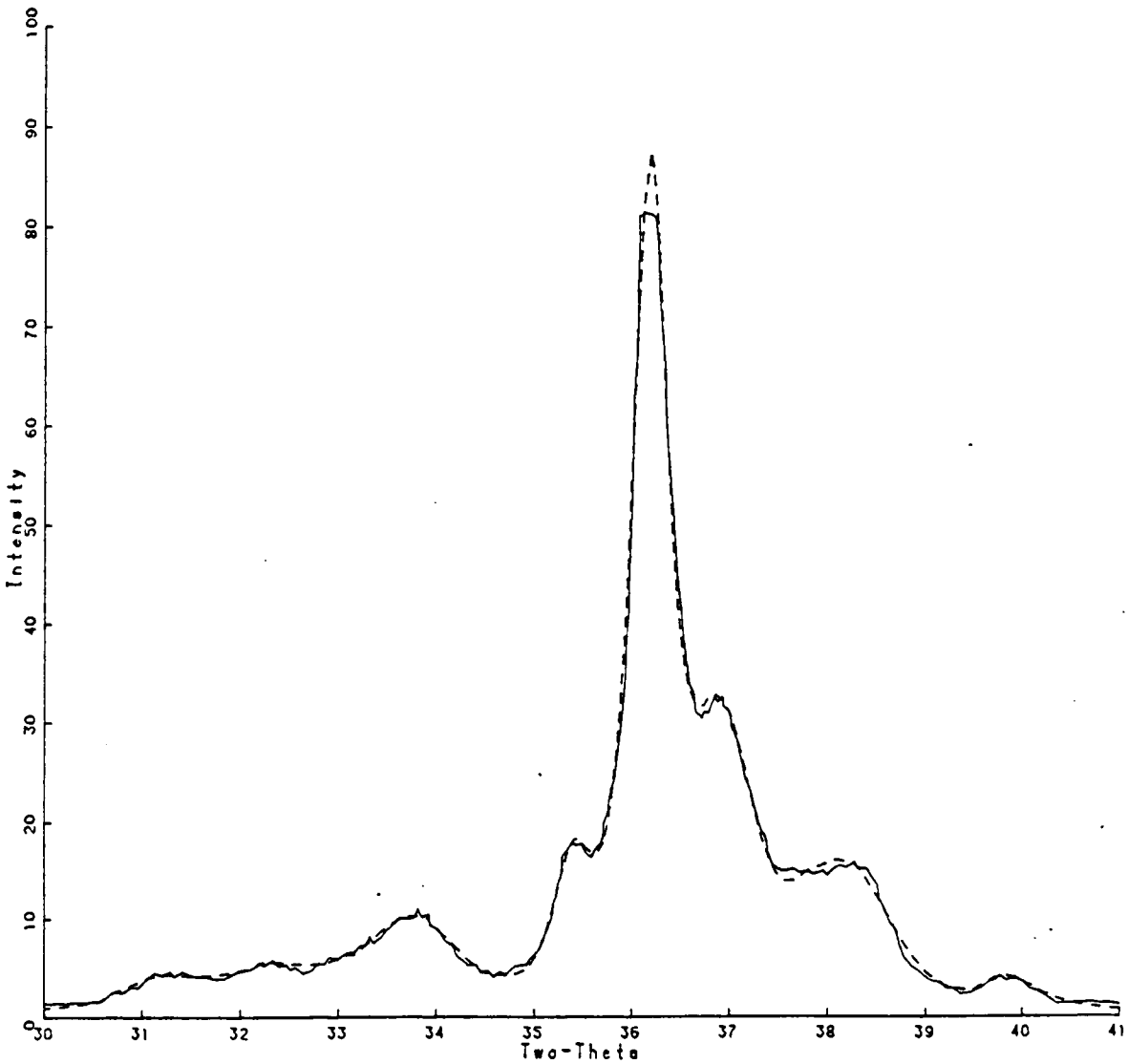

Figure A.19. Computer generated diffraction pattern curve fit for alloy 142, after optimization, at -40 °C.

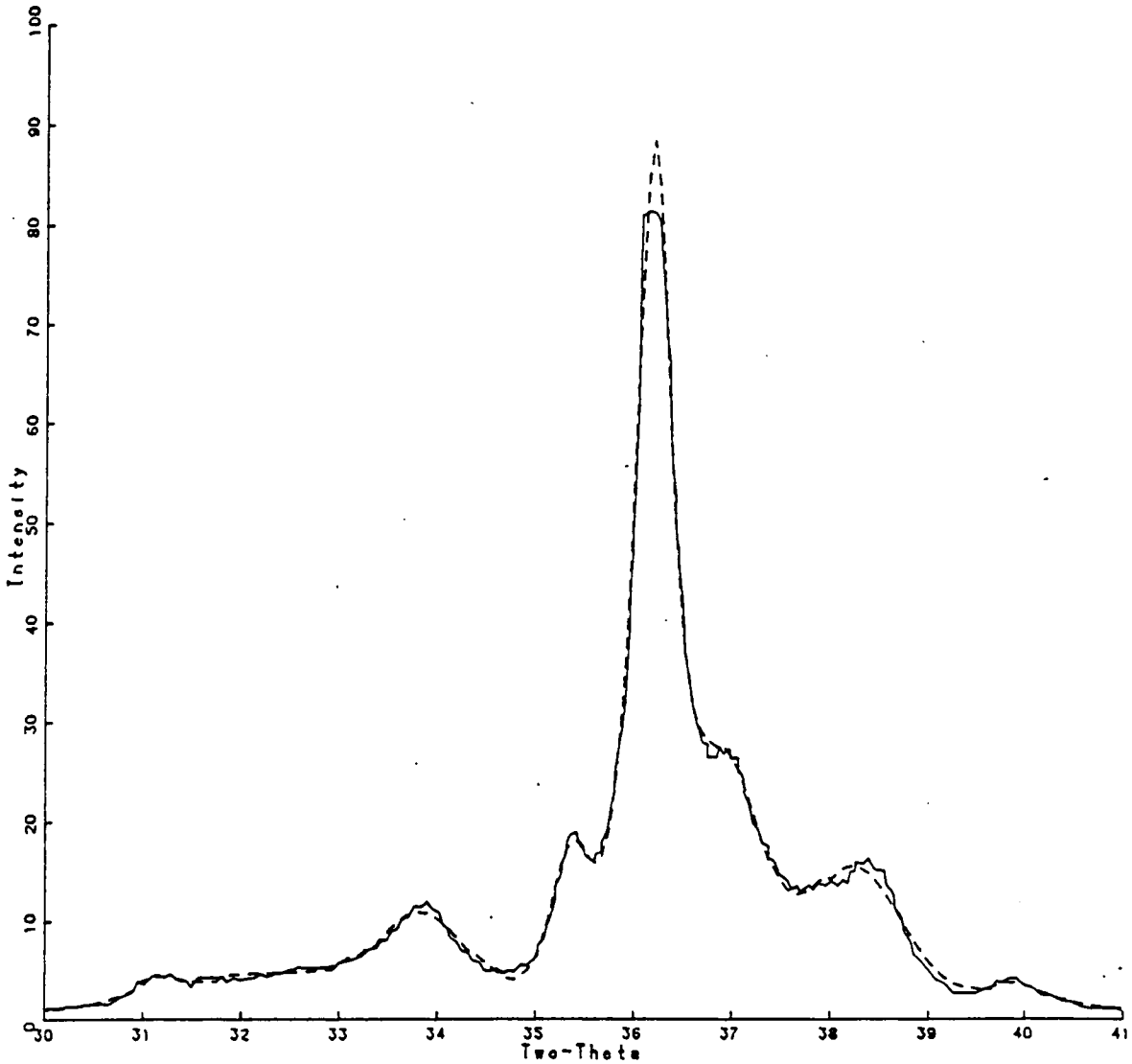

Figure A.20. Computer generated diffraction pattern curve fit for alloy 142, after optimization, at -80 °C.

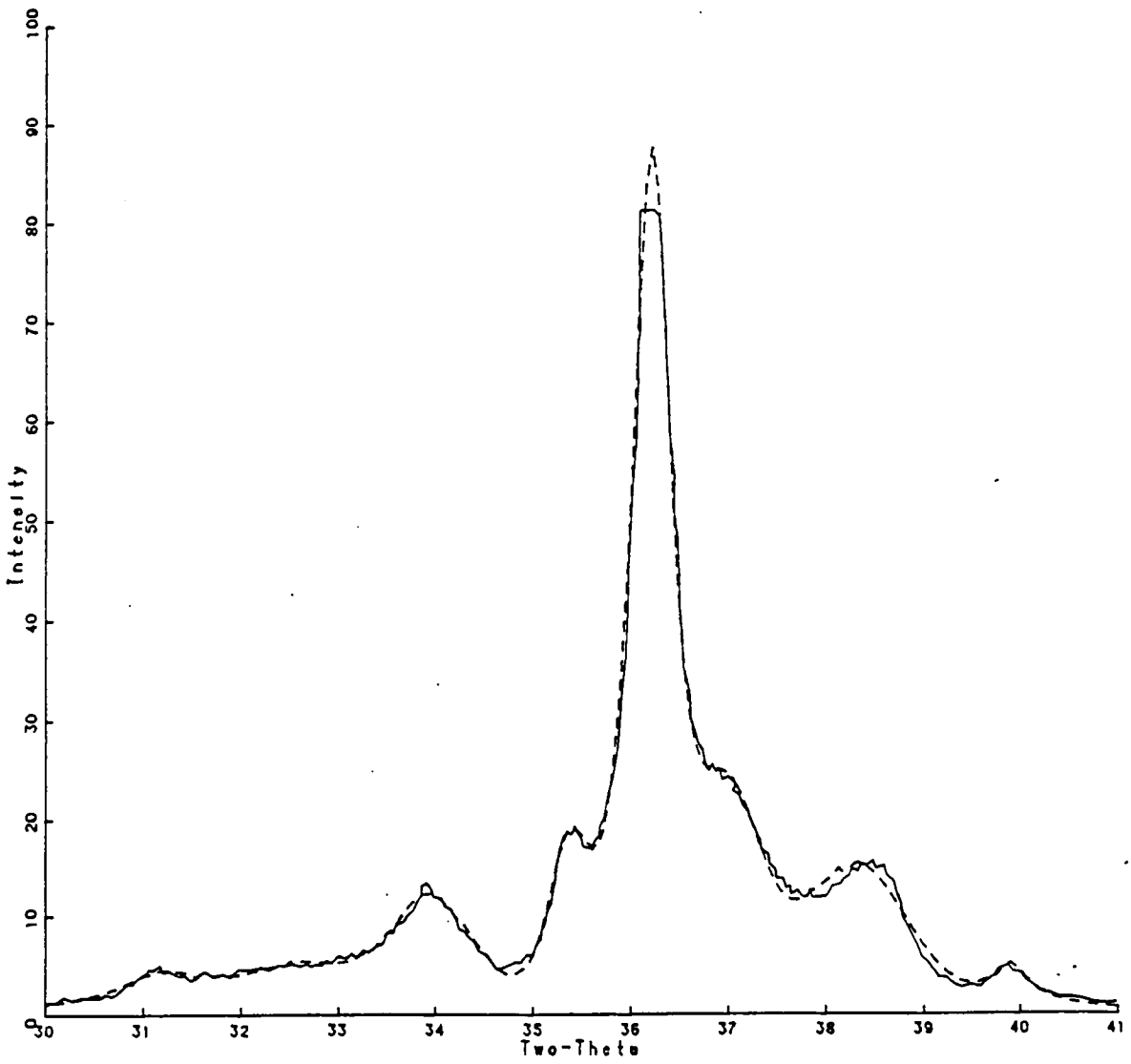

Figure A.21. Computer generated diffraction pattern curve fit for alloy 142, after optimization, at -120 °C.

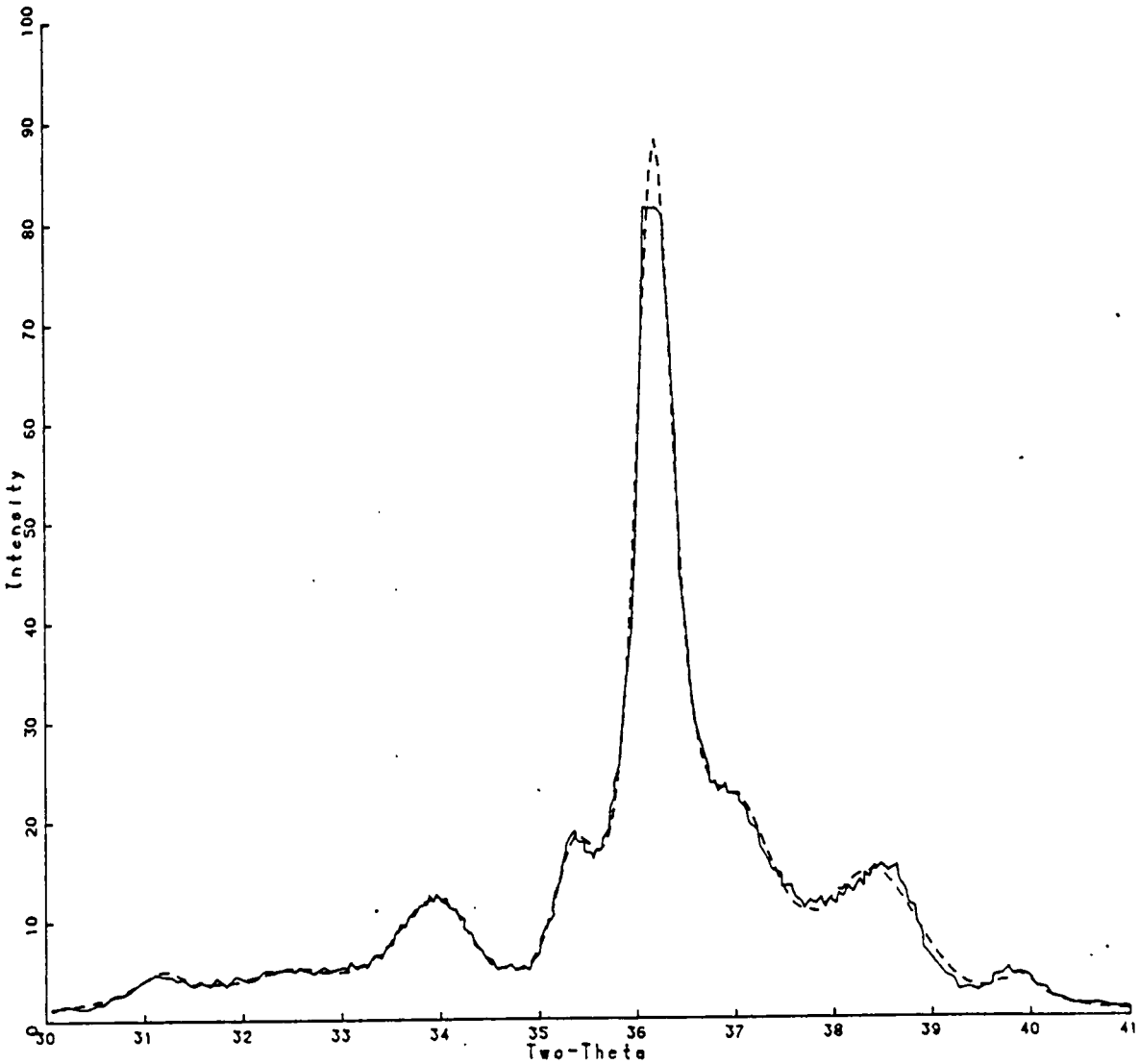

Figure A.22. Computer generated diffraction pattern curve fit for alloy 142, after optimization, at -154 °C.

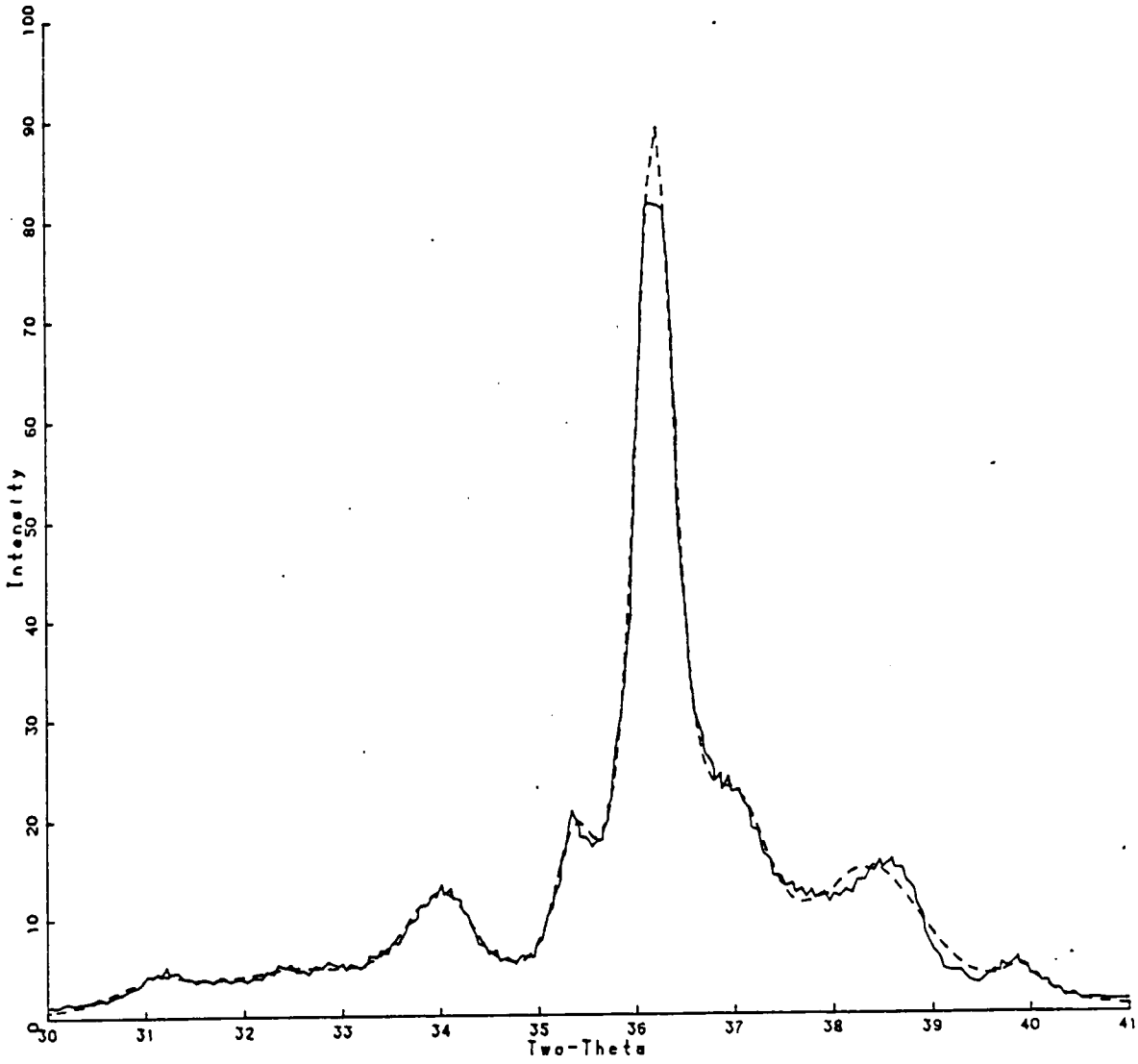

Figure A.23. Computer generated diffraction pattern curve fit for alloy 142, after optimization, at -187 °C.

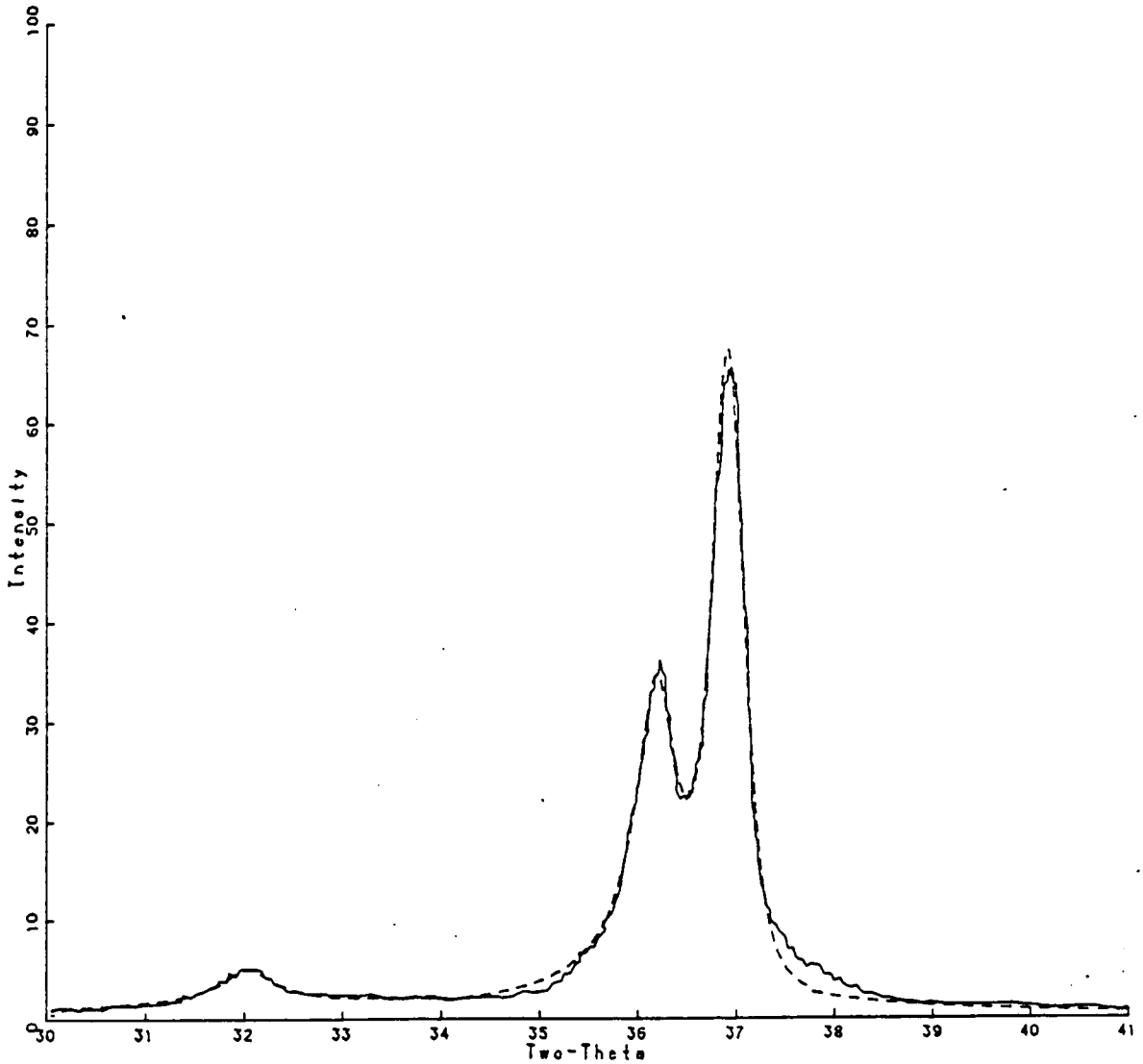

Figure A.24. Computer generated diffraction pattern curve fit for alloy 183, after optimization, at +22 °C.

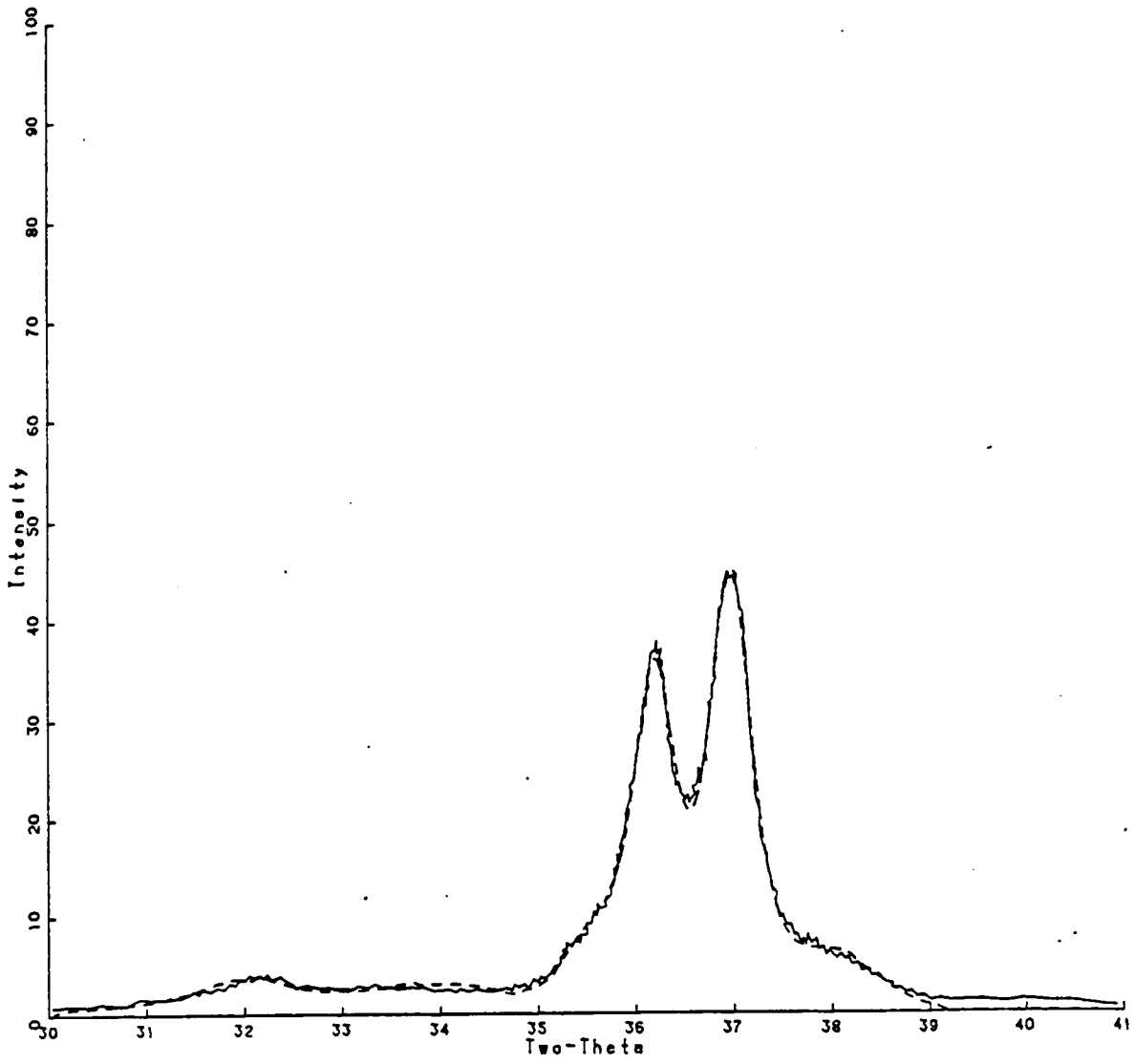

Figure A.25. Computer generated diffraction pattern curve fit for alloy 183, after optimization, at -40 °C.

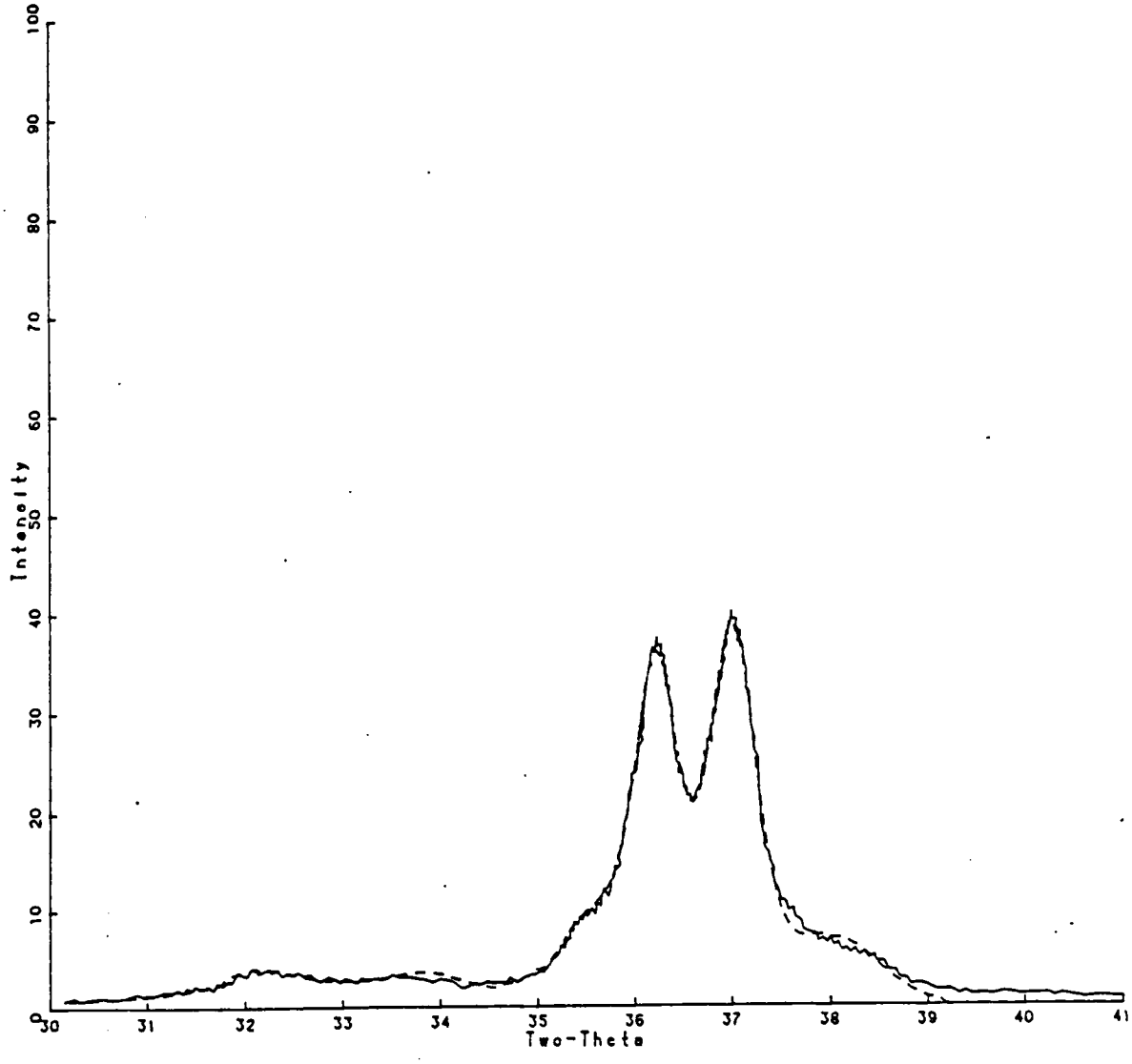

Figure A.26. Computer generated diffraction pattern curve fit for alloy 183, after optimization, at -81 °C.

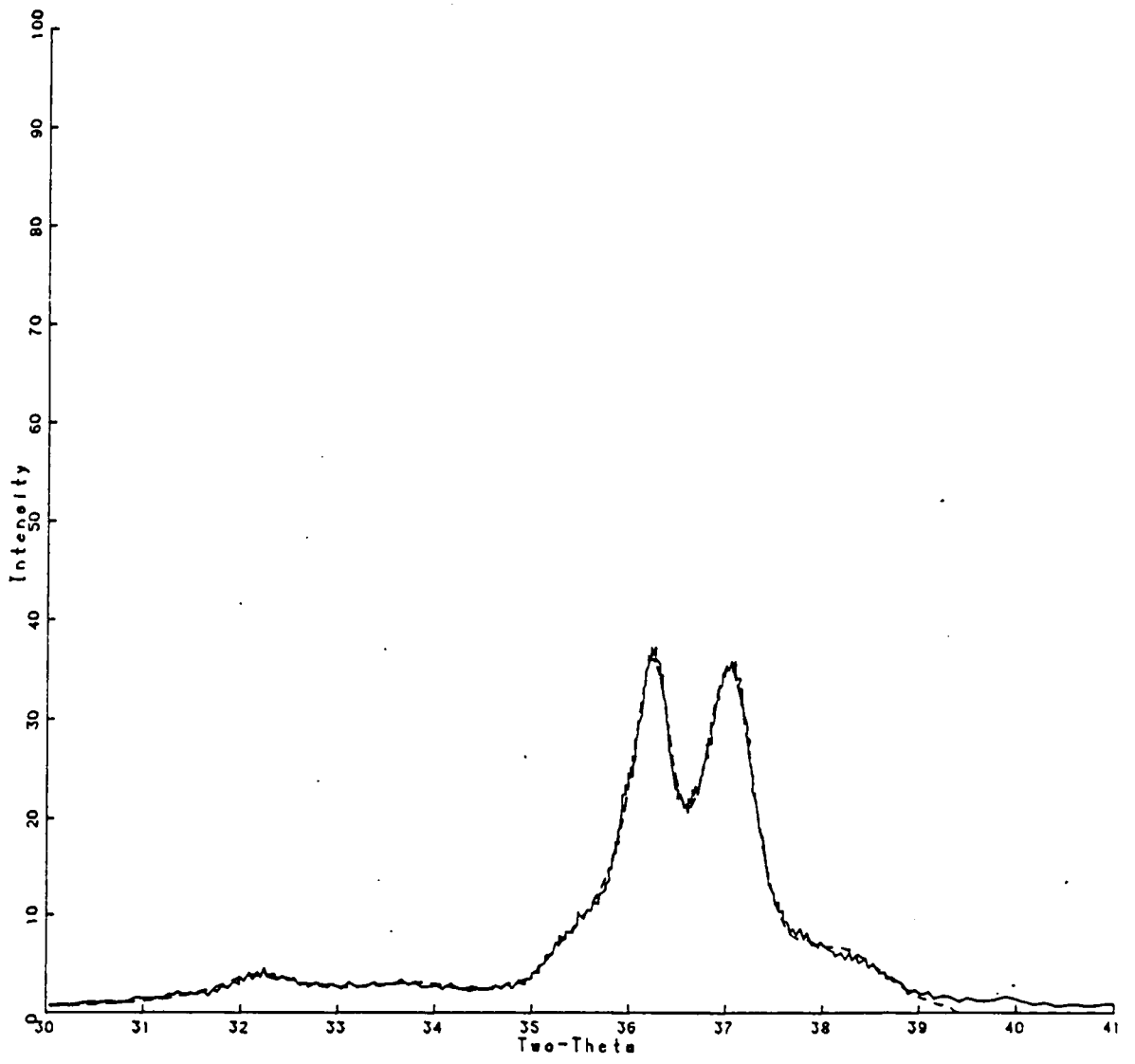

Figure A.27. Computer generated diffraction pattern curve fit for alloy 183, after optimization, at -121 °C.

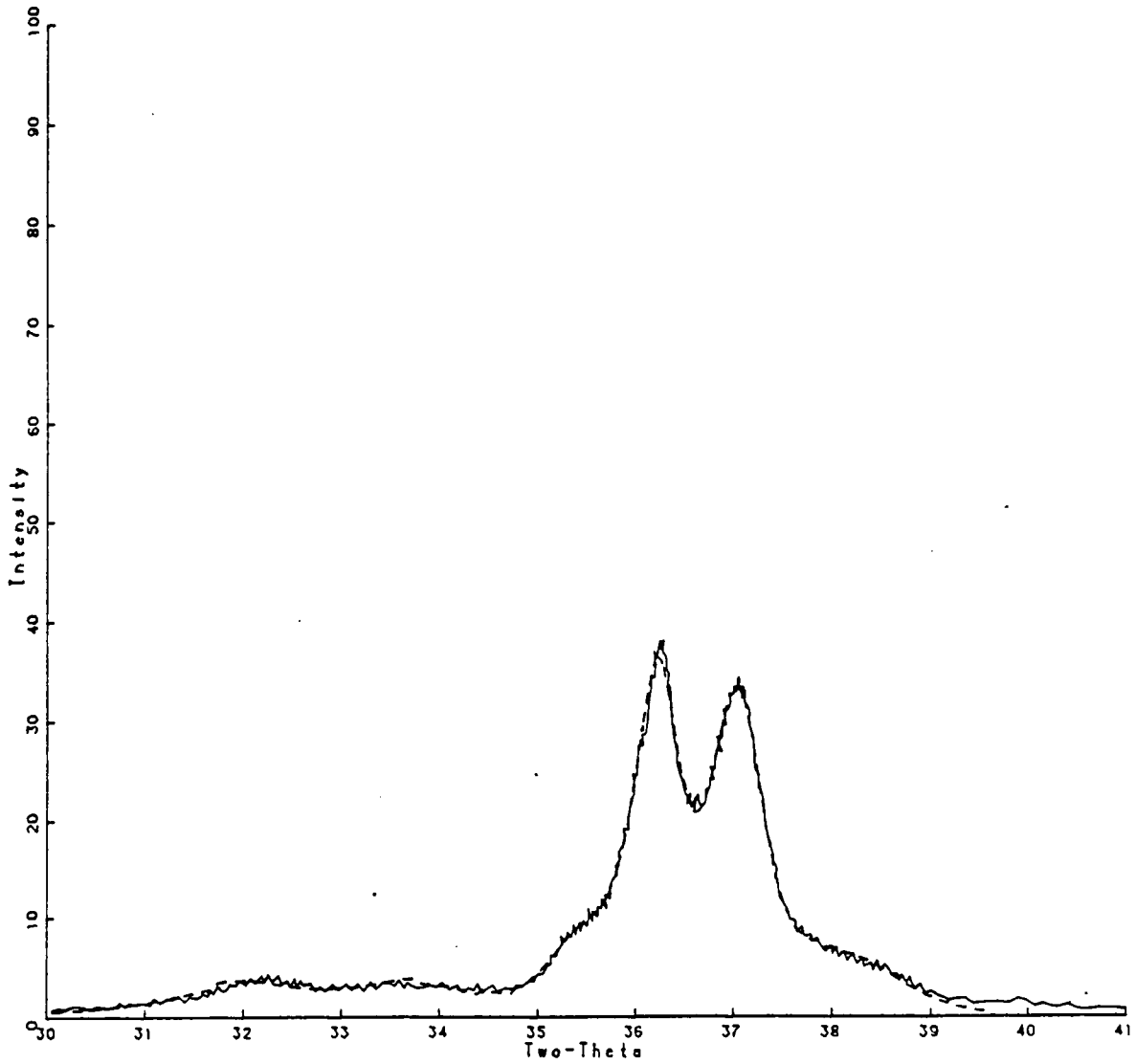

Figure A.28. Computer generated diffraction pattern curve fit for alloy 183, after optimization, at -161 °C.

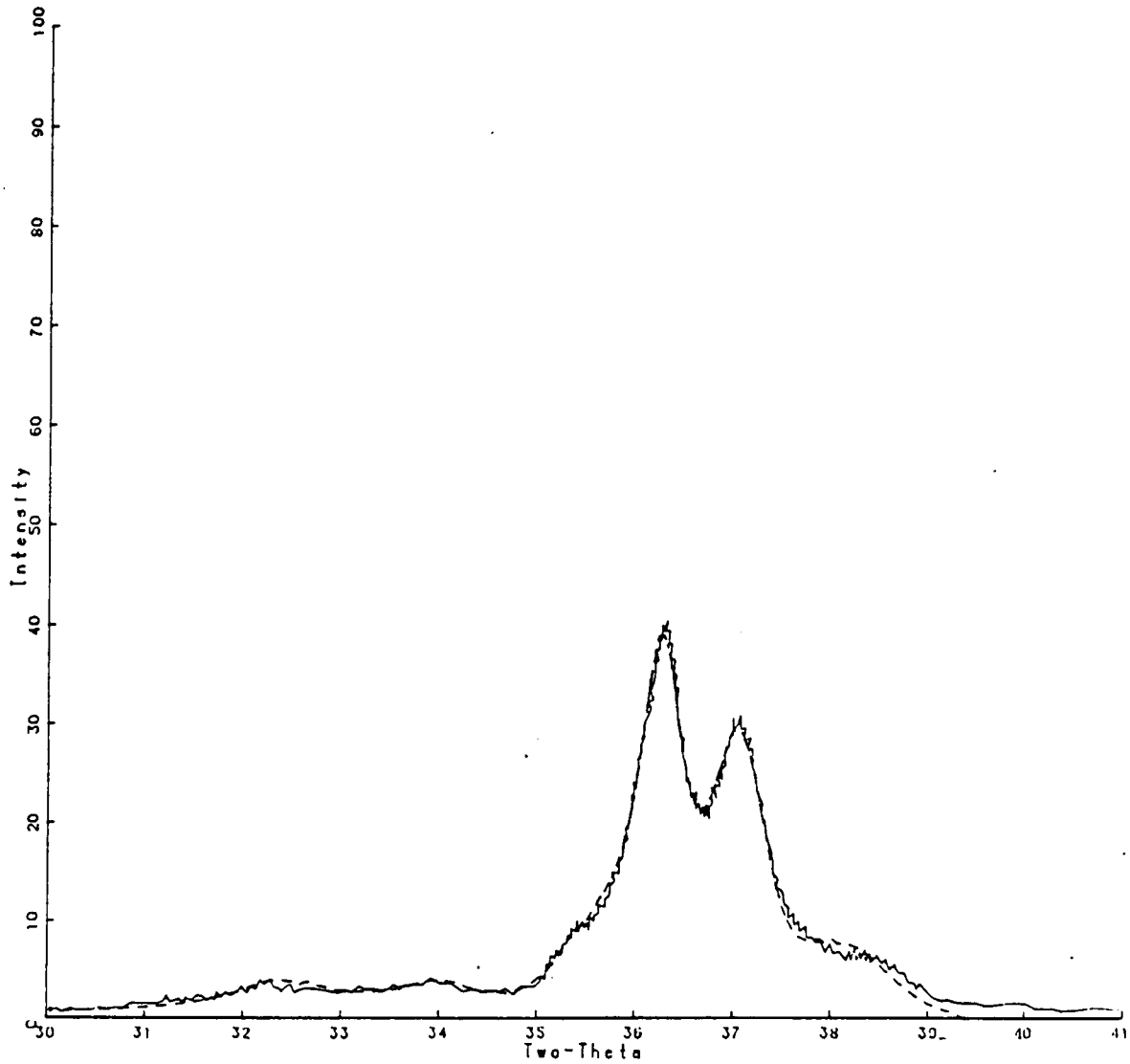

Figure A.29. Computer generated diffraction pattern curve fit for alloy 183, after optimization, at -190 °C.

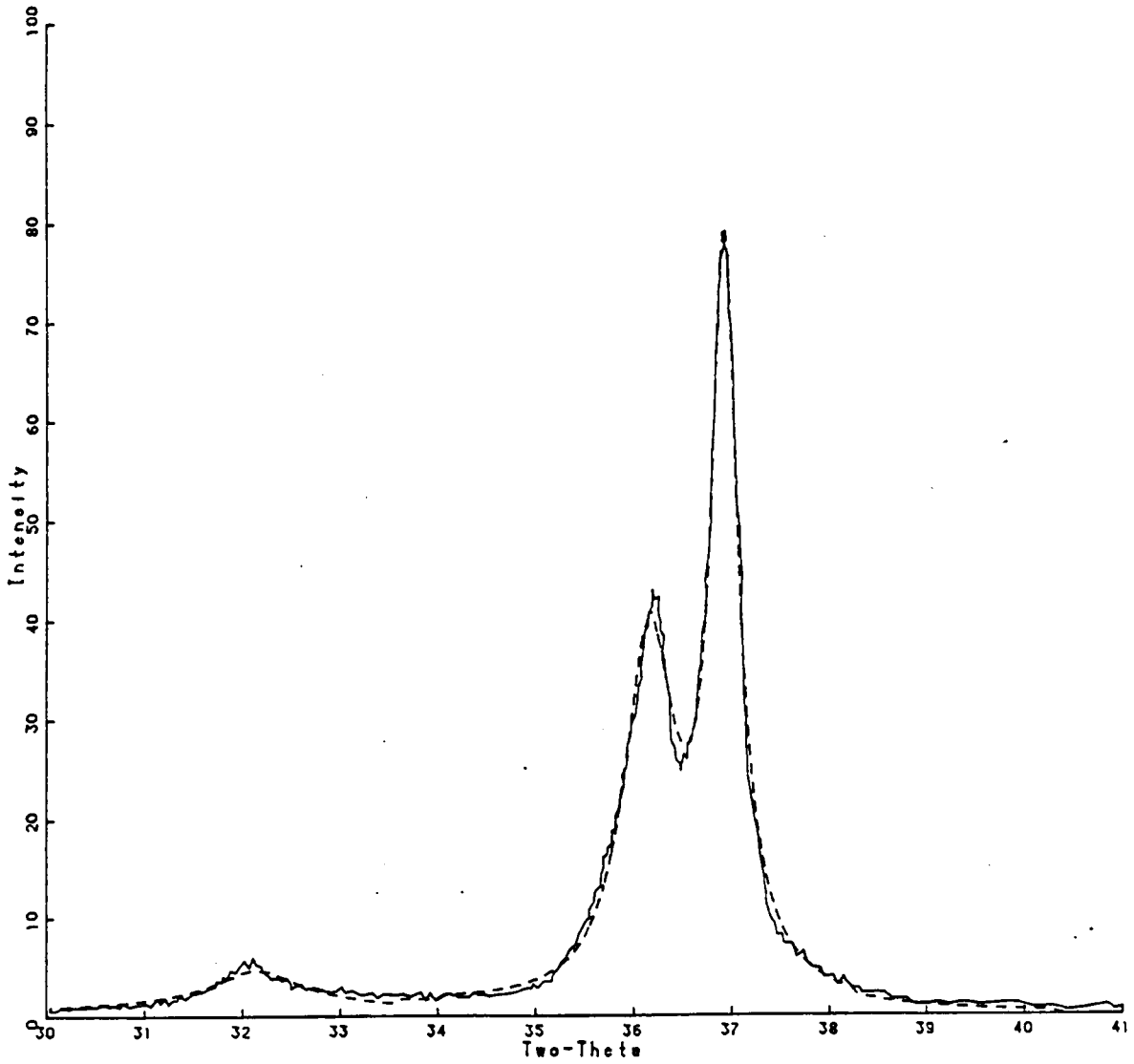

Figure A.30. Computer generated diffraction pattern curve fit for alloy 196, after optimization, at +25 °C.

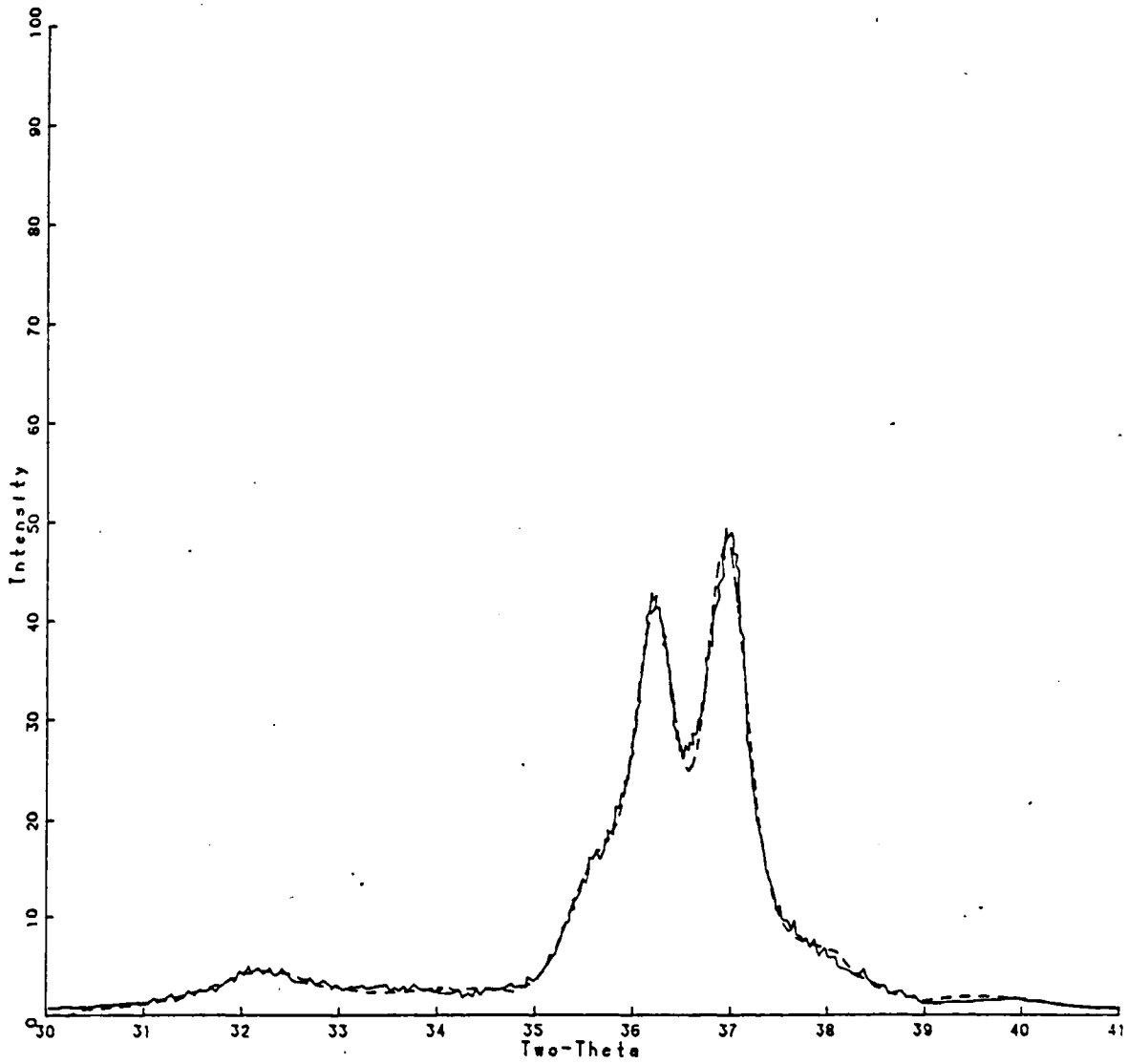

Figure A.31. Computer generated diffraction pattern curve fit for alloy 196, after optimization, at -40 °C.

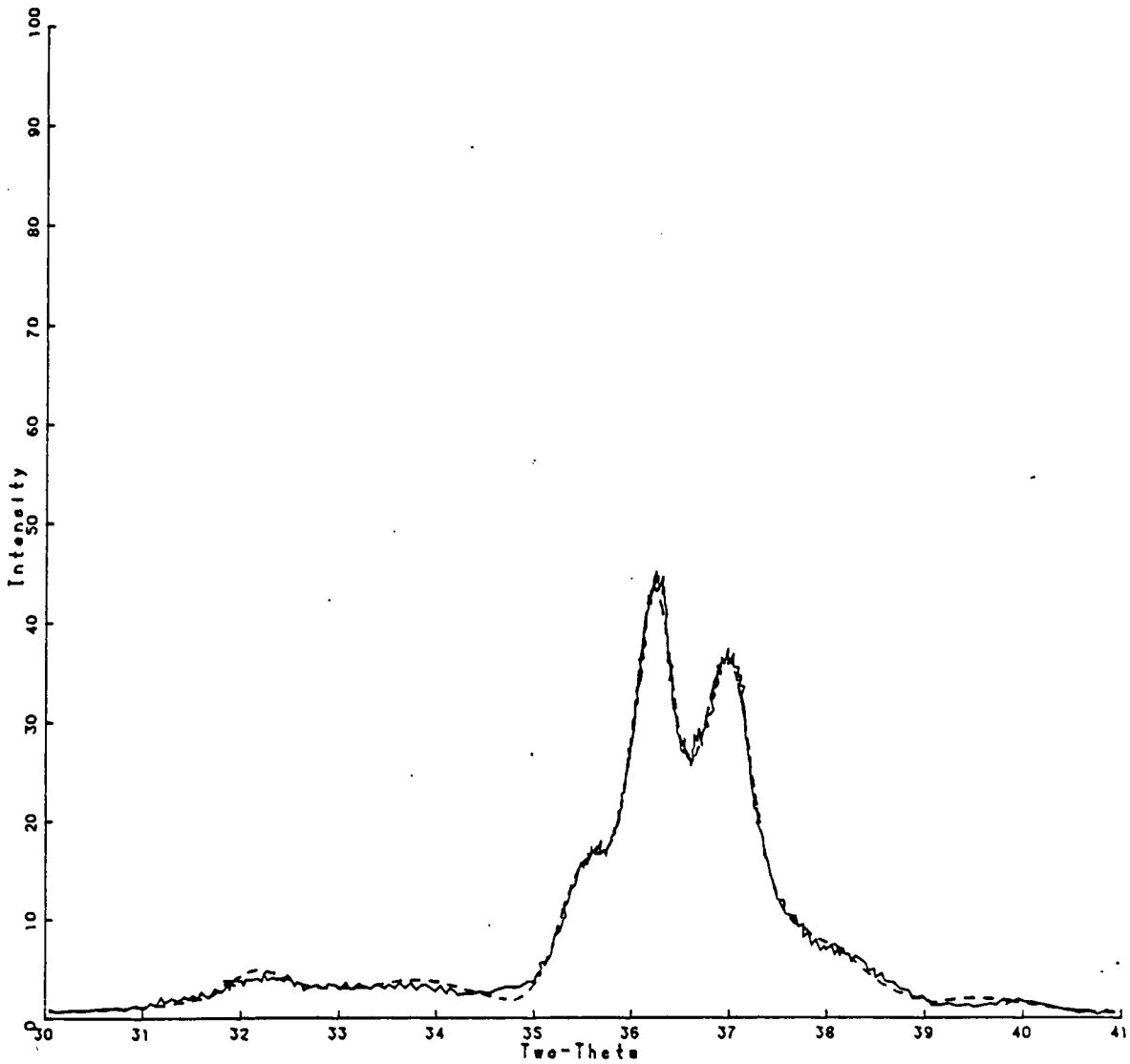

Figure A.32. Computer generated diffraction pattern curve fit for alloy 196, after optimization, at -80 °C.

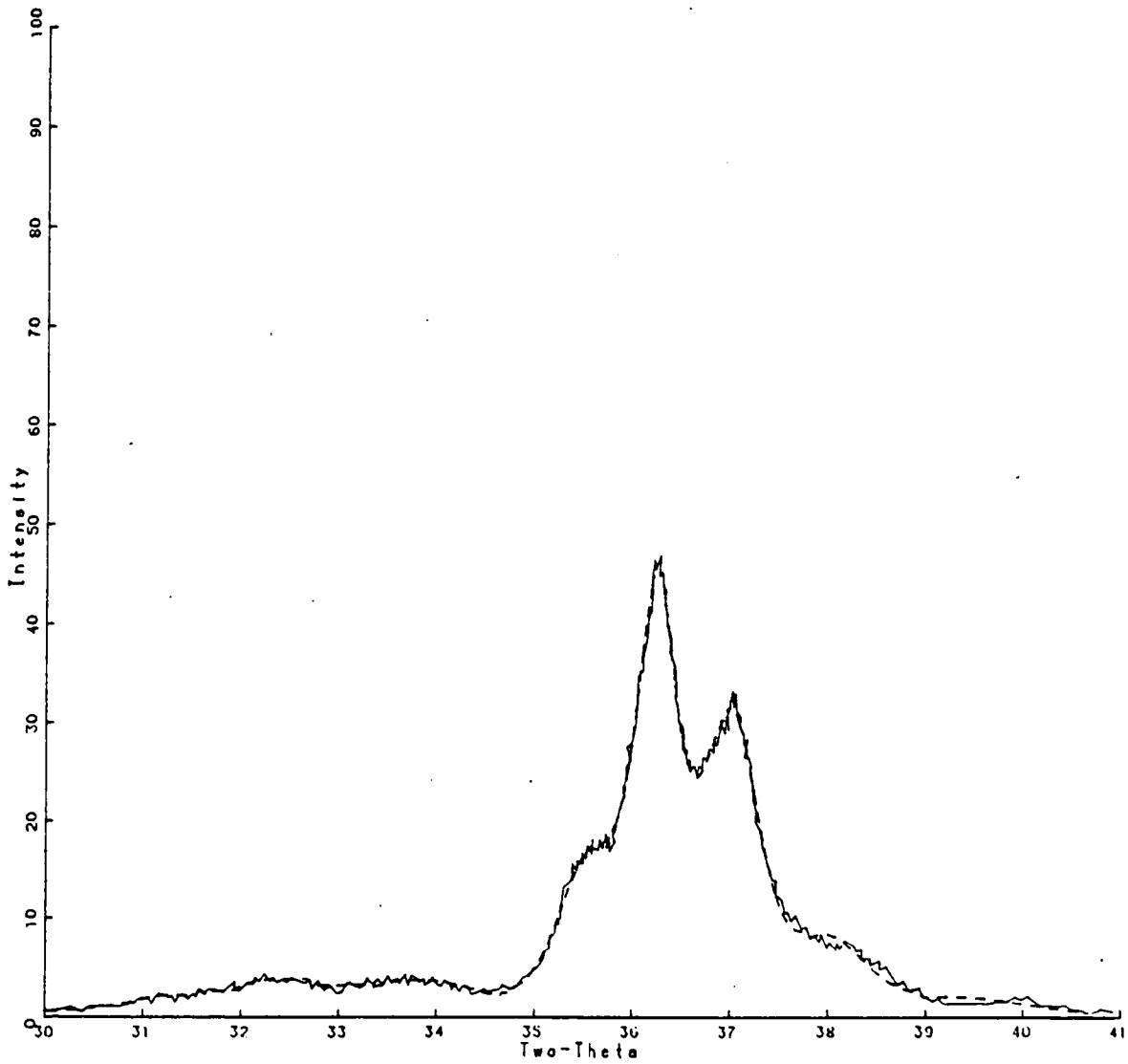

Figure A.33. Computer generated diffraction pattern curve fit for alloy 196, after optimization, at -123 °C.

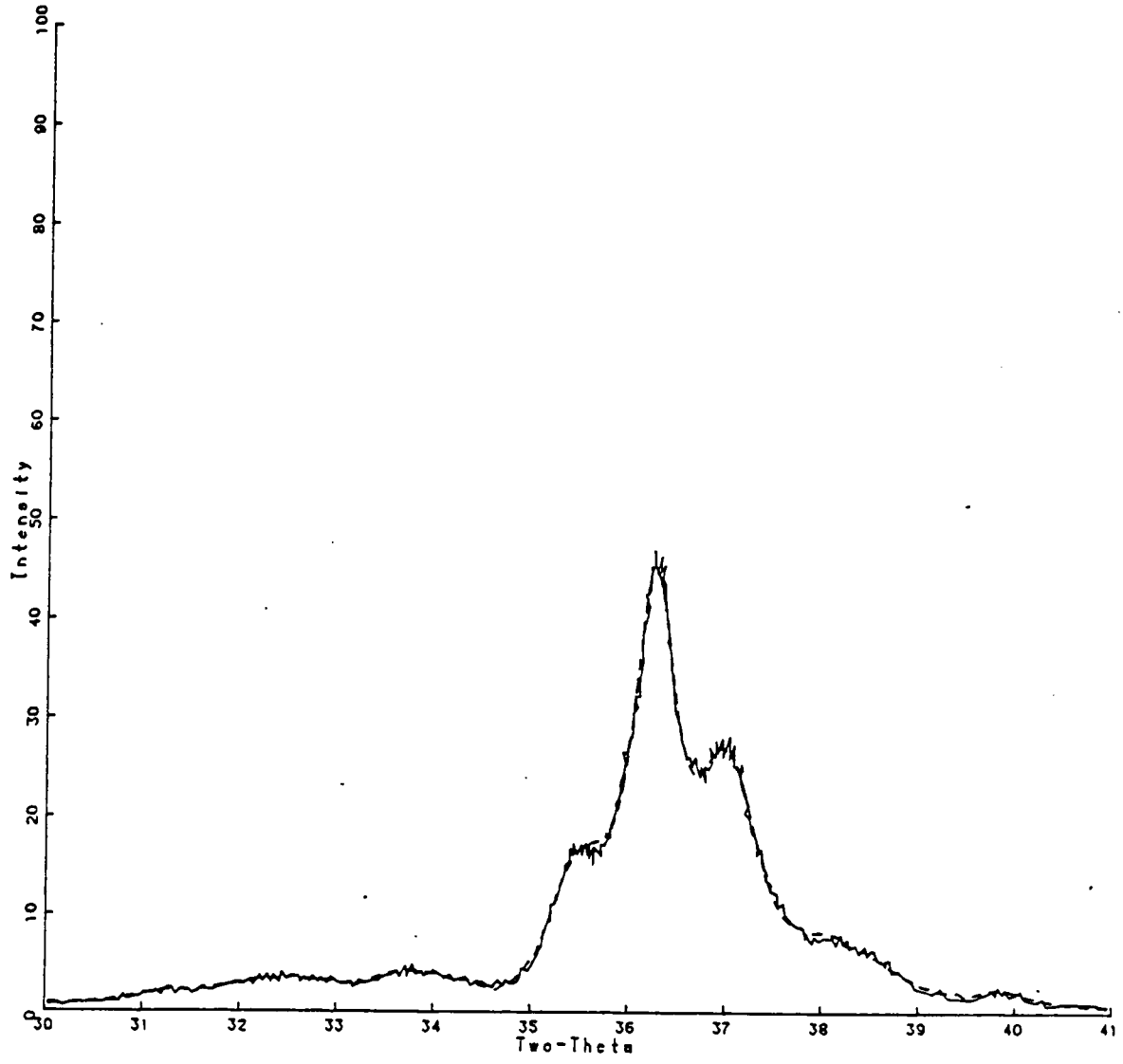

Figure A.34. Computer generated diffraction pattern curve fit for alloy 196, after optimization, at -189 °C.

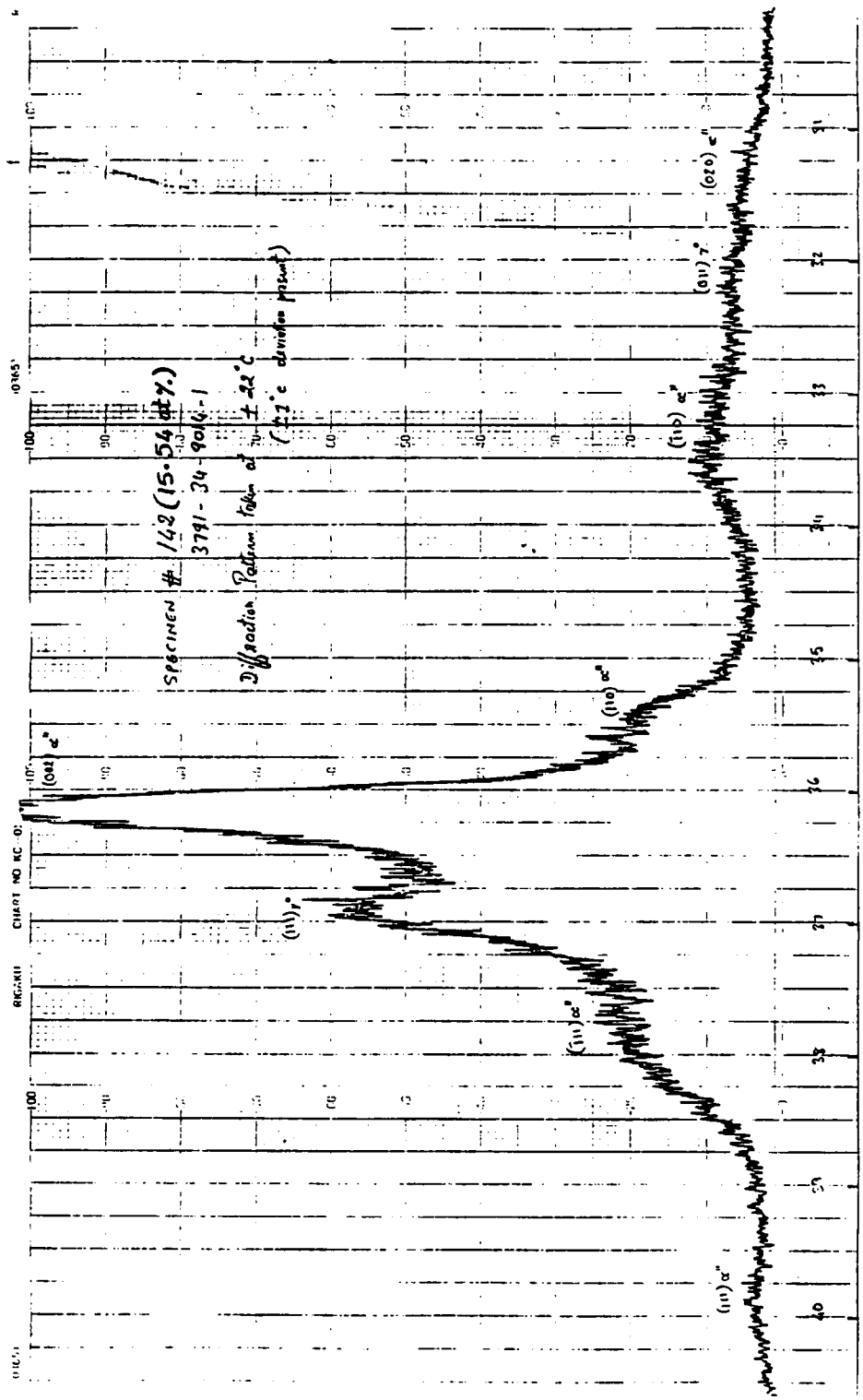

Figure A.35. Diffraction pattern of alloy 142 (15.0 at% Nb) at +22 °C.

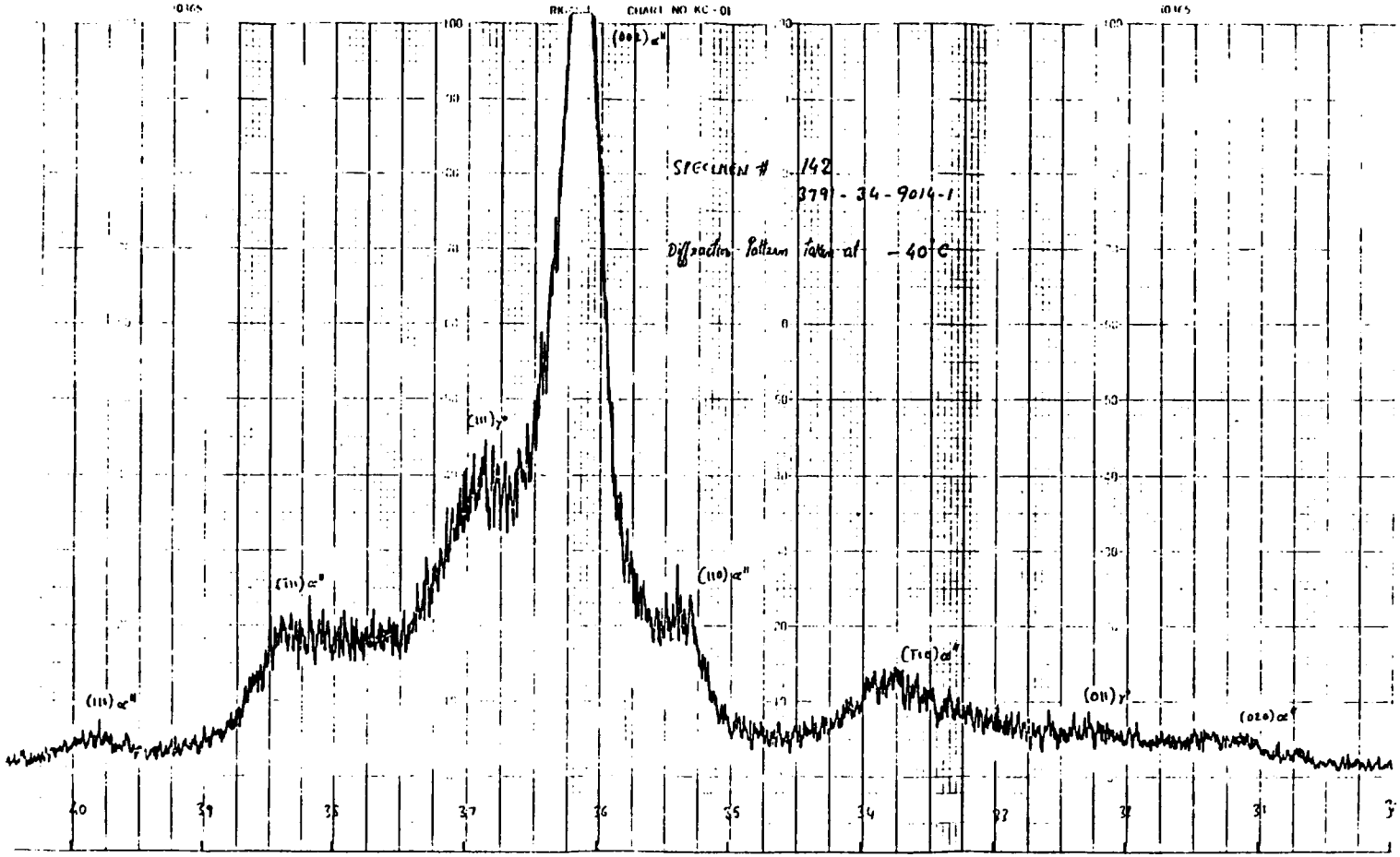

Figure A.36. Diffraction pattern of alloy 142 (15.0 at% Nb) at -40 °C.

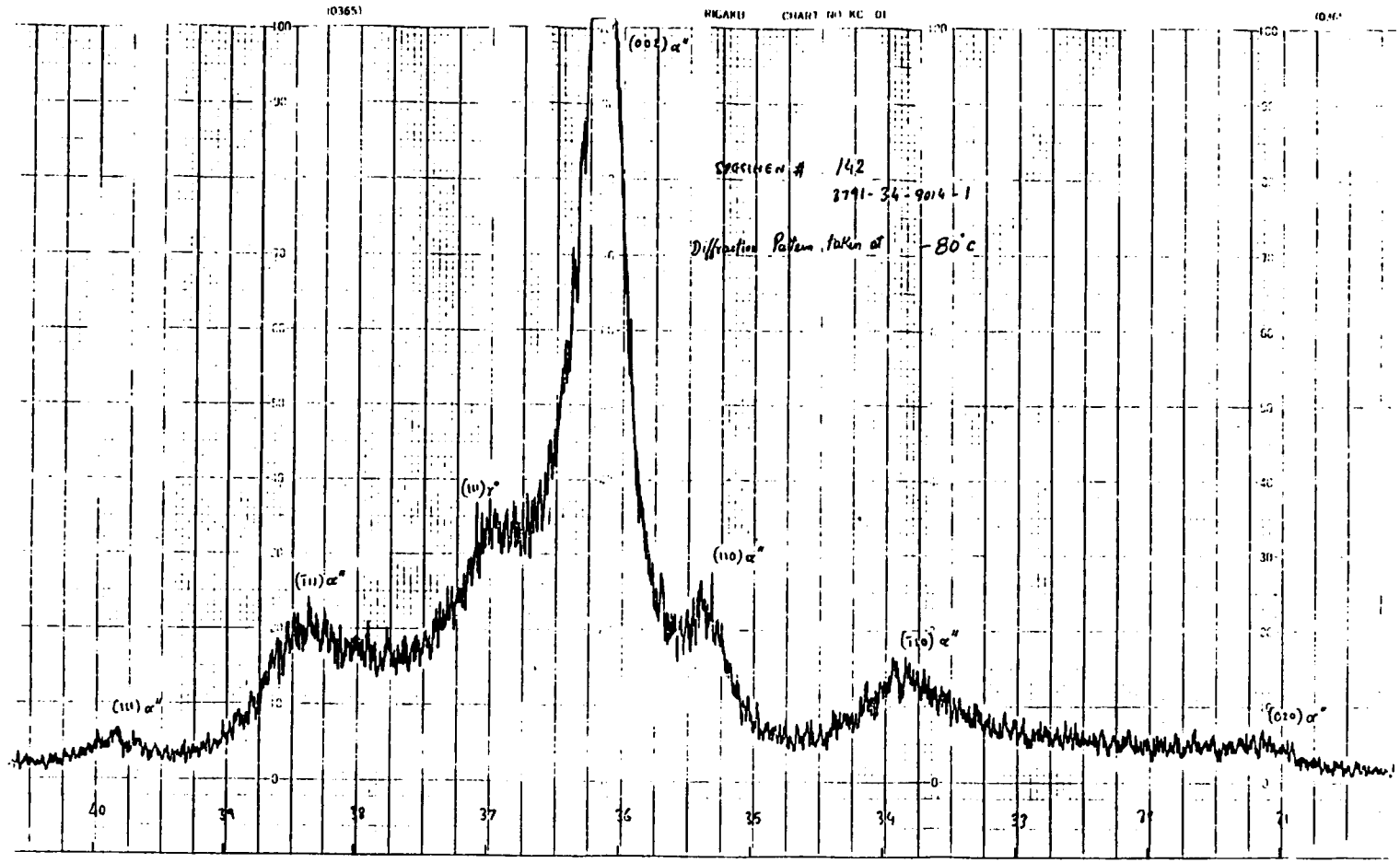

Figure A.37. Diffraction pattern of alloy 142 (15.0 at% Nb) at -80 °C.

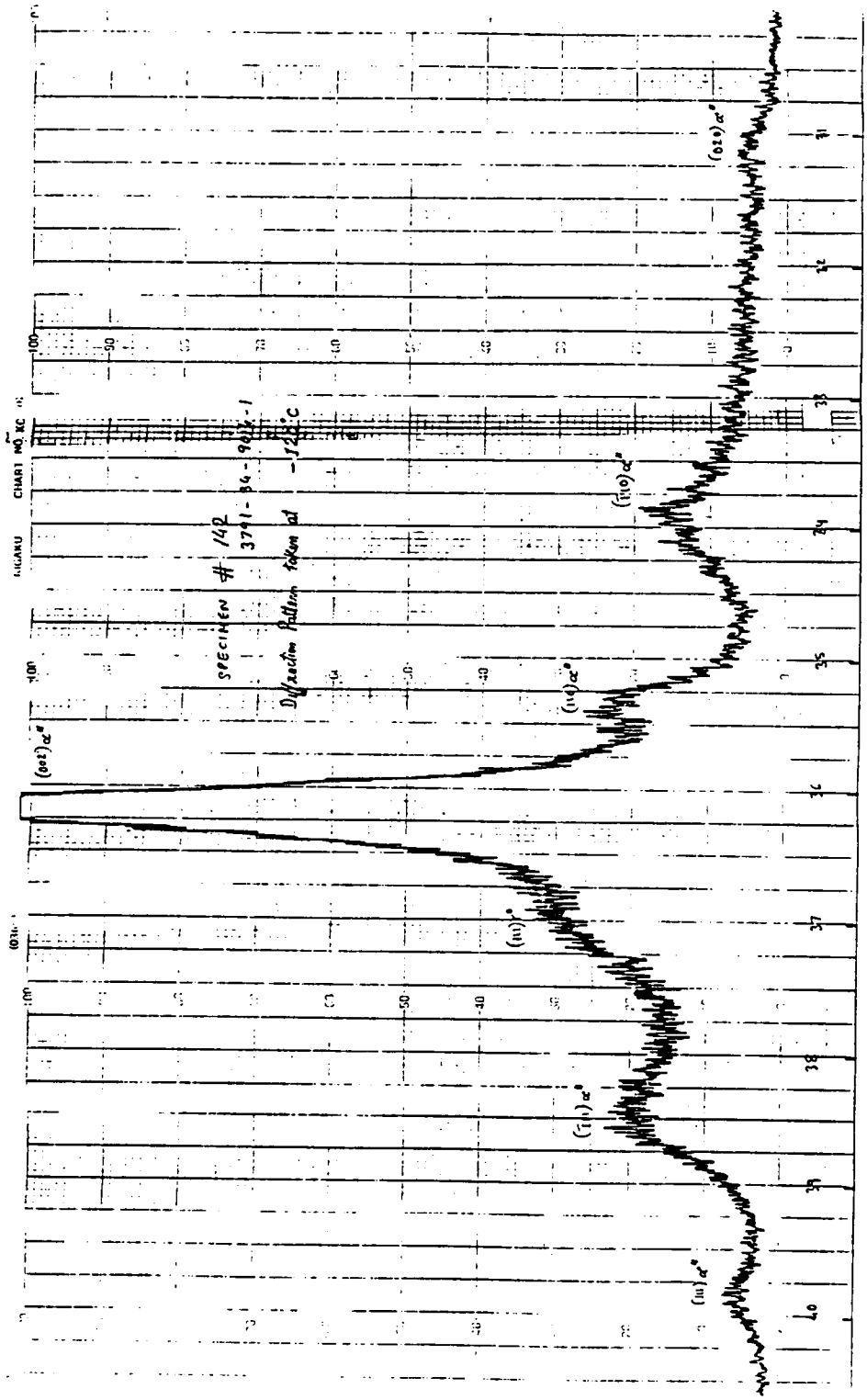

Figure A.38. Diffraction pattern of alloy 142 (15.0 at% Nb) at -120 °C.

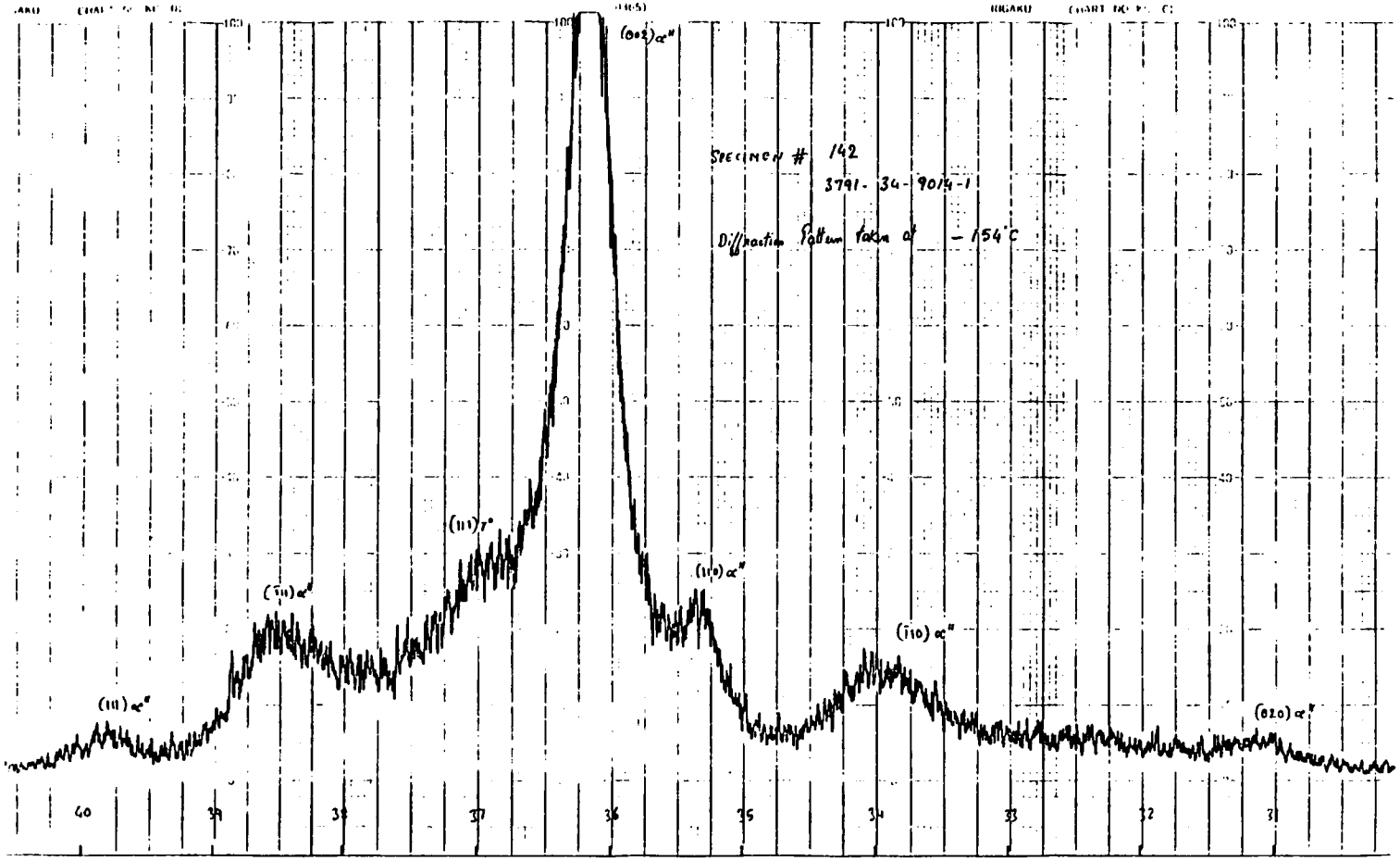

Figure A.39. Diffraction pattern of alloy 142 (15.0 at% Nb) at -154 °C.

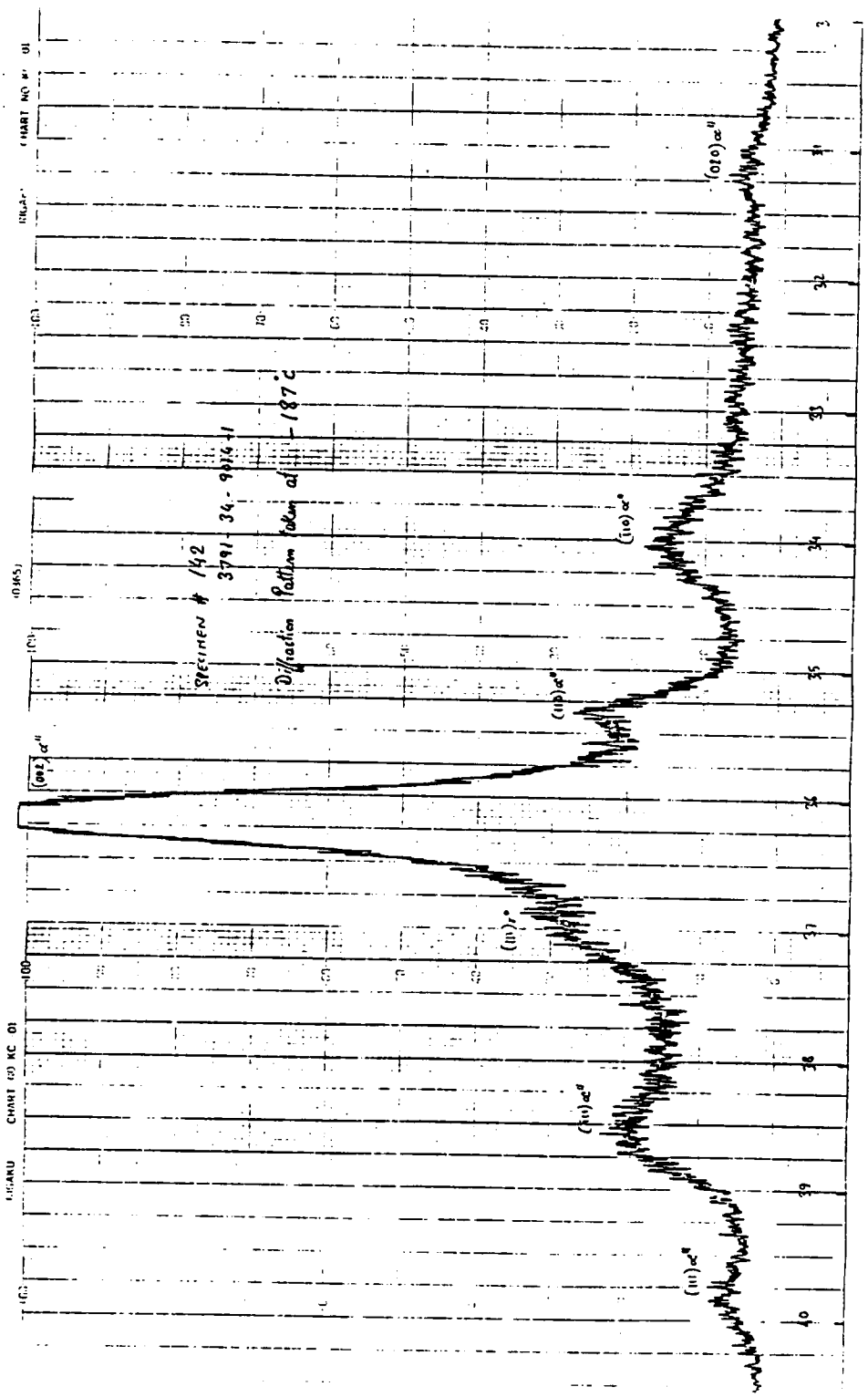

Figure A.40. Diffraction pattern of alloy 142 (15.0 at% Nb) at -187 °C.

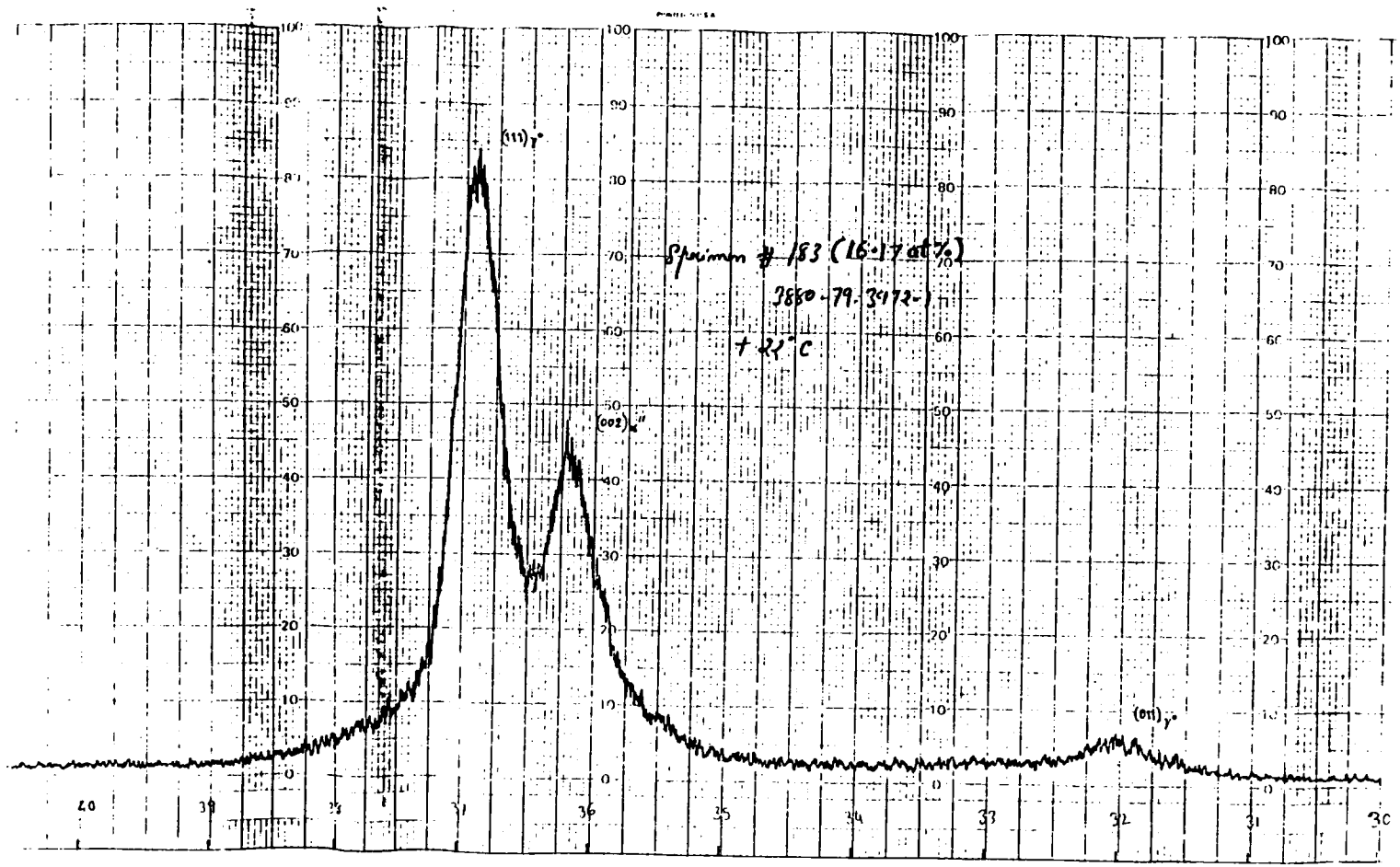

Figure A.41. Diffraction pattern of alloy 183 (15.5* at% Nb) at +22 °C.

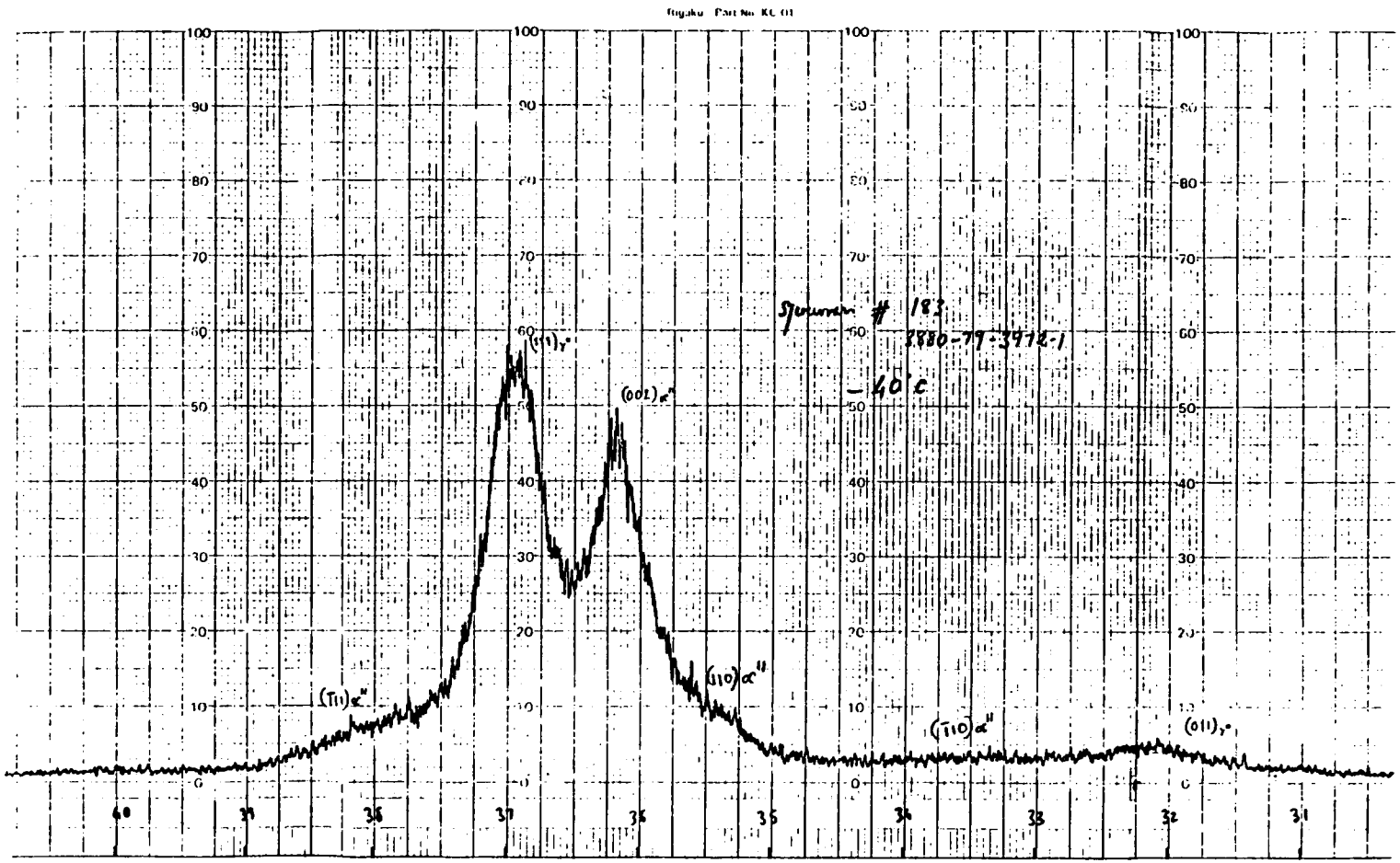

Figure A.42. Diffraction pattern of alloy 183 (15.5* at% Nb) at -40 °C.

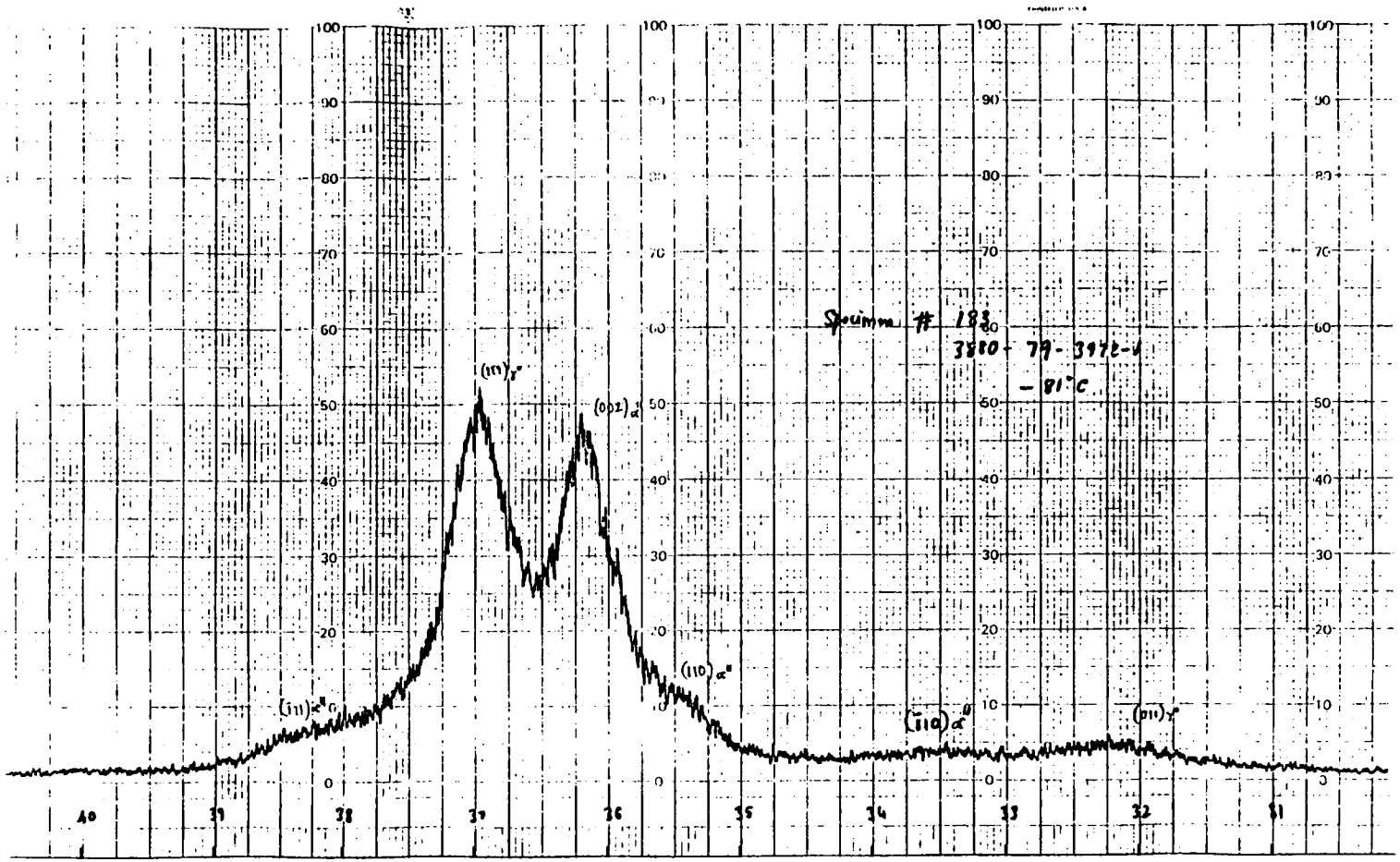

Figure A.43. Diffraction pattern of alloy 183 (15.5* at% Nb) at -81 °C.

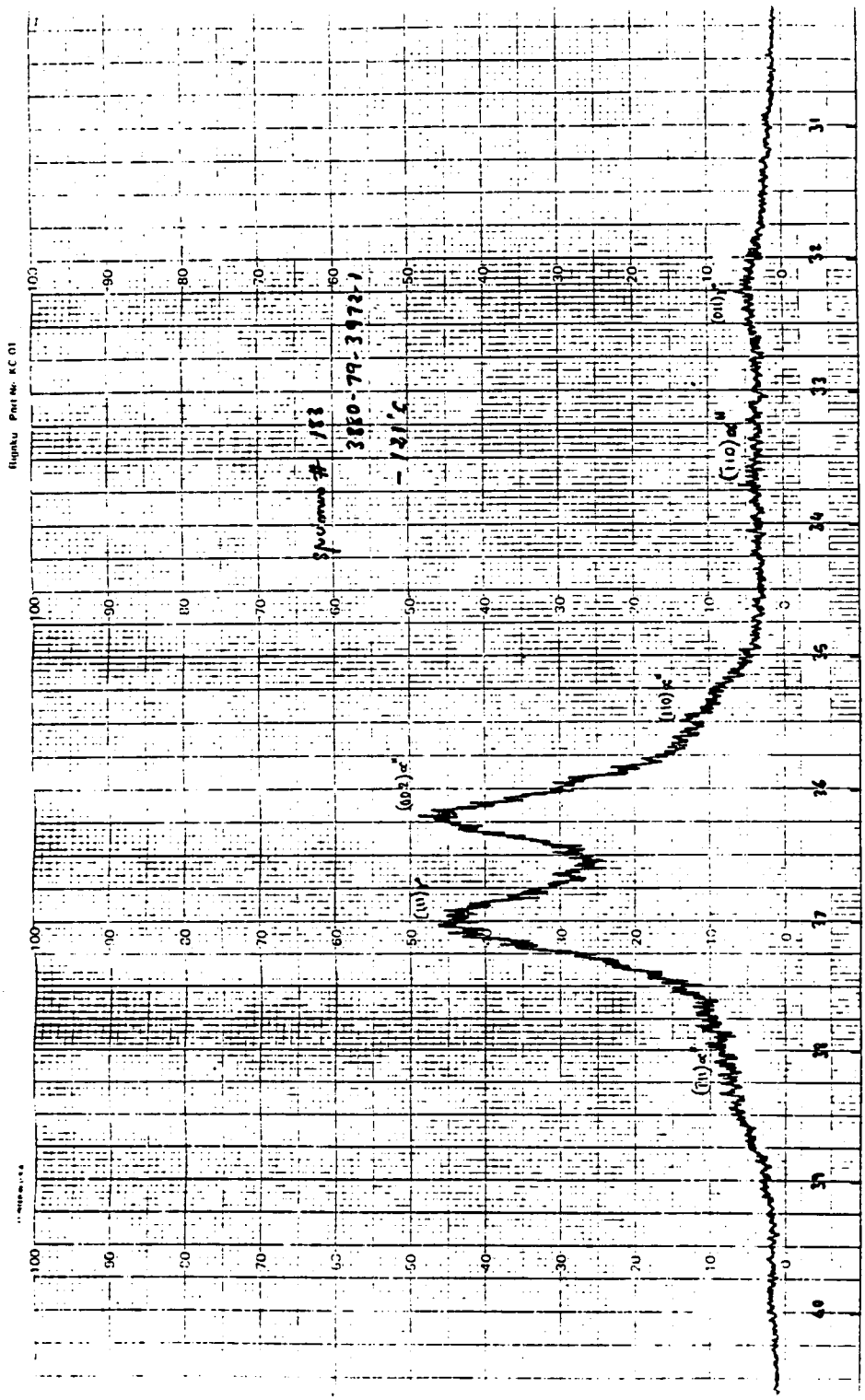

Figure A.44. Diffraction pattern of alloy 183 (15.5* at% Nb) at -121 °C.

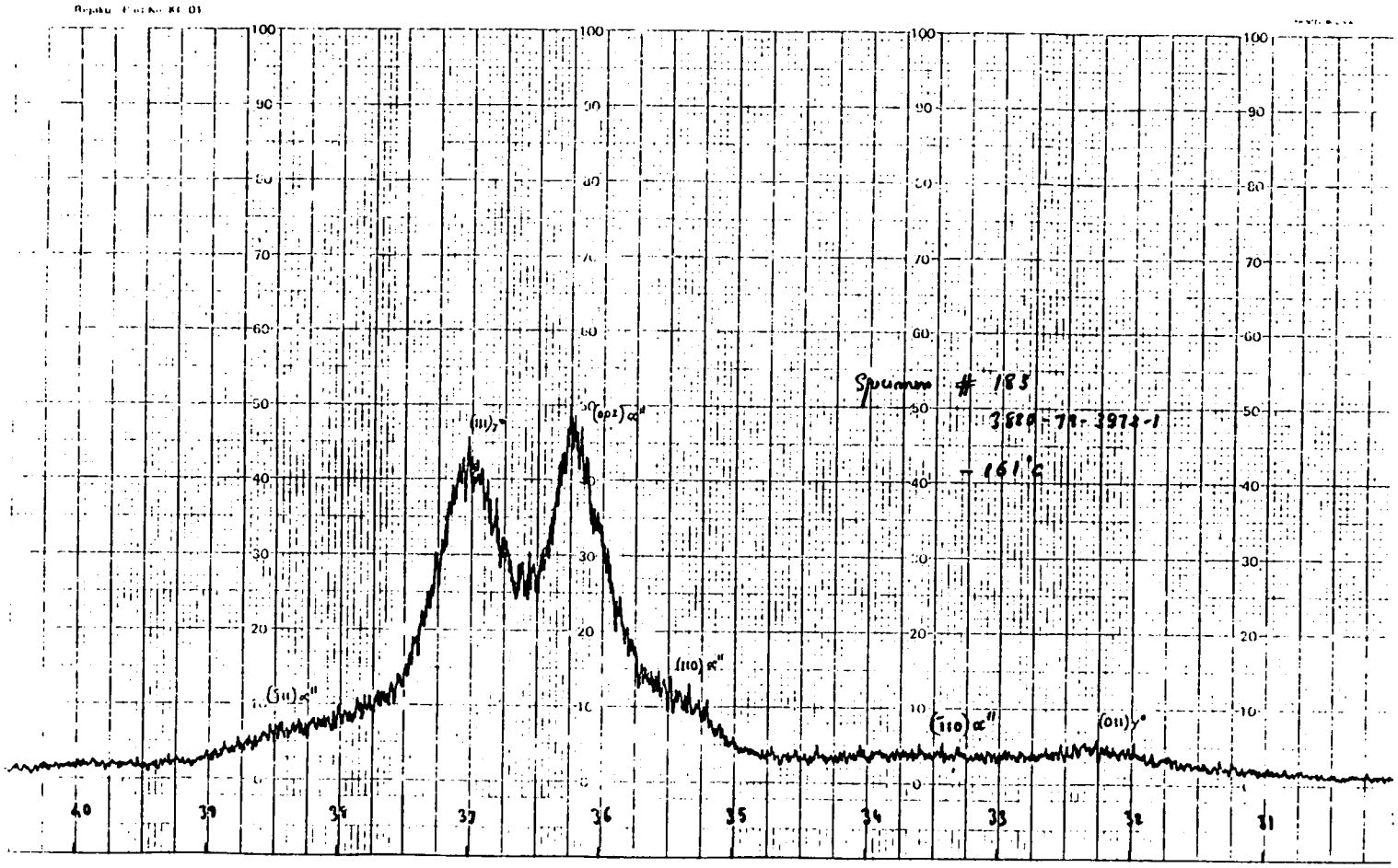

Figure A.45. Diffraction pattern of alloy 183 (15.5* at% Nb) at -161 °C.

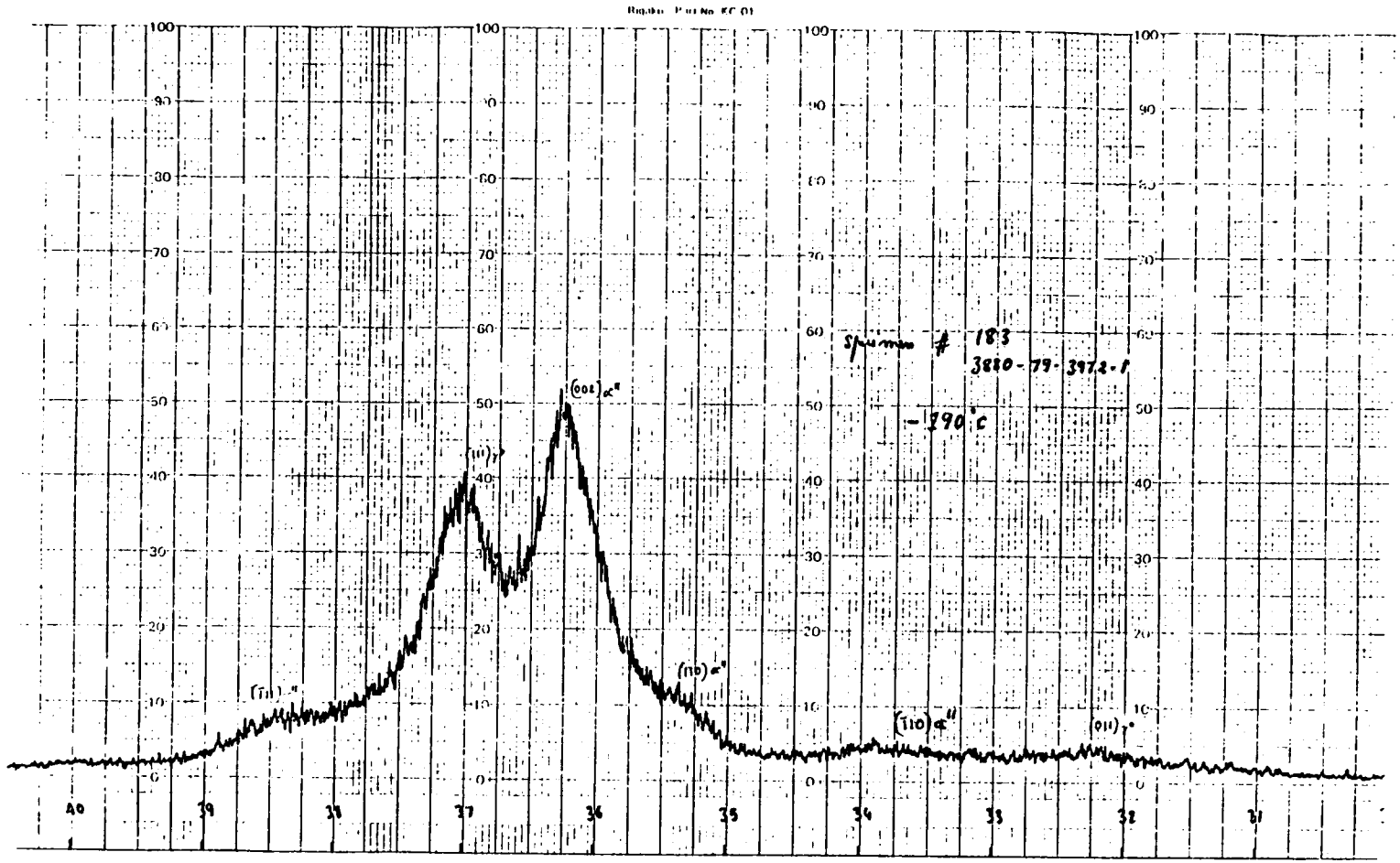

Figure A.46. Diffraction pattern of alloy 183 (15.5* at% Nb) at -190 °C.

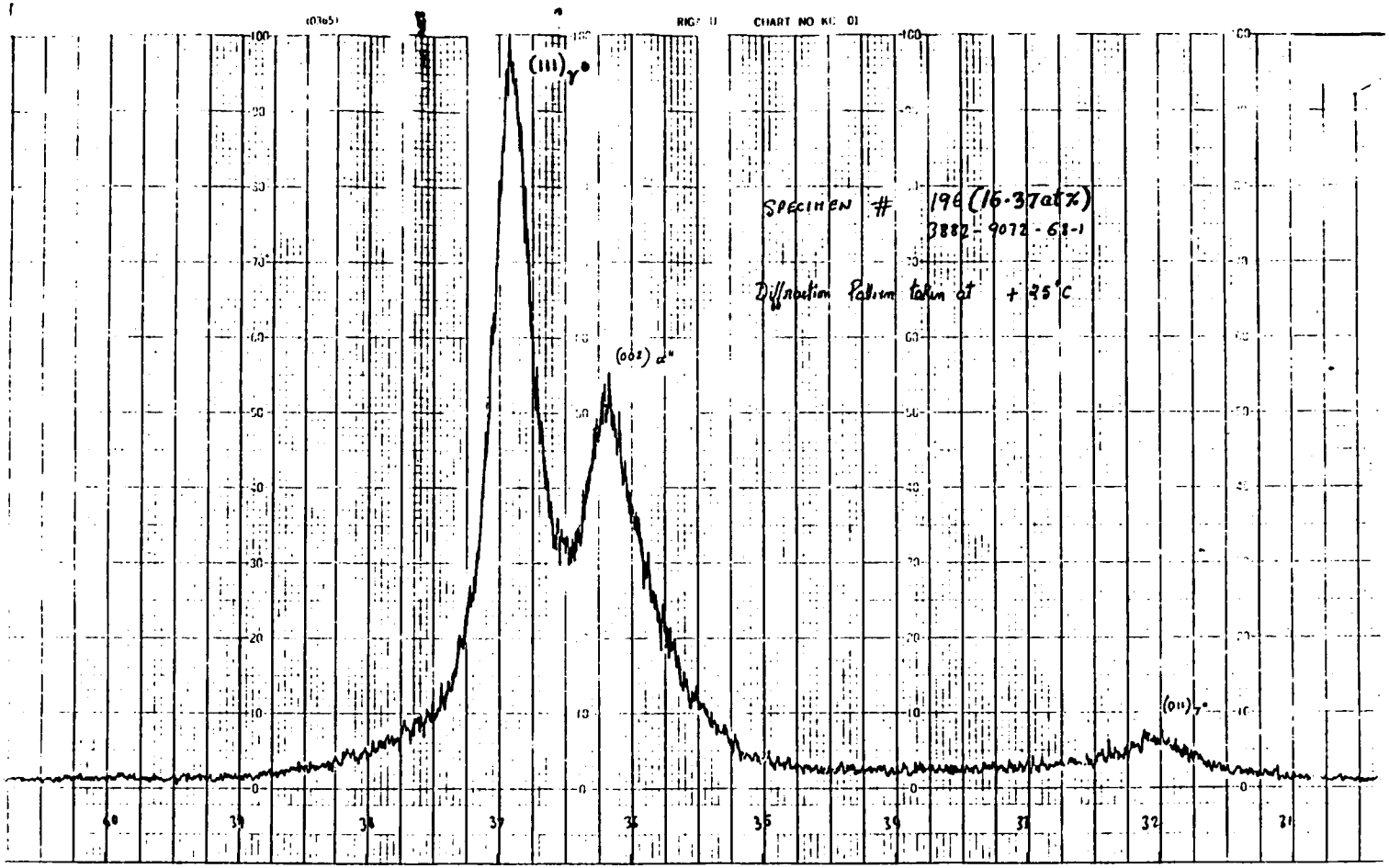

Figure A.47. Diffraction pattern of alloy 196 (15.5** at% Nb) at +25 °C.

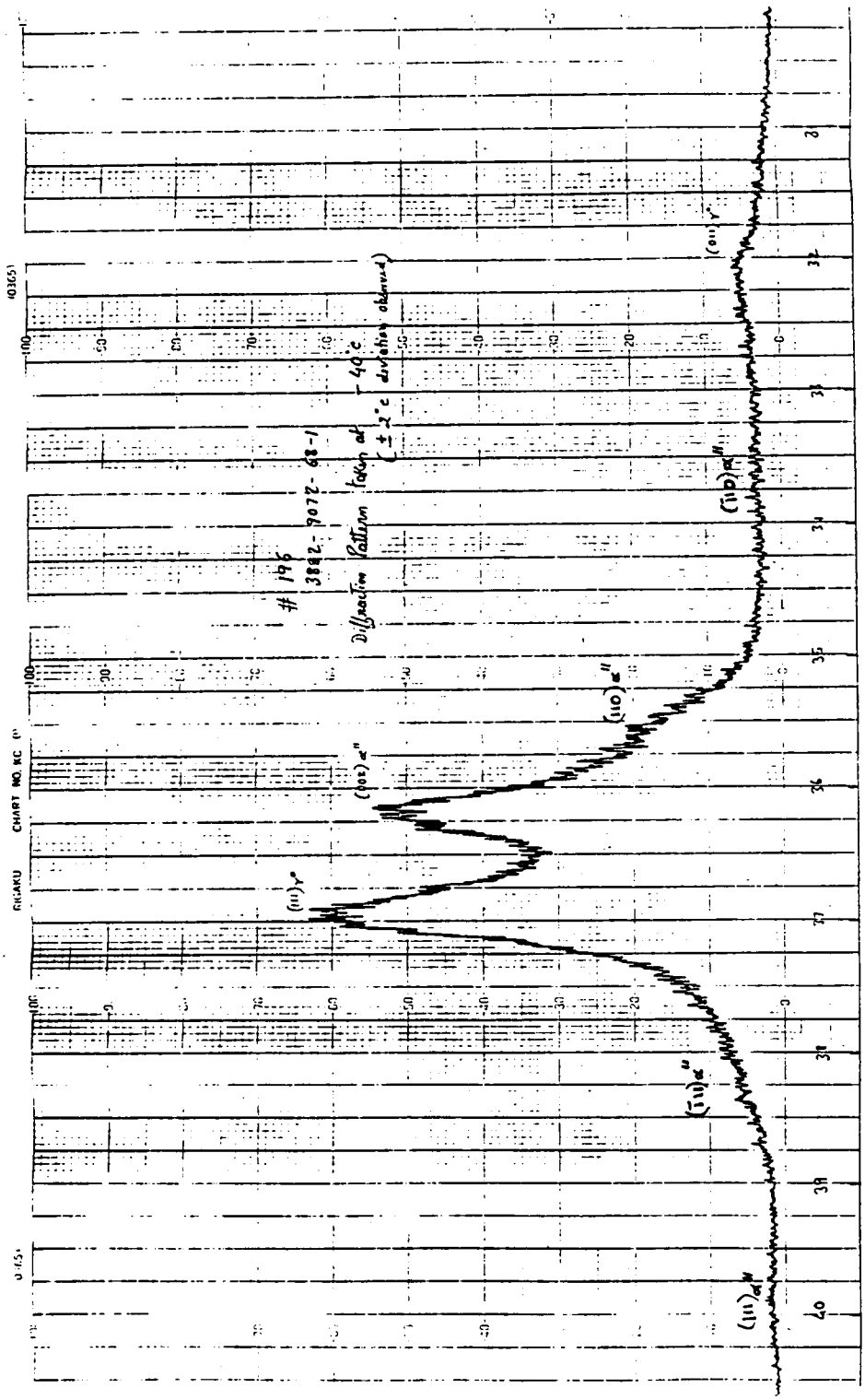

Figure A.48. Diffraction pattern of alloy 196 (15.5** at% Nb) at -40 °C.

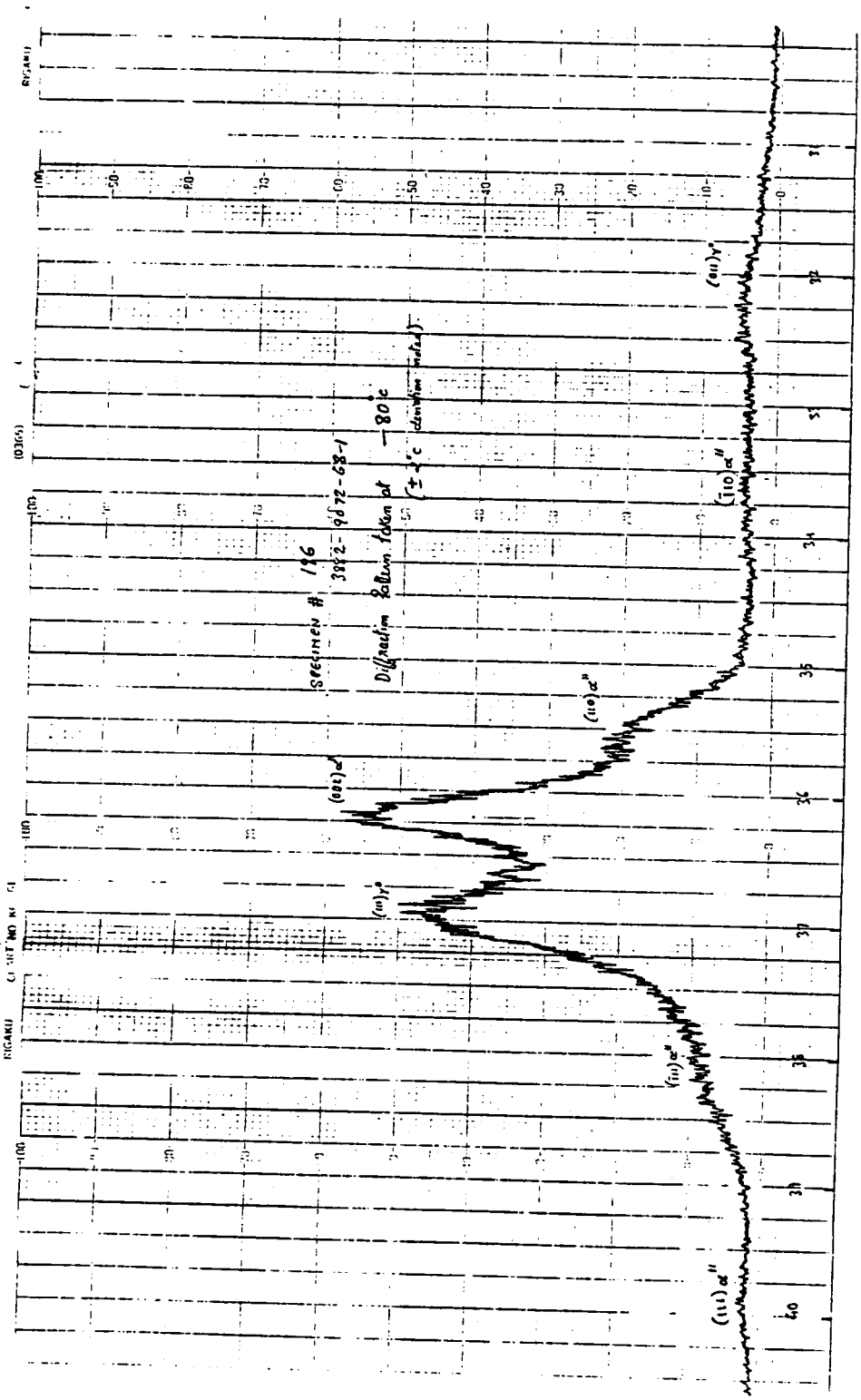

Figure A.49. Diffraction pattern of alloy 196 (15.5** at% Nb) at -80 °C.

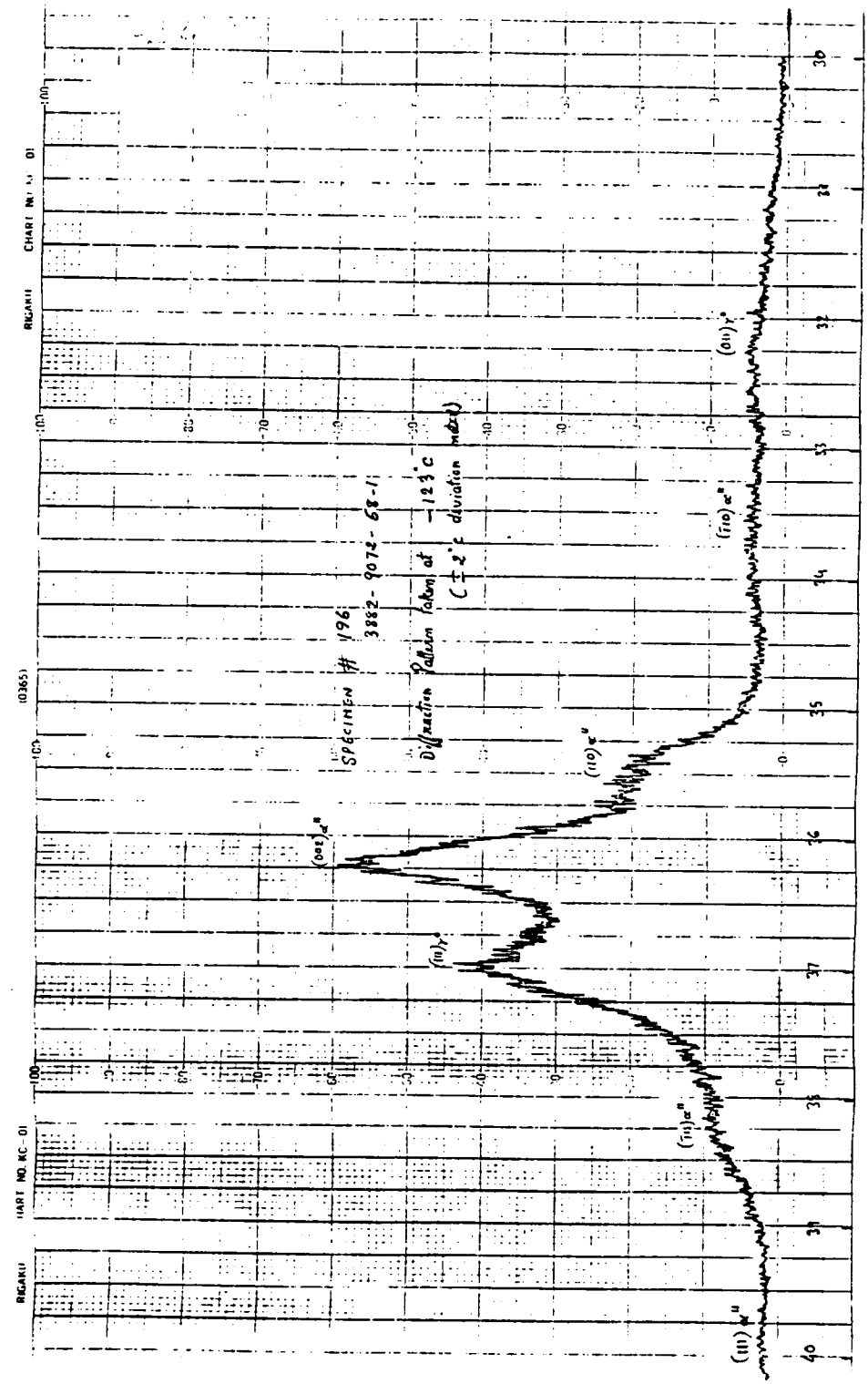

Figure A.50. Diffraction pattern of alloy 196 (15.5** at% Nb) at -123 °C.

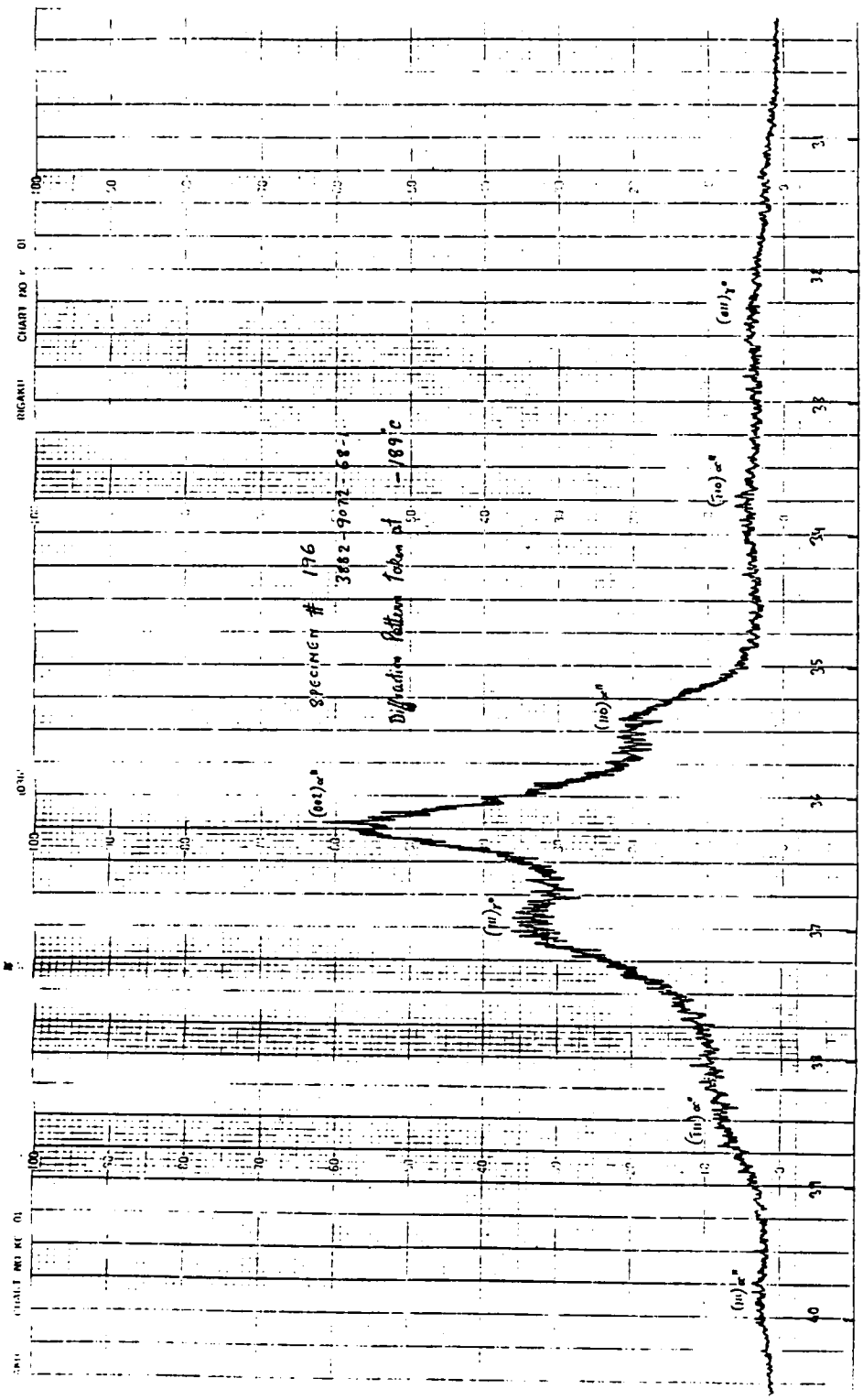

Figure A.51. Diffraction pattern of alloy 196 (15.5** at% Nb) at -189 °C.

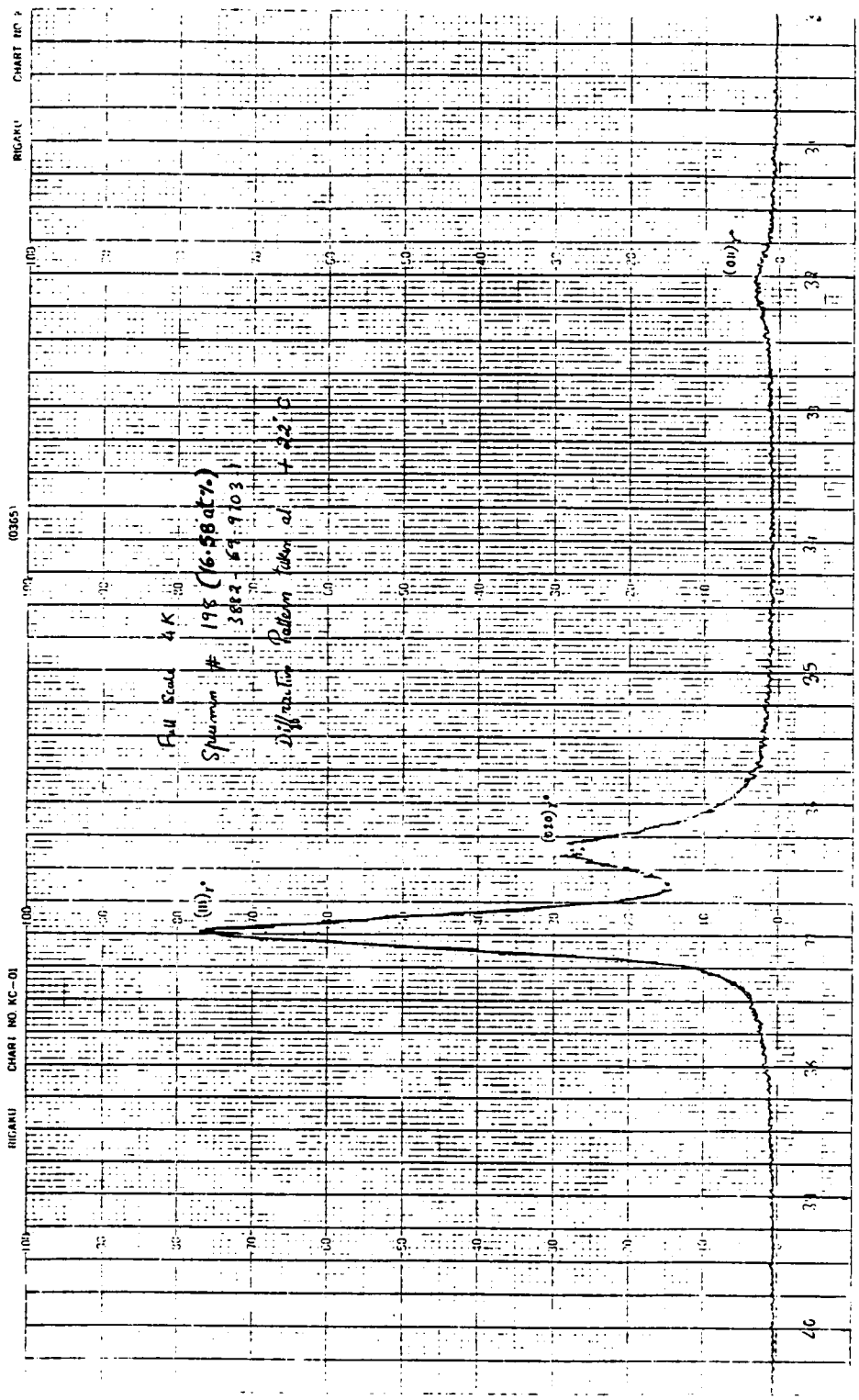

Figure A.52. Diffraction pattern of alloy 198 (16.0 at% Nb) at +22 °C.

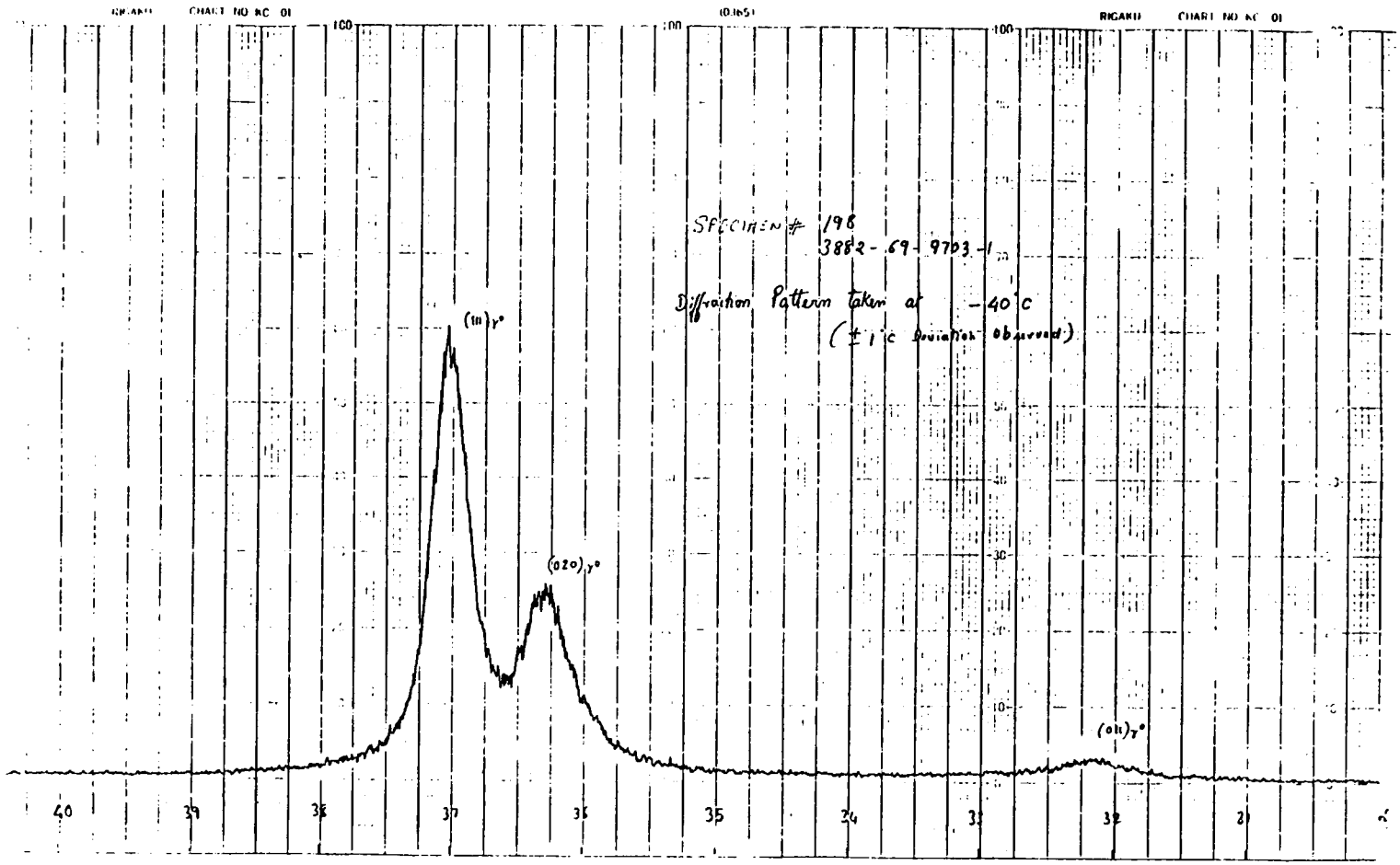

Figure A.53. Diffraction pattern of alloy 198 (16.0 at% Nb) at -40 °C.

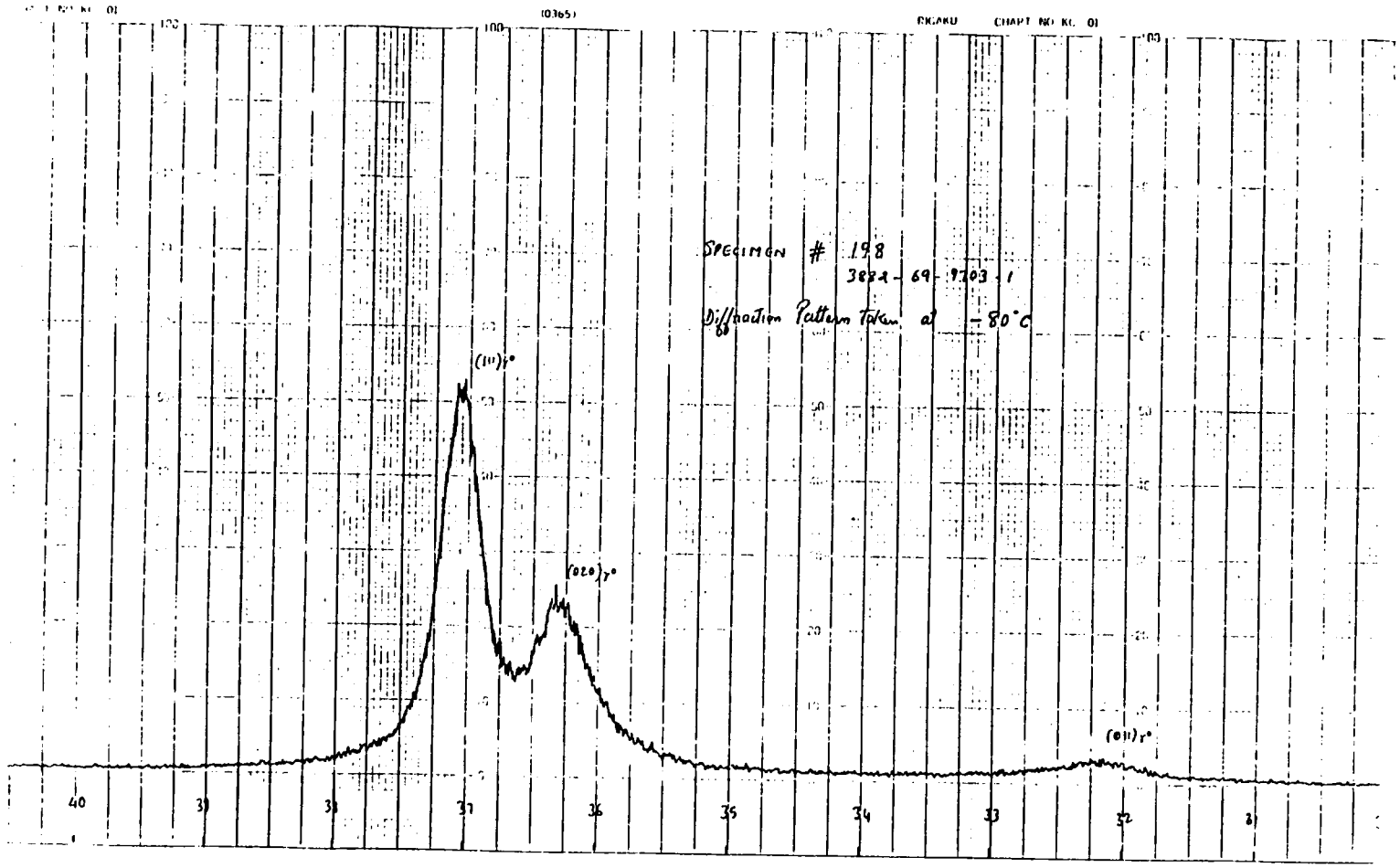

Figure A.54. Diffraction pattern of alloy 198 (16.0 at% Nb) at -80 °C.

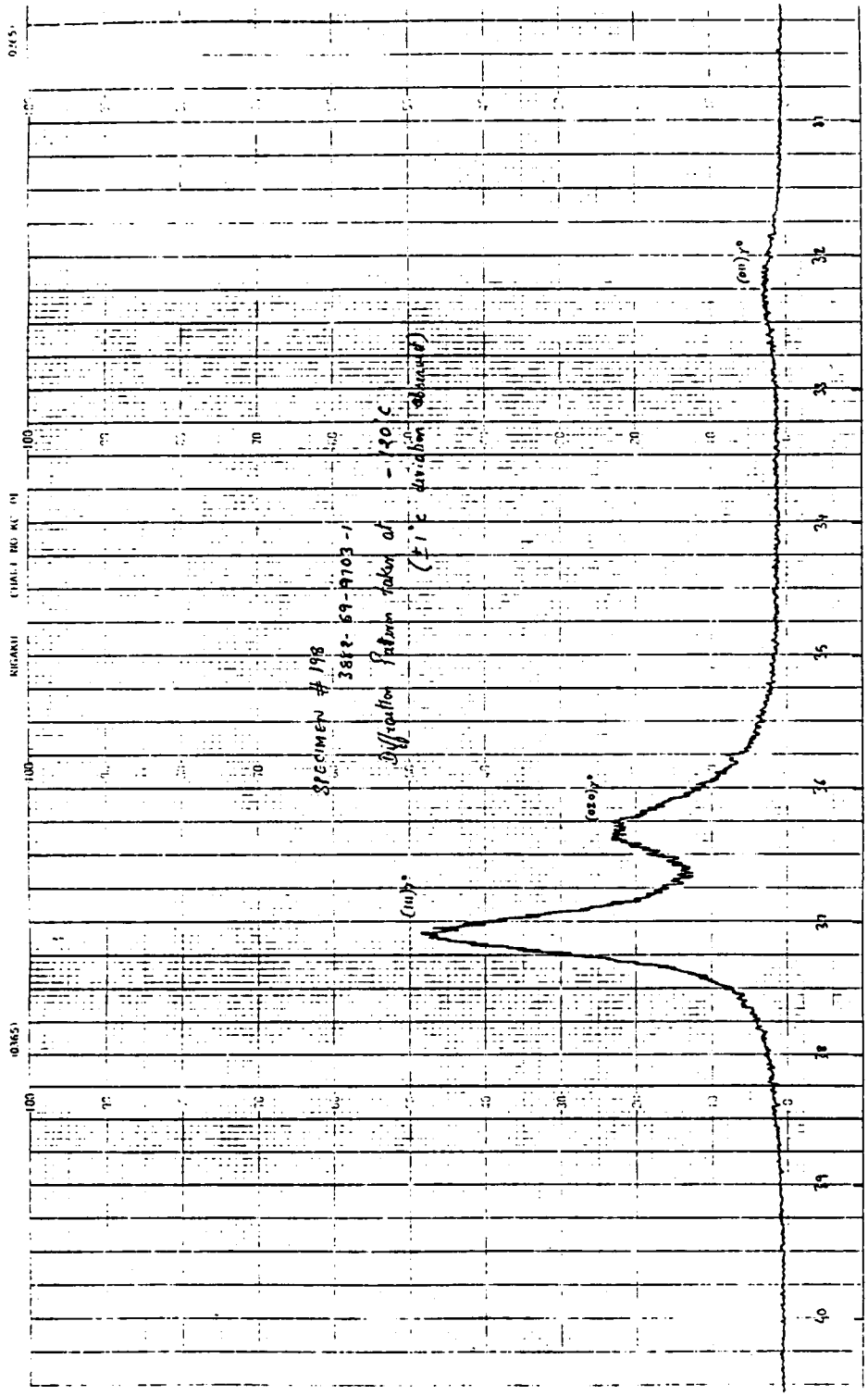

Figure A.55. Diffraction pattern of alloy 198 (16.0 at% Nb) at -120 °C.

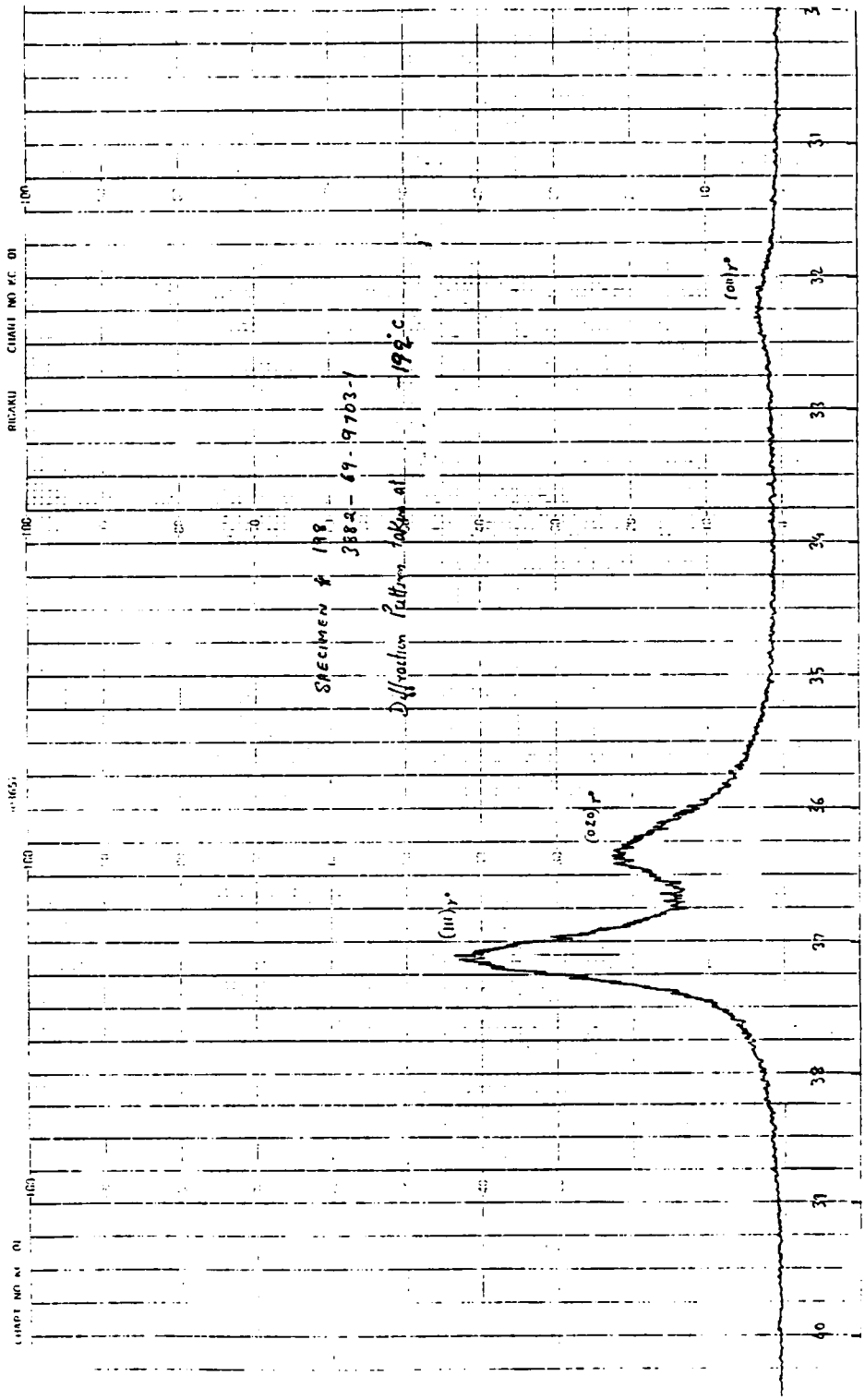

Figure A.56. Diffraction pattern of alloy 198 (16.0 at% Nb) at -192 °C.

VITA

Kalia Kothandapany was born to A. Kothandapany and K. Rajamani in Pondicherry, India, on august 23, 1958. He was the eldest child of eight, who along with his parents are currently residing in Pondicherry, India. He attended both elementary and high school in pondicherry, and graduated from high school in june 1976. He went on to pursue a degree in metallurgical engineering at the Karnataka Regional Engineering College, univeristy of mysore, India, and graduated in june 1982. He came to the United States in september 1982 and entered the graduate program in Metallurgical Engineering at The University of Tennessee, Knoxville, from which he received his Master of Science degree in March 1987.